ANALYSIS, DESIGN AND IMPLEMENTATION OF ENERGY HARVESTING SYSTEMS FOR WIRELESS SENSOR NODES

YEN KHENG TAN

NATIONAL UNIVERSITY OF SINGAPORE

2010

ANALYSIS, DESIGN AND IMPLEMENTATION OF ENERGY HARVESTING SYSTEMS FOR WIRELESS SENSOR NODES

YEN KHENG TAN
M.T.D.(Mechatronics) B.Eng(Hons.) NUS, Singapore

A THESIS SUBMITTED

FOR THE DEGREE OF DOCTOR OF PHILOSOPHY

DEPARTMENT OF ELECTRICAL AND COMPUTER ENGINEERING
NATIONAL UNIVERSITY OF SINGAPORE
2010

Acknowledgments

I remember the first time I get to know my supervisor, Associate Professor Sanjib Kumar Panda, was back in year 2001. At that time, I was taking one of his technical module. Throughout the course, I was really impressed by his marvelous teaching skill and great patience for guiding his students. From then onwards, I joined him as a final year undergraduate student and subsequently as a master student. Along the way, I am really fortunate to have his consistent encouragement and unlimited care and concern, which brought me thus far into the postgraduate program. I am also extremely grateful and obliged to my supervisor for his persistent help, advice and encouragement during my entire Ph.D study. In addition, I would like to express my sincere gratitude to Prof. Panda for spending his personal time for the correction as well as revision of this thesis. I would never forget his sacrifice for spending hours and hours with me for research discussions.

Other than the superb supervisory from Prof. Panda, I am really speechless to express my greatest gratitude to Mr. Y.C. Woo, Principal Laboratory Technologist, for his priceless help for my research project. To me personally, Mr. Woo is like a highly respectable elder and his tender loving care and concern (TLC) for me will remain in my heart forever. Whenever my spirits nose dived, he would always be there to keep on encouraging me. His parental attitude towards the lab people

dilutes the pressure and so the lab is really blessed by his presence. I would also like to express my sincere gratitude to Mr. M. Chandra, Mr. T.T. Teo, Mr. H.C. Seow and Mr. F.C. Looi for their timely helps and advices as well. I am also grateful to Mr. L.H. Chan, Mr. H.K. Seah and Mr. Anuwar of Electrical Engineering Workshop for their constant and immediate help in the mechanical arrangements for my experimental setup.

In my research laboratory here in NUS, I am really fortunate to be surrounded by a bunch of good and friendly people, who are always there to help me inregardlessly. These people, whom are all my past and present lab-mates, include Dr. Amit Kumar Gupta, Mr. Goh Qing Zhuang, Mr. Hoang Duc Chinh, Ms. Htay Nwe Aung, Mr. Ko Ko Win, Dr. Kong Xin, Mr. Krishna Mainali, Ms. Li Yanlin, Ms. Lim Shufan, Dr. Rajesh Kumar, Mr. Sangit Sasidhar, Mr. Siew Tuck Sing, Dr. Tanmoy Bhattacharya, Mr. Tran Duong, Ms. Wang Huanhuan, Dr. Wu Xinhui, Mr. Yadav Parikshit, Ms. Yu Xiaoxiao, Dr. Yin Bo, Ms. Zhou Haihua, and so on. I must express a big thank you to all of you for spending their valuable time in all possible discussions and their precious company and help. I have really spent a enjoyable and memorable life with them during my stay at NUS. In addition, I would never forget my two beloved Indian brothers, Dr. S.K. Sahoo "ji" and Mr. Souvik Dasgupta "Chhotu". Not forgetting all my FYP students and other young pupils that I have supervised before, I am deeply indebted for their contributions in some ways or another towards my research project. Thank you all for being my friends and teachers.

Last but not the least, I would like to dedicate the success of this Ph.D to my beloved family members viz. father, mother, eldest brother and his family, second

brother and his family and my highly respectable auntie. Their strong encouragement, support, patience and most importantly love for me have accompanied me through the entire time of my study, especially the darkest and hardest time. I would remember deep down in my heart all of these wonderful and unforgettable moments of my Ph.D study for the rest of my life.

Contents

Summary

With the recent advances in wireless communication technologies, sensors and actuators and highly integrated microelectronics technologies, *wireless sensor networks* (WSNs) have gained worldwide attention to facilitate monitoring and controlling of physical environments from remote locations that could be difficult or dangerous-to-reach. WSNs represent a significant improvement over wired sensor networks with the elimination of the hard-wired communication cables and associated installation and maintenance costs. The possible use of WSNs for real-time information in all aspects of engineering systems are virtually endless, from intelligent building control to health-care systems, environmental control systems, etc. As electronic hardware circuitries become cheaper and smaller, more and more of these WSN applications are likely to emerge, particularly as these miniaturized wireless sensor nodes offer the opportunity for electronic systems to be embedded unobtrusively into everyday objects to attain a "*deploy and forget*" scenario.

In great majority of autonomous sensor nodes in WSNs, electrical energy necessary for their operation is provided primarily by batteries. Batteries take up a significant fraction of the total size and weight of the overall system. Moreover, they are also the weakest link but yet the most expensive part of the system. Another very important factor to be considered is the requirement for proper main-

tenance of batteries, with the need to either replace or recharge them. This is a serious limitation to WSNs, in which there are dozens or hundreds of sensor nodes with batteries to maintain. Generally, the highest reported energy for present-day battery technologies ranges around 3.78 kJ/cm^3 [1], which implies that for an ultra-low-power miniaturized wireless sensor node with volumetric size of 1 cm^3 operating at an average power consumption of 100 μW to have a 10-year lifespan, needs as large as a 10 cm^3 size battery. Thus, energy supply is one of the major bottle neck for the lifetime of the sensor node and also constrained by the size of the battery.

The major hindrances of the *"deploy and forget"* nature of the WSNs are the limited energy capacity and unpredictable lifetime performance of the battery. In order to overcome these problems, *energy harvesting/scavenging*, which harvests/scavenges energy from a variety of ambient energy sources and converts into electrical energy to recharge the batteries, has emerged as a promising technology. With the significant advancement in microelectronics, the energy and therefore the power requirement for sensor nodes continues to decrease from few mWs to few tens of μW level. This paves the way for a paradigm shift from the battery-operated conventional WSN, that solely relies on batteries, towards a truly self-autonomous and sustainable energy harvesting wireless sensor network (EH-WSN). Various types of energy harvesting (EH) systems and their respective main components viz. energy harvester (source), power management circuit, energy storage device and wireless sensor node (load) have been investigated and analyzed in this dissertation. EH systems, based on wind energy harvesting (WEH), thermal energy harvesting (TEH), vibration energy harvesting (VEH), solar energy harvesting (SEH), hybrid energy harvesting (HEH) and magnetic energy harvesting, are designed to suit the

target applications viz. ambient conditions and event/task requirements and then implemented into hardware prototypes for proof of concept. To optimize these EH systems, several different types of power-electronic based management circuits such as active AC-DC converter, DC-DC converter with maximum power point tracking (MPPT), energy storage and latching circuit, etc. have been introduced.

Like any of the commonly available renewable energy sources, wind energy harvesting (WEH) has been widely researched for high power (> few MWs level) applications. However, few research works on the small-scale WEH can be found in the literature, that are used to power small autonomous sensors. Small-scale WEH system has the problems of low magnitude generated output voltage and low harvested electrical power, as such they pose severe constraints on the circuit design of the power management unit of the WEH wireless sensor node. To overcome the above mentioned problems, an optimized WEH system that uses an ultra-low-power management circuit with two distinct features: (1) an active rectifier using MOSFETs for rectifying the low amplitude AC voltage generated by the wind turbine-generator (WTG) under low wind speed condition efficiently and (2) a DC-DC boost converter with resistor emulation algorithm to perform maximum power point tracking (MPPT) under varying wind speed conditions are proposed. As compared to the conventional diode-bridge rectifier, it is shown that the efficiency of the active rectifier has been increased from 40 % to 70 % due to the significant reduction in the on-state voltage drop (from 0.6 V to 0.15 V) across each pair of MOSFETs used. The proposed robust low-power microcontroller-based resistance emulator is implemented with closed-loop resistance feedback control to ensure close impedance matching between the source and the load, resulting in efficient power conversion. From the experimental test results obtained, an aver-

age electrical power of 7.86 mW is harvested by the optimized WEH system at an average wind speed of 3.62 m/s, which is almost four times higher than the conventional energy harvesting method without using the MPPT.

For space constraint applications where small-scale WEH system needs to be as small as possible and highly portable, this type of conventional, large and bulky WTG is not that suitable. As such, a novel method to harvest wind energy using piezoelectric material (PZT) has been presented. The overall size of the proposed PZT structure is much smaller, as compared to the WTG. Energy harvested from the piezoelectric based wind energy harvester is first accumulated and stored in a capacitor until there is sufficient stored energy to power the sensor node, a trigger signal is then initiated to release the stored energy in the capacitor to the wind speed sensor node. Experimental results obtained show that the harvested stored energy of 917 μJ is used to detect wind speed beyond a certain threshold level of 6.7 m/s for an early warning of storm detection system.

In some places where wind energy source is not available, thermal energy harvesting (TEH) from ambient heat sources with low temperature differences have recently received great attention but impeded by the challenges of low energy conversion efficiency, inconsistency, low output power due to temperature fluctuation and higher cost. To supplement the TEH scheme, an efficient power management circuit that could maximize power transfer from the thermal energy source to its connected electronic load is desirable over a wide range of operating conditions. In this dissertation, a DC-DC buck converter with resistor emulation based maximum power point (MPP) tracker is presented for optimal TEH scheme in sustaining the operation of wireless sensor nodes. From the experimental test results obtained, an

average electrical power of 629 μW is harvested by the optimized TEH system at an average temperature difference of 20 K, which is almost two times higher than the conventional energy harvesting method without using MPPT scheme.

Electrical cables that are used in residential and industrial buildings to connect the appliance to the control switch on the wall have been a cause of nuisance as well as result in higher installation cost. Undesirable re-cabling implications may also arise over time should the cable become faulty over time. To overcome the problem, a batteryless and wireless remote controller is proposed to switch the electrical appliances such as lights and fans ON/OFF in a wireless manner. In this dissertation, two types of piezoelectric-based vibration energy harvesting (VEH) systems are presented to harvest impact or impulse forces from human pressing a button or switch action. By depressing (1) the piezoelectric pushbutton igniter or (2) the pre-stressed piezoelectric diaphragm material, electrical energy is generated and stored in the capacitor. Once sufficient energy is harvested, the batteryless and wireless remote controller is powered up for operation.

Energy harvesting system itself has an inherent problem, that is the intermittent nature of the ambient energy source; hence the operational reliability of the wireless sensor node may be compromised due to unavailability of the ambient energy source for a prolonged period of time. To augment the reliability of the wireless sensor nodes operation, two types of hybrid energy harvesting (HEH) approaches are investigated. A hybrid of wind and solar energy harvesting scheme is proposed to harvest simultaneously from both energy sources in order to extend the lifetime of the wireless sensor node. When the two energy sources of different characteristics are combined together, it is bound to have the issue of impedance

mismatch between the two different sources and the load. Hence, each energy source has its own power management unit to maintain at its respective maximum power points (MPPs). The WEH sub-system uses the resistor emulation technique while the SEH sub-system uses the constant voltage technique for MPP operation. Experimental results obtained show that an average electrical power of 22.5 mW is harvested by the optimized HEH system at an average wind speed of 4 m/s and an average light irradiance of 80 W/m^2, which is almost three times higher than the single wind-based energy source.

In another HEH research work, a hybrid of indoor ambient light and thermal energy harvesting scheme that uses only one power management circuit to condition the combined output power harvested from both energy sources is proposed to extend the lifetime of the wireless sensor node. By avoiding the use of individual power management circuits for multiple energy sources, the number of components used in the HEH system are reduced and the system form factor, cost and power losses are thus reduced. An efficient microcontroller-based ultra low power management circuit with fixed voltage reference based MPPT is implemented with closed-loop voltage feedback control to ensure near maximum power transfer from the two energy sources to its connected electronic load over a wide range of operating conditions. From the experimental test results obtained, an average electrical power of 621 μW is harvested by the optimized HEH system at an average indoor solar irradiance of 1010 lux and a thermal gradient of 10 K, which is almost triple of that can be obtained with conventional single thermal-based energy source.

Other than energy harvesting, this dissertation has also demonstrated an alternative means to remotely power low-power electronic devices through wireless

power transfer (WPT) mechanism. The WPT mechanism uses the concept of inductive coupling i.e. by harvesting the stray magnetic energy in power lines to transfer electrical power without any physical connection. The AC voltage and current in the power lines are 230 V and 1-4 A. Experimental results obtained show that the implemented magnetic energy harvester is able to harvest 685 μJ of electrical energy from the power lines to energize the RF transmitter to transmit 10 packets of 12-bits encoded digital data to the remote base station in a wireless manner. To extend the WPT distance, self-resonating coils, operating in a strongly coupled mode, is demonstrated. Experimental results obtained show that the WPT system is capable of delivering wireless output power up to 1 watt at an efficiency of 51 % over a separation distance of 20 cm to power a small light bulb.

Till this stage, the proof of concepts for the developed energy harvesting (EH) prototypes have been demonstrated. The performances of the EH systems in powering the wireless sensor node are investigated and tested under various operating conditions simulated in the laboratory. In addition, the EH prototypes are optimized according to their designed applications. However, in reality, the environmental conditions of the deployment area are not as ideal as in the laboratory environment. Hence, the next stage of this EH research, which is considered as the future work, is to carry out a series of application-specific field trials to evaluate the performances of the EH systems under real-life deployment conditions for a prolong period of time. In order for the energy harvesting mechanism to be successful, an overall system optimization with respect to energy consumption taking into account the duty-cycling operation of the WSNs for the entire chain i.e. from sensing the environmental parameter to transmitting and delivering the sensed parameter reliably is to be investigated. This part of the work is beyond the scope of

this dissertation and therefore proposed as future research work.

List of Tables

List of Figures

List of Acronyms

AM	Amplitude Modulation
CCM	Continous Conduction Mode
CV	Constant Voltage
DCM	Discontinous Conduction Mode
EH	Energy Harvesting
EH-WSN	Energy Harvesting Wireless Sensor Network
EM	ElectroMagnetic
EMF	ElectroMotive Force
ESR	Equivalent Series Resistance
FOCV	Fractional Open-Circuit Voltage
HEH	Hybrid Energy Harvesting
IC	Integrated Circuit
IncCond	Incremental Conductance
MIT	Massachusetts Institute of Technology
MPP	Maximum Power Points
MPPT	Maximum Power Point Tracking

NMOS	N-Type MOSFET
PMOS	P-Type MOSFET
PI	Proportional-Intergral
PV	Photovoltaic
PFC	Power Factor Correction
P&O	Perturbation and Observation
PPU	Power Processing Unit
PVDF	PolyVinyliDene Fluoride
PZT	Lead Zirconate Titanate
PWM	Pulse Width Modulation
QoS	Quality of Service
RF	Radio Frequency
RFID	Radio Frequency IDentification
SEH	Solar Energy Harvesting
TEG	Thermoelectric Generator
TEH	Thermal Energy Harvesting
TI	Texas Instrument
VEH	Vibration Energy Harvesting
VLO	Very Low-frequency Oscillator
WEH	Wind Energy Harvesting
WPT	Wireless Power Transfer
WSN	Wireless Sensor Network
WTG	Wind Turbine-Generator

List of Symbols

a	radius of a wire
A	wind front contact area (m^2)
A_{leg}	area of a single thermocouple leg
B	magnetic flux density
C_p	power coefficient
d_{31}	transverse piezoelectric coefficient
d_{em}	emulated duty cycle
D	duty cycle of power converter
D_{opt}	optimal duty cycle
E_y	Young's modulus of a beam
F	aerodynamic lift force
f_s	switching frequency of the gating signal of the PWM switch
g	gravitational acceleration (m/s^2)
$g_1 - g_4$	gating signals of MOSFET switches
G	instantaneous conductance
I_{TEG}	current generated by a thermoelectric generator

I_{in}, I_{out}	input and output currents of converter
I_L	light-generated current
I_{mppt}	MPPT current
I_o	dark/reverse saturation current of the p-n diodes
I_p	AC peak current
I_{pv}, I_{solar}	photovoltaic/solar output current
V_{R_L}	current flowing into an electrical load
I_{sc}	short-circuit current
$I_{wind,scaled}$	scaled voltage equivalent of DC current of wind turbine-generator
k	Boltzmann's constant
k_{31}	transverse piezoelectric coupling coefficient
l	length of wire
M	bending moment of a beam
N	number of winding turns in a coil
n_s	number of photovoltaic cells in series
P_{ac}, P_{dc}	AC and DC electrical powers
$P_{consumed}$	power consumption of associated sensing, P_{sense}, control, P_{ctrl}, and PWM generation, $P_{generate}$, electronic circuits.
P_{elec}	electrical power
P_{HEH}	electrical power throughput of hybrid energy harvester
$P_{HEH,actual}$	actual harvested power of hybrid energy harvester
$P_{HEH,mppt}$	maximum attainable power of hybrid energy harvester
P_{in}, P_{out}	input and output powers

P_L, P_{load}	load power
P_{max}	maximum power throughput
P_{pv}, P_{solar}	photovoltaic/solar output power
P_T	mechanical power
P_{TEG}	thermoelectric generator output power
P_{wind}	raw wind power
P	net pressure applied
$P_{ambient}$	ambient pressure
P_{above}, P_{below}	pressure above and below an airfoil
Q	electrical charge generated
r	radius of a coil
$R_{con(H)}, R_{con(C)}$	thermal resistances of contact and grease
$R_{g(H)}, R_{g(C)}$	on hot and cold side of thermal energy harvester
$R_{em}, R_e(d)$	emulated resistances
R_{fb}	feedback resistance signal
R_L, R_{load}	load resistor
$R_{opt,ref}$	reference resistance signal
R_{ohmic}	ohmic or absorption loss
$R_{radiative}$	radiation loss
R_s, R_{sh}	series and shunt resistances
R_{sense}	sensing resistor
$R_{s,TEG}$	internal resistance of a thermoelectric generator
R_{TEG}	thermal resistance of thermoelectric generator

R_{Total}	total thermal resistance residing in the housing structure of a thermal energy harvester
R	radius of curvature of the neutral-axis
S	Seebeck's coefficient of thermoelectric generator
t	instanteous time
t_{charge}	time taken to charge a supercapacitor
T_H, T_C	hot and cold temperatures
T_{HJ}, T_{CJ}	hot and cold junction temperatures
T_s	switching period of the gating signal of the PWM switch
U_r, μ_r	relative permeability of the magnetic core
U_o, μ_o	permeability of free air space
V_{cap}	voltage across supercapacitor
V_{dc}	DC voltage
V_{emf}	induced back-emf voltage
V_{gnd}	ground voltage
$V_{gs}(th)$	threshold gate-source voltage
V_{in}, V_{out}	input and output voltages of converter
V_{max}, V_{min}	maximum and minimum voltage levels of a capacitor
V_{mppt}	MPPT voltage
$V_{mppt,ref}$	MPPT reference voltage
V_{oc}	open-circuit voltage
V_{on}	on-state voltage drop across a diode
V_p	AC peak voltage

V_{pv}, V_{solar}	photovoltaic/solar output voltage
V_{R_L}	voltage generated across an electrical load
V_t	junction terminal thermal voltage
V_{TEG}	voltage generated by a thermoelectric generator
$V_{wind,scaled}$	scaled DC voltage of wind turbine-generator
v_1, v_2	input AC voltages of active rectifier
v	wind speed (metre/sec)
v_a, v_b	wind speed above and below an airfoil
y	beam deflection
ΔT	temperature difference between hot and cold sides
ΔT_{TEG}	temperature difference across a thermoelectric generator
L, w, t	length, width and thickness of a beam
ρ	air density
η_{conv}	efficiency of power converter
η_{diode}	efficiency of diode block
ε	mechanical strain applied
σ	mechanical stress applied
$\theta_L, \theta_W, \theta_Z$	roll, pitch and yaw angles
α	Seebeck's coefficient of a thermocouple
ϕ	magnetic flux
ω	angular speed
κ	coupling coefficient of the coils
Γ	intrinsic loss rate

Chapter 1

Introduction

The rapid growth in demand for computing everywhere has made computer a pivotal component of human mankind daily lives [2]. Whether we use the computers to gather information from the Web, to utilize them for entertainment purpose or to use them for running business, computers are noticeably becoming more widespread, mobile and smaller in size. What we often overlook and do not notice is the presence of those billions of small pervasive computing devices around us, which provide the intelligence being integrated into the real world "*Smart Environment*" [2], to help us to solve some crucial problems in the activities of our daily lives. To achieve this vision of the smart environment with *pervasive computing*, also known as *ubiquitous computing*, many computational devices are integrated in everyday objects and activities to enable better human-computer interaction. These computational devices, which are generally equipped with sensing, processing and communicating abilities, are known as *wireless sensor nodes*. When these wireless sensor nodes are connected together, they form a network called the *Wireless Sensor Network (WSN)*.

1.1 Motivation of Wireless Sensor Networks

With the recent advances in wireless communication technologies, sensors and actuators and highly integrated microelectronics technologies, *wireless sensor networks* (WSNs) have gained worldwide attention to facilitate monitoring and controlling of physical environments from remote locations that could be difficult or dangerous-to-reach. In the Massachusetts Institute of Technology (MIT) technology review magazine of innovation published in February 2003 [3], the editors have identified WSNs as the first of the top ten emerging technologies that will change the world.

1.1.1 Architecture of WSN

WSNs represent a significant improvement over wired sensor networks with the elimination of the hard-wired communication cables and associated installation and maintenance costs. The architecture of a wireless sensor network (WSN) typically consists of multiple pervasive sensor nodes, sink, public networks, manager nodes and end user [4]. Many tiny, smart and inexpensive sensor nodes are scattered in the targeted sensor field to collect data and route the useful information back to the end user. These sensor nodes cooperate with each other via wireless connection to form a network and collect, disseminate and analyze data coming from the environment. To ensure full connectivity, fault tolerance and long operational life, WSNs are deployed in ad-hoc manner and the networks use multi-hop networking protocols to obtain real-world information and perform control ubiquitously [5]. As illustrated in Figure.1.1, the data collected by *node A* is routed within the sensor field by other nodes. When the data reaches the boundary *node E*, it is

then transferred to the sink. The sink serves as a gateway with higher processing capacity to communicate with the task manager node. The connection between sink and task manager node is the public networks in the form of Internet or satellite. Once the end user receives the data from the task manager node, some processing actions are then performed on the received data.

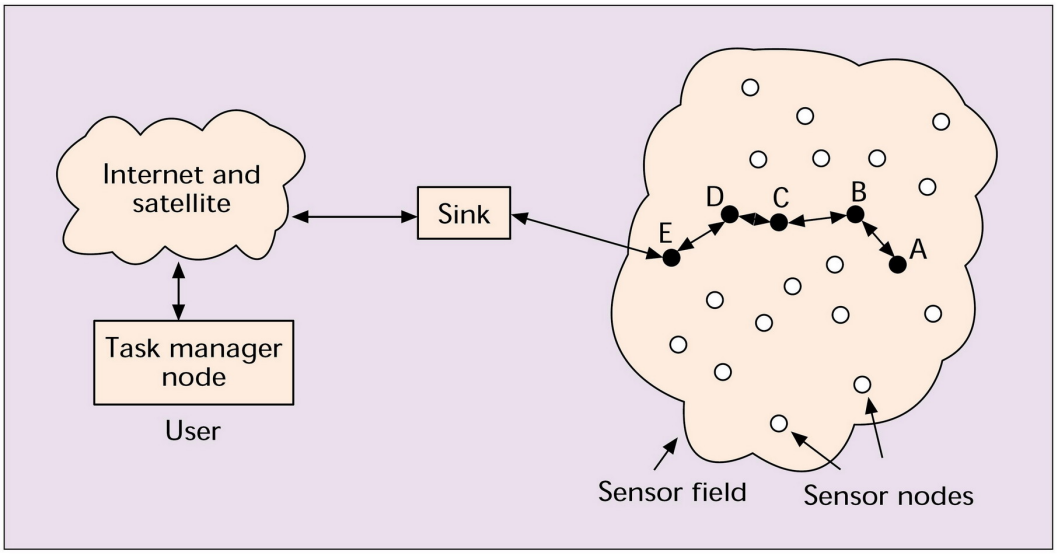

Figure 1.1: Architecture of WSN to facilitate smart environments [4]

In Figure.1.1, the sink is essentially a coordinator between the deployed sensor nodes and the end user and it can be treated like a gateway node. The need of a sink in WSN architecture is due to limited power and computing capacity of each of the wireless sensor nodes. The gateway node, typically powered by the readily available power source from the AC main, is equipped with better processor and sufficient memory space such that it is able to provide the need for extra information processing before data is transferred to the final destination. The gateway node can therefore share the loadings posed on the wireless sensor nodes and hence prolong their working lifetime. To understand how data are communicated within the sensor nodes in a WSN shown in Figure.1.1, the protocol stack model of the

WSN as shown in Figure.1.2 is investigated. With this understanding, the energy hungry portions of the wireless sensor node can be identified and then the WSN can be redesigned accordingly for lower power consumption. To start with the basic communication process, it consists of sending data from the source to the destination. Primarily, it is the case of two wireless sensor nodes wanting to communicate with each other. Hence, the sensor node at source generates information, which is encoded and transmitted to destination, and the destination sensor node decodes the information for the user. This entire process is logically partitioned into a definite sequence of events or actions, and individual entities then form layers of a communication stack. The WSN protocol stack [4] shown in Figure.1.2 consists of five network layers namely physical (lowest), data link, network, transport and application (highest) layers.

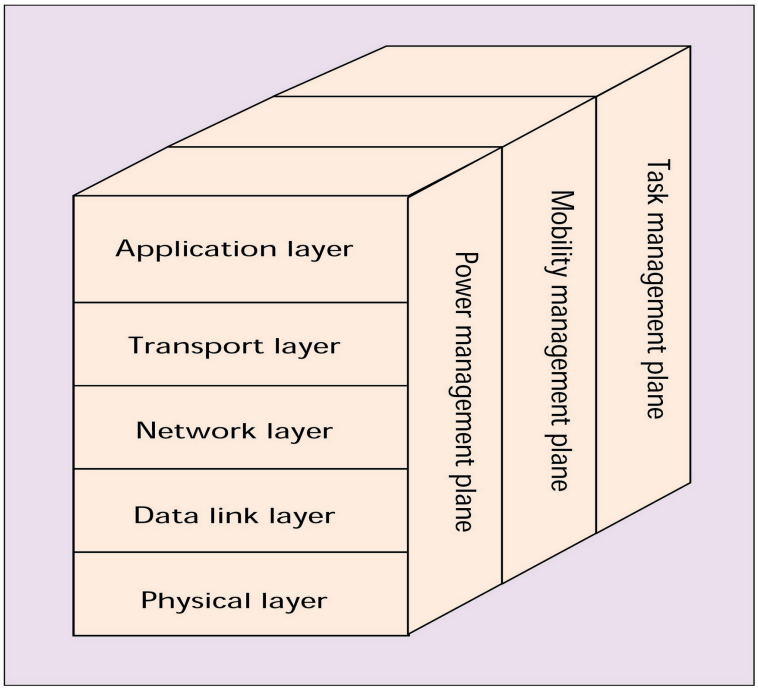

Figure 1.2: Sensor networks protocol stack [4]

Starting from the lowest level, the physical layer is to meet the needs of

receiving and transferring data collected from the hardware. It is well known that long distance wireless communication can be expensive, in terms of both energy and implementation complexity. While designing the physical layer for WSNs, energy minimization is considered significantly more important over and above the other factors like propagation and fading effects. Energy-efficient physical layer solutions are currently being pursued by researchers to design for tiny, low-power, low-cost transceiver, sensing and processing units [6]. The next higher layer is the data link layer which ensures reliable point-to-point and point-to-multi-point connections for the multiplexing of data streams, data frame detection, medium access and error control in the WSN. The data link layer should be power-aware and at the same time to minimize the collisions between neighbors' signals because the environment is noisy and sensor nodes themselves are highly mobile. This is also one of the layers in the WSN whereby power saving modes of operation can be implemented. The most obvious means of power conservation is to turn the transceiver off when it is not required. By using a random wake-up schedule during the connection phase and by turning the radio off during idle time slots, power conservation can be achieved. A dynamic power management scheme for WSNs has been discussed in [7] where five power-saving modes are proposed and inter-mode transition policies are investigated.

The network layer takes care of routing the data supplied by the transport layer. In WSN deployment, the routing protocols in the network layer are important because an efficient routing protocol can help to serve various applications and save energy. By setting appropriate energy and time delay thresholds for data relay, the protocol can help prolong the lifetime of sensor nodes. Hence the network layer is another layer in the WSN to reduce power consumption. The transport layer

helps to maintain the flow of data if the sensor networks application requires it. Depending on the sensing tasks, different types of application software can be built and used on the application layer. In contrast to the traditional networks which focus mainly on how to achieve high quality of service (QoS) provisions, WSN protocols tend to focus primarily on power conservation and power management for sensor nodes [7], [8] as well as the design of energy-aware protocols and algorithms for WSNs [5], [9] in order to reduce the power consumption of the overall wireless sensor network. By doing so, the lifetime of the WSN can be extended.

However, there must be some embedded trade-off mechanisms that give the end user the option of prolonging the WSN lifetime but at the cost of lower throughput or higher transmission delay. Conversely, the power consumption of the WSN can be reduced by sacrificing the QoS provisions i.e. lowering the data throughput or having higher transmission delay. Among the several challenging requirements posed on the design of the underlying algorithms and protocols of the WSNs, it is well-known among the academia as well as industry [10] - [12] that energy constraint is one of the most significant challenges in the WSN research field [13]. The functionalities of the WSN are highly dependent on the amount of energy that is available to be expended by each of the sensor node in the network. As such, the energy constraint challenge of WSN is substantial enough to be investigated and discussed in this thesis. It is a multi-objective optimization problem concerning various WSN parameters like QoS, transmission delays, lifetime, energy, etc.

1.1.2 Applications of WSN

WSNs can be used in virtually any environment, even where wired connections are not possible or the terrain inhospitable or physical placement of the sensors are difficult. Besides that, WSNs also enable autonomous monitoring of physical quantities over large areas on a scale that would be prohibitively expensive to accomplish with human beings. These attractive features promote the potential of WSNs for more application areas. There have been many applications suggested for WSNs in the literature and they can be roughly classified into three categories suggested in [14]:

- monitoring space
- monitoring entities
- monitoring the interactions of entities with each other and the encompassing space

The first classification includes environmental monitoring, indoor climate control, military and space surveillance. In military application for example, a large quantity of the pervasive computing devices could be deployed over a battlefield to detect enemy intrusion instead of manually deploying the landmines for battlefield surveillance and intrusion detection [10]. The second classification includes condition-based equipment maintenance, medical health diagnostics, vehicle safety, urban terrain mapping and structural monitoring where pervasive computing devices are deployed to detect for any damage in buildings, bridges, ships and aircraft [15]. The most dramatic applications fall under the third classification which

involve monitoring complex interactions, including wildlife habitats, disaster management, emergency response, asset tracking and manufacturing process flow. More of these WSN applications are likely to emerge as electronic hardware circuities becomes cheaper and smaller and these miniaturized wireless sensor nodes offer the opportunity for electronic systems to be completely connected, intuitive, effortlessly portable, constantly available and embedded unobtrusively and pervasively into everyday objects to attain a "*deploy and forget*" scenario.

1.1.3 Wireless Sensor Nodes of WSN

Wireless sensor networks (WSNs), based on the collaborative efforts of a large number of sensor nodes distributed throughout an area of interest, have become proven by many researchers as good candidates to provide economically viable solutions for a wide range of applications. These sensor nodes are coordinated based on some network topologies to cooperate with one another within the WSNs to satisfy the applications requirement. Each sensor node monitors its local environment, locally processing and storing the collected data so that other sensor nodes in the network can use it. As illustrated in Section.1.1.1, network nodes share these information via a wireless communication link. Because of the great potential in WSN, many groups around the world have invested lots of research efforts and time in the design of sensor nodes for their specific applications. These include Berkeley's Mica motes [16], PicoRadio projects [17], MIT's μAmps [18] as well as many others. In addition, the TinyOS project [19] provides a framework for designing flexible distributed applications for data collection and processing across the sensor network. All of these sensor nodes have similar goals such as small physical size, low power consumption and rich sensing capabilities. The block diagram of the wireless sensor

node of a WSN is shown in Figure.1.3. The sensor node typically consists of four sub-units namely the sensor itself, data acquisition circuit, local microcontroller and radio communication block.

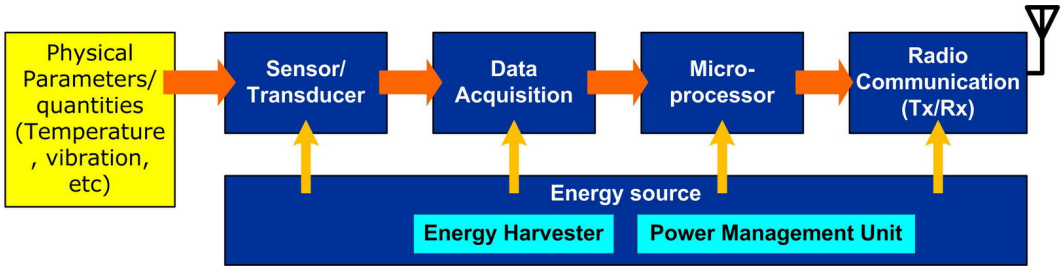

Figure 1.3: Block diagram of a wireless sensor node

Referring to Figure.1.3, the sensor/transducer converts an environmental parameter such as temperature, vibration, humidity, etc. to an electrical signal. A data acquisition circuit is incorporated in the sensor node to realize amplification and pre-processing of the output signals from sensors, for example conversion from analog to digital form and filtering. The conditioned signals are then processed and stored in the embedded microcontroller for other sensor nodes in the network to use them. Other than data processing, the microcontroller also provides some level of intelligences like time scheduling to the sensor node. To enable the sensor node to communicate with its neighbour node or the base station in a wireless manner, a radio communication block as shown in Figure.1.3 is included. All the four sub-units of the sensor node are power sink modules and they need to consume electrical energy from the power source in order to operate. Because of that, the wireless sensor node would consume all the energy stored in the battery after some times and the sensor node would then go into an idle state. Once the percentage of nodes that have not terminated their residual energy falls below a specific threshold, which is set according to the type of application (it can be either 100 % or

less) [20], the operational lifetime of the WSN ends.

1.2 Problems in Powering Wireless Sensor Nodes

As the WSN becomes dense with many sensor nodes, the problems in powering the wireless sensor nodes namely: (1) high power consumption of sensor nodes and (2) limitation of energy sources for sensor nodes becomes critical, even worst when one considers the prohibitive cost of providing power through wired cables to them or replacing batteries. Furthermore, when the sensor nodes must be extremely small, as tiny as several cubic centimeter, to be conveniently placed and used, such small volumetric devices are very limited in the amount of energy that the batteries can store and there would be severe limits imposed on the nodes' lifetime powered by the miniaturized battery that is meant to last the entire life of the node.

1.2.1 High Power consumption of Sensor Nodes

Based on the breakdown of a wireless sensor node illustrated in Section.1.1.3, the information about how much electrical power a sensor node consume during operation is determined. The power consumed by each individual components i.e. microcontroller, radio, logger memory and sensor board in a sensor node is tabulated in Table.1.1. It can been observed from Table.1.1 that all the components in the sensor node consume mW level of power during the active mode of operation and then drop to μW of power when in sleep or idle mode. If the sensor node is set to operate at full duty cycle i.e. 100 %, the current and therefore power consumption of the sensor node would as high as 30 mA.

Table 1.1: Battery life estimation for a Xbow sensor node operating at 100 % and 1 % duty cycles [21]

SYSTEM SPECIFICATIONS					
Currents			**Duty Cycles**		
	value	units	Model 1	Model 2	units
Micro Processor (Atmega128L)					
current (full operation)	8	mA	100	1	%
current sleep	8	ua	0	99	%
Radio					
current in receive	16	ma	75	0.75	%
current xmit (3dB)	17	ma	25	0.25	%
current sleep	1	ua	0	99	%
Logger					
write	15	ma	0	0	%
read	4	ma	0	0	%
sleep	2	ua	100	100	%
Sensor Board					
current (full operation)	5	ma	100	1	%
current sleep	5	ua	0	99	%
Computed average current consumed (mA)			**Model 1**	**Model 2**	
uP			8.0000	0.0879	
Radio			16.2500	0.1635	
Flash Memory			0.0020	0.0020	
Sensor Board			5.0000	0.0550	
Total current (ma) used			**29.2520**	**0.3084**	

For most practical WSN applications described in Section.1.1.2, *duty cycling* of the sensor node's operation is a common method discussed in the literature [12] - [14] to reduce its power consumption and therefore extends the lifetime of the WSN. During one operational cycle, the sensor node remains active for a brief period of time before going into the sleep mode. During the sleep period, the current consumption of the sensor node is typically in the μA range as opposed to the active period in the mA range. This results in the sensor node drawing very little amount of current in range of 2 - 8 μA for the majority of the time and short duration of current spikes in the range of 5 - 17 mA while sensing, processing, receiving and transmitting data as illustrated in Table.1.1. For the Xbow sensor node given in Table.1.1, operating at duty cycle of 1 % opposed to 100 %, the average current consumption of node with supply voltage of 3 V is significantly reduced from 30 mA to around 0.3 mA. Referring to Figure.1.4, it is clearly illustrated that there is a drastic difference in the battery life of the wireless sensor node operating at duty cycles of 1 % and 100 %. This shows the need for duty cycling the operation

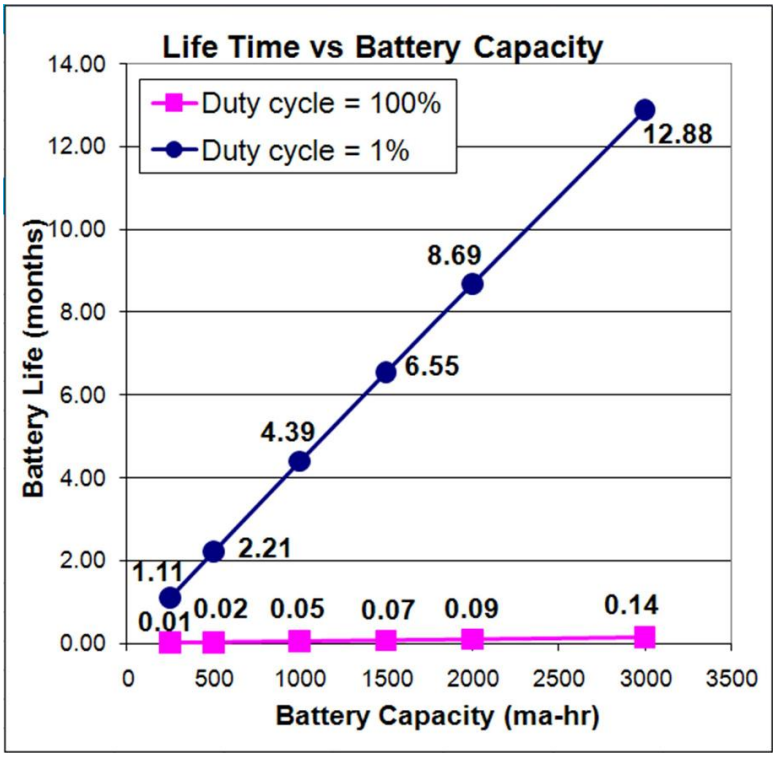

Figure 1.4: Expected battery life vs system current usage and duty cycle [21]

of the sensor node.

Even so, with the help of duty cycling the operation of the sensor node, the power consumed by the wireless sensor node has been decreased by around 75 times, the power density of its battery is still not high enough to support the high power consumption of the sensor node for a long period of time. Based on an AA alkaline battery of 3000 mA-hr, it is illustrated in Figure.1.4 that the lifetime of the battery powering the sensor node is computed to last at most 1.1 years. After which, without battery replacement, the sensor node can be considered as an expired node. This is even worst for the case of a coin type alkaline battery of 250 mA-hr, which is smaller in size than the AA battery. Referring to Figure.1.4, the coin battery can only sustain the operation of the sensor node for at most 1 - 2 months. Clearly, a lifetime of a year or so or even lower for the wireless sensor

node to operate is far from sufficient because the duration of the node's operation could last for several years for the WSN to be useful in the practical situations. This is a serious limitation to computing paradigms like ubiquitous computing or sensor networks, in which there are dozens or hundreds of small self-autonomous sensor nodes systems with batteries to maintain.

1.2.2 Limitation of Energy Sources for Sensor Nodes

In many application scenarios, the lifetime of the sensor node typically ranges from two to ten years depending on the requirement of the specific application. Take for the case of deploying sensor nodes on the ice mountain to detect the thickness of the ice on the mountain, it will take years for the melting process to be measurable. Hence the lifetime of the sensor nodes must be able to last for several years before they go into idle state. If that is the case, energy supply is one of the major bottle neck to be addressed. Many different types of energy storage technologies are already available as illustrated in Figure.1.5, alkaline/rechargeable batteries and supercapacitors are the most portable and popular energy supply option for powering the sensor nodes in WSN. Batteries convert stored chemical energy directly into electrical energy. They are generally classified into two groups namely 1) single-use/primary and 2) rechargeable/secondary batteries. The distinction between the two groups is based on the nature of the chemical reactions.

Primary batteries are discarded when sufficient electrical energy can no longer be obtained from them. Secondary batteries, on the other hand, convert chemical energy into electrical energy by chemical reactions that are essentially reversible. Thus, by passing the electrical current in the reverse direction to that during dis-

charge, the chemicals are restored to their original state and the batteries are restored to full charge again. Supercapacitor, in short supercap, is another electrochemical energy system other than batteries that has been gaining its presence in powering the wireless sensor nodes. There are several reasons for this phenomenon to occur. One reason is that supercapacitor is very scalable and its performance scales well with its size and weight. Another reason is that supercap has many desirable characteristics that favour the operations of the sensor nodes such as high power density, rapid charging times, high cycling stability, temperature stability, low equivalent series resistance (ESR) and very low leakage current [23].

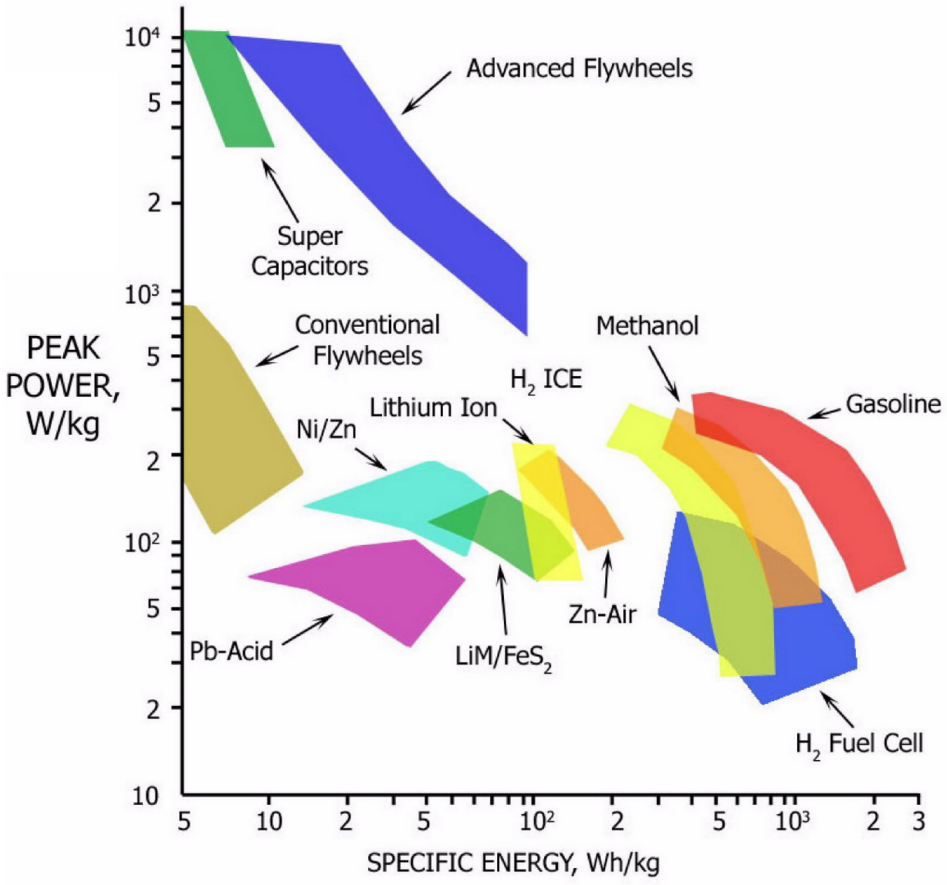

Figure 1.5: Ragone plot for comparing the energy storage technologies and their power density versus energy density characteristics [22]

Referring to the Ragone plot shown in Figure.1.5 which consolidates various energy storage technologies and compare their power density and energy density characteristics, it can be identified that supercapacitor has much higher peak power density than the other energy storage devices like batteries and fuel cells. This means that supercap can deliver more electrical power than batteries and fuel cells within a short time. As shown in Figure.1.5, the peak power densities of supercapacitors are well above 1000 W/kg level whereas the power densities of all types of batteries are in the range of 60 W/kg to 200 W/kg and fuel cells are even lower which is below 100 W/kg. Hence for burst power operation, supercapacitors are better choice than batteries and fuel cells. Conversely, batteries have much higher energy storage capacities than the supercapacitors. This means that batteries can deliver electrical power for a longer period of time as compared to supercap. Referring to Figure.1.5, it can be seen that the peak energy densities of all types of batteries are in the range of 20 Wh/kg to 200 Wh/kg whereas the power density of supercap is below 10 Wh/kg. Hence, for sustaining the extended operational lifetime of wireless sensor nodes, solely replying on supercap might not be suitable due to its very low energy density as compared to the rest of the energy storage devices. Research to increase the energy storage density of both batteries and supercap has been conducted for many years and continues to receive substantial focus [24]. While these technologies promise to extend the lifetime of wireless sensor nodes, they cannot extend their lifetime indefinitely.

Among these non-renewable energy systems or sources, the rechargeable/alkaline battery is one of the most popular methods for powering great majority of autonomous sensor nodes in WSNs. The electrical energy necessary for their operation is provided primarily by batteries. Although batteries have been widely used

in powering sensor nodes in WSN presently, the problem is that the energy density of batteries are limited and they may not be able to sustain the operation of the sensor nodes for a long period of time. Referring back to the case scenario of a Xbow sensor node given in Table.1.1 with operating duty cycle of 1 %, the average power consumption of the node with supply voltage of 3 V is around 1 mW. With reference to the highest reported energy for current battery technologies ranges around 3.78 kJ/cm^3 [1], for the ultra-low-power miniaturized wireless sensor node with volumetric size of around 10 cm^3 operating at an average power consumption of 1 mW to have a 10-year lifespan, needs as large as a 100 cm^3 size battery. The size of the battery is 10 times the sensor node's size. In fact, the calculation is a very optimistic estimate as the entire capacity of the battery usually cannot be completely used up depending on the voltage drop. Additionally, it is also worth mentioning that the sensors and electronic circuits of a wireless sensor node could be far smaller than 10 cm^3. In this case, the battery takes up a significant fraction of the total size and weight of the overall system and also the most expensive part of the system. Thus, energy supply is largely constraints by the size of the battery.

In short, batteries with finite energy supply must be optimally used for both processing and communication tasks. The communication task tends to dominate over the processing task in terms of energy consumption. Thus, in order to make optimal use of energy, the amount of communication task should be minimized as much as possible. In practical real-life applications, the wireless sensor nodes are usually deployed in hostile or unreachable terrains, they cannot be easily retrieved for the purpose of replacing or recharging the batteries, therefore the lifetime of the network is usually limited. There must be some kind of compromise between the communication and processing tasks in order to balance the duration of the WSN

lifetime and the *energy density* of the storage element. In summary, limitation in the device size and energy supply typically means restricted amount of resources i.e. CPU performance, memory, wireless communication bandwidth used for data forwarding and range allowed. The need to develop alternative method for powering the wireless sensor and actuator nodes is acute. The main research focus is to resolve the energy supply problems faced by the wireless sensor nodes in a WSN.

1.3 Energy Harvesting Solution for Wireless Sensor Node

To overcome the major hindrance of the *"deploy and forget"* nature of wireless sensor network WSN due to the limitation of available energy for the network constrained by the high power consumption of the sensor nodes and the energy capacity and unpredictable lifetime performance of the battery, *energy harvesting (EH)* technology has emerged as a promising solution to sustain the operation of WSN [25] - [26].

1.3.1 Overview of Energy Harvesting

Energy harvesting (EH) is a technique that captures, harvests or scavenges a variety of unused ambient energy sources such as solar, thermal, vibration and wind, and converts the harvested energy into electrical energy to recharge the batteries. The harvested energy is generally very small (of the order of mJ) as compared to those large-scale EH using renewable energy sources such as solar farms and wind farms of the order of several hundreds MJ. Unlike the large-scale power stations which are

fixed at a given location, the small-scale energy sources are portable and readily available for usage. Various energy harvesting sources, excluding the biological type, that can be converted into electrical energy are shown in Figure.1.6.

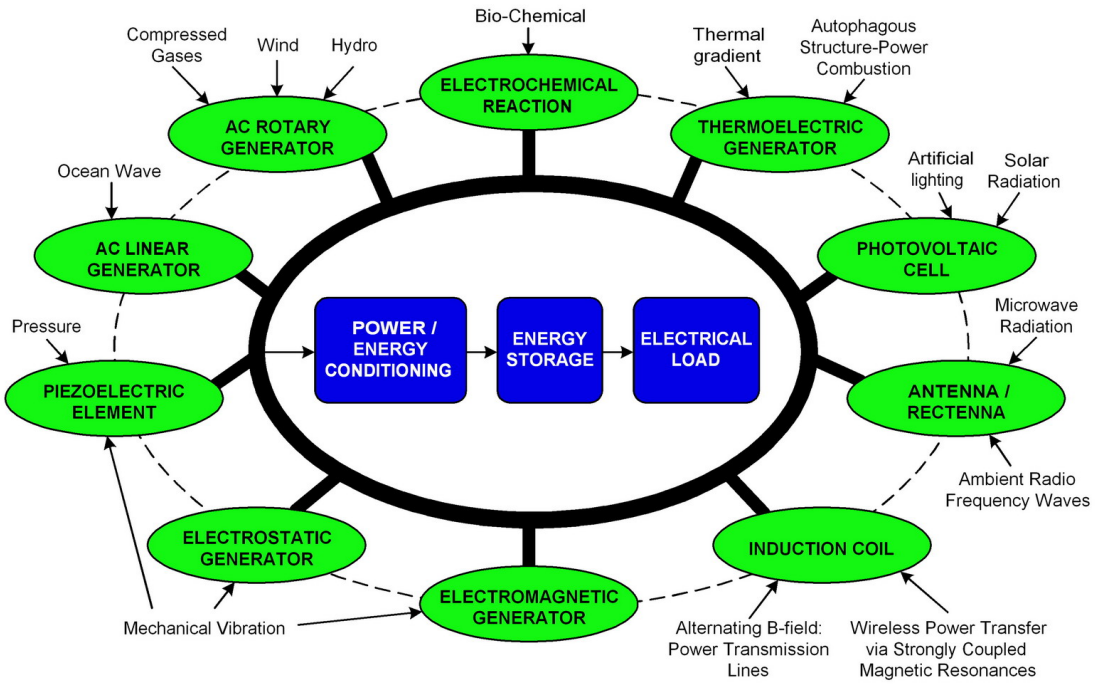

Figure 1.6: Energy harvesting sources and their energy harvesters, adapted from [29]

In our environment, there are full of waste and unused ambient energy generated from these energy sources seen in Figure.1.6. These renewable energy sources are ample and readily available in the environment and so it is not necessary to deliberately expend efforts to create these energy sources like the example of burning the non-renewable fossil fuels to create steam which in turn would cause the steam turbine to rotate to create electrical energy. Unlike fossil fuels which are exhaustible, the majority of the environmental energy sources are renewable and sustainable for almost infinite long period. Numerous studies and experiments have been conducted to investigate the levels of energy that could be harvested from the

ambient environment. A compilation list of various energy harvesting sources and their power/energy densities are listed in Table.1.2.

Table 1.2: Energy harvesting opportunities and demonstrated capabilities adapted from [27]

Energy Source	**Performance**	**Notes**
Ambient light	100 mW/cm^2 (direct sunlight)	Common polycrystalline solar cells are 16 %-17 % efficient, while standard mono-crystalline cells approach 20 %
	100 μW/cm^2 (illuminated office)	
Thermal	[a)]60μW/cm^2 at 5 K gradient [b)]135 μW/cm^2 at 10 K gradient	Typical efficiency of thermoelectric generators are $\leq$ 1% for ΔT $<$ 313 K [a)]Seiko Thermic wristwatch at 5 K body heat, [b)]Quoted for a ThermoLife® generator at ΔT = 10 K
Blood Pressure	0.93W at 100mmHg	When coupled with piezoelectric generators, the power that can be generated is order of μW when loaded continuously and mW when loaded intermittently
Vibration	4 μW/cm^3 (human motion-Hz) 800μW/cm^3 (machines-kHz)	Predictions for 1 cm^3 generators. Highly dependent on excitation (power tends to be proportional to ω, the driving frequency and y_o, the input displacement
Hand Linear Generator	2 mW/cm^3	Shake-driven flashlight of 3 Hz
Push button	50 μJ/N	Quoted at 3 V DC for the MIT Media Lab Device
Heel strike	118 J/cm^3	Per walking step on piezoelectric insole
Ambient wind	1 mW/cm^2	Typical average wind speed of 3 m/s in the ambient
Ambient radio frequency	$<$1 μW/cm^2	Unless near a RF transmitter
Wireless energy transfer	14 mW/cm^2	Separation distance of 2 metres

Table.1.2 shows the performance of each energy harvesting source in terms of the power density factor. It can be clearly observed that there is no unique solution suitable for all environments and applications. According to Table.1.2, it can be observed that solar energy source yields the highest power density. However, this may not be always the case. Under illuminated indoor condition, the ambient light energy harvested by the solar panel drops tremendously. The other energy harvesting sources could provide higher power density, depending on the renewable energy sources available at the specific application areas like outdoor bright sunny day with rich amount of solar energy, along coastal area with a lot of wind energy, bridge structure with vehicles travelling has strong vibrations, etc. In addition, there could also be possibility of two or more energy sources available for harvesting at the same time. As such, energy harvesting (EH) technology can provide numerous benefits to the end user and some of the major benefits about EH suitable for WSN are stated and elaborated in the following list [28] - [29]. Energy harvesting solution can:

1. Reduce the dependency on battery power. With the advancement of microelectronics technology, the power consumption of the sensor nodes are getting lesser and lesser, hence harvested ambient/environmental energy may be sufficient to eliminate battery completely.

2. Reduce installation cost. Self-powered wireless sensor nodes do not require power cables wiring and conduits, hence they are very easy to install and they also reduce the heavy installation cost.

3. Reduce maintenance cost. Energy harvesting allows for the sensor nodes to function unattended once deployed and eliminates service visits to replace

batteries.

4. Provide sensing and actuation capabilities in hard-to-access hazardous environments on a continuous basis.

5. Provide long-term solutions. A reliable self-powered sensor node will remain functional virtually as long as the ambient energy is available. Self-powered sensor nodes are perfectly suited for long-term applications looking at decades of monitoring.

6. Reduce environmental impact. Energy harvesting can eliminate the need for millions on batteries and energy costs of battery replacements.

Clearly, it can be deduced from the list of benefits that the EH technology is a viable solution to power wireless sensor networks and mobile devices for extended operation with the supplement of the energy storage devices if not completely eliminating the storage devices such as batteries.

1.3.2 Energy Harvesting System

In an energy harvesting (EH) system, there are generally four main components namely: energy collection and conversion mechanism (energy harvester), electrical power management/conditioning circuit, energy storage device and electrical load (wireless sensor node) as shown in Figure.1.7. Power output per unit mass or volume i.e. power/energy density is a key performance unit for the energy collection and conversion mechanisms. The harvested power must be converted to electricity and conditioned to an appropriate form for either charging the system batteries or powering the connected load directly. Proper load impedance matching between

the EH source and the electrical load is necessary to maximize the usage of the harvested energy. Appropriate electronic circuitry for power conditioning and load impedance matching may be available commercially or may require custom design and fabrication.

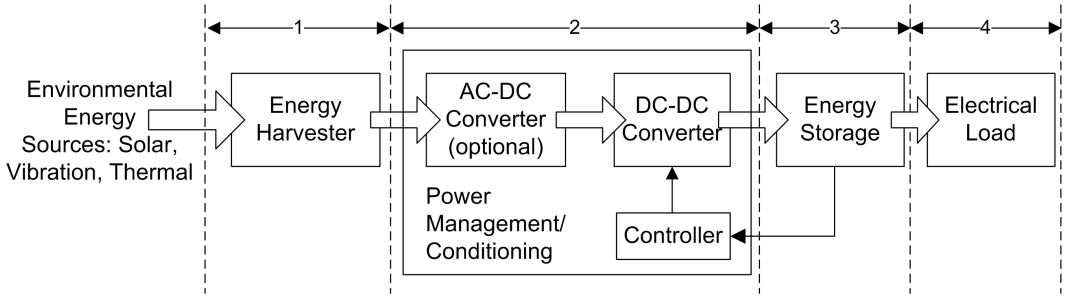

Figure 1.7: General block diagram representation of energy harvesting system unit

Referring to Figure.1.7, it can seen that the function of the energy harvester is to convert energy harnessed from environmental energy sources into electrical energy. Some typical examples of the energy harvesters, as shown in Figure.1.6, include: the Lead Zirconate Titanate (PZT) ceramic material converts mechanical (strain or stress) energy into electrical energy due to the piezoelectric effect, the photovoltaic cell converts solar energy into electrical energy, the thermoelectric generator output electrical voltage when there is a thermal gradient across it and the wind turbine converts kinetic energy from wind flow into electrical energy. The harvested electrical energy from the energy harvester needs to be conditioned by some form of power conditioning circuit before supplying it to the load. The main objective of the power electronics technology in the power conditioning circuit as seen in Figure.1.7 is to process and control the flow of electrical energy from the source to the load in such a way that energy is used efficiently. This matching process is a crucial step to ensure that maximum power is transferred from the source to the electrical load. Another function of the power conditioning circuit

involves the conversion and regulation of electrical voltage at higher levels into suitable levels for the loads.

To ensure continuity in the load operation even when the external power source is weak or temporarily unavailable, the excess energy already being harvested earlier has to be stored either in the rechargeable battery or supercapacitor as shown in Figure.1.7. Depending on the environmental condition of the ambient energy source, the characteristic of the energy harvester and the power requirement of the load i.e. wireless sensor node and control circuitry, each individual energy harvesting system is designed and optimized accordingly in order to sustain the operation of the wireless sensor node.

1.3.3 Review of Past Works on Energy Harvesting System

There are quite a significant amount of research works being recorded in the literature on harvesting or scavenging small-scale environmental energy for powering wireless sensor nodes. One important point to note is that in order to make the sensor node truly autonomous and self-sustainable in a WSN, the selection choice of the energy harvesting technique is crucial. As such, the review process of the past works on energy harvesting system is a necessity.

1.3.3.1 Solar Energy Harvesting System

Solar energy of an outdoor incident light at midday holds a power density of roughly 100 mW per square centimeter indicates that in a small volume of 1 cm^2, 100 mW of electrical power can be harvested from the sun by using the solar panel. Conversely,

the lighting power density in indoor environments such as illuminated offices drops tremendously to almost 100 μW/cm^2 [30]. Commercially off-the-shelf single crystal solar cells offer efficiencies of about 15 % and up to 20 - 40 % for the state of the art expensive research photovoltaic (PV) cells recorded by Green *et al.* in a PV progress report [31]. Thin film polycrystalline and amorphous silicon solar cells are also commercially available and cost less than single crystal silicon, but also have lower efficiency of only 10 - 13 % [30].

Recently, a number of solar energy harvesting prototypes have been presented which perform more and more efficient energy conversion. Two of the first prototypes were Heliomote [32] and Prometheus [33]. In both systems, the solar panels are directly connected with the storage device. A picture of the energy energy harvesting system, Prometheus, is depicted in Figure.1.8(a). In this case, the solar panel is directly connected to a supercapacitor. This means that especially for low supercapacitor voltages, the solar panel generates much less power than its maximum power, P_{MPP}.

Hence, an efficient solar harvesting (SEH) system should be able to adapt the electrical operating point of the solar panel to the given light condition so that P_{MPP} is always maintained. For solar panels of a few cm^2, particular care has to be taken in order not to waste the few mWs generated by the solar panel. Everlast [34] is an example that uses the fractional short-circuit current technique (see Figure.1.8(b)) to achieve maximum power point tracking P_{MPPT}. This technique is easy, simple and cheap to implement. The voltage, V_{MPP}, is estimated based on the open-circuit voltage, V_{oc}, of the solar panel, which is measured periodically by momentarily shutting down the power converter that is connected to the solar

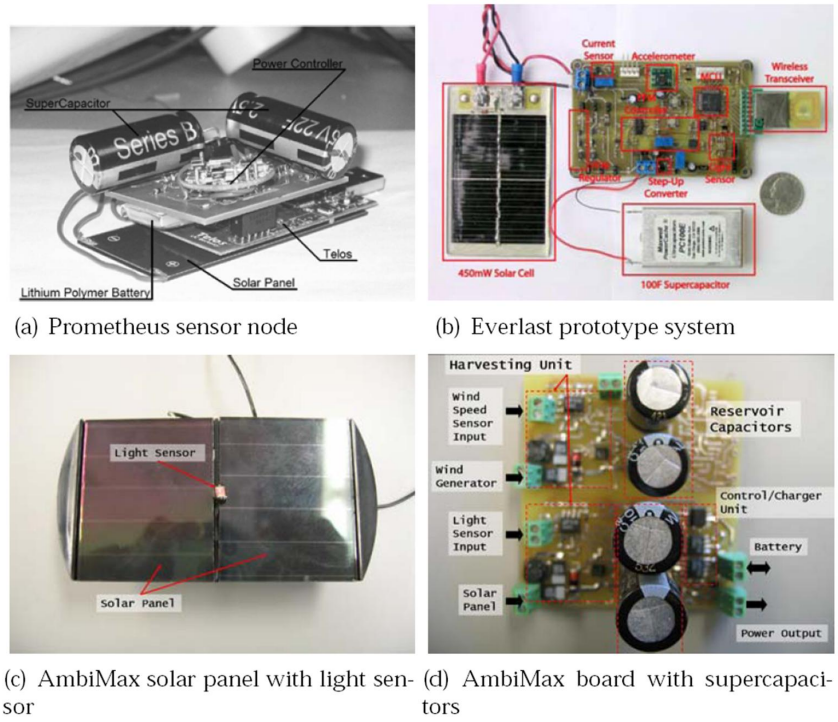

(a) Prometheus sensor node

(b) Everlast prototype system

(c) AmbiMax solar panel with light sensor

(d) AmbiMax board with supercapacitors

Figure 1.8: Examples of solar energy harvesting system [33] - [35]

panel. However, the drawback with this technique is the transient drop of power during that time where no energy is harvested.

Another SEH system, known as AmbiMax, has been proposed by Park *et al.* in [35]. The AmbiMax system exploits a small photosensor to detect the ambient light conditions and to force the solar panel to work in its MPP (see Figure.1.8(c)). In similar nature as AmbiMax, Dondi *et al.* presented another circuit in [36] that uses a miniaturized photovoltaic module as pilot panel instead of a photosensor to achieve MPPT for the SEH system. Indeed, these SEH prototypes have successfully demonstrated that solar energy is a realistic energy source for sensor nodes. However, there is still room for improvement including system form factor, performance, etc. to suit the power requirement of embedded wireless sensor nodes deployed in application areas such as indoors and overcast areas where access

to direct sunlight is often weak or not available. In some cases where solar energy source may not be a suitable choice, it is required to search for alternative energy sources either to replace the solar energy source as a whole or to supplement the solar energy source when the intensity of the light is low.

1.3.3.2 Thermal Energy Harvesting System

Thermal energy is another example of the alternative energy sources. Several approaches to convert thermal energy into electricity are currently under investigation (through Seebeck effect, thermo-couples, piezo-thermal effect) [37]. The efficiency of these approaches are related to the Carnot's law expressed by equation $\eta = (T_{max} - T_{min})/T_{max}$. According to the Carnot's equation, for a thermal gradient of 5 K with respect to the normal ambient temperature of 300 K, the thermal energy harvesting (TEH) efficiency is computed to be around 1.67 %. Consider a silicon device with thermal conductivity of 140 W/mK, as illustrated by Cottone in [38], the heat power that flows through conduction along a 1 cm length for a ΔT = 5 K is 7 W/cm^2. Hence, the electrical power obtained at Carnot's efficiency is calculated to be 117 mW/cm^2. At first sight, this heat power density of 7 W/cm^2 seems to exhibit excellent result but the TEH devices have efficiencies well below the simple Carnot's rule, so the attainable electrical power density turns out to be a small fraction of that, which is only 117 mW/cm^2. Many research works on the TEH devices have been discussed in the literature and *thermoelectric generator (TEG)* is one of the popular devices that has been developed to harvest thermal energy based on Seebeck's effect. A summary of the implemented TEGs, capable of generating from 1-60 μW/cm^2 at 5 K temperature differential, is illustrated in a review paper [37] presented by Hudak *et al.*.

For a thermal energy harvesting (TEH) system, it requires one or more TEGs, heat exchangers on the hot and cold sides of the TEG, mechanical structure for clamping the heat exchangers to the module and ensuring good thermal contact, thermal insulation to prevent heat losses through the sides and power electronics for impedance load matching [29]. One commercial application example of thermoelectric generator (TEG) is the Seiko Thermic wristwatch, as shown in Figure.1.9(a), which is powered by heat generated from the human body.

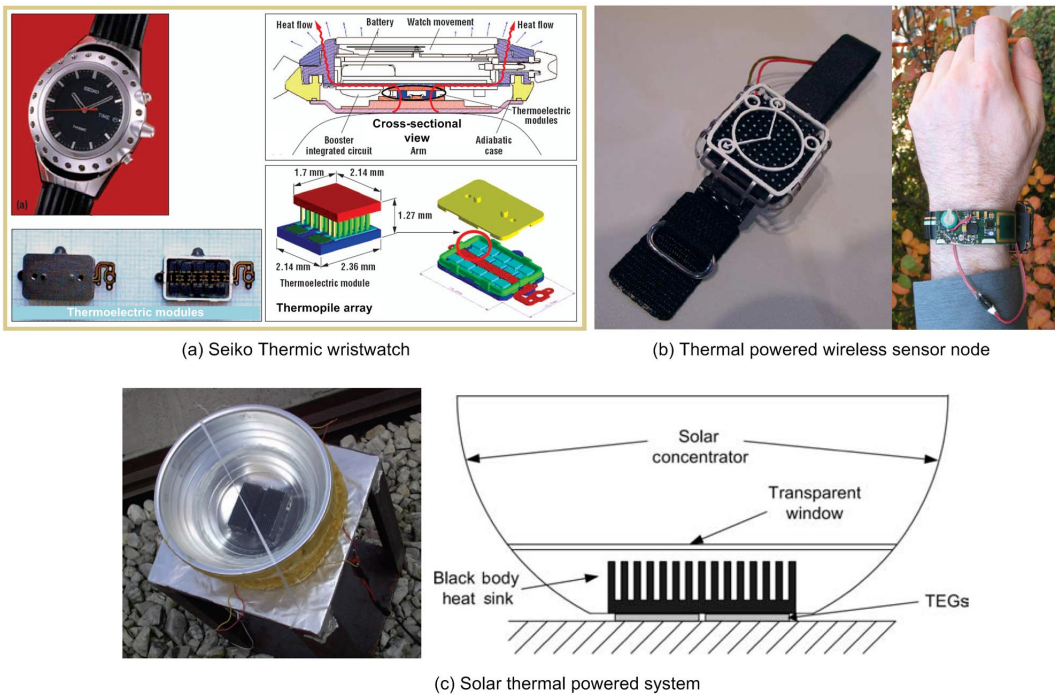

Figure 1.9: Examples of thermal energy harvesting system [37], [40], [43]

In the Seiko wristwatch shown in Figure.1.9(a), the TEH system consists of a thermoelectric module, a lithium-ion battery and a simple DC-DC step-up voltage regulator [37]. The thermoelectric module of the wristwatch is recorded to yield 60 μW/cm^2 at 5 K temperature gradient with 10 TEGs coupled together in series [39]. Similarly, Leonov *et al.* [40] have considered TEH through thermoelectric power generation from body heat to power wireless sensor nodes as shown in Figure.1.9(b).

The average power generation at daytime of about 250 μW corresponds to about 20 μW/cm^2 with temperature difference of 10 K, which is better than solar panels in many indoor situations, especially considering the TEG power is also available at night time. However, these systems does not considered proper matching between the source and the load to ensure maximum power points (MPPs) operation.

In another TEH research, both Stevens [41] and Lawrence *et al.* [42] consider the system design aspects for solar-TEH via thermoelectric conversion that exploits the natural temperature difference between the ground and air. Later, Sodano *et al.* [43] presented a solar-TEH system placed in a greenhouse with a solar concentrator as seen in Figure.1.9(c). The solar-TEH system uses a thermoelectric generator (TEG) to recharge a NiMH battery. At an estimated ΔT of 25 K, the harvested energy was able to recharge an 80 mAh battery in 3.3 min. The authors have demonstrated that TEG may be used for solar energy conversion as an alternative to photovoltaic devices. However, like before, there are little discussions on the power management aspects of the solar-TEH system.

1.3.3.3 Vibration Energy Harvesting System

The first important virtue of random mechanical vibrations as a potential energy source is that it is present almost everywhere. Mechanical vibrations occur in many environments such as building, transports, terrains, humans activities, industrial environments, military devices and so on. Their characteristics are various: spectral shape from low to high frequency, amplitude and time duration are manifolds dependently by the surroundings. Theory and experiments of many research works show that the power density that can be converted from vibrations is about

$300\mu W/cm^3$ [38]. Devices which convert mechanical motion into electricity can be categorized in electromagnetic, electrostatic and piezoelectric converters [44]-[45]. In the case of electromagnetic converters, a coil oscillates in a static magnetic field and induces a voltage. In electrostatic converters, electric charge on variable capacitor plates creates a voltage if the plates are moved. Piezoelectric converters, finally, exploit the ability of some materials like crystals or ceramics to generate an electric potential in response to mechanical stress. A prominent example for the employment of vibrational harvesters is the watch industry, where vibrational energy converters have been used with success to power wristwatches.

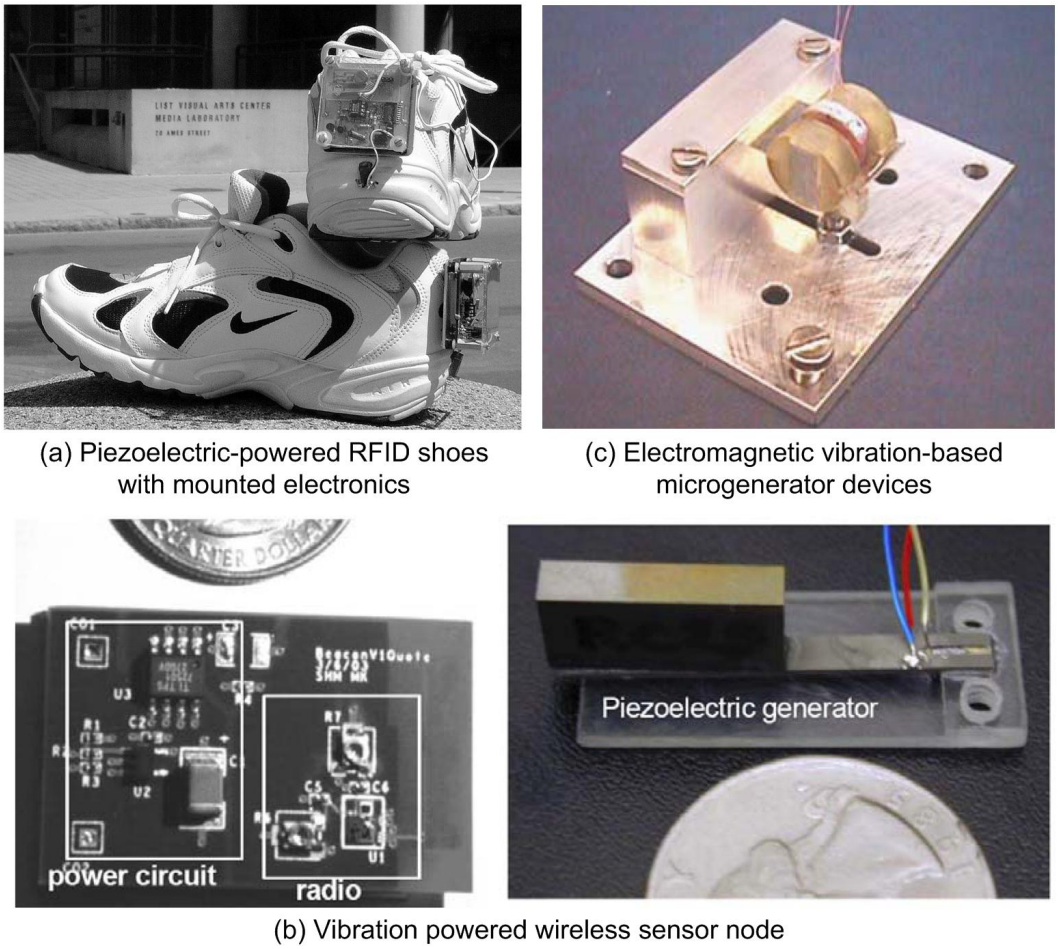

Figure 1.10: Examples of thermal energy harvesting system [46], [47], [49]

Shenck *et al.* presented a piezoelectric-powered RFID system [46] for shoes, as illustrated in Figure.1.10(a), that harvests energy from human walking activity. The developed shoe inserts are capable of generating around 10 mW of power under normal walking conditions. This shows that mechanical vibration from human activity is another promising renewable energy source worth investing effort to investigate. A similar approach has been taken by Roundy in [47], where piezoelectric generators as seen in Figure.1.10(b) have been developed as an attractive method to power wireless transceivers. Other vibration based energy harvesting (VEH) research works being reported include wearable electronic textiles [48] and electromagnetic vibration-based micro-generator devices (see Figure.1.10(c)) for intelligent sensor systems [49]. Meninger *et al.* have also demonstrated an electromagnetic vibration-to-electricity converter in their research work [50] that can produce 2.5 μW of electrical power in cm^3. Similarly, another piece of research work discussed by Mitcheson *et al.* in [51] has made an analysis indicated that up to 4 μW/cm^3 can be achieved from vibrational micro-generators (of order 1 cm^3 in volume) that typical human motion (5 mm motion at 1 Hz) stimulates and up to 800 μW/cm^3 from machine-induced stimuli (2 nm motion at 2.5 kHz). Many meso and micro-scaled energy harvesting generators have been developed in the last five years [38], however there is a lack in adequate ultra-low-power management circuit to condition their micro-power generation.

In another VEH research work, Paradiso *et al.* in [52] have successfully demonstrated a piezoelectric element with a resonantly matched transformer and conditioning electronics that, when struck by a button, generate 1 mJ at 3 V per 15 N push, enough power to run a digital encoder and a radio that can transmit over 15 metres. However, this system requires a large transformer to step-up the output

voltage generated by the piezoelectric element. The efficiency of the transformer is limited by flux leakage and core saturation when the primary current peaks. Taking an interesting turn, assuming an average blood pressure of 100 mmHg (normal desired blood pressure is 120/80 above atmospheric pressure), a resting heart rate of 60 beats per minute and a heart stroke volume of 70 milliliters (ml) passing through the aorta per beat [53], then the power generated is about 0.93 W. Ramsay *et al.* [54] found that when the blood pressure is exposed to a piezoelectric generator, the generator can generate power of the order of μW when the load applied changes continuously and mW as the load applied changes intermittently. However, harnessing power from blood pressure would only limit the application domains to wearable micro-sensors.

1.3.3.4 Wind Energy Harvesting System

Like any of the commonly available renewable energy sources, wind energy harvesting (WEH) has been widely researched for high power applications where large wind turbine-generators (WTGs) are used for supplying power to remote loads and grid-connected applications [55]-[56]. According to a study by National Renewable Energy Laboratory (NREL) [57], wind energy is the fastest growing electricity generating technology in the world. In the past 10 years, global installations of wind energy systems have grown at least tenfold - from a total capacity of 2.8 gigawatts (GW) in 1993 to almost 40 GW at the close of 2003 [58]. In spite of this continuing success of WEH at large scale, there have been very few attempts on the development of small-scale WEH, those are miniaturized in size and highly portable, to power small autonomous sensors deployed in remote locations for sensing and/or even to endure long-term exposure to hostile environment such as forest fire. Al-

though very few research works are reported in the literature on small-scale WEH, some efforts to generate power at a very small-scale have been made recently. Park *et al.* presented a maximum power point tracker for a small windmill implemented in [35]. The WEH system, as illustrated in Figure.1.11(a), exploits the near liner relationship between the wind speed and the rotating frequency of the WTG's rotor to force the WTG to work in its maximum power points (MPPs).

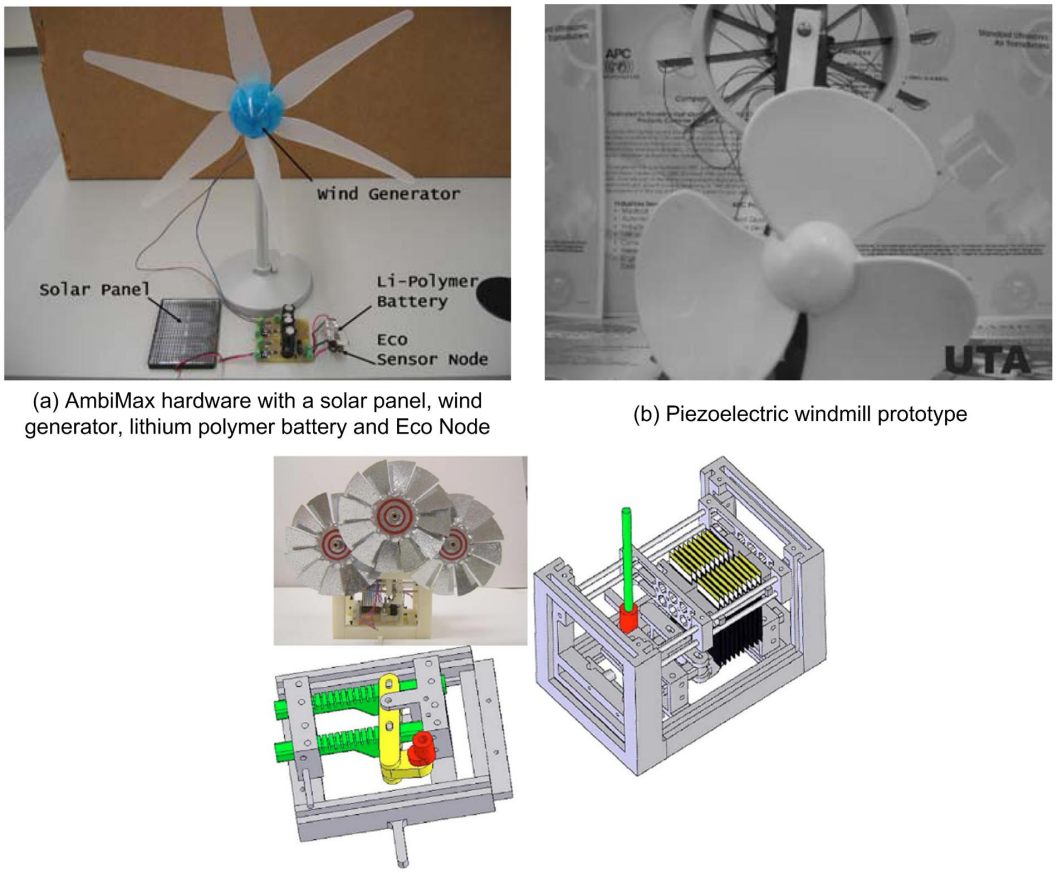

(a) AmbiMax hardware with a solar panel, wind generator, lithium polymer battery and Eco Node

(b) Piezoelectric windmill prototype

(c) Optimized design of the small scale windmill with isometric view and internal crank-shaft structure exhibiting translation mechanism

Figure 1.11: Examples of thermal energy harvesting system

Similarly, a small-scale WTG has been presented by Holmes *et al.* in [59] and the power densities harvested from air velocity are quite promising. Later, Weimer *et al.* [60] presented an anemometer-based solution to perform the WEH and sensing tasks, which are accomplished separately by two different devices. The

authors utilize the motion of the anemometer shaft to turn a coupled alternator to generate electrical power for the sensor nodes. Although the sensor nodes incorporating the harvesting solution have an increased operational lifetime, this comes with the price of larger device size, higher overall cost and higher energy conversion loss.

In another WEH research work [61], Priya *et al.* designed a windmill which uses piezoelectric elements to generate electricity from wind energy (see Figure.1.11(b)). An output power of 10.3 mW was harvested and reported for a wind flow which leads to 6 rotations per minute. Subsequently, another group of researchers, Myers *et al.* [62], developed an optimized small-scale piezoelectric windmill as shown in Figure.1.11(c) The whole structure of the windmill is made of plastic and it utilizes 18 piezoelectric bimorphs to convert wind energy, hence vibration energy into electrical energy. The windmill was tested to provide 5 mW of continuous power at an average wind speed of 4.5 m/s. Still, the physical size of the WEH systems are too large and bulky as compared to the sensor node and their harvested power exceeds the power requirement of sensor node. In addition, there is a lack of adequate power management circuit to maximize electrical power transfer from the source to the load.

1.4 Contribution of this Thesis

As described in the literature survey on the energy harvesting (EH) systems, there is no definite energy source that is suitable for sustaining the operation of a wireless sensor node in different variety of applications. Hence, this thesis is aimed at

developing various EH systems for the wireless sensor node. In many WSN applications, the environmental conditions of the sensed area, where the sensor nodes are deployed, are often not consistent. The energy sources are intermittent and fluctuating in nature while the operations of the wireless sensor nodes require a constant electrical power source. As such, adequate power management circuit is designed mainly to provide a proper match between the energy harvesting mechanism and the sensor node. The contributions of this thesis work are listed as follows: -

- Two types of small-scale WEH systems namely: (1) direct WEH approach using wind turbine-generator (WTG) and (2) indirect WEH approach using piezoelectric material have been proposed. Detailed analysis and characterization of the wind energy conversion mechanisms have been provided. Based on the characteristics of the WEH mechanisms obtained, the power management unit is designed to take care of the dynamics of both the WEH mechanisms subjected to environmental condition variation such as varying wind speeds and the wireless sensor node operating in its WSN. Since most of the conventional MPPT algorithms are not suitable for the WTG, a resistor emulation or impedance matching scheme has been introduced for MPPT. In addition, an AC-DC active rectifier has been designed using MOSFETs in replace of diodes for rectifying the low amplitude AC voltage generated by the WTG under low wind condition. Prototypes of the WEH systems have been developed to validate the performance of the systems.

- In some places, wind energy source might not be available, hence TEH has been investigated. The TEH mechanism, which houses a miniaturized thermoelectric generator, has been designed to harvest the thermal energy from the heat source. An equivalent electrical circuit model of the TEH mechanism

has been developed. Based on this equivalent model, the thermal and electrical analyses on the TEH mechanism are illustrated. Since the characteristic of the TEH mechanism is found to be similar to the WTG, a resistor emulation based maximum power point tracker is developed to naturally track the MPP of the TEH mechanism with very little control circuit.

- A batteryless and wireless remote controller has been developed to switch the electrical appliances such as lights and fans ON/OFF in a wireless manner. Two types of piezoelectric-based vibration energy harvesting (VEH) systems are presented to harvest impact or impulse forces from human pressing the button or switch action. Detailed understanding and characterization on the performance of the VEH mechanisms are carried out. Since the harvested power is lower than the power consumed by the wireless RF transmitter, an energy management circuit has been implemented. The harvested energy from the VEH mechanism is first accumulated and stored in a capacitor until there is sufficient stored energy to power the RF transmitter, the transmitter is then energized.

- For some WSN applications, multiple energy sources are available. A hybrid of wind and solar energy harvesting scheme is proposed to extend the lifetime of the wireless sensor node. In order for the developed HEH system to harvest simultaneously from both energy sources, the WEH sub-system uses the resistor emulation technique while the SEH sub-system uses the constant voltage technique for MPP operation. In another HEH research work, a hybrid of indoor ambient light and thermal energy harvesting has been proposed. Energy sources of different characteristics are connected directly together. A detailed analysis of their relationship have been conducted to

validate that the impedance mismatch issue does not affect much of the maximum attainable power from the HEH mechanism. A power management circuit is developed to condition the combined output power harvested from both energy sources.

- Like energy harvesting, two remote means of charging low-power electronic devices are proposed. A magnetic inductive approach has been investigated to transfer electrical power from the power lines to the sensor node in a wireless manner. Based on the electrical power requirements of the wireless RF transmitter and the electrical characteristic of the magnetic energy harvester, a magnetic induction system has been designed and successfully implemented. Another wireless power transfer (WPT) mechanism operating at its magnetic resonance has been proposed to further extend the distance for wireless power transmission. Detailed theoretical analysis on the WPT mechanism has been provided and then verify by the simulation results. Based on the verified theoretical findings and experimental results, the design of WPT mechanism can be optimized for improving the WPT distance, efficiency and form factor.

- Various types of EH systems and their respective main components viz. energy harvester (source), power management circuit, energy storage device and wireless sensor node (load) have been proposed, investigated and analyzed. These EH systems have been designed and optimized to suit the target applications viz. ambient conditions and event/task requirements and then implemented into hardware prototypes for proof of concept.

In addition, the contributions of this thesis work are extended to the involvement in various research projects listed as follows: -

1. "Intelligent Wireless Sensor Network incorporating Energy Harvesting mechanism for Condition-Based-Maintenance of Electrical Energy Distribution System Equipment", March 2008 - March 2010, *S$830,000 (Funded by Science And Engineering Research Council, A*Star)*, Proposal Co-Author and Research Contributor.

2. "Feasibility study of using alternative renewable energy sources for portable computing system", August 2007 - August 2009, *S$78,000 (Academic Research Fund & Defense Science Organization*, Proposal Co-Author and Research Contributor.

3. "Intelligent Wireless Sensor Network incorporating Energy Harvesting mechanism for Localized Compass-based Pedestrian Navigation System", October 2007 - October 2008, *S$10,000 (Academic Research Fund)*, Principal Investigator.

1.5 Organization of the Thesis

Chapter 1 has introduced the background of the thesis work. Motivation for this research has been stated. The problems in powering the wireless sensor nodes have been identified. To overcome these problems, an overview of the energy harvesting (EH) solution and its system design are described. A brief review of past works on various EH systems has been provided to show the state-of-the-art. Contributions of the thesis work have been listed.

Chapter 2 discusses on the wind energy harvesting (WEH) research. Two types of WEH approaches based on wind turbine-generator (WTG) and piezoelec-

tric based wind energy harvester have been explored. For the first approach, the issues of small-scale WEH using a WTG for sustaining the operation of a wireless sensor node are discussed. To resolve the problems, an ultra-low-power management circuit consisting of a resistance emulator and an active rectifier is specially designed to optimize the WEH system. Detailed analysis on the WEH system are provided and then validated by the experimental results. For space constraint applications, conventional WTG is not suitable. In the second part of Chapter 2, a novel method to harvest wind energy using piezoelectric material (PZT) has been proposed. Energy harvested from the piezoelectric based wind energy harvester is first accumulated and stored in a capacitor until sufficient energy is harvested, a trigger signal is then initiated to release the stored energy in the capacitor to power an autonomous wind speed sensor node. Experimental results are provided to verify the novel method proposed in this work.

Chapter 3 discusses on thermal energy harvesting (TEH) from ambient heat sources with low temperature differences. TEH have recently received great attention but impeded by the challenges of low energy conversion efficiency, inconsistency and low output power due to temperature fluctuation and higher cost. To supplement the TEH scheme in sustaining the operation of a wireless sensor node, this chapter presents a DC-DC buck converter with resistor emulation based maximum power point (MPP) tracker. The resistance emulator approach uses a specially designed ultra-low-power power management circuit to perform close impedance matching between the thermal energy harvester and the sensor node to achieve maximum power point tracking (MPPT) under varying thermal conditions. Detailed design steps are provided for obtaining various parameters of the resistance emulator used in this work. Experimental results validate the performance of the

optimized TEH system.

Like any of the commonly available renewable energy sources, vibration is another type of energy source. Human activity can be the source of vibrational energy. Chapter 4 presents two types of piezoelectric-based vibration energy harvesting (VEH) systems to harvest impact or impulse forces from human pressing a button or switch action. The issues with conventional approach of using electrical cables in residential and industrial buildings to connect the appliance to the control switch on the wall have been a cause of nuisance. To resolve the problem, a batteryless and wireless remote controller has been developed to switch the electrical appliances such as lights and fans ON/OFF in a wireless manner. The experimental results verify that by depressing: (1) the piezoelectric pushbutton igniter or (2) the pre-stressed piezoelectric diaphragm material, electrical energy is generated and stored in the capacitor. Once sufficient energy is harvested, the batteryless and wireless remote controller is powered up for operation.

Energy harvesting system itself has an inherent problem, that is the intermittent nature of the ambient energy source; hence the operational reliability of the wireless sensor node may be compromised. To augment the reliability of the wireless sensor nodes operation, Chapter 5 discuss on two hybrid energy harvesting (HEH) approaches. A hybrid of wind and solar energy harvesting scheme is proposed to harvest simultaneously from both energy sources in order to extend the lifetime of the wireless sensor node. When the two energy sources of different characteristics are combined together, it is bound to have the issue of impedance mismatch between the two different sources and the load. To overcome the problem, each energy source has its own power management unit to maintain at its respec-

tive maximum power points (MPPs). Experimental results obtained show that the electrical power harvested by the optimized HEH system is much higher than the single-source based WEH. Chapter 5 also presents a hybrid of indoor ambient light and thermal energy harvesting scheme that uses only one power management circuit to condition the combined output power harvested from both energy sources. An efficient microcontroller-based ultra low power management circuit with fixed voltage reference based MPPT is implemented with closed-loop voltage feedback control to ensure near maximum power transfer from the two energy sources to its connected electronic load over a wide range of operating conditions. Experimental results are provided to validate the proposed HEH scheme by directly connecting the two energy sources in parallel configuration.

Other than energy harvesting, Chapter 6 has also demonstrated an alternative means to remotely power low-power electronic devices through wireless power transfer (WPT) mechanisms. The WPT mechanism uses the concept of inductive coupling i.e. by harvesting the stray magnetic energy in power lines to transfer electrical power without any electrical connection. Experimental results obtained validates the performance of the developed WPT system. To extend the WPT distance, self-resonating coils, operating in a strongly coupled mode, is demonstrated. Detailed theoretical analysis on the WPT system have been provided and then verify by the simulation results. Experimental validation of the performance of the WPT system is provided.

Chapter 7 concludes the thesis. It briefly states the focus areas and then discusses the proposed solutions. It also lists the possible future work in this line of research.

1.6 Summary

This chapter introduces the problem of limited energy supply of battery, hence operational lifetime of wireless sensor nodes and explains the motivation for the thesis work. The basic of energy harvesting and its system design are described. A literature survey on the past work in this area is provided. The main contribution of this thesis are then listed. The structure of this thesis is provided along with the focus area of each chapter. The next chapter elaborates on the small-scale wind energy harvesting research.

Chapter 2

Wind Energy Harvesting System

Like any of the common renewable energy sources, wind energy harvesting (WEH) has been widely studied and researched for high power applications where large wind turbine-generators are used for supplying power to remote loads and grid-connected applications [55] - [56]. However, to the author's best knowledge, few research works can be found in the literature that discuss the issue of small-scale WEH [35] and [60], those are miniaturized in size and highly portable, to power small autonomous sensors deployed in remote locations for sensing and/or even to endure long-term exposure to hostile environment such as forest fire. On top of energy harvesting from the wind source, the incoming wind speed can be sensed to determine the outbreak of a disaster and raise an emergency warning to the people in that area so that the people have enough time to respond to the emergency situation. This would thus reduce the number of causalities caused by the disaster.

In this chapter, two types of small-scale WEH schemes have been introduced namely: (1) direct WEH approach using wind turbine-generator in Section 2.1 and (2) indirect WEH approach using piezoelectric material in Section 2.2. Several

challenges are associated with these types of small-scale WEH systems in contrast to the large-scale WEH systems and they are listed respectively as follows:

1. Random wind at conceal deployment site of small-scale WEH, rather than regular wind flow in open field, results in extremely intermittent and fluctuating wind energy supply.

2. Low wind speeds at low height and conceal ground, in the range of 2-7 m/s, as compared to large-scale WEH systems with tall towers up to 90 m, exposure to high wind speeds of >10 m/s, significantly reduce the harvested power by a factor of cube root.

3. Weak aerodynamic force generated with very small windfront area of few sq. inches in comparison to huge wind turbine further lessen the available wind power for harvesting.

4. Small size, light weight and low cost WEH system required by miniaturized ubiquitous wireless sensor nodes instead of large-scale WEH system for power generation.

Due to the challenges, the proposed direct and indirect WEH systems have to be small in size and light weight, comparable to the miniaturized wireless sensor node, and able to harvest sufficient energy from the weak and uncertain wind energy source to sustain the operation of the sensor node for a long period of time.

2.1 Direct WEH Approach using Wind Turbine-Generator

To better understand the functionality and performance of the direct wind energy harvesting (WEH) system, the circuit architecture of a wind-powered wireless sensor node is presented in Figure.2.1. The wind-powered sensor node in Figure.2.1 consists of three main building blocks: (1) energy harvester incorporating the wind-turbine coupled to the electrical generator; (2) power management unit, which consists of power conditioning circuit and energy storage and (3) wireless sensor node itself.

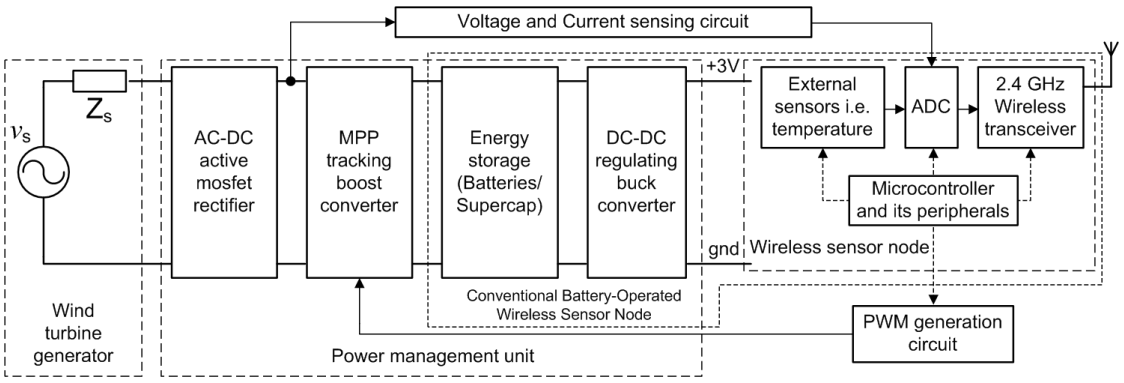

Figure 2.1: Functional block diagram of wind energy harvesting (WEH) wireless sensor node

For a space-efficient WEH system operating at low wind speeds, the AC voltage, V_p (peak), generated by the wind turbine-generator is in the range of 1-3 V, which is relatively smaller than that of the large wind turbine of MW power rating and output voltage of hundred of volts [55]. It is thus challenging for the AC-DC rectifier using conventional silicon-based diodes, which has high on-state voltage drop, V_{on}, of 0.7 V to 1 V, to rectify and convert the low amplitude AC voltage into a form usable by the electronic circuits. Based on the instantaneous output DC voltage given by $V_{dc} = V_p - 2 * V_{on}$, it can be seen that the efficiency of

the AC-DC rectifier using diodes is especially low for small-scale WEH system. To overcome this challenge, MOSFETs are used in place of the conventional diodes because the voltage drop across MOSFET is smaller than that with diode. A MOSFET-based active rectifier using comparators to sense the zero-crossings of the input AC voltage has been proposed in the literature [63] - [65] to achieve high AC-DC power conversion efficiency in very low voltage applications. The problem with this approach of sensing voltage is that if the input voltages of each of the comparators are too close to each other, excessive oscillations occur and the AC-DC rectifier's efficiency is drastically reduced. To enhance the performance of this active rectifier, a current sensing approach for generating the gating signals for the MOSFET-based active rectifier has been designed and implemented in the chapter.

Another challenging issue addressed in this chapter is the electrical power harvested by the WEH system for powering the wireless sensor nodes is often very low, of the order of mW range or less. The situation is even worst if the wind turbine-generator is not operating at its maximum power point. The primary concern is to develop a high efficiency power converter using micro-power associated electronic circuits to track and maintain maximum output power from the wind turbine-generator to sustain the wireless sensor node operation over a wide range of operating conditions. MPPT techniques have been commonly used in large-scale WEH systems [66] - [68] for harvesting much higher amount of energy from the environment. However, these MPPT techniques require high computational power to fulfill their objective of precise and accurate MPP tracking. Implementation of such accurate MPPT techniques for small-scale WEH whereby the power consumed by the complex MPPT circuitry is much higher than the harvested power itself and therefore is not desirable. So far, very limited research works can be found in the

literature that discuss on a simple but compatible MPPT algorithm in addressing the issue of small-scale WEH system. In this chapter, the resistor emulation approach has been investigated for a micro wind turbine-generator. The rationale behind the resistor emulation approach is that the effective load resistance is controlled to emulate the internal source resistance of the wind turbine-generator [69] - [71] so as to achieve good impedance matching between the source and load and hence the harvested power is always at its maximum at any operating wind speed.

Emphasis of this chapter is placed on resolving the two above mentioned challenges associated with small-scale wind energy harvesting (WEH) wireless sensor node using the designed ultra-low-power management circuit with little overhead power consumed. The rest of the chapter is organized as follows: Section 2.2.1 describes the details of the wind energy conversion system and also determines the output power available at each stage of the system. Section 2.2.2 discusses the issues related to the design of efficient power management circuit to interface the wind turbine-generator and the wireless sensor node. Following that, the experimental results of the optimized WEH wireless sensor node prototype are illustrated in Section 2.2.3, with the conclusion reported in Section 2.2.4.

2.1.1 Wind Turbine-Generator

Within the wind energy harvesting (WEH) system, the energy harvester, which converts the raw wind energy harnessed from the ambient environment into electrical energy of AC or DC form depending on the type of generator used, is first investigated. In this case, the energy harvester is a horizontal-axis micro wind turbine with blade radius of 3 cm directly coupled to a single-phase AC generator

of volumetric size of 1 cm^3. The process starts with quantifying the wind power, P_{wind}, using the relationship between the input wind speed, v, in m/s and the output power available in wind, P_{wind}, in W expressed as [72],

$$P_{wind} = \frac{1}{2}\rho A v^3 \tag{2.1}$$

where A is the given windfront contact area in m^2. Using the nominal daily wind speed recorded throughout the month in a sample remote area environment as shown in Figure.2.2 [73], the average wind speed throughout the month is calculated to be around 3.62 m/s. Based on the Beautfort scale, the calculated average wind speed is termed as fairly light, which is equivalent to a gentle breeze and the amount of energy available in the wind for harnessing is therefore quite limited. Under the gentle breeze condition, the power available in the wind is computed based on eqn.2.1 to be 82 mW. As can be seen in Figure.2.2, it is noted that the fluctuation in the wind speed is quite significant; wind speed can go as high as 6 - 7 m/s and resides at low wind speed of around 2 m/s for many days. This high fluctuation in the wind speed, due to the geographical condition of the sample remote area, requires the power management circuit to have wide input operating bandwidth to be able to cover the minimum as well as maximum harvested electrical power.

Figure.2.3 shows the functional block diagram of the wind turbine-generator system showing the conversion of raw wind power to electrical power indicating the corresponding power available at different stages for example, the raw wind power, P_{wind}, the mechanical power, P_T, and the electrical power, P_{elec}. When wind flow pass the blades of the wind turbine, some parts of the power available in the wind is harvested by the wind turbine to generate electricity. It is experimentally tested that the aerodynamic efficiency (also known as the power coefficient, C_p) of the wind turbine with a wind speed of 3.62 m/s is around 39% ($C_p = 0.39$). Using all

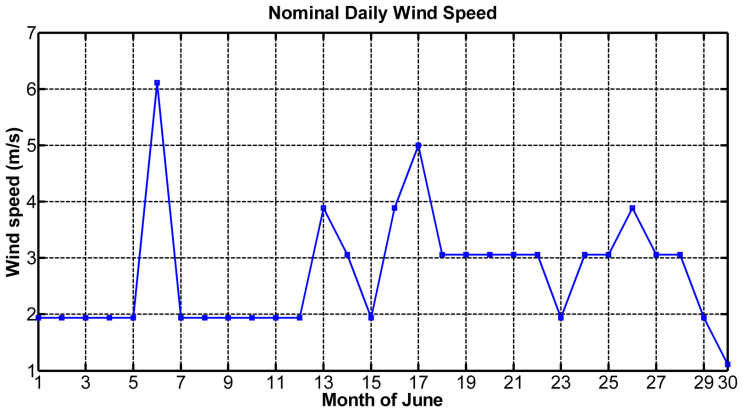

Figure 2.2: Nominal monthly wind speed in a typical deployment location over a period of 30 days in year 2006

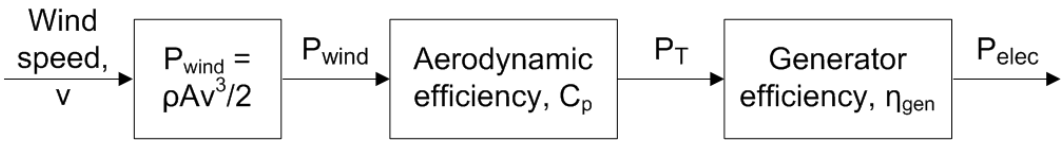

Figure 2.3: Functional block diagram of wind turbine-generator

the technical information gathered for the wind turbine-generator, the theoretical power, P_T, generated by the wind turbine at an average wind speed of 3.62 m/s can be calculated as,

$$\begin{aligned} P_{T,3.62m/s} &= C_p P_{wind} \\ &= \frac{1}{2}(0.39)(1.225)[\pi(0.03^2)](3.62^3) = 32mW \end{aligned} \tag{2.2}$$

The estimated power of 32 mW is the mechanical power available at the rotor shaft of the wind turbine based on the aerodynamic blade effect as well as the rotor shaft of the direct-coupled electric generator. Referring to Figure.2.3, taking the generator efficiency, η_{gen}, into the power flow calculation, the amount of electrical power harvested by the wind turbine, P_{elec}, can be described in terms of the incoming

wind speed by the following equation,

$$\begin{aligned} P_{elec,3.62m/s} &= \eta_{gen} P_{T,3.62m/s} \\ &= (0.41)(32mW) = 13.12mW \end{aligned} \tag{2.3}$$

The electrical powers, P_{elec}, obtained experimentally from the wind turbine over a range of simulated wind speeds of 1.3 - 8.5 m/s are tested with different resistance loadings and the power curves of the wind turbine are shown in Figure.2.4. For the wind speeds ranging from 2.3 m/s to 7 m/s available at the deployment site as shown in Figure.2.2, it is observed from Figure.2.4 that the harvested electrical power ranges from 2 mW to 70 mW respectively. For the average wind speed at the target site of 3.62 m/s, the electrical average output power generated by the wind turbine is 13 mW. This maximum electrical power of 13 mW can only be harvested from the wind turbine at matching load resistance of 100 Ω.

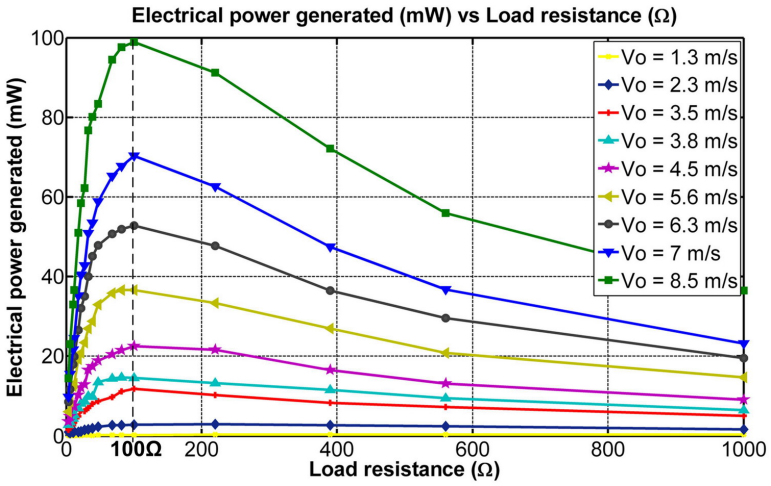

Figure 2.4: Power curves of wind turbine generator over a range of load resistances

2.1.2 Design of Efficient Power Management Circuit

In the wind energy harvesting (WEH) system, the power management unit is used to take care of the dynamics of both the wind turbine-generator subjected to environmental condition variation such as varying wind speeds as well as the power-aware wireless sensor node operating at the deployment site. Inside the power management unit, a supercapacitor, which has fast dynamic response, is employed to decouple the inter-relationship between the fluctuating energy supply of the wind turbine-generator and the duty-cycling operation of the wireless sensor node. It is necessary to optimize the power management unit with consideration of the characteristic of the wind turbine-generator and the performance of the sensor node in order to meet the application requirement. As such, a wind energy harvesting (WEH) system optimized using a specially designed ultra-low-power management circuit with two distinct highlights has been presented; (1) an AC-DC active rectifier using MOSFETs in replace of diodes for rectifying the low amplitude AC voltage generated by the wind turbine-generator under low wind condition and (2) a DC-DC boost converter with resistor emulation algorithm to perform maximum power point tracking (MPPT).

2.1.2.1 Active AC-DC Converter

The active AC-DC converter can be separated into two stages: (i) the negative voltage converter and (ii) the active diode. The first stage of the active rectifier circuit, as can be seen in Figure.2.5, is made up of four standard MOSFETs; two high-side P-type MOSFETs, PMOS1 and PMOS2, employed to deliver the positive and negative half-cycles, v_1 and v_2 respectively, of the AC voltage to the output

DC voltage, V_{dc} and two low-side N-type MOSFETs (NMOS1 and NMOS2) that provide a path for the ground node, V_{gnd}, to return to the lower potential of either v_2 or v_1 respectively. By doing so, the first stage of the active rectifier converts the negative half wave of the input sinusoidal wave into positive one. Moreover, no additional start-up circuit is necessary in this configuration because the current has an alternative path through the body diode of the MOSFET whenever the MOSFET switch is not activated.

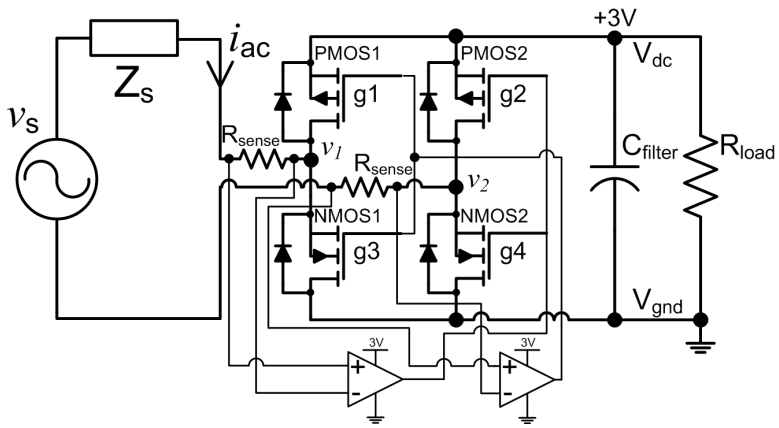

Figure 2.5: Schematic diagram of full bridge active mosfet rectifier

The main function of the second stage of the rectifier is to control the ON and OFF switching sequences of the MOSFETs residing in the first stage of the active rectifier to facilitate the rectification process. According to Lam *et al.* [64] and Seeman *et al.* [65], the proposed active diode stage uses a fast and low power comparator circuit that continuously samples the voltage across each of the MOSFET switches. The problem with this kind of voltage sensing approach is that if the voltage difference between the input AC voltage, v_1 or v_2, and the output DC voltage, V_{dc}, is small and/or the comparator is too slow, then there are excessive oscillations occurring during the on and off switching transitions as illustrated in the zoomed waveforms of Figure.2.6. Due to these unwanted oscillations, some

part of the harvested electrical energy is lost, thus resulting in the reduction in the overall efficiency.

To overcome the problem associated with very small sensing voltage across the MOSFET switches g_1 - g_4 as shown in Figure.2.5, an alternative approach is to sense the AC source current, i_{ac}, as shown in Figure.2.5, to generate the respective gating signals for the MOSFET switches g_1 - g_4 in the active rectifier circuit. The proposed current sensing circuit is specially designed to be simple and power saving using two precise zero-crossing comparators (LMC7215) with very low overhead power consumption of 90 μW. The source voltage of the comparators of 3 V is taken from the storage capacitor as shown in Figure.2.5.

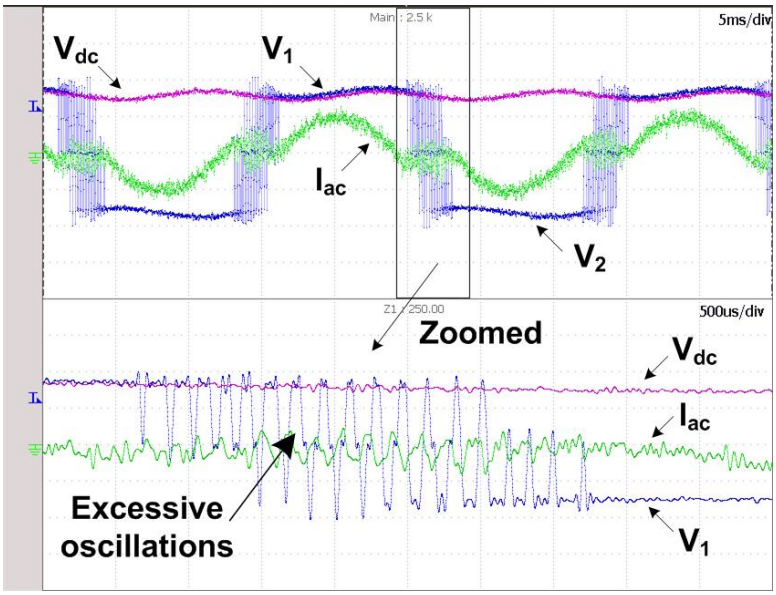

Figure 2.6: Experimental waveforms of active MOSFET full-bridge rectifier using voltage sense approach resulting in excessive oscillation

Whenever the peak value of the input AC voltage either during the positive or negative half-cycles, v_1 or v_2 respectively, is higher than the output DC voltage, V_{dc}, current, i_{ac}, flows through the sensing resistor, R_{sense}, and the zero-crossing com-

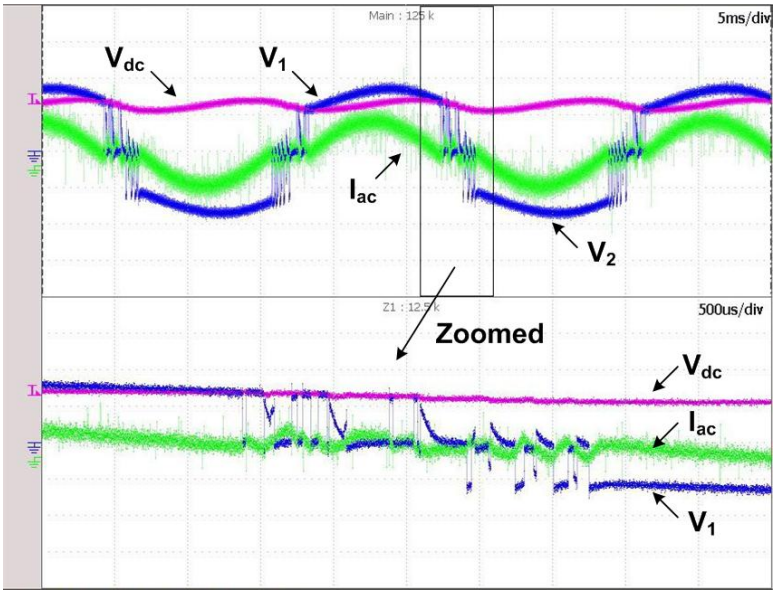

Figure 2.7: Experimental waveforms of active MOSFET full-bridge rectifier using proposed current sense approach at optimal load condition

parators sense the flow of the AC current by measuring the voltage across R_{sense}. The comparators generate the control signals to turn the respective combinations of the MOSFET switches ON or OFF i.e. 1) +ve half AC cycle: PMOS1 and NMOS2 ON, PMOS2 and NMOS1 OFF and 2) -ve half AC cycle: PMOS2 and NMOS1 ON, PMOS1 and NMOS2 OFF. During the switching transition of the MOSFET switches between on and off states, it can be clearly observed from the zoomed waveforms of Figures. 2.6 and 2.7 that using the voltage sense approach introduces more unwanted oscillations (Figure.2.6) than that using the current sense approach (Figure.2.7). The use of voltage sense approach leads to more energy loss incurred in the active rectifier, thus reduces its overall power conversion efficiency. Hence, the current sense approach, which yields better performance than its counterpart, is employed in the active rectifier to control the switching of the MOSFET switches in the bridge rectifier bridge.

The performance of the MOSFET-based active rectifier using proposed cur-

rent sense approach is compared with the conventional diode-based passive rectifier to seek for a better solution for rectifying low amplitude AC voltages generated by micro wind turbine, especially at low wind speeds. The performance comparison is based on the voltage drops measured across the two diodes and the two MOSFETs of the rectifiers and they are plotted over a range of the load resistances as shown in Figure.2.8. At optimal load of 150 Ω, it is observed that the voltage drop in the passive rectifier at a wind speed of 3.62 m/s is around 0.6 V, which is four times more than the voltage loss in the active rectifier of around 0.15 V. With lesser voltage drop in the active rectifier, the active rectifier is able to rectify much lower amplitude input AC voltages than that of the passive rectifier, which allows the wind turbine to keep harvesting even for very low incoming wind speed. Additionally, more electrical power is harvested from the wind turbine (See Figure.2.9)), thus a higher AC-DC power conversion efficiency is achieved over a wide range of wind speeds as shown in Figure.2.10.

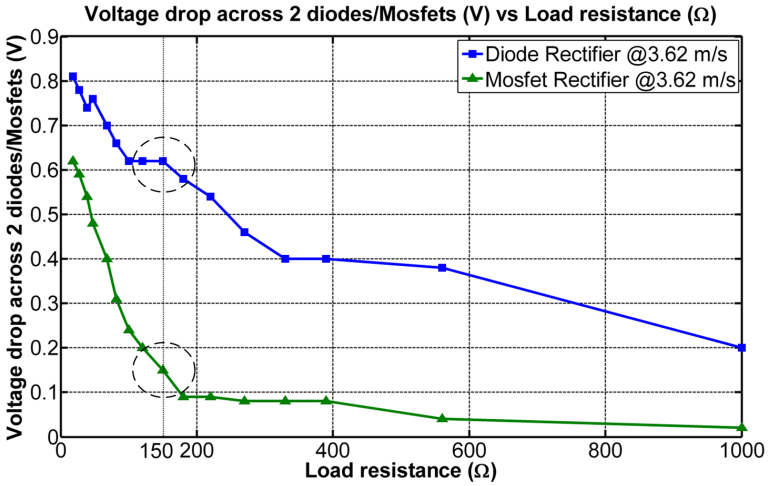

Figure 2.8: Voltage drop comparison between diodes and MOSFETs (V) over a range of load resistance (Ω)

Consolidating all the experimental data collected for both the passive and

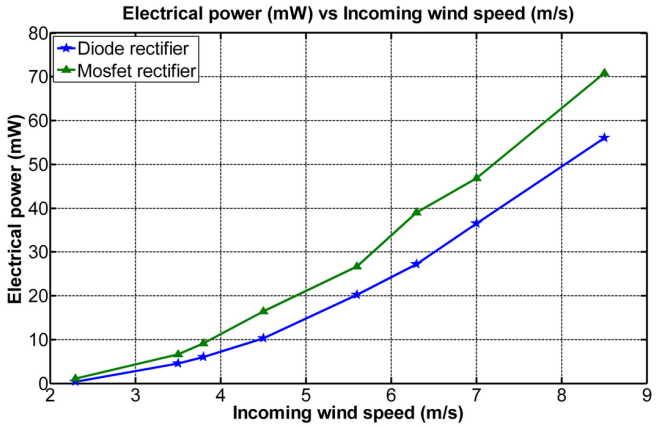

Figure 2.9: Electrical power generated by active and passive rectifiers at optimal load condition

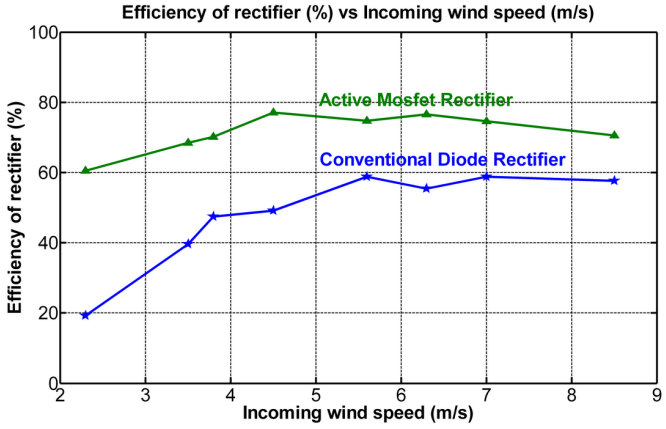

Figure 2.10: Efficiency comparison between active and passive rectifiers under optimal load condition

active rectifiers, the efficiencies of both rectifiers are calculated using eqn.2.4 (under unity power factor operation as illustrated in Figure.2.7) and then plotted in Figure.2.10 for comparison.

$$\eta_{rect} = \frac{P_{dc}}{P_{ac}} * 100\% = \frac{V_{dc,meas}^2 / R_{load}}{V_{ac,meas} * I_{ac,meas} * (cos\phi \simeq 1)} * 100\% \tag{2.4}$$

Over the span of wind speeds from 2.3 m/s to 8.5 m/s, the efficiency of the MOSFET-based active rectifier is on average 15% - 25% higher than the diode-based passive rectifier (See Figure.2.10). This improvement in the efficiency of the AC-DC conversion process is mainly due to the replacement of diodes with very

low on-state voltage drop MOSFETs and its associated ultra-low-power current sensing and control circuit. It is worth noting that the power loss incurred in the current sensing and control circuit is only 90 μW, which is a small fraction of the total harvested power as seen in Figure.2.9, so it does not pose any significant electrical loading to the main wind energy harvesting (WEH) system. Additionally, even though the components used in active rectifier such as MOSFETs and operational amplifiers are more expensive than a simple diode rectifier, the surplus in harvested power is very crucial in small-scale WEH system. Hence the proposed active rectifier holds great importance in the design of the power management unit of the WEH system.

2.1.2.2 Boost Converter With Resistor Emulation Based MPPT

Unlike standard voltage regulating boost converters, the main functions of the boost converter in the power management unit of the wind energy harvesting system are: (1) to step up the low DC voltage output of the wind turbine, V_{dc}, to charge the energy storage device and (2) to perform maximum power point tracking (MPPT) so that maximum power transfer takes place. Depending on the energy storage level of the supercapacitor, the output voltage of the wind generator, V_{dc}, is manipulated to transfer maximum power to the supercapacitor by adjusting the duty cycle of the PWM gate signal of the boost converter such that V_{dc} is as close as possible to V_{mppt}, the voltage at which the harvested power is at its maximum.

There are different algorithms proposed to date for seeking the maximum power point (MPP) for stand-alone photovoltaic systems [74] as well as for large-scale wind turbine [66]. According to Salas *et al.* [74], the MPPT algorithms can be

grouped into *direct* and *indirect* methods. The direct method involves iterative and oscillating search for the MPPs, resulting in excessive energy loss during the search process that is very undesirable for small-scale wind energy harvesting (WEH) system. As for the commonly used indirect methods, refer to the electrical power harvested curves against the generated voltage and current as shown in Figures. 2.11 and 2.12 respectively, it is observed that the MPPT voltage (V_{mppt}) and current (I_{mppt}) at which the harvested power is maximum are different for different incoming wind speed, hence variables such as V_{mppt} and I_{mppt} cannot be set as references for the indirect MPPT method.

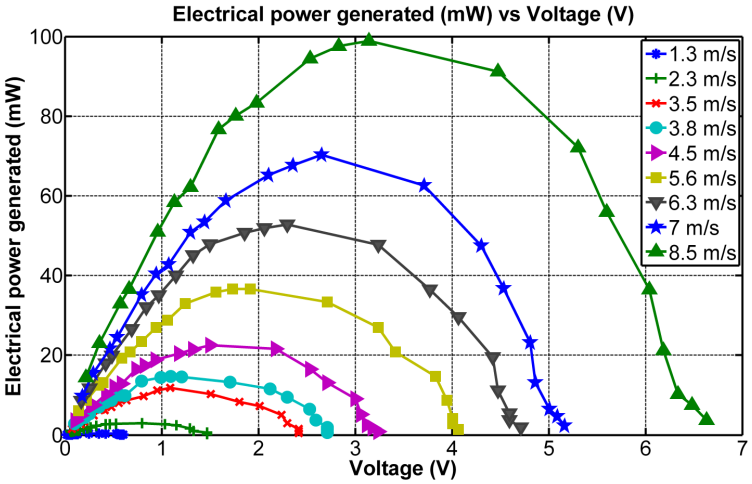

Figure 2.11: Power harvested by wind turbine generator plot against generated voltage for a range of wind speeds

Since most of the conventional MPPT algorithms are not suitable for the WEH system, this chapter presents an alternative MPPT technique based on the concept of emulating the load impedance to match the source impedance as described by Paing *et al.* and Erickson *et al.* in [69] and [70] respectively. This technique is also known as resistor emulation or impedance matching. The power curve plotted in Figure.2.4 shows that when the load resistance matches the source

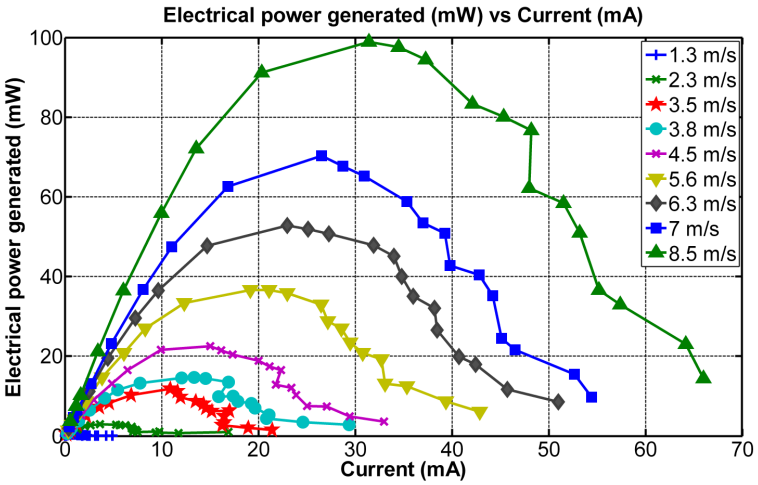

Figure 2.12: Power harvested by wind turbine generator plot against generated current for a range of wind speeds

resistance of the wind turbine-generator, the harvested power is always maximum for different wind speeds. However, for other loading conditions, shifting away from the internal resistance of the wind turbine-generator, either very light or heavy electrical loads, the electrical output power being generated by the generator drops significantly. This exhibits that the MPPT technique based on resistor emulation is a possible option to assist the small-scale WEH system to achieve maximum power harvesting from the wind turbine-generator.

K. Khouzam & L. Khouzam [69] discussed the direct-coupling approach for optimum load matching between the energy harvester and its load by carefully selecting the harvester's rated parameters with respect to the load parameters. Another resistor emulation approach proposed by Paing *et al.* in [70] is to operate the boost converter as an open-loop resistor emulator with proper selection of the components to naturally track the MPP to match the optimal load impedance for the energy harvester. Both approaches require some form of initial tuning as well as the load impedance needs to be fixed. However, in practice, this may not be the

case as the load impedance tends to change just like the charging and discharging process of the supercapacitor, therefore the direct-coupling method as well as the simple open-loop resistor emulation method may not be suitable in this context. To overcome that, a microcontroller-based resistance emulator with closed-loop feedback resistance control scheme is proposed as the MPP tracker of the wind energy harvesting (WEH) wireless sensor node for various dynamic conditions. The proposed scheme does not require any initial tuning, unlike those two existing approaches, because there is a microcontroller, together with its feedback resistance, to automatically tune the WEH system to its MPPT points. In addition, the proposed MPP tracker is embedded with the closed-loop control feature to continuously track and emulate the reference optimal resistance as the load impedance changes. The designed boost converter circuitry with resistor emulation MPPT

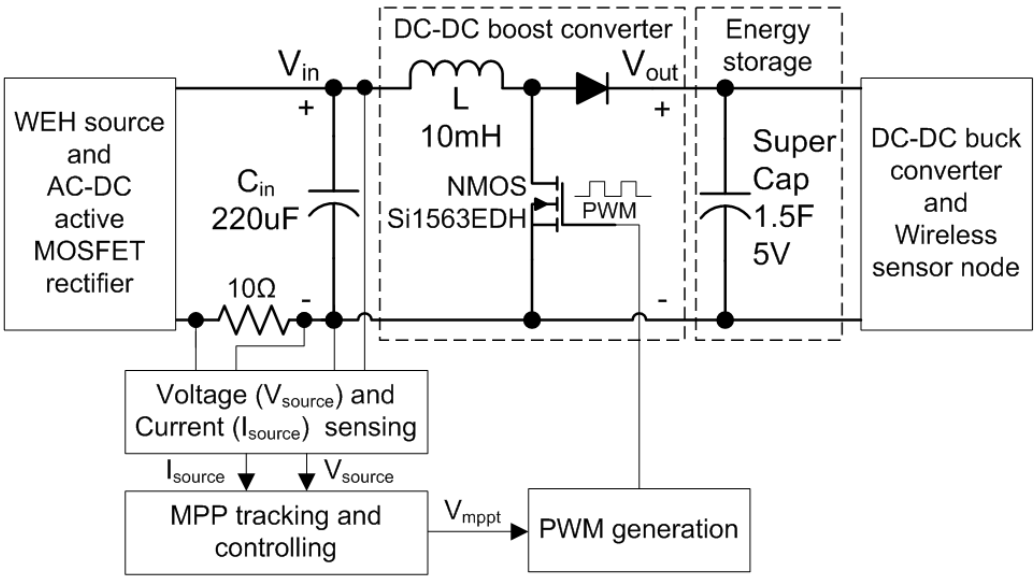

Figure 2.13: Overview of DC-DC boost converter with MPPT

approach is depicted in Figure.2.13 and it is essentially composed of three main building blocks: (1) a boost converter to manage the power transfer from the wind turbine to the load i.e. power management unit, supercapacitor and WSN, (2)

a MPP tracker based on resistor emulation approach and its sensing and control circuit that manipulates the operating point of the wind turbine to keep harvesting power at the maximum power point and (3) PWM generation circuit. Using the voltage and current sensing circuit, the feedback resistance signal, R_{fb}, is obtained and compared with the reference resistance signal, $R_{opt,ref}$, in a microcontroller to perform the closed-loop MPPT control of the boost converter via the PWM generation circuit. The PWM generation circuit is used to multiply the low frequency PWM control signal, <100 Hz, generated from the low-power microcontroller to a much higher switching frequency, 10 kHz, so that smaller filter components are used in the boost converter to miniaturize the overall WEH system.

To experimentally verify the concept of resistor emulation approach to perform maximum power point tracking (MPPT) for small-scale wind energy harvesting (WEH), the input resistance of the boost converter, which is known as the emulated resistance of the wind turbine, R_{em}, is electronically controlled to sweep through a wide range of values (10-800 Ω) as shown in the power curve (left side) and I-V curve (right side) of Figure.2.14. Based on the fundamental equations of the DC-DC boost converter under continuous conduction mode (CCM), the emulated resistance at the input port of the converter is governed by eqn.2.5,

$$R_{em} = (1 - D)^2 R_{load} \tag{2.5}$$

Under static load condition, a fixed resistor, R_{load}, of 1.2 $k\Omega$ is selected to represent the average power consumption of the wireless sensor load. Since R_{load} is a constant, the input resistance, R_{em}, of the converter is related to the duty cycle, D, of the boost converter as expressed in eqn.2.5. As such, R_{em} is manipulated to match with the internal resistance of the wind turbine of 150 Ω to attain MPPT by controlling

the duty cycle, D, of the boost converter's gating signal.

$$D = 1 - \sqrt{\frac{R_{em}}{R_{load}}} \tag{2.6}$$

Referring to the sweeping process captured in the oscilloscope as shown by the power curves in Figure.2.14, it is observed that all the maximum power points are centralized around the optimal resistance of 150 Ω for different wind speeds. The experimental results obtained illustrate that using the designed boost converter circuitry with resistor emulation MPPT approach, maximum power is indeed transferred from the wind turbine-generator to the wireless sensor load.

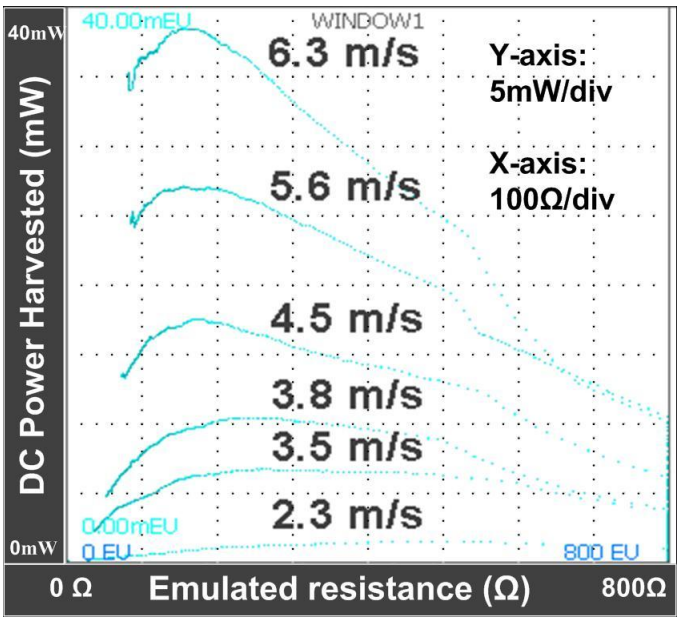

Figure 2.14: Experimentally obtained power and I-V curves for various incoming wind speeds

The MPPT performance of the designed boost converter together with its proposed closed-loop resistance emulator is also tested experimentally under dynamic condition i.e. changing wind speeds from 2.3 m/s to 6.3 m/s as illustrated in Figure.2.15. At first, a light wind of 2.3 m/s is blown at the wind turbine-generator and the start point marked in Figure.2.15 is the initial condition of the wind energy

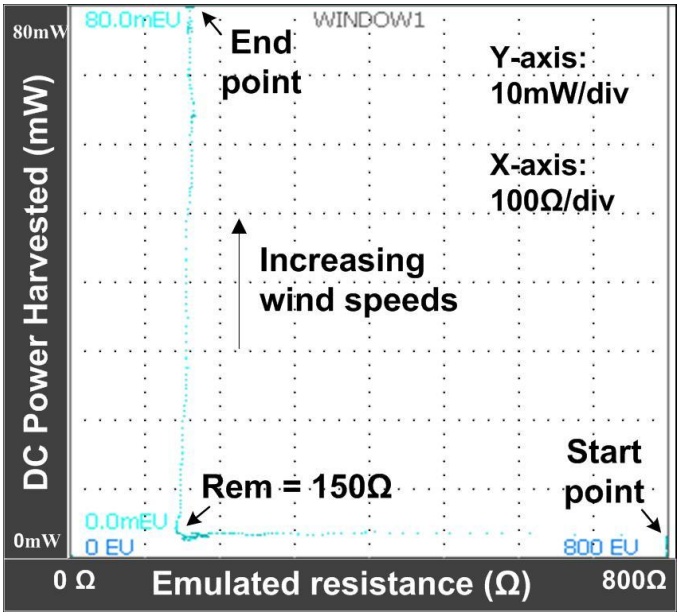

Figure 2.15: Performance of MPP tracking boost converter under varying wind speeds

harvesting (WEH) system. The MPP tracker utilizes the closed-loop PI controller to manipulate the duty cycle of the boost converter according to eqn.2.6, which in turn controls the input resistance of the boost converter towards (left side) the optimal resistance value of 150 Ω. Once the maximum power point (MPP) of the power curve for wind speed of 2.3 m/s is reached, the closed-loop resistance emulator controls the boost converter to maintain power harvested from the wind turbine-generator for all the other MPPs occurring at different wind speeds. Referring to Figure.2.15, it is observed that the emulated resistance, R_{em}, is maintained at around 150 Ω with increasing wind speeds, until the MPP of the power curve for wind speed of 6.3 m/s, marked as end point in Figure.2.15, is reached. This shows that the dynamic condition of the environment is well taken care off by the proposed closed-loop resistor emulator of the designed boost converter.

The designed boost converter with resistor emulation MPPT approach has already been demonstrated to yield excellent performance in extracting maximum

power from the wind turbine-generator, but this comes at the expense of additional power losses in the converter and its associated control, sensing and PWM generation circuits. It is thus necessary to investigate the significance of these power losses as compared to the total harvested power. The first investigation is to determine the efficiency of the boost converter, η_{conv}, as a function of its output load power, P_{load}, over its input DC power, P_{dc}. Taking the target deployment area with average wind speed of 3.62 m/s as an example, the efficiency of the converter is calculated to be as follows,

$$\begin{aligned} \eta_{conv} &= \frac{P_{out}}{P_{in}} * 100\% = \frac{V_{out}^2/R_{load}}{V_{in}I_{in}} * 100\% \\ &= \frac{9.71V^2/1200\Omega}{1.15V * 8.14mA} * 100\% = 84\% \end{aligned} \tag{2.7}$$

For all other wind speeds, the efficiencies of the boost converter are calculated using eqn.2.7 to be between 80% - 90% and the computed results are shown in Figure.2.16. It can be seen that even for light wind speed condition where the power harvested is small (around 2 mW), the boost converter is still able to achieve a reasonably good efficiency of 86%. This exhibits the ability of the DC-DC boost converter to attain high efficiency in very low power rating condition.

Another investigation being carried out is to determine the power consumption of the associated control, sensing and PWM generation electronic circuits and its significance as compared to the harvested power. Based on the voltage and current requirements of each individual component in the sensing and processing circuits, the total power consumption of the electronic circuits is calculated to be

$$\begin{aligned} P_{consumed} &= P_{sensing} + P_{processing} + P_{PWMgeneration} \\ &= 3V * (74\mu A + 15\mu A + 30\mu A) = 0.357mW \end{aligned} \tag{2.8}$$

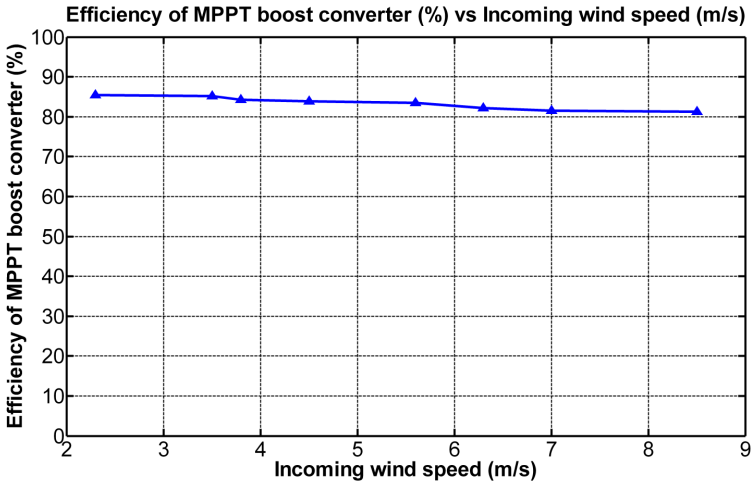

Figure 2.16: Efficiency of MPP tracking boost converter for various incoming wind speeds

Taking into account both the power loss across the boost converter and the power loss in the associated control, sensing and PWM generation circuits mentioned by eqns.2.7 and 2.8 respectively, the performance comparison between the wind energy harvesting (WEH) system with maximum power point tracking (MPPT) and without MPPT are tabulated in the bar chart shown in Figure.2.17. For all the wind speed measurement points shown in Figure.2.17, it is observed that the performance of the WEH system with MPPT, including the converter's efficiency loss and circuits' power loss, is more superior than the WEH system without MPPT. It is even more obvious for higher wind speeds, as seen in Figure.2.17, where the difference in the harvested power between the WEH system with MPPT scheme and without MPPT scheme is significant; up to four times more electrical power can be harvested from the wind turbine at a wind speed of 8.5 m/s. This exhibits the importance as well as the contribution of implementing MPPT in the WEH system.

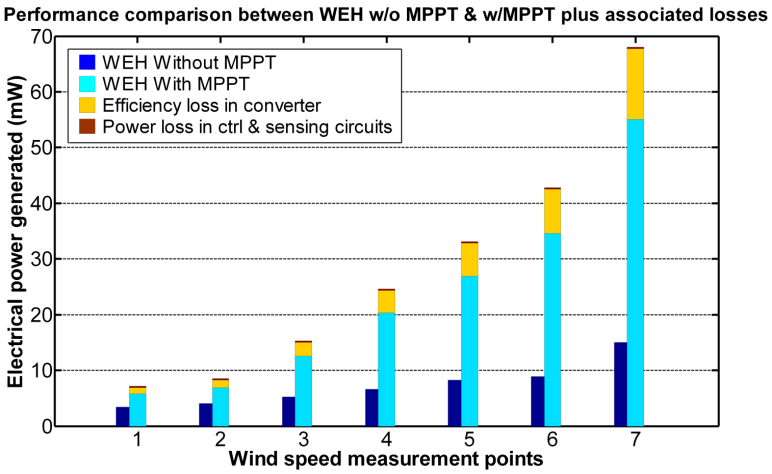

Figure 2.17: Performance comparison between the WEH system without MPPT and the WEH system with MPPT plus its associated losses for various incoming wind speeds

2.1.2.3 Energy Storage

For long term deployment of the wireless sensor node, it is required to have an energy storage device such as supercapacitor and batteries onboard the sensor node to sustain its operation throughout the lifetime. It is also crucial to ensure that this energy storage device has operational lifespan of equivalent length or even longer so that the wireless sensor network (WSN) lifetime is prolonged. Comparing between the choice of using supercapacitors or batteries as the energy storage for the WEH system, supercapacitor has been chosen. The reason is that the supercapacitor exhibits several superior characteristics over the batteries that are useful for the WEH system. These characteristics include numerous full charge cycles (more than half a million charge cycles), long lifetime (10-20 years operational lifetime) and high power density (an order of magnitude higher continuous current than a battery) to provide high instantaneous power to the sensor node during burst mode operation such as radio transmission [34].

Unlike the discrete capacitors which have very small capacitance values of μF range and usually used in supply rails for decoupling purposes, the supercapacitor has very large capacitance value of Farads range suitable for energy storage purpose. When a large capacitor that is in the Farads range is initially attached to the energy source, the component with minimum energy stored acts as a short circuit to the energy source and the supply rail voltage drops to the capacitor voltage level. The same situation occurs when the large capacitor is attached to the wind turbine generator as well. Although the wind turbine still charges the supercapacitor under this condition, it does not do so efficiently. This is because the charging process is not executed at the maximum power point (MPP), which is the voltage and current combination that maximizes power output under a given wind speed condition. A supercapacitor that is charged in this manner reduces the wind energy harvesting (WEH) efficiency by a factor of 2-4 as illustrated in Figure.2.18. Hence the dynamic response of the supercapacitor is of importance to be considered in the design of the boost converter so as to ensure constant maximum power point tracking (MPPT) operation is achieved by having a closed-loop resistor emulator instead of the open-loop resistor emulation method suggested in [70] where the load impedance is assumed to be constant.

For a time period of 500 seconds as shown in Figure.2.18, the supercapacitor is charged by the WEH system from its discharged stage. At $V_{cap}(500sec)$, the supercapacitor of 1.5 F is being charged to the voltage levels of 2.14 V with MPPT scheme and 0.66 V without MPPT scheme. Comparing between the two schemes, it is obvious that the charging performed by the WEH system with MPPT is much higher than its counterpart without the MPPT scheme. This is because more electrical power is transferred from the wind turbine through the boost converter

with resistor emulation MPPT scheme to the supercapacitor. Under dynamic load condition, changing R_{load}, the closed-loop resistance emulator is still able to manipulate the duty cycle, D, of the boost converter given by eqn.2.6, to maintain R_{em} always at the optimal resistance value, so that MPPT operation takes place. When the WEH system is operating with MPPT scheme, the amount of energy accumulated in the supercapacitor after 500 seconds is 3.43 J, which is 10 times more than its counterpart of 0.33 J, hence this exhibits the superior performance of the WEH system with MPPT scheme over its counterpart under dynamic load condition.

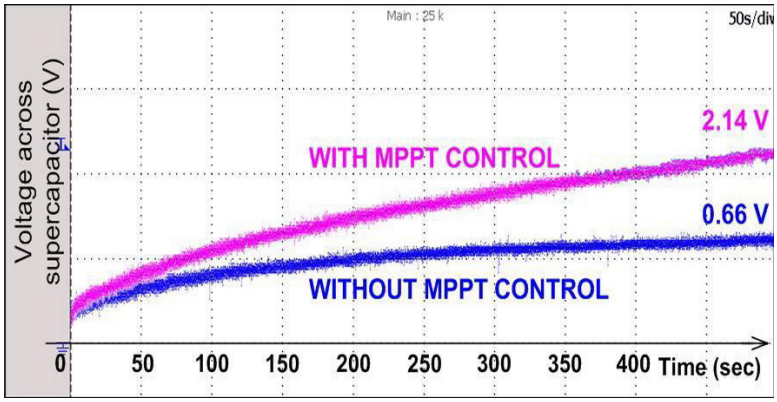

Figure 2.18: Performance of wind energy harvesting (WEH) system with MPPT and without MPPT for charging a supercapacitor

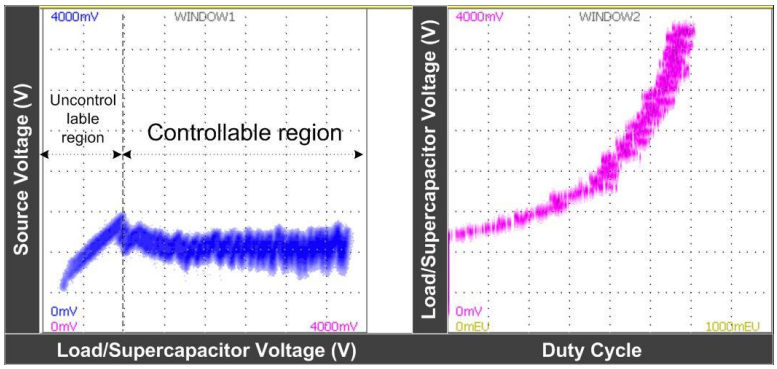

Figure 2.19: Illustration of the supercapacitor's charging process using the WEH system with MPPT

The charging process, as seen in Figure.2.19, is divided into two regions namely uncontrollable and controllable regions. Initially, the supercapacitor is fully discharged, so the wind energy harvesting (WEH) system charges the supercapacitor freely without much control over the duty cycle of the boost converter. The controllable region only starts when the supercapacitor voltage builds up to the MPPT voltage, $V_{mppt} = 1.15$ V, of the WEH system at wind speed of 3.62 m/s. After which, the supercapacitor continues to be charged with maximum power harvested from the WEH system. The whole process is illustrated by the source vs load voltage diagram (left side) of Figure.2.19. Based on the governing equation expressed in eqn.2.5, as the voltage of the supercapacitor charges up, the effective resistance of the supercapacitor increases, hence the duty cycle is adjusted according to eqn.2.6, as shown in Figure.2.19, to maintain MPPT at optimal resistance. By adding a supercapacitor, whose charging characteristics are nonlinear in nature, as an energy buffer between the source and the load, it is shown that the closed-loop resistance emulator of the boost converter is still able to operate the WEH system at its MPPs.

2.1.2.4 Wireless Sensor Node

The wind energy harvesting (WEH) system is designed to power a commercially available wireless sensor node supplied by Texas Instrument (TI) known as the wireless target board, eZ430-RF2500T. The operations of the wireless sensor node deployed in an application field comprises of: (1) sensing some external analog signals such as voltage and current signals of the wind turbine-generator, temperature signal, and (2) communicating and relaying the sensed information to the gateway node in every 1 second time. Upon receiving the data at the base station, the

collected data are then post-processed into usable information for any follow up action.

Using the readily available wireless development tool, eZ430-RF2500, for the TI wireless sensor node which consists of MSP430 microcontroller and CC2500 RF transceiver, all the hardware and software required to develop the entire wireless project with the MSP430 is easily performed in a convenient USB stick. The eZ430-RF2500T uses the MSP430F2274 16-bit ultra-low-power microcontroller, which has 32kB flash, 1K RAM, 10-bit ADC and 2 op-amps and is paired with the CC2500 multi-channel RF transceiver designed for low-power wireless applications. Since the MSP430 microcontroller is part of the wireless sensor node, it is very convenient to make use of the onboard microcontroller, without incurring much extra overhead power, to achieve the proposed MPPT scheme based on resistor emulation approach rather than implementing the MPPT scheme with analog circuit mentioned in [36] and [70].

Long term operation is an important goal of the wireless sensor network (WSN) system. One attempt to achieve this goal is to reduce energy consumption of the sensor node. Energy reduction is carried out by improving hardware design and more intelligent power management, which entails turning off unused components or slowing down energy hungry devices such as microcontroller during idle periods. One approach taken is lowering the clock frequency from 1 MHz to 12 kHz which uses the internal very-low-power, low-frequency oscillator (VLO) without requiring a crystal. The active mode supply current @3 V supply voltage is tremendously reduced by a factor of 20, from 390 μA to 15 μA respectively, thus reducing the power consumed. To compensate for the slow switching frequency, an

external PWM generation circuit, which consumes few tens of μW, is designed and implemented to multiply the low frequency PWM control signal generated from the low-power microcontroller to 10 kHz range so as to miniaturize the size of the passive magnetic components. Another approach taken to reduce the energy consumption is duty cycling the transmission time of the energy-hungry radio module at a slower rate of every second preset for this chapter.

2.1.3 Experimental Results

The proposed concept of a self-powered wind energy harvesting (WEH) wireless sensor node using efficient power management circuit, as illustrated in Figure.2.20, has been implemented in hardware prototype for laboratory testing. Several tests are conducted during the experiments to validate the performance of the optimized WEH system using AC-DC active rectifier and maximum power point tracking (MPPT) with resistor emulation approach in sustaining the operation of the wireless sensor node.

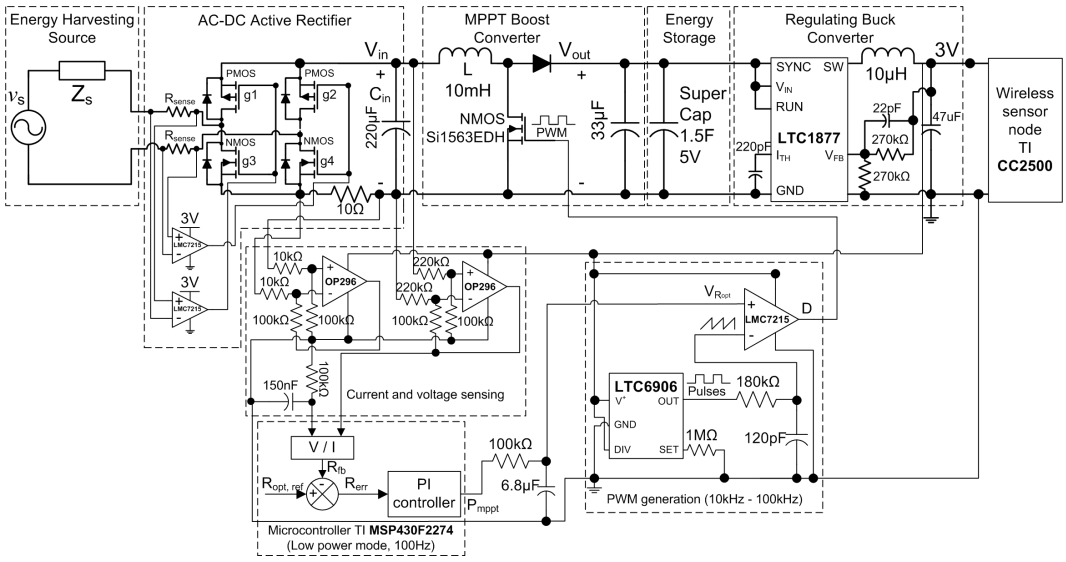

Figure 2.20: Schematic diagram of the self-powered wind sensor system

2.1.3.1 Performance of Wind Energy Harvesting System with MPPT scheme

The experimental tests are conducted in accordance with the wind condition of the deployment ground illustrated in Figure.2.2 where the average wind speed is given as 3.62 m/s. There are three experimental tests conducted as shown by three different operating regions in Figure.2.21 to differentiate the performance of the WEH system and its resistor emulation MPPT scheme in powering the load consisting of a supercapacitor, sensing and control circuit and wireless sensor node. The electrical load is at first powered with WEH system without MPPT, then with WEH system with MPPT and lastly without WEH system and MPPT. Referring to Figure.2.21, it is observed that the supercapacitor voltage, V_{cap}, keeps decreasing during the period when the WEH system is not equipped with MPPT and even more obvious for the case where neither WEH system nor MPPT is integrated into the sensor node. This phenomenon indicates that by solely dependent on the energy storage or the electrical power harvested by the WEH system without MPPT scheme is not sufficient to sustain the operation of the sensor node. It is only when the WEH system is incorporated with MPPT scheme to provide sufficient power for both the operation of the wireless sensor node as well as to charge up the supercapacitor. Whenever the WEH system is operating in its MPPT mode (see Figure.2.21), the generated output voltage of the wind turbine, V_{in}, is controlled by the microcontroller to follow the MPPT voltage (V_{mppt} = 1.15 V) based on the resistor emulation algorithm.

The effect of maximum power point tracking (MPPT) on the wind energy harvesting (WEH) system is further examined using the waveforms as shown in

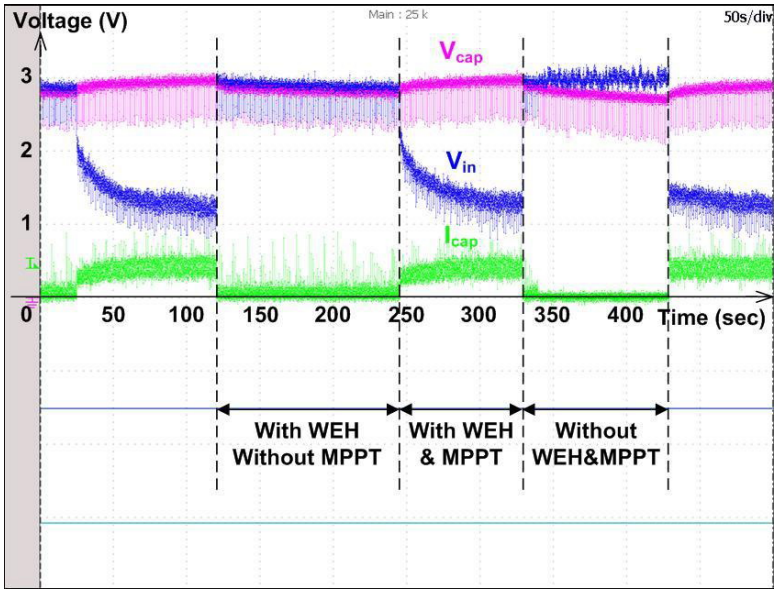

Figure 2.21: Operation of the sensor node under various powering schemes

Figure.2.22. At first, it is observed that the voltage across the supercapacitor, V_{cap}, drops from 2.9 V to 2.75 V after 350 seconds. In similar manner, the output DC voltage of the wind turbine, V_{in}, as shown in Figure.2.22 also drops from 2.9 V to 2.75 V. Based on the characteristic curve of the wind turbine-generator shown in Figure.2.11, the amount of electrical power harvested by the WEH system at wind speed of 3.62 m/s and V_{in} of between 2.75 V to 2.9 V is found to be around 1-2 mW. Since the power consumption of the wireless sensor node, including the sensing and control circuit (∼0.4 mW), of around 3.6 mW @1 second per transmission is more than the harvested power of 1-2 mW, the power harvested by the WEH system alone is not sufficient to maintain the operation of the sensor node. However, when the source and load impedances are nicely matched using the boost converter and its closed-loop resistance emulator, the harvested power from the wind turbine increases tremendously, generating sufficient power to charge the supercapacitor, V_{cap}, from 2.75 V back to 2.9 V in 150 seconds as shown in Figure.2.22 which is less than half of the previous discharge time. At a wind speed of 3.62 m/s, the electrical

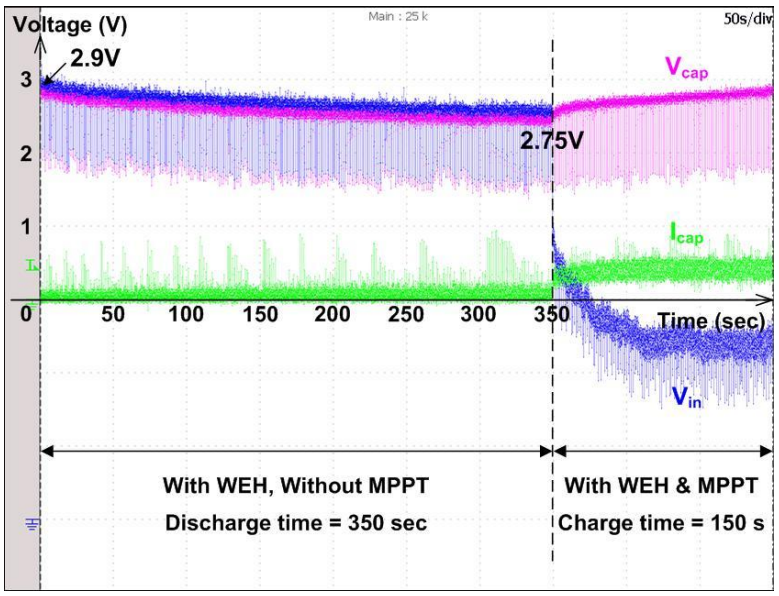

Figure 2.22: Performance of WEH system w/MPPT and w/o MPPT

power harvested by the WEH system with its MPPT mode is approximately 7.86 mW, even if we consider the losses in the converter where 3.6 mW of power is consumed by the wireless sensor node, the rest of the harvested power of 4.26 mW is supplied to charge the supercapacitor. As such, the WEH system with MPPT scheme is definitely able to sustain the sensor node's operation.

Another experimental test is carried out to compare the performance of a conventional sensor node, which operates solely on the energy storage, and a WEH sensor node as shown in Figure.2.23. As the conventional sensor node consumes 3.6 mW of average power from the supercapacitor, the voltage across the supercapacitor drops from 2.8 V to 2.55 V in around 275 seconds, which is calculated to be 1 J of energy transferred to the load. Comparing with the WEH system without MPPT, as shown in Figure.2.22, the discharge rate of the supercapacitor is much higher in this case because there is no extra power generated from the WEH system to supplement the sensor node's operation. Once the WEH system with MPPT is activated, the harvested power of 7.86 mW is used to power the sensor node as

well as to charge the supercapacitor back to 2.8 V in 225 seconds.

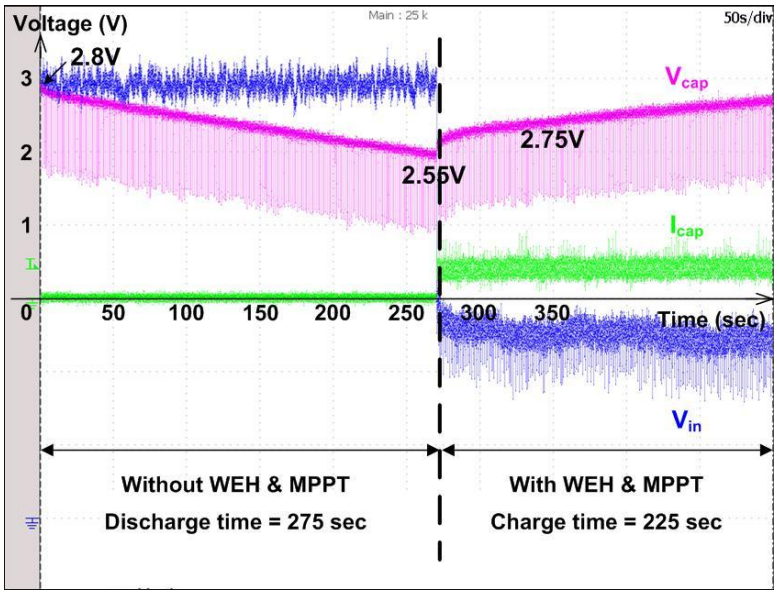

Figure 2.23: Performance comparison between conventional sensor node and WEH sensor node

Among the three testing options, the WEH wireless sensor node with MPPT scheme yields the most superior performance. This is because the WEH sensor node is incorporated with a wind energy supply designed to harvest power at its optimal point, to charge the supercapacitor and sustain the operation of the sensor node. To further validate the superior performance of the wind energy harvesting (WEH) wireless sensor node with MPPT scheme incorporated, the sensor node is tested in light wind condition of 3 m/s wind speed where 5 mW of power is available at output of the active rectifier as observed in Figure.2.9. After taking the losses of the DC-DC converter into consideration, the available power of 3.74 mW has a surplus after taking into account the power consumption of the wireless sensor node. Hence the charging voltage, V_{cap}, waveform as shown in Figure.2.24, illustrates that the WEH system with MPPT scheme, operating at lower wind speeds, is still able to supply power to the sensor node as well as to charge the supercapacitor.

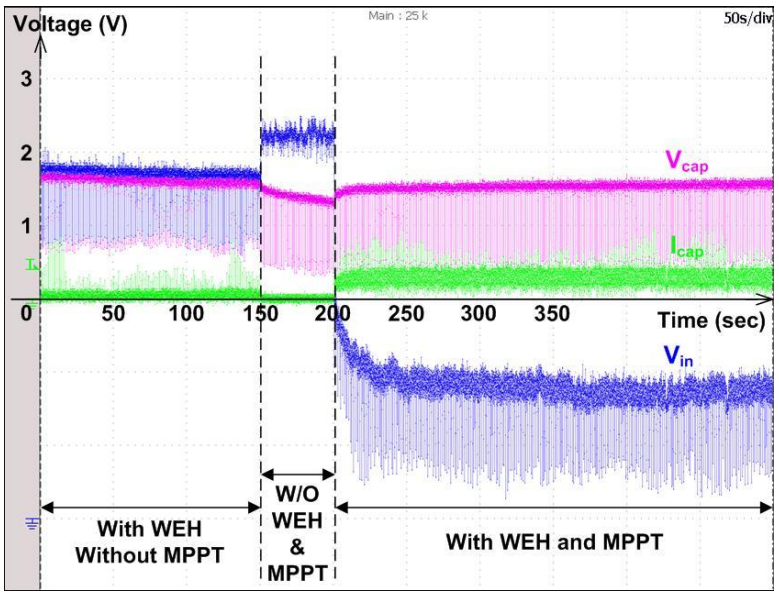

Figure 2.24: Operation of sensor node at light wind speed of 2.3 m/s

2.1.3.2 Power Conversion Efficiency of WEH System

The wind energy harvesting (WEH) system as a whole is a complex system that is made up of many different sub-systems. In order to understand how to improve the overall efficiency of the WEH system, it is important to study the performance of each of these sub-systems and perform some power analysis to better understand how power is distributed at each power conversion stage of the WEH system. Line diagrams are drawn in Figures. 2.25 and 2.26 to illustrate the input and output power available for each sub-system so that the power conversion efficiency of the sub-system can be determined.

Referring to Figure.2.25, the line diagram starts from the input with a wind speed of 3.62 m/s where 82 mW of raw wind power is supplied to the wind turbine with efficiency of 39% and 32 mW of mechanical power is available for harvesting. Using standard diode-based full bridge rectifier, 50% of the raw electrical power

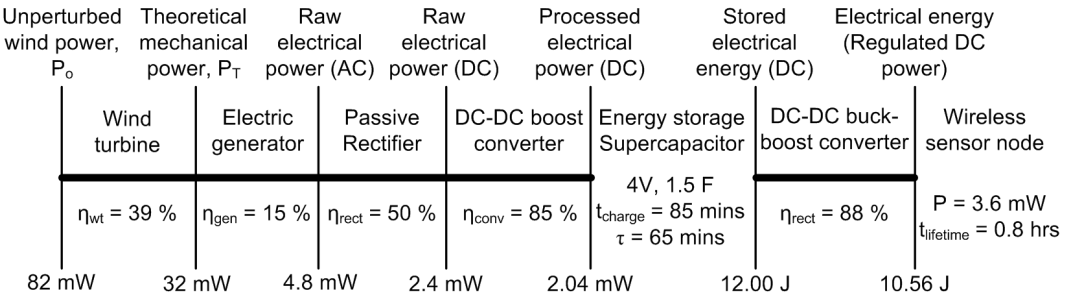

Figure 2.25: Line diagram of the power distributed in the wind energy harvesting system without active rectifier and MPPT scheme

(AC) generated at the output of the wind turbine generator of approximately 4.8 mW is converted into raw electrical power (DC) of 2.4 mW. With a standard boost DC-DC converter being used in the WEH system, it is observed in Figure.2.25 that the electric generator has relatively low efficiency of 15% because its internal source impedance is not properly matched with the subsequent sub-systems. Hence the processed DC power to charge the supercapacitor is only 2.04 mW.

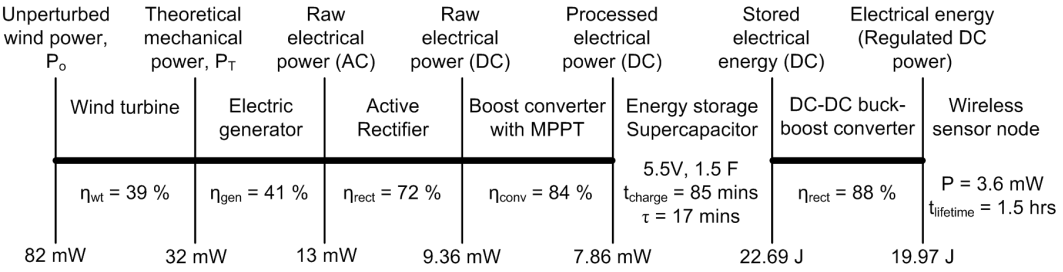

Figure 2.26: Line diagram of the power distributed in the proposed wind energy harvesting system

Another line diagram, shown in Figure.2.26, is drawn to illustrate the power distribution in the wind energy harvesting (WEH) system with active rectifier and resistance emulation MPPT scheme. When active rectifier is employed, the AC-DC conversion efficiency has been improved from 50% to 72%. The WEH system is further enhanced by using the closed-loop resistance emulator to perform impedance matching and it is shown in Figure.2.26 that there is about 3 times

more the raw electrical power (AC) harvested from the wind turbine and then converted into electrical power (DC) of 7.86 mW to charge the supercapacitor. The performance comparison between the line diagrams exhibited in Figures. 2.25 and 2.26 illustrates the significant contribution of the proposed power management circuit in the overall wind energy harvesting system incorporated into the wireless sensor node.

For a 1.5 F, 5.5 V supercapacitor, the maximum amount of energy stored in the supercapacitor is 22.69 J @5.5 V. To fully charge the supercapacitor, the required charging time t_{charge} is computed to be 85 mins when 7.86 mW of electrical power is supplied. To make a fair comparison, the same charging time of 85 mins is used and the WEH system with standard power management circuit is able to transfer 12 J of energy into the supercapacitor, which is about half the maximum capacity of the supercapacitor. Comparing the two line diagrams shown in Figures. 2.25 and 2.26, the operational lifetime of the sensor node powered by the WEH system with MPPT scheme is twice of the sensor node powered by the WEH system with standard power management circuit, hence making the WEH system with MPPT scheme a viable solution for extending the lifetime of the WSN.

2.1.4 Summary

There is a need for a paradigm shift from the battery-operated conventional wireless sensor node towards a truly self-autonomous and sustainable energy harvesting wireless sensor node. Small-scale wind energy harvesting (WEH) through micro wind turbine generator is one of the options to power small autonomous sensors deployed in remote locations for sensing under long-term exposure to hostile envi-

ronment such as forest fire. Two challenging problems associated with small-scale WEH, such as rectification of low amplitude AC voltage and impedance mismatch between source and load, have been addressed. An efficient power management unit of the WEH system, consuming very little power of 0.447 mW, has been designed to overcome these challenges. It has been demonstrated with experimental results that with the proposed active rectifier and resistance emulation based maximum power point tracking (MPPT) scheme, more electrical power (from 2.04 mW to 7.86 mW) is harvested from the wind turbine with higher overall power conversion efficiency from 2.5% to 9.6%. As such, it is more viable to achieve a truly self-autonomous and sustainable wireless sensor node with optimal wind energy harvesting using efficient power management circuit.

2.2 Indirect WEH Approach using Piezoelectric Material

With the great advancement of microelectronic technologies in many areas such as integrated circuit (IC) designs, chip fabrications, etc., the power requirement for wireless sensor nodes continue to decrease from mW to μW level. This paves the way for micro wind energy harvesting (WEH) for some wireless sensor network (WSN) applications, whereby there is a need for the small-scale wind energy harvesting (WEH) system to be as small as possible and highly portable, so as not to interfere with the normal operation of the deployment area. The direct WEH approach using wind turbine-generator, as illustrated in Section 2.1, has been successfully demonstrated in powering the miniaturized wireless sensor node. However, there are certain limitations with this type of conventional wind power generator that uses a large rotational turbine of blade radius of 3 cm to harvest energy from the wind flow. The limitations include large windfront contact with the wind is required for good WEH, mechanical constraint on the miniaturization of the electric generator and gearbox (if any), etc.

The physical size of wind turbine-generators that have been reported in Section 2.1 as well as the academic literature are still relatively bulky comparable to the sensor node. Weimer *et al.* presents a compact anemometer-based solution in [60] for remote area wind energy harvesting, the space needed by the anemomter is still relatively large compared to the miniature sensors. Another research study carried out by Priya *et al.* in [61] describes about the "Piezoelectric Windmill" that consists of several piezoelectric actuators arranged along the circumference of the mill in the cantilever form. The design of this windmill is very large and com-

plex such that the power generated, which is in the mW range, exceeds the power requirement of the ultra-low-power sensor node. Hence these large and bulky WEH system are not cost effective and appropriate for wireless sensor network (WSN) applications which require miniaturized devices.

In this section, an indirect wind energy harvesting (WEH) approach using piezoelectric material has been proposed for powering miniaturized wireless sensor node. The proposed piezoelectric wind energy harvester is very different from the conventional bladed wind turbine whereby a novel way of harvesting wind energy through piezoelectric effect has been explored to address the limitations of wind turbine-generator.

2.2.1 Vibration-Based Piezoelectric Wind Energy Harvester

A novel way of harvesting electrical energy from wind energy using bimorph piezoelectric material has been proposed in this research work. The novel piezoelectric wind energy harvester collects the vibration energy induced from the wind flow and the vibration creates stress on the piezoelectric material to generate electrical energy. The application of this novel piezoelectric based wind energy harvester is similar to the wind turbine research work which is for low-powered autonomous wind speed sensor. The piezoelectric wind harvester is a unique system that combines the concept of wind and piezoelectric effect together. Making use of the force generated by the flow of wind to vibrate the piezoelectric material, the mechanical energy harvested from the vibration of the piezoelectric material is converted into electrical energy. The advantages of the piezoelectric wind energy harvester are: compact and sensitive to low speed wind. Although the amount of energy that can

be harvested is quite limited, it is shown experimentally in the later part of the section that the piezoelectric energy harvester is sufficient to power the wireless electronic circuits to transmit 5 digital 12-bits signals to the remote base station. Once the trigger signal is received, the warning siren would be activated.

Figure.2.27 illustrates the power conversion process of the proposed vibration-based piezoelectric wind energy harvester; starting from the incoming wind flow, v, to the output electrical power generation, P_{elec}. The power conversion process can be divided into three main stages namely: aerodynamic stage in Section 2.2.1.1, cantilever bending beam stage in Section 2.2.1.2 and piezoelectric stage in Section 2.2.1.3. Referring to Figure.2.27, it can be seen that each of these power conversion stages has its own set of representative analytical models, which would be elaborated in details in the subsequent sections. Before that, the operating principle of the vibration-based piezoelectric wind energy harvester, as illustrated in Figure.2.28, is first discussed and explained as follows: -

- Difference in wind speeds above, v_a, and below, v_b, the airfoil/blade creates a net pressure, P, that results in a lift force, F, at the tip of blade. This phenomenon can be explained based on the Bernoulli's principle.
- Net pressure, P, is applied at the tip ($x = L$) of the piezoelectric wind energy harvester, which is free to vibrate, and its the other end is fixed with a clamp ($x = 0$). Due to the wind, v, flowing across the piezoelectric wind energy harvester, the tip of the harvester deflects up and down (δ_L) and hence vibration is generated on the piezoelectric material. This phenomenon can be explained with the Euler-Bernoulli cantilever beam theory.
- As the blade of the harvester swings, the piezoelectric material, which is

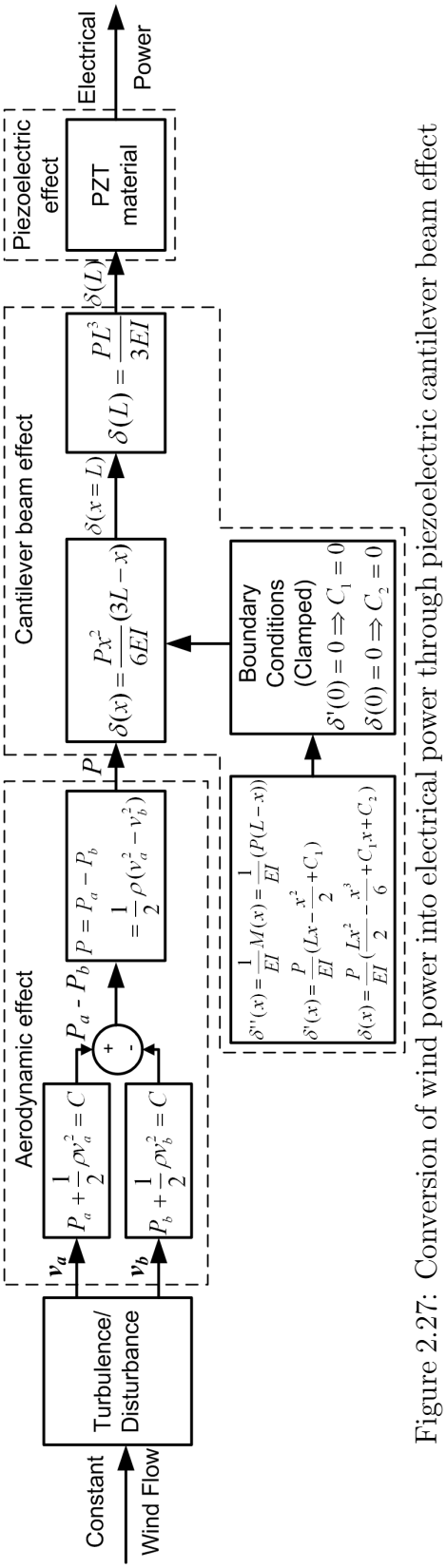

Figure 2.27: Conversion of wind power into electrical power through piezoelectric cantilever beam effect

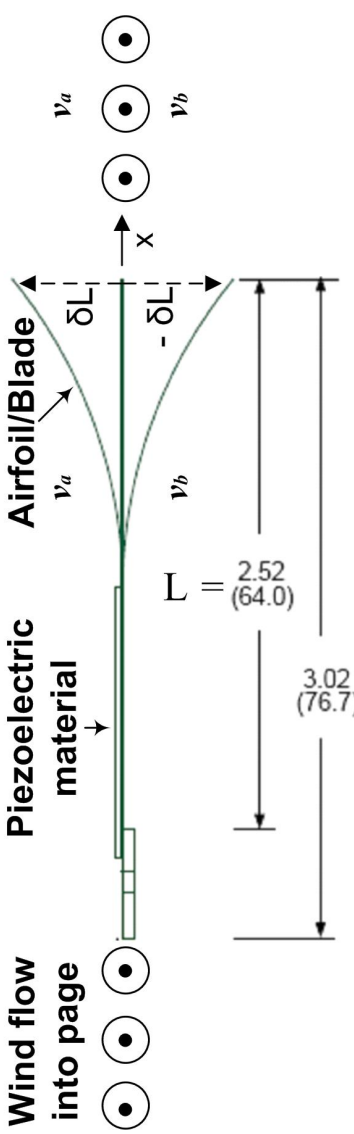

Figure 2.28: Illustration diagram of the vibration-based piezoelectric wind energy harvester

bonded to the blade, experiences the mechanical stress, σ, of the generated vibration. Electrical AC power is thus harvested from the vibration-based piezoelectric wind energy harvester. This phenomenon can be explained using the piezoelectricity theory.

2.2.1.1 Aerodynamic Theory

The aerodynamic effect of air flow on the piezoelectric wind energy harvester is described based on a well-known fluid mechanic principles i.e. Bernoulli's principle. According to Bernoulli's principle, it states that in fluid flow, an increase in velocity occurs simultaneously with decrease in pressure. This principle is a simplification of Bernoulli's equation which states that the sum of all forms of energy in a fluid flowing along an enclosed path is the same at any two points in that path. The fluid can be either a liquid or a gas, but for Bernuolli's principle to be applicable, the fluid is assumed to have the following qualities [75]:-

- Fluid flows smoothly
- Fluid flows without any swirls (also known as eddies)
- Fluid flows everywhere throughout the pipe (which means there is no "flow separation")
- Fluid has the same density everywhere (it is "incompressible" like water)

To understand how and why Bernoulli's principle works, the development of the relationship of the static and dynamic pressures using Bernoulli's equation has

to be investigated. The Bernoulli's equation along a streamline can be summarized as follows:

$$P_1 + \frac{1}{2}\rho v_1^2 + \rho g z_1 = P_2 + \frac{1}{2}\rho v_2^2 + \rho g z_2 = a\ constant \tag{2.9}$$

where

- 1 is the first point along the pipe in Figure.2.29
- 2 is the second point along the pipe in Figure.2.29
- P is the static pressure of the fluid (Pa)
- ρ is the density of the fluid (kg/m^3)
- v is the velocity of the fluid (m/s)
- g is gravitational acceleration (m/s^2)
- z is height (m)

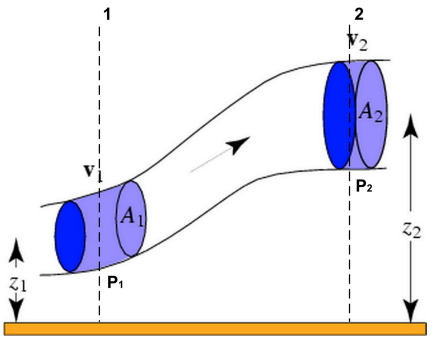

Figure 2.29: Diagram of a pipe through which and ideal fluid is flowing at a steady rate

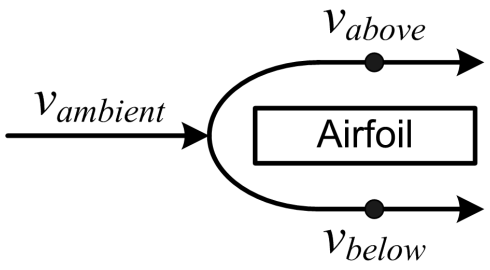

Figure 2.30: Different points along the same streamline for the application of the Bernoulli's equation

Referring to the Bernoulli's principle applied for the airfoil case shown in Figure.2.30, the different points that fall along the same streamline flow of the wind i.e. the effects due to gravity are small compared to the effects due to kinematics

and pressure, $z_1 \approx z_2$, hence the ρgz term in eqn.2.9 can be cancelled out on both sides. Referring to Figure.2.29, the point labelled as 1 is a point on the streamline far in front of the airfoil labelled in Figure.2.30 as ambient wind. The static pressure at point 1 is thus equated as $P_1 = P_{ambient}$. Similarly, by representing the point 2 labelled in Figure.2.29 to be at a point above the surface of the airfoil as observed in Figure.2.30, eqn.2.9 can be expressed as,

$$P_{ambient} + \frac{1}{2}\rho v_{ambient}^2 = P_{above} + \frac{1}{2}\rho v_{above}^2 = a\ constant \tag{2.10}$$

In another condition below the surface of the airfoil, point 1 seen in Figure.2.29 is again a point on the streamline in front of the airfoil in Figure.2.30 and the values of $P_{ambient}$ and $v_{ambient}$ and the wind parameters are the same as the above airfoil condition. Point 2 labelled in Figure.2.29 is represented by a point below the surface of the airfoil observed in Figure.2.30. Hence, eqn.2.10 is restructured into,

$$P_{below} + \frac{1}{2}\rho v_{below}^2 = P_{above} + \frac{1}{2}\rho v_{above}^2 = a\ constant \tag{2.11}$$

For horizontal wind flow, an increase in the wind speed would result in a decrease in the static pressure. As such, when the air flowing over the top of the airfoil, v_{above}, travels faster than the air flowing under the airfoil, v_{below}, there is less pressure on the top, P_{above}, than on the bottom, P_{below}, resulting in the net pressure expressed as,

$$P = P_{above} - P_{below} = \frac{1}{2}\rho(v_{below}^2 - v_{above}^2) \tag{2.12}$$

This resultant net pressure, P, is the input variable of the next power conversion stage of the piezoelectric wind energy harvester, which is the cantilever bending beam stage to be described in the next section.

2.2.1.2 Cantilever Beam Theory

The main objective is to determine how much would the vibration-based piezoelectric wind energy harvester vibrates when wind flow past the harvester. As the positive/negative net pressure, P, generated due to the aerodynamic effect of the blade swing is loaded on the tip of the cantilever beam, the beam deflects downward/upward respectively. The relationship between the net pressure created by the wind flow, v, and the beam deflection, y, is investigated and discussed. Once this relationship is established and together with the wind speed flowing above and below the wind energy harvester is known, the amount of vibration being generated on the piezoelectric material can then be calculated.

In this research, the vibration of the piezoelectric wind energy harvester is examined based on a simple beam theory studied in structural mechanics to understand the beam deflection behaviour. When a beam is subjected to a bending moment, M, of small deflections as shown in Figure.2.31: the outside of the bend is stretched, the inside is compressed and in between them, there is the neutral axis or neutral plane which does not experience any tensile stress at all [76]. The bending process of a section of the beam exhibited in Figure.2.31 is subjected to pure bending. For a homogeneous and symmetrical material, the neutral axis should be located at the geometrical centre.

Considering an element of the beam as shown in Figure.2.31(a) for bending analysis, the radius of curvature of the neutral-axis, NA, is R and the element of the beam includes an angle ϕ at the centre of curvature. An incremental change in the distance, z, from the NA has the length of $(R \pm z)\ \phi$ along the NA and so the

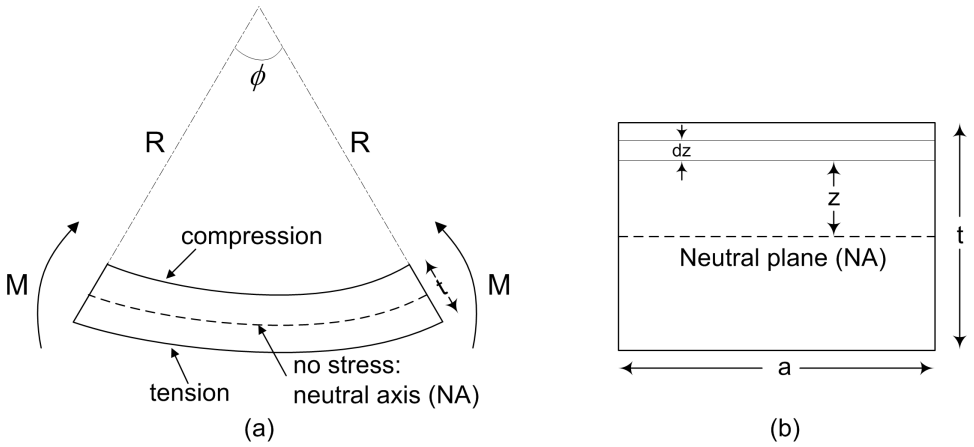

Figure 2.31: Section of the beam subjected to pure bending

extension/compression of the incremental distance is $\pm z\phi$ and the strain is $\pm z\phi/R\phi$ $= \pm z/R$. Now consider a symmetrical beam with thickness of t and width of w pointing out of the page as shown in Figure.2.31(b). When the symmetrical beam bends, the rectangle shown in Figure.2.31(b) would be rotated and the bending moment needed can be calculated by considering the tensile forces involved. Since the strain, ε, and stress, σ, on the element dz caused by the bending are $\pm z/R$ and $E_y(z)^*\varepsilon$ respectively, the force, F, required to achieve the moment, M, can be expressed as,

$$F = (stress)(area) = E_y(z)(\frac{\pm z}{R})a\ dz \tag{2.13}$$

where $E_y(z)$ is the Youngs modulus of the beam as a function of its thickness, z. With reference to Figure.2.31(b), the moment of the force about the neutral plane, NA, is given as: -

$$F.z = \frac{\pm E_y(z)z^2 a dz}{R} \tag{2.14}$$

The total bending moment on the rectangle beam is the sum of the individual moments on all the elements dz [76], which can be expressed as: -

$$Bending\ Moment = \frac{a}{R}\int_{-t/2}^{t/2} E_y(z)z^2 dz \tag{2.15}$$

This bending moment is equal to the applied moment at each point in the beam

(which depends on the applied force and its distance from the specific point). The geometric moment of inertia, I, which describes the effect of the rectangular shape of the beam cross section, is given as [77]: -

$$I = \int az^2 dz \tag{2.16}$$

$$\therefore I = a[\frac{z^3}{3}]^{\frac{t}{2}}_{\frac{-t}{2}} = \frac{at^3}{12} \tag{2.17}$$

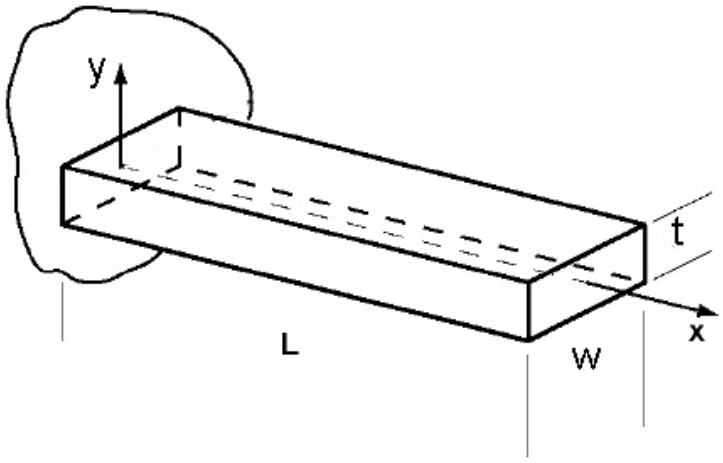

Figure 2.32: A cantilever beam

Now, consider the cantilever beam as shown in Figure.2.32, the beam has a length of L, width of w and thickness of t with one of the end fixed in cantilever form. The cantilever beam is homogeneous and symmetrical and has a constant value of E_y. A force, F, is applied to the free end of the beam and the amount of deflection, y, at a distance L from the fixed end can then be determined. Radius of curvature, R, is defined as [76]: -

$$\frac{1}{R} = \frac{\frac{d^2y}{dx^2}}{(1 + (\frac{dy}{dx})^2)^{\frac{3}{2}}} \tag{2.18}$$

For small deflections, $\frac{dy}{dx}$ is small and hence $(\frac{dy}{dx})^2 << 1$ and therefore the radius of curvature can be simplified to

$$\frac{1}{R} = \frac{d^2y}{dx^2} \tag{2.19}$$

Next, the bending moment at some distances, x , from the wall is equated to the applied bending moment shown in eqn.2.15. Using eqns.2.15, 2.16 and 2.19, the bending moment derived in eqn.2.15 can be described in a simpler form as shown below:-

$$Bending\ Moment = E_y I \frac{d^2y}{dx2} = F(L - x) \tag{2.20}$$

From the simplified bending moment equation, the beam curvature can found as: -

$$\frac{d^2y}{dx2} = \frac{F}{E_y I}(L - x) \tag{2.21}$$

Integrating eqn.2.21 with respect to x for once to derive the beam slope, which is expressed as,

$$\frac{dy}{dx} = \frac{F}{E_y I}(Lx - \frac{x^2}{2}) + K \tag{2.22}$$

Based on the boundary condition which states that at $x = 0$, $dy/dx = 0$ and so $K = 0$. Integrating the beam curvature equation a second time gives the beam deflection as: -

$$y = \frac{F}{E_y I}(\frac{Lx^2}{2} - \frac{x^3}{6}) + K^{'} \tag{2.23}$$

There is a boundary condition that, at $x = 0$, $y = 0$ and so $K^{'} = 0$. Hence at $x = L$, the tip deflection is found to be: -

$$y_L = \frac{FL^3}{3E_y I} \tag{2.24}$$

The relationship between the aerodynamic force, F, created by the wind flow and the tip deflection of the piezoelectric wind energy harvester is established. When a positive/negative net force is loaded on the tip of the piezoelectric wind energy harvester mounted in cantilever form, the tip downward/upward deflection of the harvester can be estimated using eqn.2.24. A summary of the theoretical and experimental deflections of the piezoelectric wind energy harvester with respect to various wind speeds is tabulated in Table.2.1.

Table 2.1: Relationship between incoming wind speed and tip deflection of the cantilever piezoelectric wind harvester beam

v_a **(m/s)**	v_b **(m/s)**	**Force (N)**	**I (m^4)**	**Young's Modulus of Mylar/Polyethylene terephthalate, E_y (GPa)**	**Theoretical deflection (mm)**	**Experimental deflection (mm)**
7	1	0.0134	1.29E-14	2.5	6.49	6.5
5	2	0.0059	1.29E-14	2.5	2.84	3.0
3	1	0.0022	1.29E-14	2.5	1.08	1.0

Figure.2.33 exhibits the experimental setup used to measure the tip deflection of the piezoelectric wind energy harvester when wind flow across the harvester. It can be seen from Figure.2.33 that there is a measurement ruler held vertically by a blue colour clamp besides the piezoelectric wind energy harvester. The ruler acts like a measurement scale to determine the magnitude of the deflection at the tip of harvester and the neutral/starting point of the measurement scale has been offset by 9 cm. A silver colour electric fan is placed in the background of the four figures to simulates as wind source to the wind piezoelectric energy harvester. The wind flow generated by the electric fan excites the harvester to vibrate and the amount of deflection observed at the tip of the harvester is read from the measurement ruler. Figures.2.34, 2.35 and 2.36 illustrate the three experiments carried out for incoming wind speeds of $V_a = 7$ m/s and $V_b = 1$ m/s, $V_a = 5$ m/s and $V_b = 2$ m/s and $V_a = 3$ m/s and $V_b = 1$ m/s respectively. The experimental deflections read from the 3 figures are 6.5 mm, 3 mm and 1 mm respectively and they are recorded in Table.2.1 to verify the theoretical value of the beam deflection calculated using eqn.2.24.

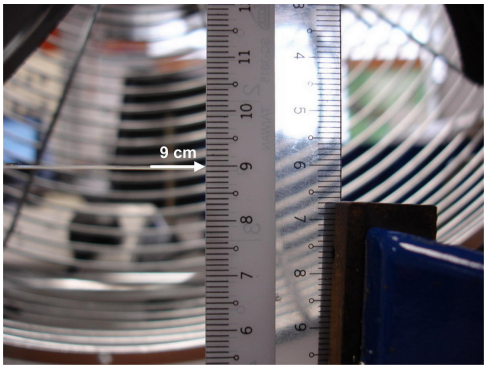

Figure 2.33: Piezoelectric wind energy harvester under no wind speed

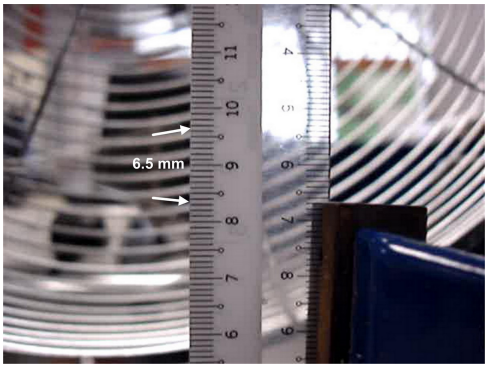

Figure 2.34: Piezoelectric wind energy harvester under wind speed of $V_a = 7$ m/s and $V_b = 1$ m/s

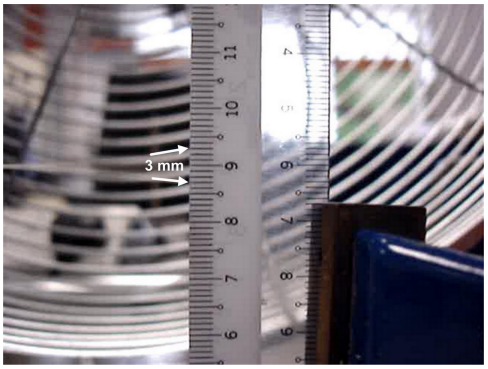

Figure 2.35: Piezoelectric wind energy harvester under wind speed of $V_a = 5$ m/s and $V_b = 2$ m/s

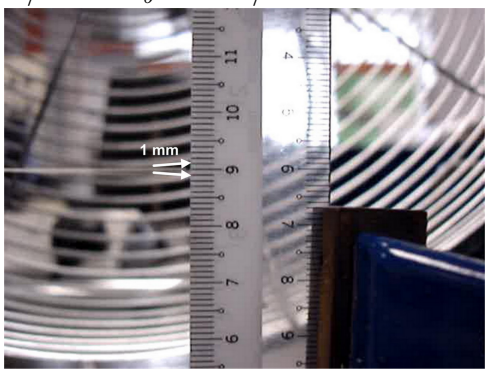

Figure 2.36: Piezoelectric wind energy harvester under wind speed of $V_a = 3$ m/s and $V_b = 1$ m/s

Referring to Table.2.1, the percentage of deviation between the calculated theoretical and measured experimental values for the tip deflections of the piezoelectric wind energy harvester is found to be less than 1 %. This shows that the proposed relationship developed between the Bernoulli's aerodynamic theory and the cantilever beam theory is pretty accurate and established. Additionally, the derived equations, starting from the incoming wind speed differences to the beam deflection, are good representations of the experimental results. Hence, for further expansion in the research work, these derived equations can be used as the baseline to predict and estimate the performance of the piezoelectric wind energy harvester for the required specification and operating condition. Furthermore, with good

understanding on the working concept and technical derivation of the piezoelectric wind energy harvester, the present design of the harvester can be easily altered and optimized for different operating conditions. Take for an instance, by altering the geometric moment of inertia, I discussed in eqn.2.16, which describes the effect of the rectangular shape of the beam cross section, the tip deflection of the harvester is expected to change. The remaining step left to do is to find out the relationship between the deflection of the cantilever wind energy harvester and the electric power generation from the piezoelectric material.

2.2.1.3 Piezoelectric Theory

For a piezoelectric generator mounted in cantilever form, transverse mode (mode 31) of operation is considered. The mechanical force, F, applied on the piezoelectric generator is perpendicular to its output electrodes, hence the surface where the charge is collected and the surface where the force is applied are independent. According to [78]and [80], for a series connected bimorph bender subjected to the following excitations: an electric voltage V across its thickness, a uniformly distributed external body load p, an external tip force F perpendicular to the beam and an external moment M at the free end, the generated electrical charge can be expressed as,

$$Q = \frac{3d_{31}L}{t^2}M + \frac{3d_{31}L^2}{2t^2}F + \frac{d_{31}wL^3}{2t^2}p + \frac{\varepsilon_{33}^X Lw(1-k_{31}^2/4)}{t}V \tag{2.25}$$

where L, w and t are the bimorph piezoelectric generator length, width and thickness respectively. ε_{33}^X is the dielectric constant of the piezoelectric material under a free condition. d_{31} is the transverse piezoelectric coefficient and k_{31} is the transverse piezoelectric coupling coefficient. When only an external tip force, F, is acting on

the tip of the bimorph piezoelectric generator (x=L), the generated electric charge in the bimorph defined as eqn.2.25 becomes [80]

$$Q = \frac{3d_{31}L^2}{2t^2}F \tag{2.26}$$

For a bimorph piezoelectric generator, two pieces of piezoelectric material are mechanically bonded together as a whole, hence the overall dielectric constant of the bimorph piezoelectric generator is smaller than the free dielectric constant of only the piezoelectric material. As such, the overall dielectric constant, ε_b, is given as,

$$\varepsilon_b = \varepsilon_{33}^X(1 - k_{31}^2/4) \tag{2.27}$$

The total capacitance of the bimorph piezoelectric generator can be obtained by: -

$$C = \frac{(overall\ dielectric\ constant)(electrode\ surface\ area)}{thickness\ separating\ the\ electrodes} \tag{2.28}$$

$$C = \frac{\varepsilon_{33}^X Lw(1 - k_{31}^2/4)}{t} \tag{2.29}$$

Based on eqns.2.26 and 2.28, the open circuit electric voltage, V_{oc}, generated by the bimorph piezoelectric generator when an external tip force is applied is expressed as: -

$$V_{oc} = \frac{Q}{C} = \frac{3d_{31}L}{2\varepsilon_{33}^X wt(1 - k_{31}^2/4)}F \tag{2.30}$$

The dielectric constant, ε_{33}^X, piezoelectric constant, d_{31}, coupling coefficient, k_{31}^2, of the piezoelectric material and the dimensions of the bimorph are given by the vendor in the technical datasheet. The properties of the piezoelectric material are tabulated in Table.2.2.

Alternatively, the open circuit electric voltage, V_{oc}, generated by the bimorph piezoelectric generator can also be a function of the tip deflection, y_L. Rearranging eqn.2.24, it can be seen that the external tip force, F, is related to the tip deflection

Table 2.2: Properties of piezoelectric material

Description of properties	**Unit**	**Symbol**	**Value**
Piezoelectric material	Piezo Systems	PSI-5A4E	Lead Zirconate Titanate
Piezoelectric Strain/Field Coefficient	Metres/Volt	d_{33}	390 x 10^{-12}
Piezoelectric Charge Density/Stress Coefficient	Coulombs/Newton	d_{31}	-190 x 10^{-12}
Piezoelectric Strain/Charge Density Coefficient	Metres/Coulomb metre	g_{33}	24 x 10^{-3}
Piezoelectric Field/Stress Coefficient	Volt/Newton metre	g_{31}	-11.6 x 10^{-3}
Coupling Coefficient		k_{31}	0.35
Elastic Modulus	Newtons/metre^2	Y_{E1}	6.6 x 10^{10}

of the piezoelectric generator by: -

$$F = \frac{3E_y I y_L}{L^3} \tag{2.31}$$

Since the Young's Modulus, E_y, of the piezoelectric material is known in Table.2.2 and the moment of inertia, I, of the cantilever piezoelectric generator can be calculated using eqn.2.16, the open circuit electric voltage, V_{oc}, generated by the vibration-based piezoelectric wind energy harvester can be estimated based on the tip deflection, y_L, of the piezoelectric generator, which is expressed as,

$$V_{oc} = \frac{9d_{31}E_y I}{2\varepsilon_{33}^X L^3 wt(1 - k_{31}^2/4)} y_L \tag{2.32}$$

2.2.2 Characteristic and Performances of Piezoelectric Wind Energy Harvester

Wind flowing with a certain range of speeds is able to stir a certain amount of vibration on the plastic flapper attached to the piezoelectric material which thus

passes the vibrational energy to the piezoelectric material. The harvested vibrational energy from the piezoelectric material would then be converted into electrical energy at the output of the piezoelectric wind energy harvester.

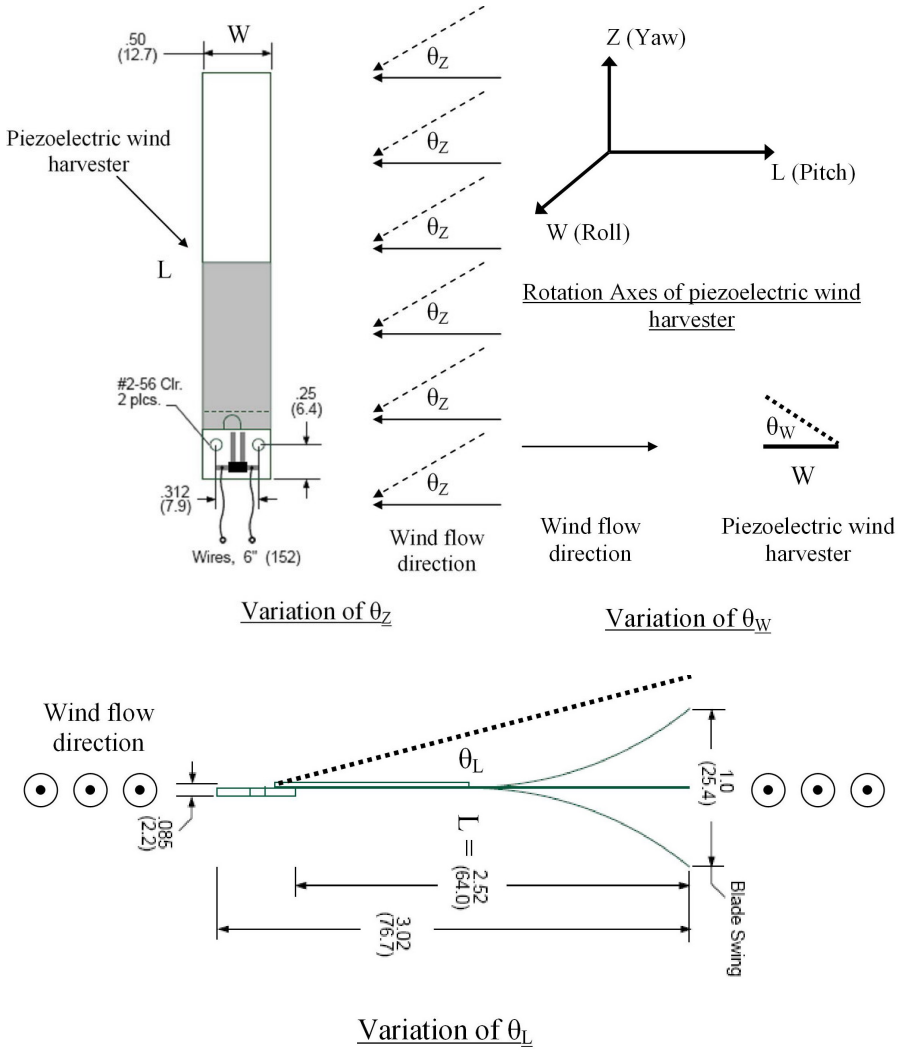

Figure 2.37: Orientations and rotating angles of the vibration-based piezoelectric wind energy harvester

The relationships between the harvested electrical energy and the incoming wind depends on the orientations and rotating angles between the piezoelectric wind energy harvester with respect to the directions of the incoming wind flow as shown in Figures.2.38, 2.39 and 2.40. Taking the concept about the flight dynamics of a vehicle rotating in three dimensions around its coordinate system origin, the

three rotating angles defined in this research work, θ_L, θ_W and θ_Z are equivalent to roll, pitch and yaw angles respectively. Experiments have been conducted to find out the amount of electrical power that is generated by the piezoelectric wind energy harvester when placed in different orientations.

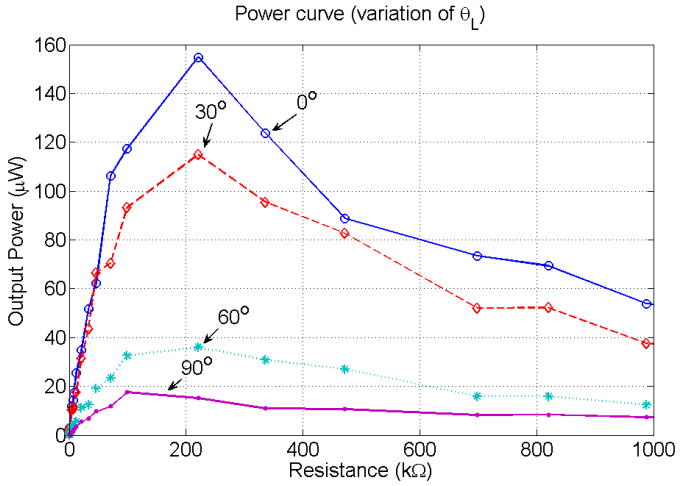

Figure 2.38: Power generated by the harvester with angle of θ_L

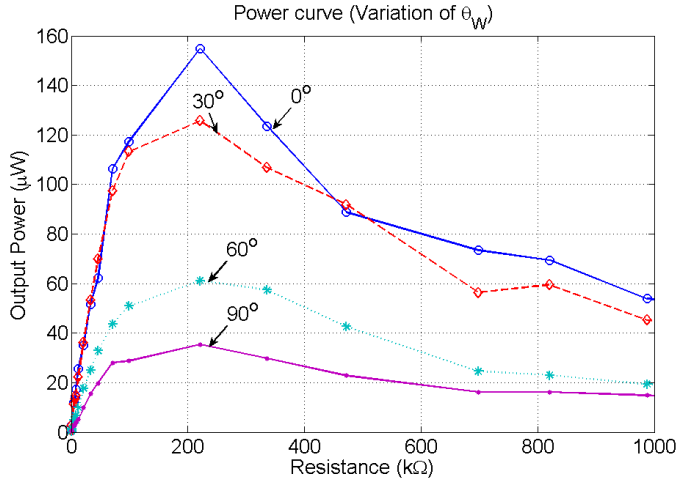

Figure 2.39: Power generated by the harvester with angles of θ_W

Figures.2.38, 2.39 and 2.40 illustrates the power curves of the piezoelectric wind energy harvester with different rotating angles θ_L, θ_W and θ_Z ranging from 0^o to 90^o. Similar sets of experimental tests have been collected for the rotating angles ranging -90^o to 0^o and the results turn out to be quite symmetrical. Therefore experimental results are provided only for rotating angles ranging from 0^o to 90^o.

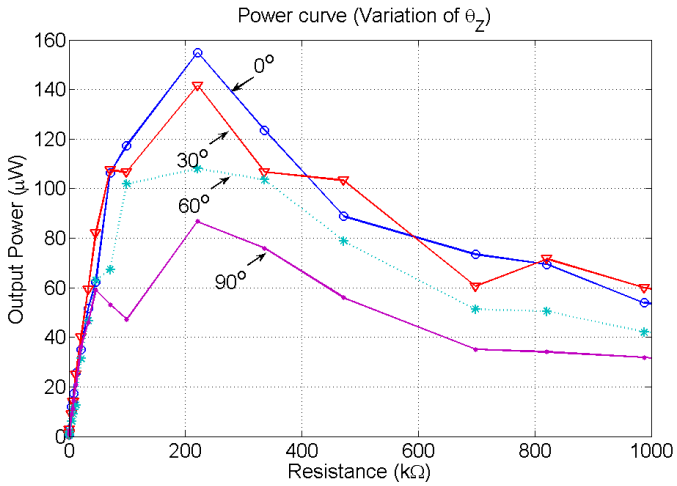

Figure 2.40: Power generated by the harvester with angles of θ_α

From the three figures, one common phenomenon that can be observed; as the rotating angle increases from 0^o to 90^o, the amount of electrical power generated by the piezoelectric wind energy harvester decreases. This phenomenon is due to the reduction in the net lift force created by the pressure difference between the top and bottom surfaces of the piezoelectric wind energy harvester. According to the Bernoulli's equation in fluid dynamics, it states that as the speed of a fluid (air/water) flow increases, its pressure decreases. Hence it is clear that the pressure difference around the piezoelectric wind energy harvester are brought about by the variations in wind speed (caused by the disruption and turning of the air flowing past the piezoelectric wind energy harvester) at all points of the piezoelectric wind energy harvester. From these experimental tests performed, it can be concluded that to get the maximum power output, θ_L, θ_W and θ_Z should be set at $0\ ^o$ with respect to the wind flow direction.

Piezoelectric based wind energy harvester offers several advantages over the conventional wind turbine harvester. These include: instant starting with no dead time (due to the inertia of the wind turbine generator); small size and ultralight

weight; extremely low magnetic permeability (suitable for use in high magnetic field environments); and almost no heat dissipation. Therefore the piezoelectric wind energy harvester is suitable to power miniaturized autonomous sensor used in many application areas such as structural and automation applications. To study the feasibility of using the piezoelectric wind energy harvester as a generator to supply power to the power conditioning circuit and the RF transmitter for practical application, some characterization works have been conducted to better understand the capability level of the piezoelectric wind energy harvester. One of the characterization works carried out on the harvester is to determine the relationship between the open circuit rectified DC voltage and the wind speed as shown in Figure.2.41.

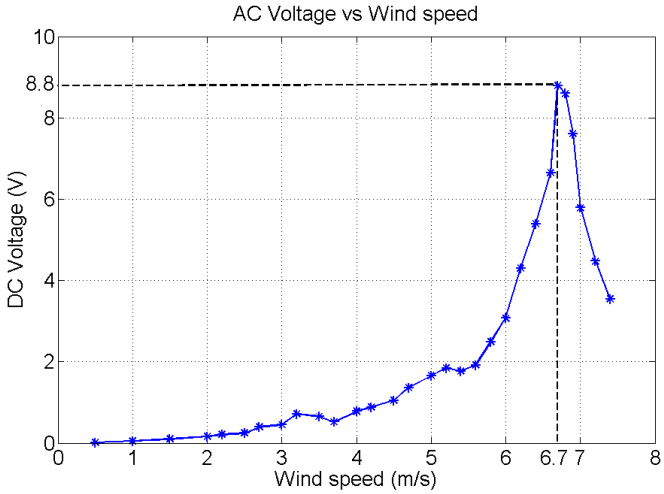

Figure 2.41: Open circuit AC voltage over a range of wind speeds

Based on the plot in Figure.2.41, the DC output voltage of the piezoelectric wind energy harvester can be used to predict the speed of the incoming wind. For a given wind speed (any wind speed beyond this threshold value would trigger a 12-bits digital signal to be transmitted to the base station in a wireless manner), the corresponding preset voltage level for the power management circuit can be

determined from Figure.2.41. Take for an instance, at wind speed of 6.7 m/s, the DC output voltage of the piezoelectric wind energy harvester is measured to be around 8.8 V. If this is the preset wind speed threshold for sounding the siren at the remote base station, then the DC output voltage of 8.8 V is used to power the wireless RF transmitter to transmit several 12-bits digital signals to the base station in a wireless manner. Another characterization work illustrated by Figure.2.42 shows the typical output electrical power characteristic of the piezoelectric wind energy harvester as a function of the load resistances at different wind speeds. In simple words, the figure shows how much power the piezoelectric wind energy harvester can supply continuously to the load.

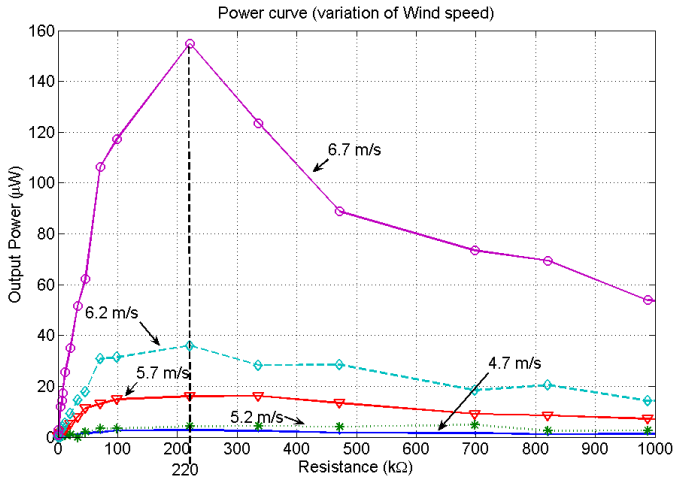

Figure 2.42: Piezoelectric wind energy harvester power source curves over a range of wind speeds

Note that in Figure.2.42, a constant load resistance of 220 kΩ results in maximum output power over the full range of wind speeds. At wind speed of 6.7 m/s and the load resistance fixed at 220 kΩ, Figure.2.42 shows that the maximum amount of output power that can be harvested from one piece of piezoelectric wind energy harvester is around 155 μW. If the number of piezoelectric wind energy

harvesters is to be increased, then the amount of power that can be generated would be multiple of 155 μW. With the present microelectronic technology, to power the sensor continuously with 155 μW is quite impossible, hence an energy storage with some triggering circuit has to be included in the power management system to ensure that the electric energy stored in the storage element is sufficient before supplying the power to the RF wireless transmitter and its associated power management circuit.

2.2.3 Power Processing Unit

The harvested power of the piezoelectric wind energy harvester is first fed into the power processing unit (PPU) and then the regulated output voltage from the PPU is used to power the radio frequency (RF) transmitter. The main function of the power processing unit is to convert and condition the unregulated raw electrical voltage into usable regulated voltage for the RF transmitter load. In the PPU, the unregulated raw power needs to undergo three different stages of power conditioning before the usable regulated power is provided to the RF transmitter load. The first stage of the power conversion, which is AC to DC power conversion, is well-known and straightforward so it would not be elaborated further. The second stage of the PPU is the energy storage and supply circuit which has the ability to store electrical energy from the harvester before supplying it to the load. Energy harvested from the piezoelectric wind energy harvester is first stored in a capacitor and when sufficient energy to power the wireless RF transmitter is accumulated, a triggering signal would trigger the storage circuit to release the stored energy to the RF load. The last stage of the PPU is the voltage regulation stage whereby the output voltage supplied to the RF transmitter load is regulated by a voltage regulator to

be 3.3 V.

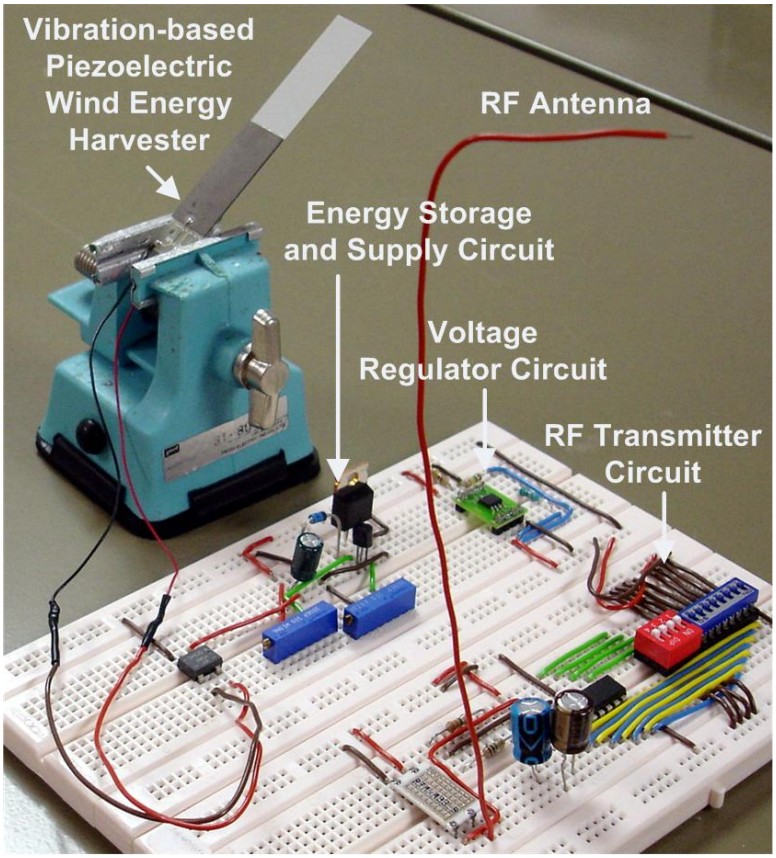

Figure 2.43: Photograph of the piezoelectric wind energy harvester system

The vibration-based piezoelectric wind energy harvester and its related power processing unit is implemented into hardware prototype to power the wireless RF transmitter load as shown in Figure.2.43. The physical dimensions of a piezoelectric wind energy harvester (half grey and half white colours) is 76.7 mm x 12.7 mm x 2.2mm and it is held tightly at one end by the blue clamp (cantilever mounting) and the other end is left to flap freely. When wind blows at the piezoelectric wind energy harvester, AC voltage is generated and converted into DC voltage by the diode bridge rectifier chip. After which, the DC voltage is stored in a 33 μF capacitor until the preset voltage of around 8.8 V and subsequently discharged to the RF transmitter load. A detailed schematic diagram of the piezoelectric wind energy harvester system is shown in Figure.2.44. It can be seen from the schematic

diagram that the Q1 and Q2 power semiconductor devices residing in the energy storage and supply system acts like a control switch that would initiate on or off signal to the storage capacitor to release the stored energy. The design of the energy storage circuit is adapted from a similar circuit designed by Massachusetts Institute of Technology (MIT) for digital RFID of piezoelectric shoes [81]. The significant improvement in the revised circuit discussed in this research work is that less components have been used in the revised circuit while it can still operate to deliver similar performance. One distinct difference between the proposed design and the MIT design is the turn off process of Q1. In the proposed design, turning Q1 off is determined by the voltage drop across R3 instead of MIT method of transmitting a negative pulse from MAX666 through C3 to turn off Q1.

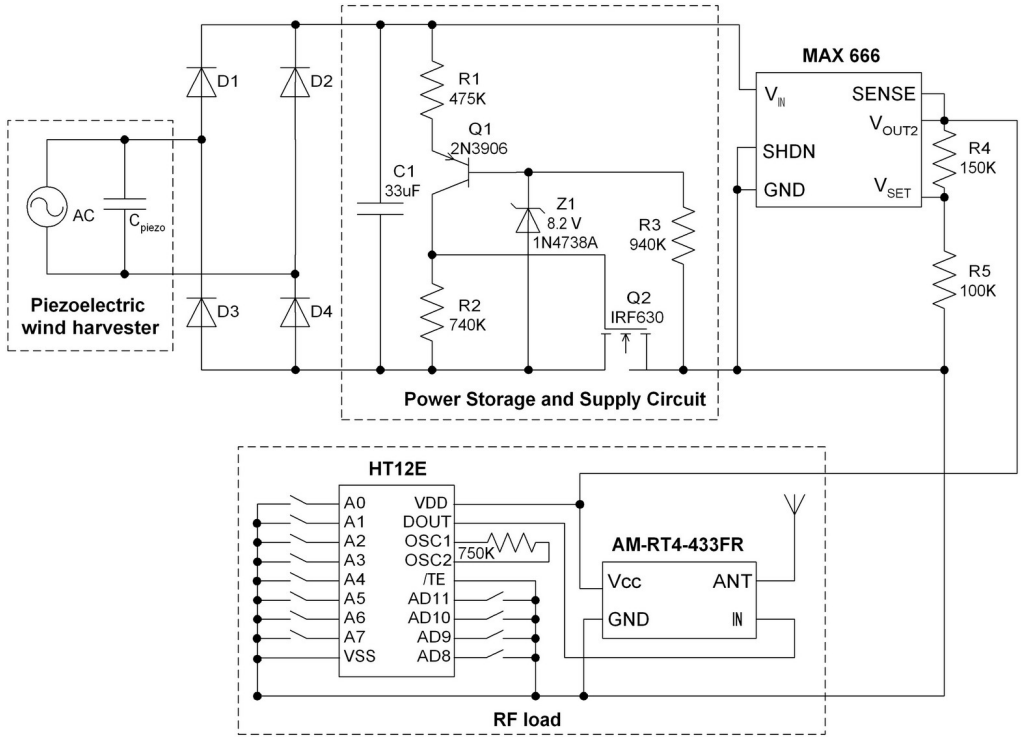

Figure 2.44: Schematic diagram of the piezoelectric wind energy harvester system

Initially, both Q1 and Q2 are off so the ground lines of the voltage regulator

(MAX666) and the RF AM transmitter (AM-RT4-433FR) are disconnected from C1. As C1 charges beyond the preset 'ON' voltage threshold of around 8.8 V (the preset voltage level is determined by the zener diode Z1 - 8.2 V and the base-emitter junction of Q1 - 0.6 V), the control switch Q1 turns on. The moment when Q1 is on, there is a voltage drop across R2 that is higher than the threshold gate-source voltage ($V_{gs}(th)$) of Q2 in order to activate the control switch Q2. Once Q2 is activated, Q1 is latched. This connects the ground lines of MAX666 and AM-RT4-433FR with C1, allowing C1 to discharge through the circuitry. MAX666 is a low power series voltage regulator, which produces a stable +3.3 V for the serial ID encoder (HT12E) and the RF AM transmitter (AM-RT4-433FR) throughout the discharge of C1. When the voltage across C1 drops below the 'OFF' voltage threshold of around 4.58 V, the voltage drop across R3 causes Q1 to turn off and hence in turn deactivates Q2 from the latched stage. When this happens, the ground lines of MAX666 and AM-RT4-433FR are disconnected from C1 and the discharge of C1 is stopped. Subsequent wind flow through the piezoelectric wind energy harvester increases the voltage on C1, allowing the cycle to start afresh.

2.2.4 Experimental Results

In the experiments, the performances of the piezoelectric wind energy harvester system are explored and evaluated based on a wind speed of 6.7 m/s, which is the preset threshold wind speed in Figure.2.41 to trigger the RF wireless transmitter. Whenever the wind speed reaches the preset wind speed of 6.7 m/s, the electrical energy stored in the capacitor is supplied to the RF transmitter. The encoded digital information is then transmitted to the base station in a wireless manner. Referring to Figure.2.45, it can be seen that the output voltage of the harvester

takes about 10 sec to charge the storage capacitor to maximum voltage, V_{max}, of around 8.8 V. As soon as the capacitor reaches V_{max}, the electrical energy stored in the capacitor is discharged to the RF load and the voltage across the capacitor starts to decrease to the minimum voltage, V_{min}, of 4.58 V in 100 ms. After which, the cycle starts again.

To find out the amount of energy that has been stored in the storage capacitor during the time when the capacitor is charged from V_{min} to V_{max}, eqn.2.33 is applied. The energy stored in the capacitor is calculated to be 917 μJ.

$$E_{cap} = \frac{1}{2}C\left(V_{max}^2 - V_{min}^2\right) \tag{2.33}$$

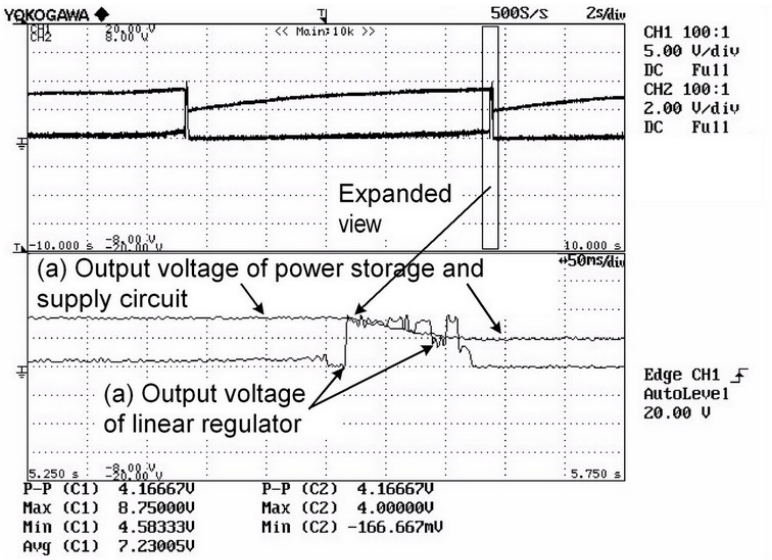

Figure 2.45: Waveforms of (a) Charging and Discharging of the output voltage of energy storage and supply circuit and (b) Output voltage of voltage regulator

The electrical power consumed by the RF transmitter load is dependent on the number of digital encoded data word being transmitted. For each data word, the time taken for one transmission is 20 ms i.e. 10 ms of active time and 10 ms of idle time. During the active transmission time, the RF load requires supply voltage

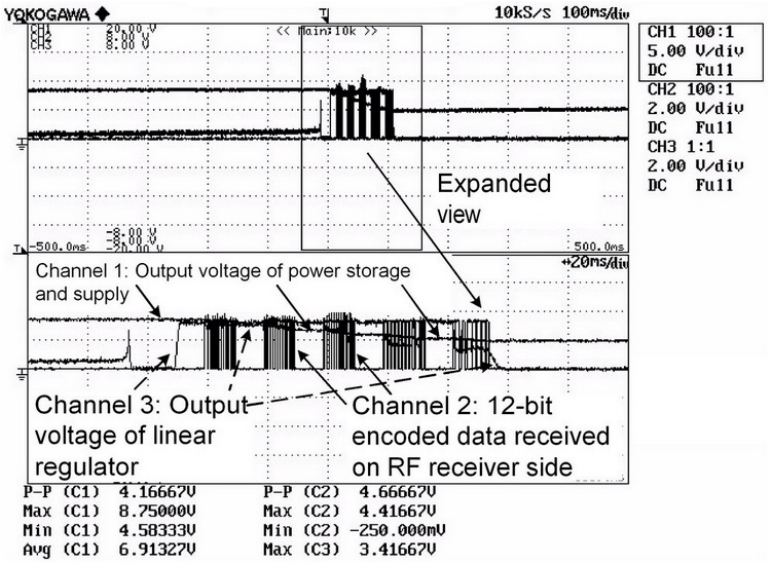

Figure 2.46: Waveforms collected at the RF receiver side to display number of encoded data words received using the harvested energy

and current of 3.3 V and 4 mA respectively to operate. As for the remaining time of 10 ms, the RF load is operating in idle mode which means that very minimal amount of energy would be consumed, so it is reasonable to exclude the power being consumed by the RF load during the idle time. By calculation, the average power and hence the energy consumed by the RF transmitter are 13.2 mW and 132 μJ respectively. Taking into consideration the power loss in the voltage regulator, the total power required for one digital 12-bit data word is 167 μJ. Based on the harvested electrical energy of 917 μJ stored in the capacitor, five packets of 12-bit digital encoded data words (each packet consumes 167 μJ) can be transmitted. This is verified by the five packets of digital encoded data words received at the base station shown in Figure.2.46. Referring to Figure.2.46, Channels 1 and 3 exhibit the output voltages of the storage capacitor and the voltage regulator where Channel 2 shows the encoded data words received over at the RF receiver end.

For the transmission of five packets of 12-bit encoded digital data words, 835

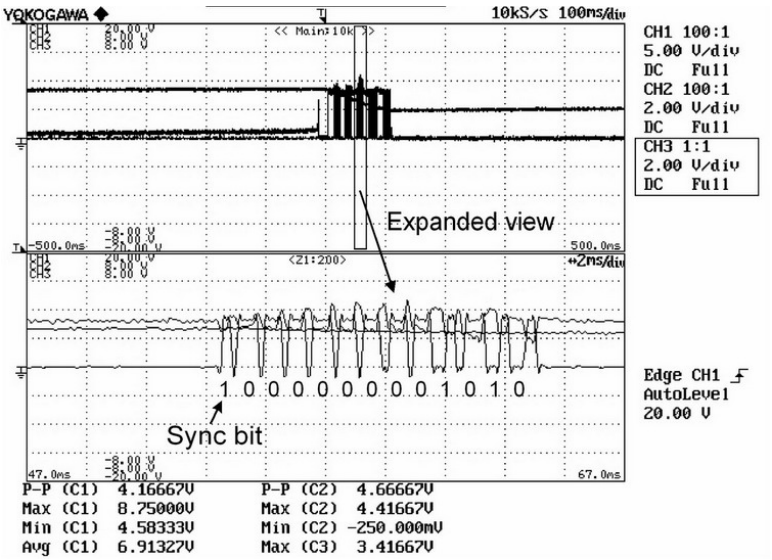

Figure 2.47: Waveforms collected at the RF receiver side to verify the 12-bit encoded data word

μJ of electrical energy is drawn from the bank (917 μJ) of electrical energy stored in the capacitor. Out of the 835 μJ of electrical energy drawn, the actual useful energy being consumed by the RF transmitter is 660 μJ. Therefore the efficiency of the system is around 72 %. Power loss is incurred in the power management circuit. Additionally, it can be observed in Figure.2.46 that during the discharge period of 100 ms, as the capacitor voltage is decreasing from 8.75 V to 4.58 V, the voltage regulator is able to maintain its output voltage at 3.3 V for around 90 ms. After which, the output voltage of the voltage regulator starts to decay with the voltage across the storage capacitor. Figure.2.47 shows the waveform of a 12-bit decoded data word that is generated by the HT12D decoder at the receiver end. The decoded data sequence of the waveform is read as [0000 0000 1010]. Comparing the decoded data sequence with the encoder data sequence at the transmitter side (starting with a synchronization bit following an 8-bit address [0000 0000] and 4-bit data [1010]), the two data sequences match each other quite accurately. The positive outcome concluded from the experimental results has verified that the RF

transmitter is able to successfully transmit five encoded digital data words over to the RF receiver at the base station in a wireless manner using the wind energy harvested by the proposed piezoelectric wind energy harvester system.

2.2.5 Summary

A novel way of harvesting wind energy using piezoelectric material for a low power autonomous wind speed sensor has been proposed and demonstrated with experimental setup. Unlike the conventional wind turbine, the piezoelectric wind harvester together with its related electronic circuits are relative smaller in size and lighter in weight, hence it is more portable and suitable for low power autonomous sensors. Experimental results show that the designed piezoelectric wind harvester system with efficiency of 72 % is able to power a wireless RF transmitter load to transmit five digital 12-bit encoded data words to the receiver end during one wireless transmission. The proposed piezoelectric based wind harvester can be used in applications that need to detect wind speed beyond certain threshold level for instance in early warning of storm detection. When the ambient wind speed is beyond the preset value, a 12-bit digital signal will be transmitted in a wireless manner to the base station to set off the warning siren.

Chapter 3

Thermal Energy Harvesting System

Thermal energy harvesting is the process of converting thermal energy to electrical energy by using thermoelectric generator (TEG) made of thermocouples. Thermoelectric power generators have been successfully developed for decades for kilowatt-scale power generation by using waste heat from industrial processes such as vehicle exhaust, space travel, etc. [84]. Such systems involve heat flows at kilowatt scale and temperature of hundreds of ^{o}C. However, small-scale TEGs [85] and [86] for obtaining power of the order of milliwatts or lower from ambient thermal energy sources with small temperature differences have just recently been researched [37]. The challenges with utilizing TEG technology in small-scale TEH are low energy conversion efficiency, inconsistency and low output power due to temperature fluctuation and high cost [85]. As such, there is a significant need for an efficient power management circuit to maximize the power transfer from the TEG source to its connected electronic load over a wide range of operating conditions.

For decades, maximum power point tracking (MPPT) schemes such as [87] -

[90] have been proposed for large-scale power generation systems. However, these MPPT schemes are not suitable for small-scale energy harvesting systems as they consume significant amount of power for their continuous operation. At lower power levels of mW of interest in this chapter, implementation of such accurate MPPT schemes for small-scale thermal energy harvesting (TEH), whereby the power consumed by the complex MPPT circuitry could be higher than the harvested power itself, is not desirable. It is thus important to ensure that the gain in input energy is always higher than the additional losses that are caused by the MPP tracking operation. So far, limited research works can be found in the literature that discuss on a simple but yet compatible MPPT algorithm in addressing the issue of small-scale thermal energy harvesting (TEH) system. This chapter presents a resistor emulation approach and its associated circuitry for harvesting near maximum energy from the thermal energy source. The rationale behind the resistor emulation approach [69] - [71] is that the effective load resistance is controlled to emulate the source resistance of the thermoelectric generator so as to achieve impedance matching between the source and load and hence the harvested power is always at its maximum at any operating temperature difference. A power-electronic based converter with minimal open-loop control overhead is realized to act as a near constant resistance at its input port to emulate the TEH source while transferring energy to the time-varying load resistance, which consists of an energy storage element and a wireless sensor node.

The rest of the chapter is organized as follows: Section 3.1 describes the thermal energy harvesting system and energy conversion effect. Section 3.2 discusses on the resistor emulation based maximum power point tracker for TEH where as Section 3.3 describes its implementation using a DC-DC buck converter. Following

that, the experimental results of the optimized TEH wireless sensor node prototype are discussed in Section 3.4, followed by a summary of the TEH research work in Section 3.5.

3.1 Thermal Energy Harvester

The thermal energy harvester employed in this chapter for converting thermal energy into electrical energy is shown in Figure.3.1. The thermal energy harvester is designed for two main purposes: (1) to house the miniaturized thermoelectric generator for ease of deployment and (2) to channel the thermal energy, generated from the heat source at certain high temperature of T_H, to the enclosed thermoelectric generator (TEG) via a thin film of thermally and electrically conductive silver grease between them and then release the residual heat accumulated in the heatsink to the surrounded ambient air at a lower temperature T_C.

Table 3.1: Main parameters of Thermo Life® prototype.

Geometrical Parameter	**Unit**	**Value**
Total height of device	mm	0.85 +/- 0.05
Outer diameter of device	mm	9.60 +/- 0.05
Volume of device	mm^3	62 +/- 5
Mass of device	mg	185 +/- 2
Number of thermocouples (n)		5200
Thermal Parameter		
Total thermal resistance (R_{TEG})	K/W	14.1 +/- 1.0
Seebeck's coefficient of TEG (S)	V/K	1.1
Seebeck's coefficient of a thermocouple (α)	mV/K	0.21

Figure 3.1: Thermal energy harvester consisting of a housing structure and a TEG

3.1.1 Description of Thermoelectric Generator

Thermoelectricity describes the relationship between heat flow and electrical potential in conducting materials. The ability to generate electrical power from a temperature gradient in materials is due to the Seebeck's effect [91]. This Seebeck's effect can be observed in a thermocouple made of two dissimilar conductors. If the two junctions are maintained at different temperatures i.e. T_{CJ} and T_{HJ}, an open-circuit voltage proportional to the temperature difference, ΔT_{TEG}, would be developed. For thermoelectric power generator (TEG), which is composed of n thermocouples connected electrically in series and thermally in parallel, the open-circuit voltage, V_{oc}, of the TEG is given as: -

$$V_{oc} = S * \Delta T_{TEG} = n * \alpha(T_{HJ} - T_{CJ}) \tag{3.1}$$

where α and S represents the Seebeck's coefficient of a thermocouple and a TEG respectively. In this thermal energy harvesting (TEH) research, a Thermo Life® thermoelectric generator is used; it is based on the development of a unique thin film technology for the deposition of highly efficient thermoelectric materials of the Bi_2Te_3-type on thin Kapton foils® [91]. Based on the technical datasheet provided by Thermo Life®, the essential geometrical and thermal parameters of the TEG prototype are presented in Table.3.1. The high output voltage of Thermo Life® TEG, due to over 5200 thermocouples in series as well as the relatively high thermal resistance, make this device ideal for energy scavenging, where only a small temperature gradient is available such as in body and waste heat applications [91].

3.1.2 Analysis of Thermal Energy Harvester

To illustrate the thermal and electrical characteristics of the thermal energy harvester, an equivalent electrical circuit model is provided in Figure.3.2.

3.1.2.1 Thermal analysis

Referring to Figure.3.2, it can be observed that the thermoelectric generator (TEG) is connected to the hot and cold reservoirs via the thermal contact and thermal grease resistances, which are given by $R_{con(H)}$, $R_{g(H)}$ and $R_{g(C)}$, $R_{con(C)}$ respectively. Considering all these thermal resistances, R_{Total}, (see Figure.3.2 (left circuit)) residing in the housing structure of the thermal energy harvester and comparing them with the TEG's internal thermal resistance, R_{TEG}, the actual temperature

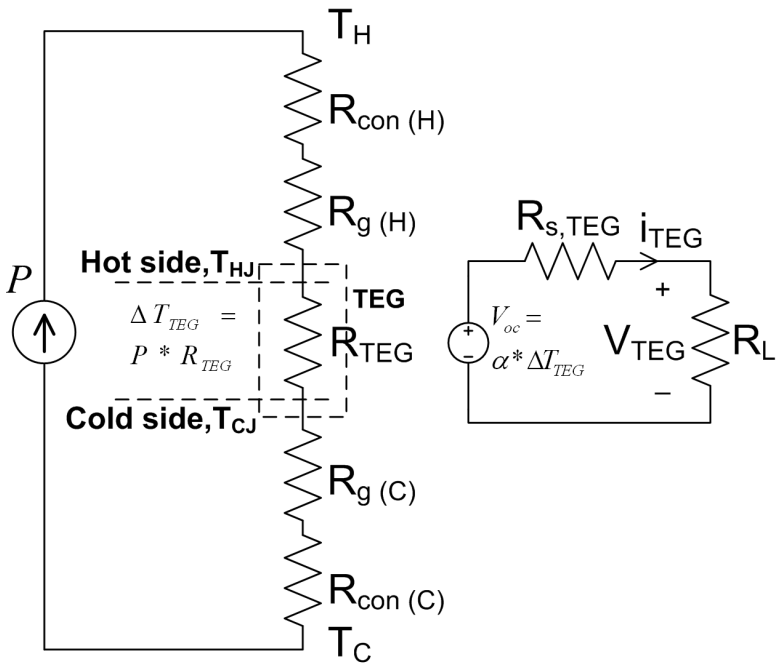

Figure 3.2: Equivalent electrical circuit of the thermal energy harvester

drop across the thermoelectric generator, ΔT_{TEG}, may then be expressed as

$$\begin{aligned} \Delta T_{TEG} &= \Delta T * \frac{R_{TEG}}{R_{Total}} \\ &= (T_H - T_C) * \left[\frac{R_{TEG}}{R_{con(H)} + R_{g(H)} + R_{TEG} + R_{g(C)} + R_{con(C)}} \right] \end{aligned} \quad (3.2)$$

Due to the finite thermal resistances of the thermal energy harvester, the temperature difference, ΔT_{TEG}, across the junctions of the thermoelectric generator (TEG) is lower than the temperature gradient, ΔT, that is externally imposed across the thermal energy harvester. To minimize this negative effect, the thermal resistance, R_{TEG}, of the TEG must be as high as possible or, in another words, the rest of the thermal resistances of the thermal energy harvester must be minimized.

The unwanted thermal resistances of the thermal energy harvester, which is defined as $R_{Thermal} = \Delta x/KA$, can be minimized by carrying out some appropriate hardware design on the thermal energy harvester: (1) increasing the contact

surface, A, of the heat transfer area, (2) reducing the thickness of the material, Δx, used like the fins of the heatsink and lastly (3) selecting the aluminium material which has very high thermal conductivity, K, for good thermal conduction. To maintain the temperature difference across the thermal energy harvester, the teflon material is inserted between the hot and cold sides of the housing structure shown in Figure.3.1 to prevent the adverse effect of parallel parasitic thermal resistance [92].

3.1.2.2 Electrical analysis

It should be noted that the effective temperature gradient ΔT_{TEG} depends not only on the thermal and electrical properties of the thermoelectric generator (TEG) but also on the resistive load that is connected. When connecting a load resistance R_L to the thermoelectric generator (TEG) as shown in Figure.3.2, a current I_{TEG} flows, which is given by [93]

$$I_{TEG} = \frac{V_{oc}}{R_{s,TEG} + R_L} = \frac{S * \Delta T}{R_{s,TEG} + R_L} \tag{3.3}$$

Depending on the dimension of the TEG, i.e. h and A_{leg}, which are the height and the area of a single thermocouple leg respectively, and the electrical resistivity, ρ, of the materials used, the internal electrical resistance of the TEG, $R_{s,TEG}$, which composes of n thermocouples of p-type and n-type semiconductor materials is given by [93]

$$R_{s,TEG} = n * 2 * \frac{\rho h}{A_{leg}} \tag{3.4}$$

The output power, P_L, delivered by the TEG to the load, R_L, can be expressed as:

-

$$\begin{aligned} P_L &= I_{TEG}^2 R_L \\ &= S^2 \Delta T_{TEG}^2 \frac{R_L}{(R_{s,TEG} + R_L)^2} \end{aligned} \tag{3.5}$$

Referring to eqn.3.5, it can be seen that the output power, P_L, is dependent on both the TEG electrical resistance, $R_{s,TEG}$, and the electrical resistance of the external load, R_L. Under impedance matching condition where the load resistance, R_L, is equal to the internal electrical resistance, $R_{s,TEG}$, the thermoelectric generator is generating the maximum output power given by,

$$P_{L,MPPT} = \frac{S^2 \Delta T_{TEG}^2}{4 R_{s,TEG}} \tag{3.6}$$

During operation of the thermoelectric generator (TEG), the output voltage is reduced by the ohmic voltage drop across its internal resistance, $R_{s,TEG}$. Consequently, the voltage at its maximum power, V_{MPPT}, is about half that of the open-circuit voltage, V_{oc}, ($V_{oc} = S\Delta T \approx 2V_{MPPT}$) and the maximum power changes with temperature difference as ΔT^2.

3.1.3 Characterization of Thermal Energy Harvester

Based on the thermal analysis, the thermal energy harvester has been designed to maximize the overall output power of the thermoelectric generator (TEG). The geometric design parameters, such as Δx and A, and the thermal interface related parameters are the main design factors of the thermal energy harvester. The physical size of the optimized thermal energy harvester prototype is 20 mm x 20 mm x 20 mm. Some characterization works are performed by applying a temperature difference (T_H - T_C) between the energy harvester faces and measuring both the output

voltage and current with different loads connected. This operation is repeated for temperature differences in the range between 5 K and 30 K.

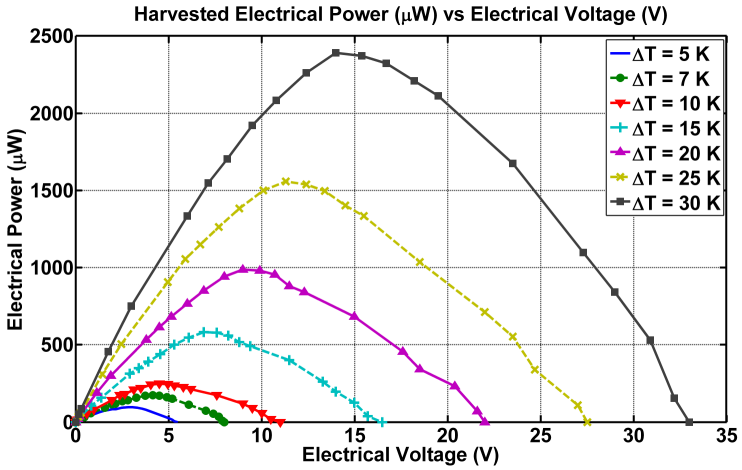

Figure 3.3: P-V curves of thermoelectric generator at different thermal gradients

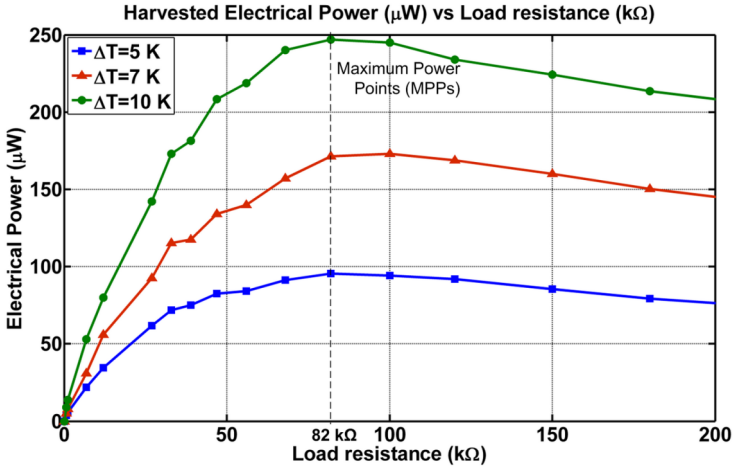

Figure 3.4: P-R curves of thermoelectric generator at different thermal gradients

Referring to the power curve (Power vs Load voltage) shown in Figure.5.20, it can be observed that the maximum obtainable power for each thermal gradient corresponds to an output voltage of the thermal energy harvester. This is unlike the case of the other energy harvesting sources like solar, vibration, etc. where their power curves peak near a particular output voltage of the energy source. As

such, it is not possible to utilize this simple and ultra-low power maximum power point tracking (MPPT) approach i.e. fixed reference voltage to the thermal energy harvester. In order to overcome that, Kim *et al.* [90] has proposed the adaptive and tracking MPPT approaches that are suitable for thermal energy harvesting (TEH), however these energy hungry approaches require high computational power and cost with respect to the milliwatt or even lower harvested power levels of interest in this chapter.

Since most of the conventional MPPT approaches are not suitable for thermal energy harvesting, this chapter presents an alternative MPPT technique based on the concept of emulating the load impedance to match the source impedance as illustrated by the power curves in Figure.5.21. This technique is also known as the resistor emulation or impedance matching approach. The power curve plotted in Figure.5.21 shows that when the load resistance matches the source resistance of the thermal energy harvester of 82 kΩ, the harvested power is always maximum for different temperature difference. However, for other loading conditions, shifting away from the internal resistance of the thermal energy harvester, either very light or heavy electrical loads, the electrical output power being generated by the generator drops significantly. This exhibits that the MPPT technique based on resistor emulation is a possible option to assist the small-scale TEH system to achieve maximum power harvesting from the thermal energy harvester.

3.2 Resistor Emulation based Maximum Power Point Tracker

Resistor emulation techniques have been widely used in the impedance matching applications [69] - [71]. Take for instances, Paing *et al.* [70] have successfully demonstrated the resistor emulation approach in energy harvesting from variable low-power radiative radio frequency (RF) sources. K. Khouzam & L. Khouzam [69] have also discussed the resistor emulation concept used in their direct-coupling approach for optimum impedance matching between the energy harvester and its load by carefully selecting the harvester's rated parameters with respect to the load parameters. However, very limited research works can be found in the literature that discuss on the design and implementation of resistance emulation techniques and its approximation for small-scale thermal energy harvesting (TEH) system so as to achieve resistor emulation based maximum power point tracking (MPPT).

In this chapter, the proposed maximum power point tracker uses a power converter as an open-loop resistance emulator to naturally track the MPP of the thermal energy harvester with very little control circuit overhead. A buck converter topology is selected for the power converter due to the high output voltage of 5 - 35 V (See Figure.5.20) generated by the thermal energy harvester (input voltage, V_{in}, to the buck converter). The main purpose of the buck converter is to match the optimal resistance of the thermal energy harvester i.e. $R_{s,TEG} = R_{opt} = 82$ kΩ at the converter input port and efficiently transfer the energy to its output port based on the voltage and charge characteristics of the energy storage element. A previous approach [70] has shown that over a certain range of input power level, operation of a boost (step-up) converter in discontinuous conduction mode (DCM) with a fixed

duty cycle results in maximum output power. The results as reported in [70] and [94] can be related to this research work by showing that the DC-DC converters viz. buck, boost and buck-boost in DCM acts as a near constant resistance at its input port for large step-up/down conversion ratio.

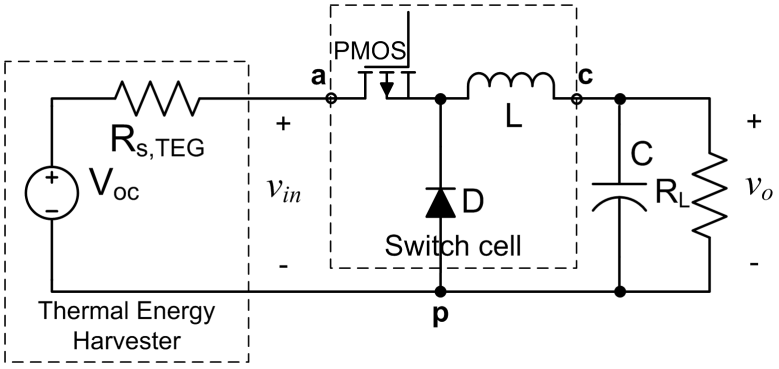

Figure 3.5: Buck converter

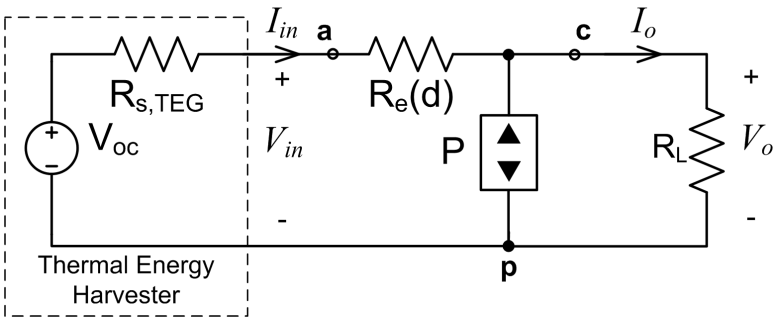

Figure 3.6: Averaged equivalent circuit of a buck converter

To fully understand how the buck converter, when operating in DCM, emulates the source resistance of the thermal energy harvester ($R_{s,TEG}$=82 kΩ) to achieve MPPT, the electrical model of the buck converter shown in Figure.3.5 has been modelled into an averaged equivalent circuit model as shown in Figure.3.6. The modelling process is based on the analysis made by Erickson *et al.* in [71] that shows the average voltage and current of the semiconductor switch are proportional, thus obeying the Ohm's law and the switch can be simply replaced by an

effective resistor, $R_e(d)$. In similar context, the average diode's voltage and current obey a power source, P, characteristic, with power equal to the power effectively dissipated by $R_e(d)$. Hence, the buck converter in Figure.3.5 can be represented by the averaged equivalent circuit shown in Figure.3.6, where the switch and diode are replaced with an effective resistor, $R_e(d)$, and a dependent power source, P, respectively [71].

Based on the dc analysis of buck converter in DCM [95], the conversion ratio, M, of the buck converter can be derived [96] as follows: -

$$M = \frac{V_o}{V_{in}} = \frac{2}{1 + \sqrt{1 + 4R_e(d)/R_L}} \tag{3.7}$$

Additionally, the emulated resistance of the buck converter in DCM, $R_e(d)$, is obtained as follows [71]: -

$$R_e(d) = \frac{2L}{d^2 T_s} \tag{3.8}$$

where d and $T_s = 1/f_s$ are the duty cycle and the switching period/frequency of the gating signal of the PWM switch respectively. In practical cases, the step-down conversion ratio, M, of the buck converter ($V_{in} \gg V_o$) may not be large enough such that the correction factor, $1/(1-M)$, is approximately unity. As such, taking into account the effect of the correction factor, M, on the emulated resistance, $R_e(d)$, equation of the buck converter derived in eqn.3.8, the overall emulated resistance, R_{em}, then becomes

$$\begin{aligned} R_{em} &= R_e(d)\left(\frac{1}{1-M}\right) \\ &= \frac{2Lf_s}{d^2}\left(\frac{1}{1-\left(\frac{2}{1+\sqrt{1+8Lf_s/d^2R_L}}\right)}\right) \end{aligned} \tag{3.9}$$

Knowing that the source resistance of the thermal energy harvester, $R_{s,TEG}$, as obtained experimentally in Figure.5.21 is fixed at 82 kΩ, the input port of the

buck converter has to constantly emulate this resistance value such that maximum power point tracking (MPPT) can be achieved. In this discontinuous conduction mode (DCM) of operation, the converter parameters such as L and f_s are fixed whereas the duty cycle, d, is tuned to the required value to achieve an equivalent emulated resistance. Hence, the equation expressed in eqn.3.9 has been resolved to determine the duty cycle, d_{em}, that can emulate the source resistance of the thermal energy harvester ($R_{s,TEG}$=82 kΩ) so as to achieve MPPT, which is given by,

$$d_{em} = \sqrt{\frac{2Lf_s}{R_{em} \pm \sqrt{R_{em} * R_L}}} \tag{3.10}$$

To demonstrate the competency of the buck converter as a resistor emulation based maximum power point (MPP) tracker and to verify its governing equation expressed in eqn.3.10, the buck converter has been experimentally tested under varying temperature differences and different loading conditions. Firstly, a fixed resistance of 10 kΩ is used as the test load for the operation of resistor emulation based MPP tracker under varying temperature differences and the experimental results are shown in Figure.3.7.

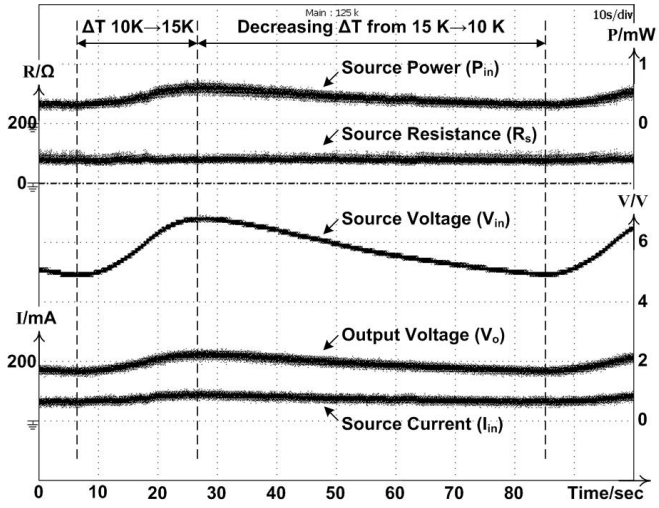

Figure 3.7: Operation of resistor emulation based MPP tracker under varying temperature differences

Referring to Figure.3.7, as the temperature difference, ΔT, across the thermal energy harvester increases from 10 K to 15 K, the harvested power, P_{in}, which is the resultant of the product of the source voltage, V_{in}, and source current, I_{in}, increases from around 300 μW to 600 μW. During this time when ΔT is increasing, it can be seen from Figure.3.7 that the source resistance, R_s, is emulated by the resistor emulation maximum power point (MPP) tracker to remain steadily at the optimal resistance of 82 kΩ.

Based on Seebeck's effect, as the temperature difference across the thermal energy harvester rises from 10 K to 15 K, the source voltage increases from 5 V to 7 V and the step-down voltage, V_o, output from the buck converter with resistor emulation based MPP tracker also increases from 1.8 V to 2.2 V respectively. Given that the converter parameters are chosen as L = 30 mH, f_s = 18 kHz and d_{em} = 0.14, using eqns.3.7, 3.8 and 3.9, the source resistance obtained experimentally, as shown in Figure.3.7, is verified to be around 82 kΩ. The buck converter is able to maintain the thermal energy harvester near its MPPs for various input operating conditions. Hence, the buck converter yields good performance as a simple resistor emulation based maximum power point (MPP) tracker under varying temperature differences. These observations and analyses apply to the decreasing temperature difference condition as well.

Secondly, the operation of resistor emulation based MPP tracker for different loading conditions are experimentally tested and the experimental results are shown in Figures.3.8 and 3.9. The equation expressed in eqn.3.10 is used to determine the duty cycle that emulates the source resistance of the thermal energy harvester ($R_{s,TEG}$=82 kΩ) for maximum power transfer between the source and the load.

The operating range of the loading conditions are determined based on the two extreme ends of the operational bandwidth of the buck converter when connected to a supercapacitor of 0.1 F, the initial charging and final charged states of the supercapacitor can be emulated by two load resistances, R_L, of 10 kΩ and 56 kΩ respectively. Based on eqn.3.10, the emulated duty cycles of the two resistance values, i.e. 10 kΩ and 56 kΩ, are calculated to be 0.14 and 0.27 respectively.

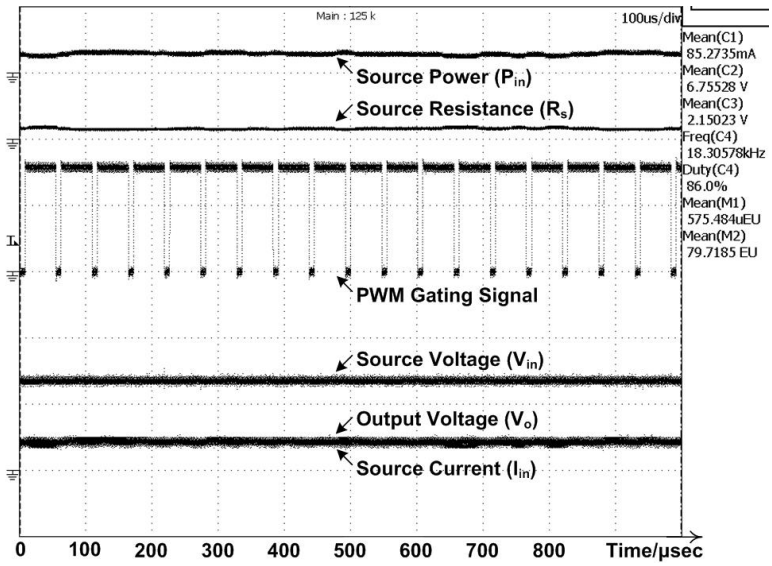

Figure 3.8: Operation of resistor emulation based MPP tracker at 10 kΩ loading

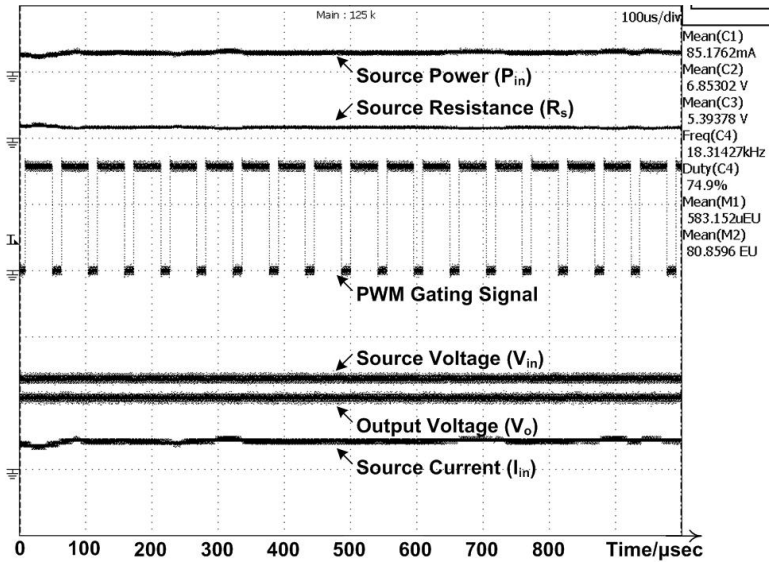

Figure 3.9: Operation of resistor emulation based MPP tracker at 56 kΩ loading

Referring to Figures.3.8 and 3.9, the complementary emulated duty cycles (a P-MOSFET (PMOS) is used instead of an N-MOSFET (NMOS) as the high-side switch of the buck converter) obtained experimentally are 0.14 and 0.251 for the load resistances, R_L, of 10 kΩ and 56 kΩ respectively and the experimental results tally with the calculated duty cycles of 0.14 and 0.27. At the emulated duty cycles, it can be observed in both Figures.3.8 and 3.9 that the approximate desired R_{em}=82 kΩ is achieved and the maximum electrical power P_{MPPT} = 580 μW (see Figure.5.21) is harvested.

3.3 Implementation of Optimal TEH Wireless Sensor Node

The schematic diagram of a self-autonomous wireless sensor node powered by the designed thermal energy harvesting (TEH) system and its ultra-low-power and efficient power management circuit is illustrated in Figure.3.10. Referring to Figure.3.10, the designed power management circuitry with resistor emulation MPPT approach can be essentially consist of three main building blocks: (1) a buck converter with MPP tracker and its control and PWM generation circuit that manipulates the operating point of the thermal energy harvesting to keep harvesting power at the maximum power point, (2) an energy storage element i.e. supercapacitor to buffer the energy transfer between the source and the load and (3) a regulating buck converter to provide constant voltage to the wireless sensor node and other electronic circuitries.

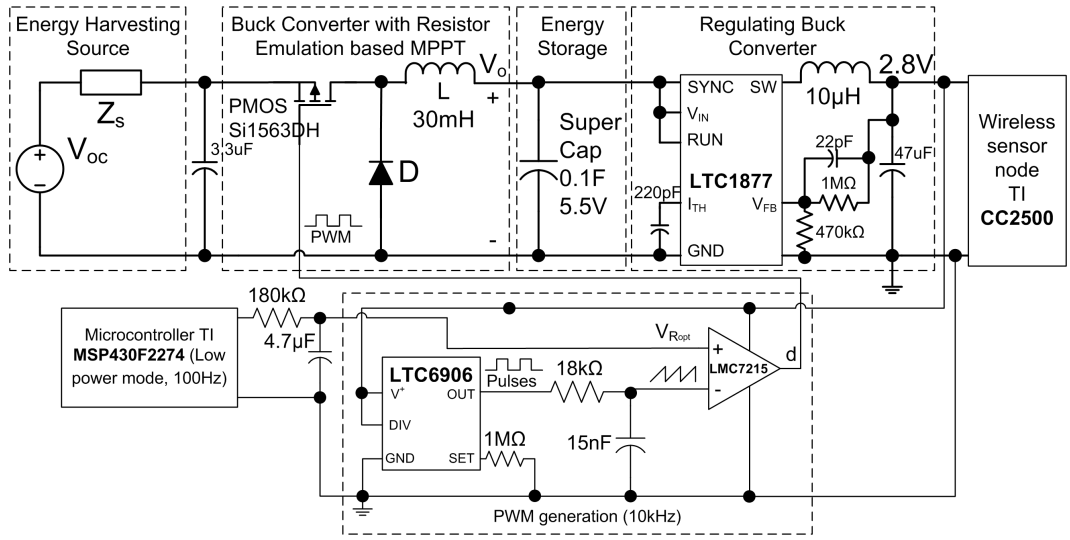

Figure 3.10: Schematic diagram of the TEH system

3.3.1 Buck Converter With Resistor Emulation Based MPPT

The buck converter in discontinuous conduction mode (DCM) has been illustrated to perform well as a near constant resistance at its input port so as to manipulate the thermal energy harvester to transfer maximum power to its output port, which is connected to a supercapacitor of 0.1 F, based on the duty cycle, d, of the PWM gate signal applied to the buck converter [70]. Within the operational bandwidth of the buck converter under different loading conditions, in the range of 10 kΩ to 56 kΩ, a duty cycle value of 0.16 has been selected to operate the buck converter to its near maximum power points. Substituting the duty cycle value, $d = 0.16$, into eqn.3.9, the emulated resistances, with the connected load of 10 kΩ and 56 kΩ, are calculated to be 68 kΩ and 126 kΩ respectively. Referring to Figure.5.21, it can be observed that the power losses at these resistance values, which are near to the maximum power points (MPPs), are less than 5 % of the maximum obtainable power at $R_{em} = 82$ kΩ. This power waste (few tens of μW) is much less than the power consumed by the high-power overhead of complex control circuitry required

to perform the accurate and precise closed-loop MPPT techniques.

The operation of the buck converter as an open-loop resistance emulator is as follows: a low frequency PWM control signal, ∼100Hz, of the desired duty cycle of 0.16 is generated by a Texas Instruments microcontroller (TI MSP430F2274). A ultra-low-power PWM generation circuit is designed to transform the low frequency PWM control signal generated from the reduced clock speed microcontroller to a higher switching frequency of 10 kHz, so that smaller filter components are used in the buck converter to miniaturize the overall TEH system. The PWM generation circuit is made up of a micro-power resistor set oscillator (LTC6906) used for saw-tooth generation and a micro-power, rail-to-rail CMOS comparator (LMC7215), which compares its reference signal ($d_{em} * V_{ref} = 0.16 * 2.5V = 400$ mV) with the high frequency sawtooth signal to generate the PWM gate signal to control the buck converter.

3.3.2 Energy Storage

For long term deployment of the thermal energy harvesting (TEH) wireless sensor node, it is required to have an energy storage device such as supercapacitor and batteries onboard the sensor node to accumulate the input energy generated from the heat source and use it to sustain the node's operation throughout the lifetime. The supercapacitor has superior characteristics over batteries which include numerous full charge cycles (more than half a million charge cycles), long lifetime (10-20 years operational lifetime) and high power density (an order of magnitude higher continuous current than a battery) [34]. Unlike the discrete capacitors which have very small capacitance values of pF - μF range, the supercapacitor has very large

capacitance value of Farads range suitable for energy storage purpose. For the design of the buck converter as a resistor emulation based MPP tracker, it is important to consider the dynamic response of the supercapacitor to ensure constant maximum power point tracking (MPPT) operation is achieved.

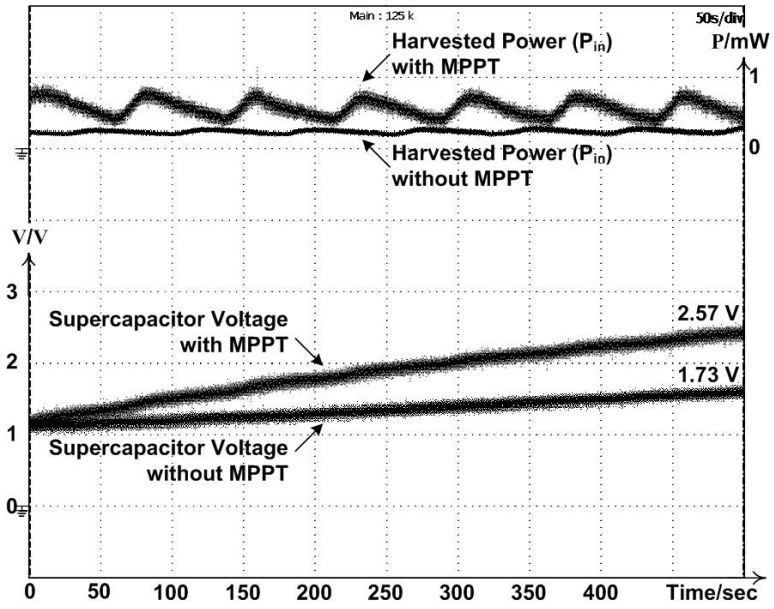

Figure 3.11: Performance of thermal energy harvesting (TEH) system w/MPPT and w/o MPPT for charging a supercapacitor

For a time period of 500 seconds as shown in Figure.3.11, the supercapacitor is charged by the TEH system from its initial state of 1 V. As the supercapacitor is charging, the dynamic response of the supercapacitor changes according to the operating conditions of the TEH system, the impedance of the supercapacitor is equivalent to the range of load resistances, R_L, between 10 kΩ to 56 kΩ. At $V_{cap}(500sec)$, the supercapacitor of 0.1 F is being charged to the voltage levels of 2.57 V with MPPT scheme and 1.73 V without MPPT scheme. Comparing between the two schemes, it is obvious that the charging performed by the TEH system with MPPT is much higher than its counterpart without the MPPT scheme. This is because the thermal energy harvester is maintained at its near MPPs and

hence more electrical power is transferred to the supercapacitor. When the TEH system is operating with MPPT scheme, the amount of energy accumulated in the supercapacitor after 500 seconds is 0.28 J, which is 2 times of its counterpart of 0.15 J, hence this exhibits the superior performance of the TEH system with MPPT scheme over its counterpart under dynamic loading condition.

3.3.3 Regulating Buck Converter and Wireless Sensor Node

The thermal energy harvesting (TEH) system is designed to power a commercially available wireless sensor node supplied by Texas Instrument (TI) known as the wireless target board, eZ430-RF2500T. A buck converter (LTC1877) obtained from Linear Technology is inserted between the supercapacitor and the wireless sensor node to provide a constant operating voltage of 2.8 V_{DC}. The efficiency of the buck converter is around 80-90 %, consuming an operating current of 12 μA. In this chapter, the operation of the wireless sensor node deployed in an application field is illustrated in Figure.3.12.

As seen in Figure.3.12, the sensor node's operation comprises of: (1) sensing some external analog signals of sensors such as temperature, and (2) communicating and relaying the sensed information to the gateway node in every 5 seconds time. Upon receiving the data at the base station, the collected data are then post-processed into usable information for any follow up action. This duty cycling approach could significantly reduce the power consumption of the energy-hungry radio module of the sensor node with a slower transmission rate of every few seconds.

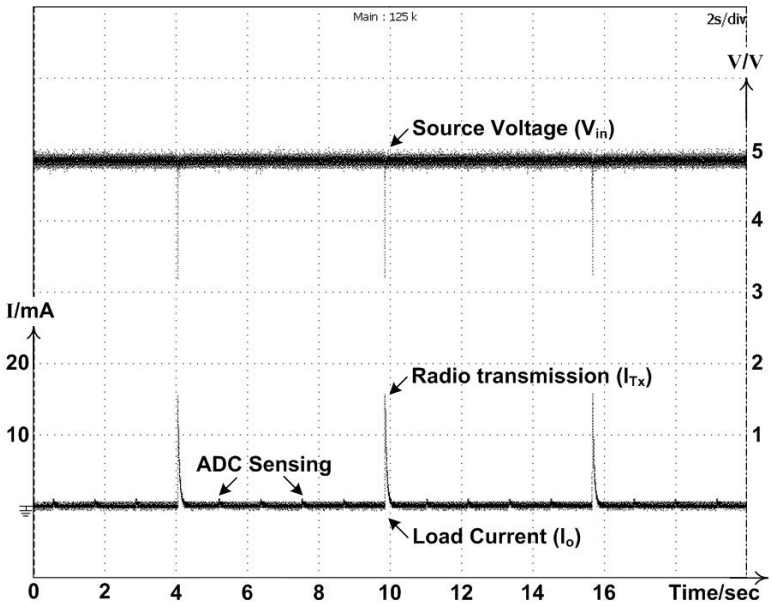

Figure 3.12: Operation of the wireless sensor node

3.4 Experimental Results

The optimal thermal energy harvesting (TEH) wireless sensor node has been successfully implemented in hardware prototype for laboratory testing. Several experimental tests have been conducted to differentiate the performance of the TEH system and its resistor emulation maximum power point tracking (MPPT) scheme in powering the connected load consisting of a supercapacitor, control and PWM generation circuitries and wireless sensor node. The operation of the electrical load, as shown in Figure.3.13, is first powered solely by its onboard supercapacitor and then the TEH system with its integrated MPPT harvesting at temperature difference of 20 K.

Referring to Figure.3.13, it can be observed that the supercapacitor voltage, V_o, keeps decreasing during the period of time when neither the TEH system nor its integrated MPPT is connected to the sensor node. The conventional sensor node,

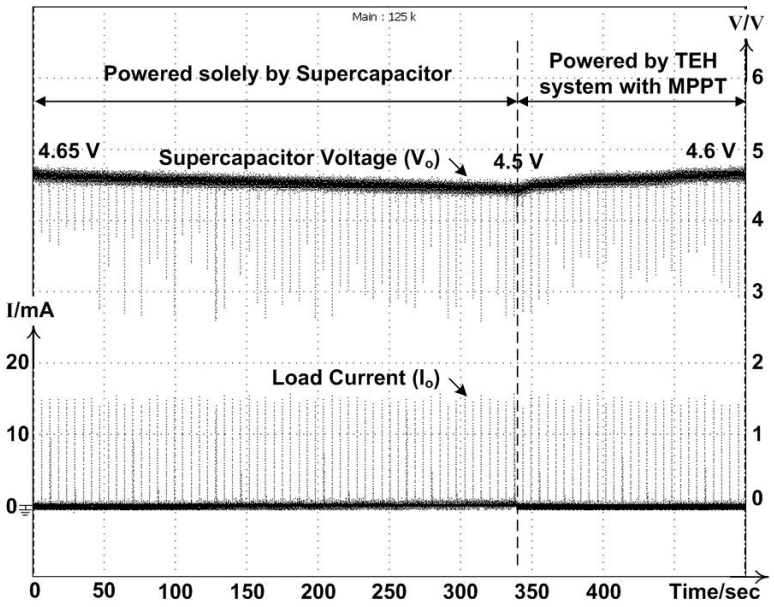

Figure 3.13: Operation of wireless sensor node

which operates solely on the supercapacitor, consumes 200 μW of average power from the supercapacitor of 0.1 F, hence the voltage across the supercapacitor drops from 4.65 V to 4.5 V in around 330 seconds, which is calculated to be 69 mJ of energy transferred to the load. Once the TEH system with MPPT is activated, the harvested power of around 450 μW is used to power the sensor node as well as to charge the supercapacitor back to 4.6 V in 170 seconds. This indicates that solely depending on the energy storage to sustain the operation of the sensor node is not sufficient, it is only when the TEH system with its MPP tracker is employed where sufficient power is provided for both the operation of the wireless sensor node as well as to charge the supercapacitor.

The designed buck converter with resistor emulation MPPT approach has already been demonstrated to yield good performance in extracting maximum power from the thermal energy harvester, but this comes at the expense of additional power losses in the converter and its associated control and PWM generation cir-

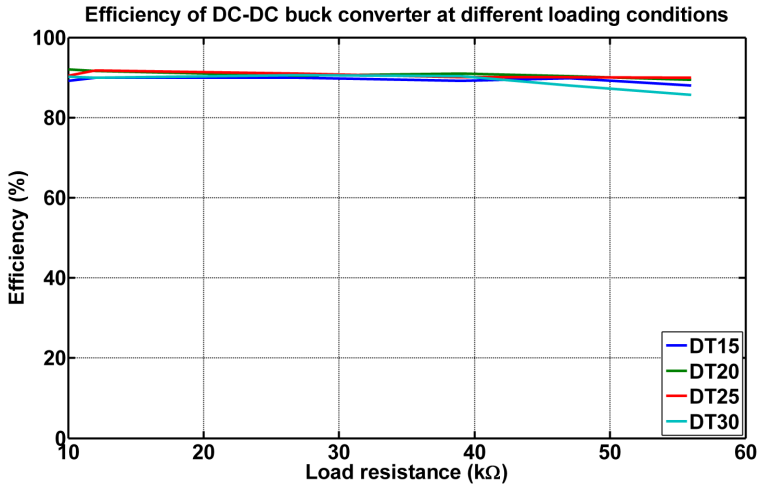

Figure 3.14: Efficiency of buck converter with resistor emulation based MPPT for various temperature differences

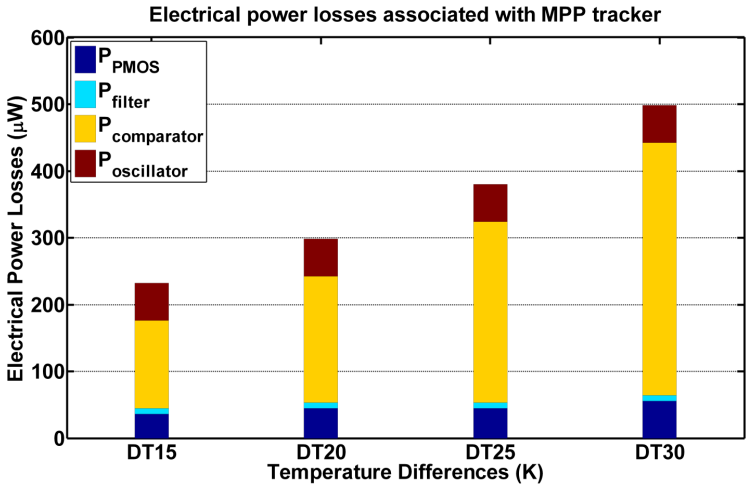

Figure 3.15: Power losses associated with MPP tracker

cuits. It is thus necessary to investigate the significance of these power losses as compared to the total harvested power. The first investigation is to determine the efficiency of the buck converter, η_{conv}, as a function of its output load power, P_{load}, over its input DC power, P_{dc}, under different temperature differences and loading conditions. Take for an example, at temperature difference and output load resistance of 20 ^{o}C and 10 kΩ respectively, the efficiency of the buck converter is given

by,

$$\begin{aligned} \eta_{conv} &= \frac{P_{out}}{P_{in}} * 100\% \\ &= \frac{2.7V^2/10k\Omega}{9V * 88\mu A} * 100\% = 92\% \end{aligned} \tag{3.11}$$

For all other temperature differences and loading conditions, the efficiencies of the buck converter are calculated using eqn.3.11 to be on an average of 90% and the computed results are shown in Figure.3.14. This high-efficiency buck converter is very favourable and desirable in very low power rating condition of milliwatts or even lower. Another investigation being carried out is to determine the power consumption of the associated control and PWM generation electronic circuits and its significance as compared to the harvested power. Based on the voltage and current requirements of each individual component in the thermal energy harvesting (TEH) system shown in Figure.3.10, the total power consumption of the electronic circuits can be calculated as follows,

$$\begin{aligned} P_{consumed@20K,10k\Omega} &= P_{PMOS@V_{MPPT}} + P_{comparator@V_{MPPT}} + P_{filter@2.8V} \\ &\quad + P_{oscillator@2.8V} \\ &= 9V * (4\mu A + 21\mu A) + 2.8V * (3\mu A + 20\mu A) = 289\mu W \end{aligned} \tag{3.12}$$

These power losses associated with the resistor emulation based maximum power point (MPP) tracker at different temperature differences are illustrated in Figure.3.15. Taking into account both the power loss across the buck converter and the power loss in the associated control and PWM generation circuits mentioned by eqns.3.11 and 3.12 respectively, the performance comparison between the TEH system with maximum power point tracking (MPPT) and without MPPT are tabulated in the bar chart shown in Figure.3.16. For all the temperature differences shown in Figure.3.16, it can be observed that the electrical power harvested by

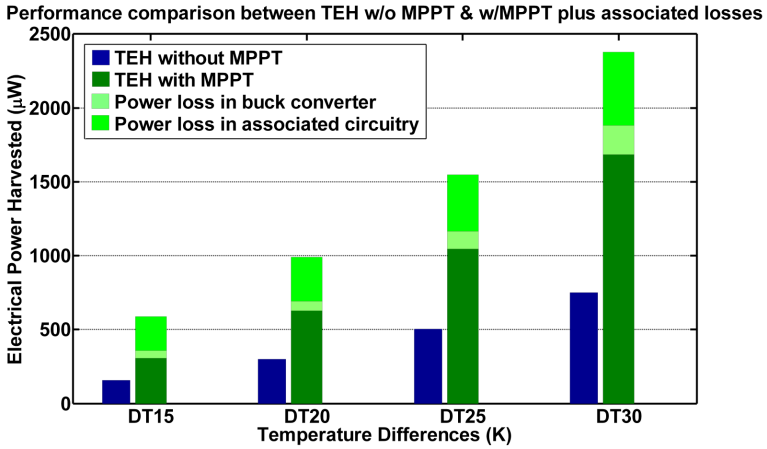

Figure 3.16: Performance comparison between TEH w/o MPPT and w/MPPT

the TEH system with MPPT is at least 2-3 times more than the TEH system without MPPT. Taking into account the power losses of the buck converter and its associated circuitry, the net harvested power from the TEH system with MPPT scheme is still more than the case without MPPT scheme. Hence, this exhibits the importance as well as the contribution of implementing MPPT in the TEH system.

3.5 Summary

In this chapter, an efficient thermal energy harvesting (TEH) system and its power management circuit have been proposed to maximize power transfer from the heat source to its connected wireless sensor node. The electrical characteristic of the TEH system is unlike the case of the other common energy harvesting sources like solar and vibration where most of the conventional MPPT approaches with very little control overhead are not suitable. This chapter presents a resistor emulation based maximum power point tracking (MPPT) technique to emulate the load impedance to match the impedance of the TEH system. Experimental results show that the self-autonomous wireless sensor node powered by the designed thermal

energy harvesting (TEH) system and its ultra-low-power and efficient power management circuit yields better performance than the conventional battery-operated wireless sensor node. At a temperature difference of 20 K, the efficiency of the buck converter is 92 % and its associated power management circuit consumes 289 μW of power to operate. From the experimental test results obtained, an average electrical power of 629 μW is harvested by the optimized TEH system at an average temperature difference of 20 K, which is almost 2 times higher than the conventional energy harvesting method without using MPPT.

Chapter 4

Vibration Energy Harvesting System

Many environments like highways, railways, etc. are subjected to ambient vibration energy that are not commonly used. To use these ambient vibrations as a power source, many researchers have successfully built and tested three basic methods for generating electrical energy from this vibration energy source namely: electromagnetic induction [49], electrostatic generation [97] and piezoelectric materials [98]. While each of the aforementioned techniques can provide a useful amount of energy, piezoelectric materials have received the most attention due to their ability to directly convert applied strain energy into usable electric energy and the ease at which they can be integrated into a system [98]. Unlike the electrostatic and electromagnetic approaches where they require a complex 'two-part' design (the two plates of the variable capacitor in the electrostatic configuration, the coil and the magnet in the electromagnetic one), the piezoelectric approach is relatively simpler in design and implementation. On top of that, Roundy *et al.* demonstrated in [99] that piezoelectric type has the highest energy density. Based on these positive findings, piezoelectric approach has been employed in this vibration energy harvesting

(VEH) research for powering the electrical load.

Piezoelectricity is the ability of some materials, i.e. crystals, to convert mechanical energy into electrical energy, and the inverse [100]. When an external force mechanically strains the piezoelectric material, the material becomes electrically polarized and the degree of polarization is proportional to the applied strain. The opposite effect is also possible: when the piezoelectric material is subjected to an external electrical field, it is deformed. The relationships between the applied force and the subsequent response of a piezoelectric material depend upon three factors [101]: (1) the dimensions and geometry of the material, (2) the piezoelectric properties of the material and (3) the directions of the mechanical or electrical excitation. The first relationship is straightforward. As for the second relationship, the behaviour of piezoelectricity can be modelled with the following constituent equations: -

$$D = dX + \varepsilon^X E \tag{4.1}$$

$$x = s^E X + dE \tag{4.2}$$

Based on the describing electromechanical expression of a piezoelectric material expressed in eqn.4.1, the electrical displacement, D, relates with the mechanical stress, X, applied and the electrical field, E, is generated. The proportionality constants are the d coefficient and the dielectric constant, ε^X, measured at constant stress. As for the expression in eqn.4.2, it relates the mechanical strain developed when an electrical field, E, is applied with the field and the mechanical stress, X, is developed. The proportionality constants are the same d coefficient and the elastic compliance, s^E, measured at constant electrical field. For the third relationship, according to Gonzalez *et al.* in [79], the piezoelectric materials are visualized as

3-D structures where the mechanical and electrical magnitudes can be applied or measured in any of the three axes. The axes are defined in Figure.4.1 where the impact-based piezoelectric generators in parallel and transverse modes of operation are illustrated.

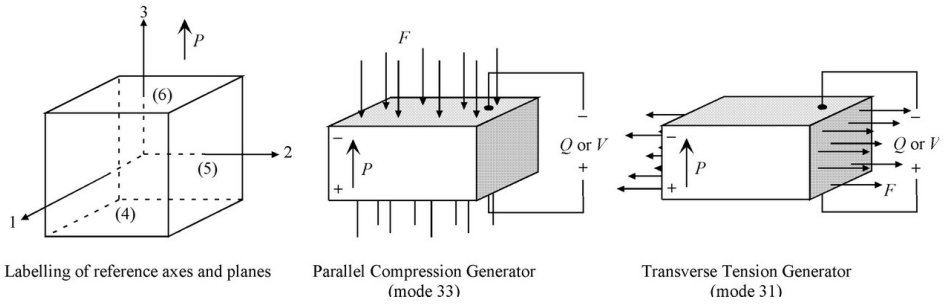

Figure 4.1: Parallel and Transverse tension modes of operation for piezoelectric generator [79]

In this vibration energy harvesting (VEH) research, two types of piezoelectric generators that are designed to harvest impact or impulse forces are explored namely: (1) piezoelectric pushbutton igniter described in Section 4.1 and (2) prestressed piezoelectric diaphragm material described in Section 4.2. With reference to Figure.4.1, the piezoelectric igniter operates in the parallel compression mode or 33-mode of operation where the electrical field is generated i.e. axis-3 across the same axis where an external mechanical force, F is applied to create a mechanical resonance in the piezoelectric element [79]. As for the other type of piezoelectric generator, which uses a prestressed piezoelectric diaphragm material, transverse mode or 31-mode of operation as shown in Figure.4.1 is considered [102]. The mechanical strain applied on the piezoelectric material is perpendicular to its output electrodes, so the surface where the charge is collected and the surface where the force is applied are independent. When the piezoelectric material is excited in 31-mode operation, elongation or compression normal to the 1 axis is induced and

hence an electric field normal to the 3 axis is generated.

Impact-based piezoelectric energy harvesting has been widely discussed in the literature to harvest waste kinetic energy from human motions, ammunitions, etc. for powering low-power electronic devices. According to Beeby *et al.* [103], the earliest example of a piezoelectric kinetic energy harvesting system extracted energy from impacts. Umeda *et al.* [104] pioneered the analysis of the energy generated by the impact of a steel ball on a piezoelectric membrane. Initial work explored the feasibility of this approach by dropping a 5.5 g steel ball bearing from 20 mm onto a piezoelectric transducer. Keawboonchuay *et al.* [105] studied high-power impact piezoelectric generator that can be incorporated into ammunitions. Subsequently, impact coupling of a piezoelectric transducer designed for use in human applications has been described by Renaud *et al.* [106]. The authors presented some analysis related to the impact harvester, which comprised of an inertial mass confined within a frame but free to slide along one axis, for human applications and assessed the relevance of such a system for harvesting energy from large-amplitude and low-frequency excitations. Energy is generated when the sliding mass strikes steel/PZT cantilevers located at each end of the frame. Several studies on direct straining of, or impacting on, a piezoelectric element for human applications has also been reported. One of the earliest examples of a shoe-mounted generator incorporated a hydraulic system mounted in the heel and sole of a shoe coupled to cylindrical PZT stacks [107]. The hydraulic system amplifies the force on the piezoelectric stack whilst reducing the stroke. A subsequent device has been developed at the Massachusetts Institution of Technology (MIT) in the 1990s [81] as an insole in a sports training shoe where the bending movement of the sole strains both polyvinylidene fluoride (PVDF) stacks to produce electrical power.

4.1 Impact-Based VEH using Piezoelectric Push-button Igniter

Self-powered pushbutton is an interesting application that utilizes impact-based energy harvesting [27] for powering self-powered remote controller. Back in 1956, Robert Alder designed a self-powered remote control for Zenith televisions called the Space Commander. It featured a set of buttons that struck aluminum rods to produce ultrasonic waves when decoded at the television receiver end change channels appropriately. Joe Paradiso and Mark Feldmeier took this theme further in 2001 by using a piezoelectric element with a resonantly matched transformer and conditioning electronics that, when struck by a button, generate electrical power to run a digital encoder and a radio transmitter [108]. Furthermore, a German company, EnOcean [109], developed some self-powered radio transmitters, energized by a bi-stable piezoelectric cantilever that snaps when pressed, conditioned by a switching voltage regulator. In this impact-based vibration energy harvesting (VEH) research, the proposed piezoelectric pushbutton igniter system, as depicted in Figure.4.2, is designed to be compact, simple, low cost in terms of power density and energy requirements, at the same time, able to harvest sufficient energy from the impulse force generated by human pressing to power the remote controller.

Referring to Figure.4.2, the key components of self-powered wireless transmitter system include a micro-power impact-based piezoelectric generator, an energy storage device, a power processing unit and a radio transmitter. When a small mechanical force is depressed on the piezoelectric pushbutton, the kinetic energy is harvested by the piezoelectric igniter and converted into electrical energy. The electrical energy is temporarily stored in an energy storage device like capacitor or

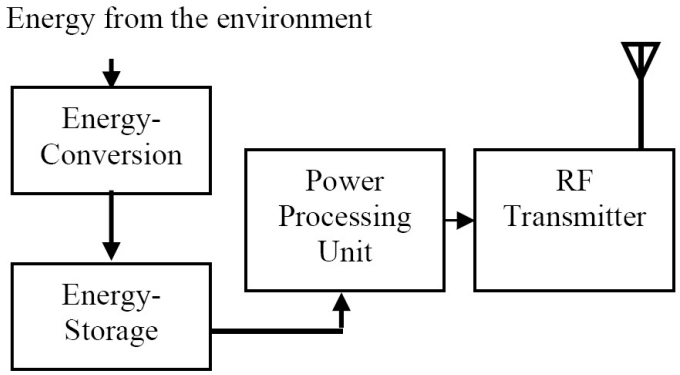

Figure 4.2: Block diagram of a self-powered wireless RF transmitter

battery and then regulated by the power processing unit into regulated output voltage. After which, the regulated DC power provides energy for the radio frequency (RF) transmitter circuit to perform serial transmission via the radio transmitter to communicate with the environmental sensors, control and actuating systems deployed in the smart environment.

4.1.1 Piezoelectric Pushbutton

Piezoelectric pushbuttons shown in Figure.4.3 have been widely used in industries for several purposes. One example is the integration of a pushbutton in an igniter for gas lighting; generates very high voltage at very low mechanical impact force and this high voltage is applied to an air gap to generate an electric arc. Referring to Figure.4.3, the piezoelectric igniter consists of a cylindrical metal base that connects to the negative wire and the other positive wire is internally connected to the piezoelectric element. A depressible ignition button-like structure is found on the top part of the igniter body. When the piezoelectric pushbutton is depressed, a spring inside will be compressed. When the pressure exceeds a threshold, the spring-loaded hammer will be released, which delivers a dynamic mechanical force

to compress the piezoelectric element as illustrated in Figure.4.4. Referring to Figure.4.4, the external force mechanically strains the internal piezoelectric element, these polarized unit cells shift and align in a regular pattern in the crystal lattice. The discrete dipole effects accumulate, developing an electrostatic potential between opposing faces of the element [110].

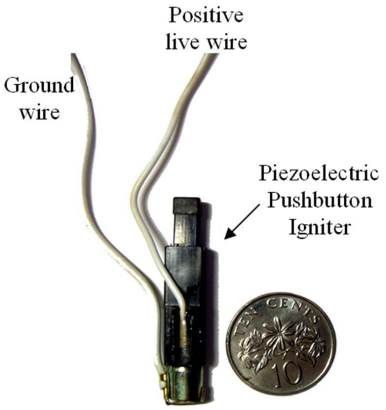

Figure 4.3: Piezoelectric pushbutton igniter and its components

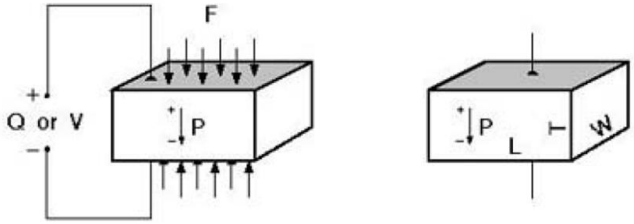

Figure 4.4: Illustration of parallel compression on a piezoelectric element [111]

In the parallel mode of operation [79], the electrical field is generated i.e. axis-3 in this case as shown in Figure.4.4 across the same axis where the external mechanical stress, σ, is applied by the spring-loaded hammer. The short circuit charge displacement Q_3 generated on the surface of the piezoelectric generator of area $A = L * W$ along the axis-3 can be expressed as: -

$$Q_3 = d_{33} F_3 \tag{4.3}$$

where L is the length along the axis-2 and W the width along the axis-1. The applied stress, σ, is a function of the applied mechanical force, F, and the surface area, A. The piezoelectric voltage constant, g, is the quotient of the electric field, E generated and the stress, T applied [79]. Additionally, the electric field is a

function of the open circuit voltage, V_{oc} of the piezoelectric generator divided by its thickness, T, hence the open circuit electric field, E_{oc} generated [111]can be expressed as: -

$$E = \frac{V_{oc,3}}{t} = \frac{g_{33}F_3}{A} \tag{4.4}$$

Knowing that the piezoelectric charge constant, d, [79] is given as,

$$d_{33} = \varepsilon_{33}^{T}\varepsilon_o g_{33} \tag{4.5}$$

where ε_o is the permittivity of free space (8.85 x 10^{-12}) and ε_{33}^{T} is the permittivity of the material at constant stress. It can be demonstrated that the piezoelectric generator can be modelled as a capacitor of value [111],

$$C_3 = \frac{\varepsilon_{33}^{T}\varepsilon_o WL}{t} \tag{4.6}$$

Hence the electrical power P_3 generated by the piezoelectric generator can be calculated as the rate of the energy stored in the capacitor which is given by: -

$$P_3 = \frac{1}{2}C_3V_3^2 f = \frac{1}{2}g_{33}d_{33}F_3^2\frac{t}{A}f \tag{4.7}$$

where f is the frequency of the vibration. The above derived relationship shows that for a given piezoelectric material of fixed area, A, and thickness, T, the generated electrical power, P under the force, F is dependent upon the piezoelectric material charge constant, d, and voltage constant, g. In order to obtain a high performance impact-based piezoelectric generator, the piezoelectric ceramic element with high figures of merit (d and g) has to be selected. On top of that, the volume of the piezoelectric element and the amount of stress exerted on the element are also the key factors to be considered in converting mechanical input to electrical energy.

The next step is to determine the electrical characteristic of the piezoelectric pushbutton igniter so as to facilitate the design of the power processing unit for

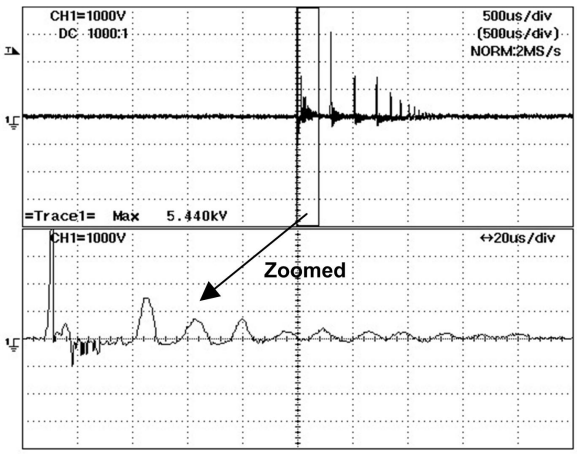

Figure 4.5: Illustration of piezoelectric pushbutton igniter

powering the wireless transmitter load. The dimension of the piezoelectric pushbutton used in this research is 35 mm long and 5 mm in diameter, and has a deflection of 4.5 mm at a maximum force of 15 N. With reference to [108], when an actuation force of 15 N is applied onto the piezoelectric pushbutton, the internal hammer is released to strike the piezoelectric element as shown in Figure.4.5. The excitation force of the hammer generates a pressure wave on the piezoelectric element to output a very high voltage of 6 kV. The high output voltage generated follows closely to an AC signal due to dynamic polarization of the piezoelectric element. Each strike of the hammer creates a mechanical resonance in the piezoelectric element as illustrated in the zoomed version of Figure.4.5 whereby 10 small AC voltage pulses are observed. Subsequently, about nine more iterations of the hammer striking the piezoelectric element are observed in Figure.4.5 and the harvested energy pulses from the piezoelectric pushbutton generator occur for a short time span of around 1.5 ms.

Since each input actuation force provided by the human is not continuous but rather behaves in a pulse like manner, the output voltage will gradually attenuate following the attenuation of the mechanical vibrations in the piezoelectric element.

Hence, it is critical to ensure that the harvested energy is sufficient to transmit a few packets of information through the RF transmitter in a wireless manner. Figure.4.6 shows the 12-bit data encoded by a HT-12E encoder to be sent out by the RF wireless transmitter.

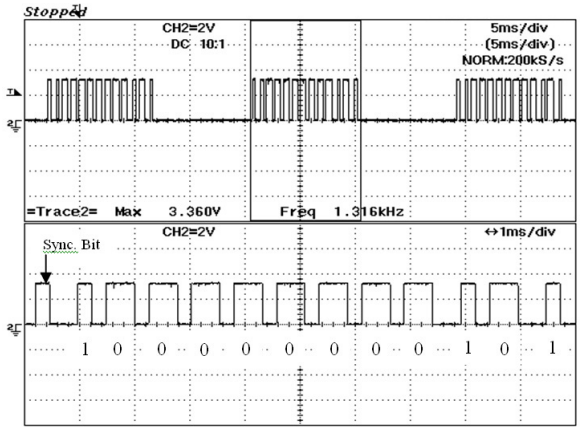

Figure 4.6: Enlarged diagram of the 12-bit data sent out by HT12-E encoder

The encoder first generates a synchronization starting bit following an 8-bit address [1000 0000] and 4-bit data [0101] sequence serially. The address/data pins of the HT-12E encoder has been prefixed to [1000 0000 0101] sequence to be sent to the transmitter. The key for low energy consumption lies in the fact that in many applications, transmitters are idle in most of the time. Therefore the proposed concept of piezoelectric pushbutton power generation fits snugly since transmission will only be required when the pushbutton is being depressed like the case of typical wireless remote controllers. In order to power the RF transmission operation, which takes approximately tens of ms for a complete 12-bit information transmission as shown in Figure.4.6, the electrical energy has to be stored properly in order to ensure complete transmission operation even when the external power source is temporarily unavailable. During this time, the transmission operation is constantly consuming energy until the process is completed where only minimal

amount of energy is needed by the transmitter circuit during the standby mode.

4.1.2 Energy Storage and Power Processing Unit

The power processing unit (PPU) converts the AC output voltage from the piezoelectric generator into a DC source through AC-DC full wave diode bridge rectification. After which, the capacitor connected across the output of the full wave bridge rectifier doubles as a storage device since energy from the piezoelectric generator is finite and occurs for only a short pulse as well as a filter which helps to smoothen the voltage ripples in the rectified DC voltage. Hence by choosing a capacitor with higher capacitance value, the rectified DC voltage can be stepped down to a lower level effectively by the capacitor, at the same time, the capacitor can better smoothen the DC voltage and also provide more energy storage for the harvested energy. Thereafter the capacitor output voltage, the unregulated DC voltage is further regulated by a voltage regulator circuit into regulated DC voltage.

Due to the several design constraints imposed on the impact-based vibration energy harvesting system like miniature size, simple design and low cost requirements, a simple voltage regulator is used. According to Dewan *et al.* [112], if the voltage difference between the input and output of the linear voltage regulator is kept to minimum, then the linear regulator's efficiency is maximized. This is because small amount of voltage is dropped across the voltage regulator hence little energy is wasted. Switched-mode voltage regulator on the other hand suffers from ripples in the output voltage due to its switching rates and has very high quiescent current compared to linear voltage regulator especially in low powered operations where load current are very low in the order of μA. Having to say that, although

switch-mode voltage regulator is relatively more complex, it has some superior advantages over linear regulator as well like high power conversion efficiency, voltage step up and step down capability, etc. After considering both the advantages and disadvantages of applying the two types of voltage regulators for the research work, linear regulator is more suitable for this vibration energy harvesting research work.

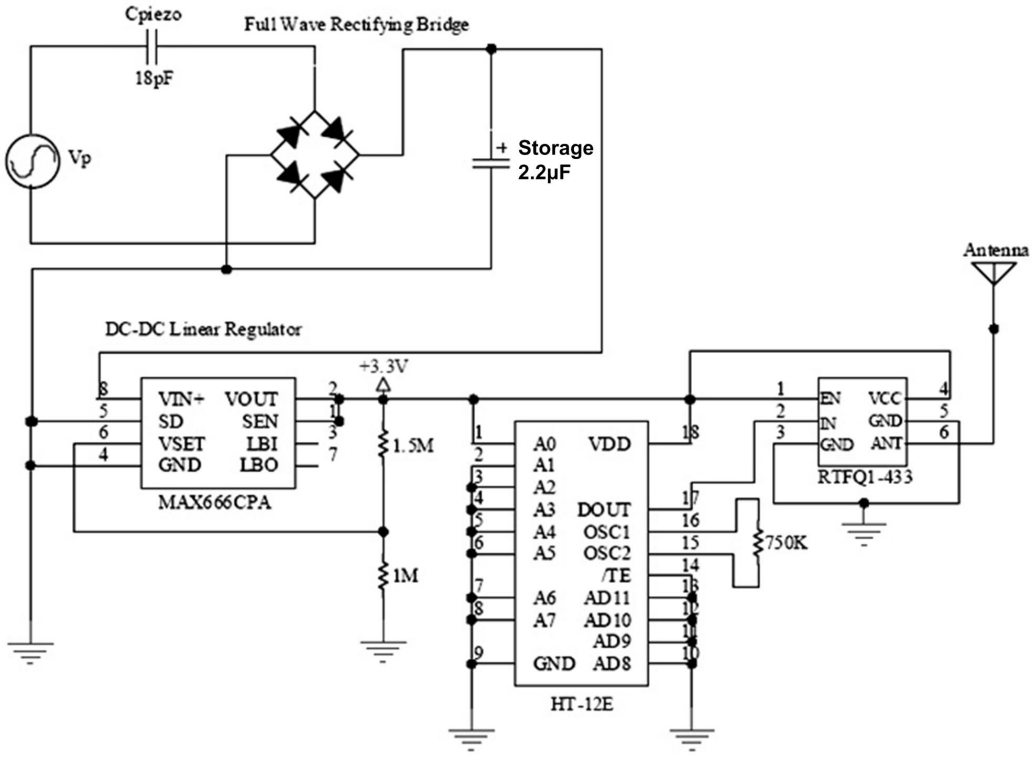

Figure 4.7: Circuit schematic of piezoelectric energy harvesting circuit

The schematic diagram of the proposed piezoelectric energy harvesting system is shown in Figure.4.7. Referring to Figure.4.7, the principle of operation of the piezoelectric energy harvester for powering a self-powered wireless transmitter is illustrated. When the piezoelectric pushbutton is depressed, around 5-7 kV of AC voltage is generated. The generated AC voltage is rectified into DC voltage by the full wave rectifying diode bridge and the DC voltage is stored temporarily in

the 2.2 μF capacitor. The presence of the capacitor is not just to store harvested energy but also helps to clamp down the DC voltage to about 8 V and also to smoothen the DC voltage to constant voltage. The unregulated DC voltage from the capacitor is regulated by the MAX666 linear regulator. The regulated output DC voltage of MAX666 is 3.3 V which is then used to operate the HT-12E encoder to transmit 12-bit address/data information via the radio transmitter. The whole piezoelectric pushbutton transmitter system is mounted on a PCB with a total area size of 25 cm^2 and its assembled prototype [113] is shown in Figure.4.8.

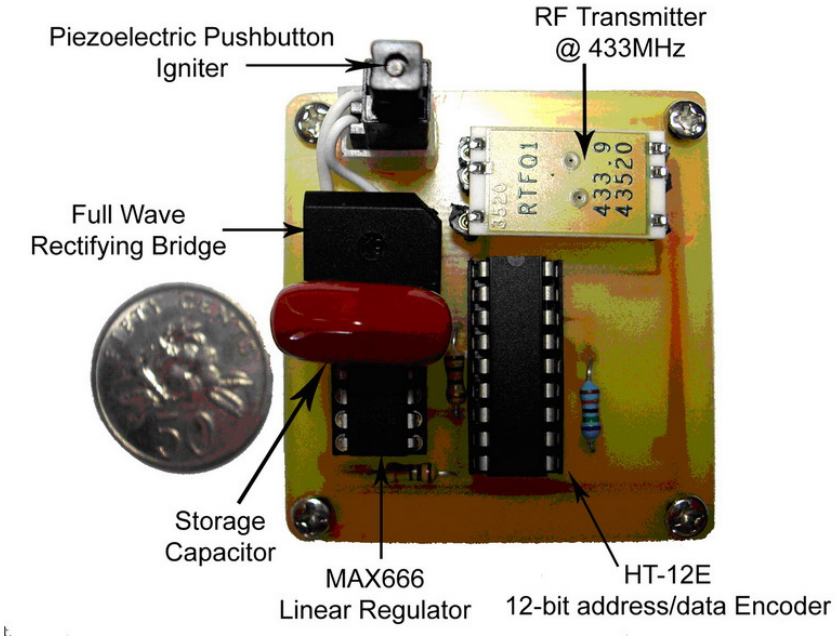

Figure 4.8: Photograph of the assembled prototype showing the key components

Key components of the system are listed in Figure.4.8. They include the piezoelectric pushbutton igniter, full wave rectifying diode bridge, 2.2 μF storage capacitor, MAX666 linear regulator, HT-12E 12-bit address/data encoder and a RF transmitter operating at 433MHz. A Singapore 50 cent coin has been included for relative size comparison. Comparing the sizes between of the piezoelectric push-button transmitter system and the coin as illustrated in Figure.4.8, the requirement

of miniature design for the system has been achieved. In addition, the whole assembly is very light as well, weighing about 12 grams. Taking into account all the components used in the circuit design, the total cost of assembly is less than SGD$35.00, which meets the low manufacturing cost requirement. Hence, the small in size, light in weight and low in cost features of the piezoelectric pushbutton transmitter system make it suitable for many wireless applications like wireless remote controller.

4.1.3 Experimental Results

Several experimental tests were conducted to evaluate the performance of the designed piezoelectric pushbutton igniter system. The open-circuit AC voltage generated by the piezoelectric igniter as seen in Figure.4.9 is fed into a full wave diode bridge rectifier where the AC voltage is converted into DC voltage and then the DC voltage is stored in the capacitor. The DC voltage waveform at the output of the diode bridge rectifier is shown in Figure.4.10. Referring to Figure.4.10, it can be seen that the peak DC voltage is around 600 V. The zoomed view of the output DC voltage of the full wave diode bridge rectifier is shown in the bottom waveform of Figure.4.10.

The sawtooth waveform observed in Figure.4.10 is the rectification of the AC voltage pulses of the piezoelectric pushbutton igniter. After the AC-DC rectification, the unregulated DC voltage is filtered by a parallel connected capacitor of 2.2 μF added to provide some smoothing effects on the DC voltage as well as to store the harvested energy. The waveforms of the capacitor and the output of linear regulator are shown in Figure.4.11 where Channel 1 is the DC voltage across the

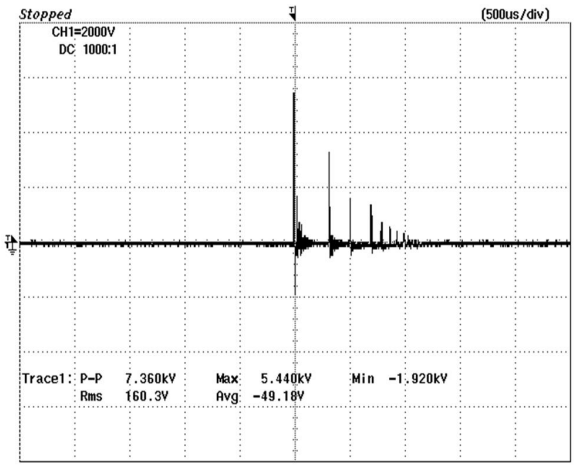

Figure 4.9: Open circuit voltage of piezoelectric pushbutton igniter

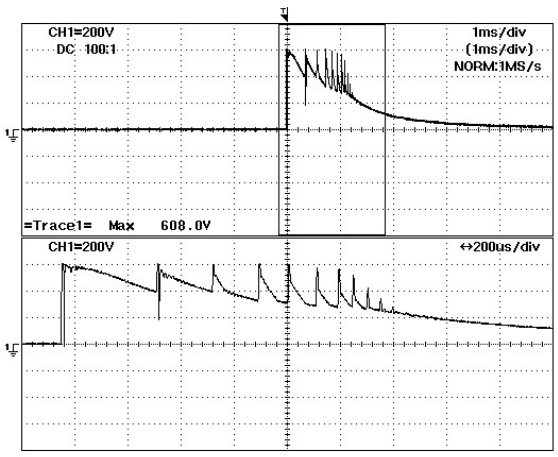

Figure 4.10: Output DC voltage of the full wave diode bridge rectifier

capacitor and Channel 2 is the regulated voltage output from the linear regulator voltage.

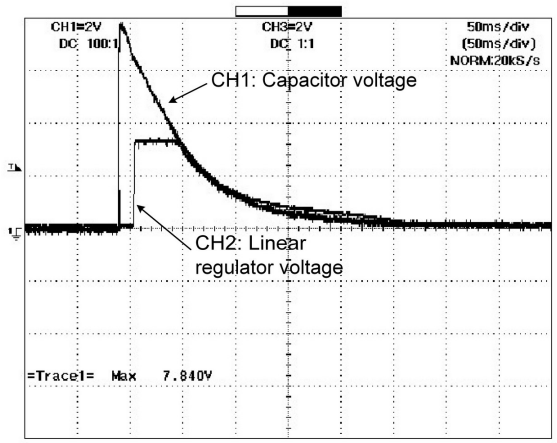

Figure 4.11: Voltage waveforms of capacitor and output of linear regulator

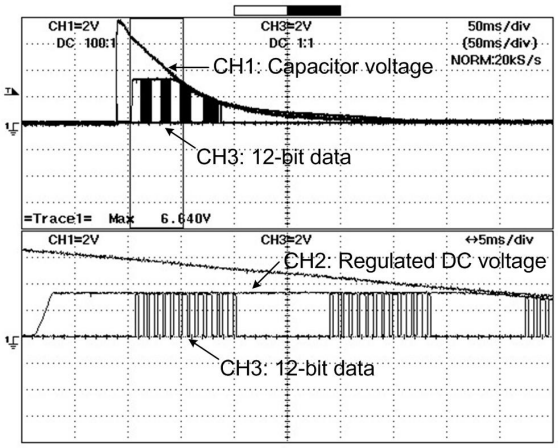

Figure 4.12: Output waveforms of capacitor discharge, 3.3V DC regulation and 12-bit address/data transmission

It can be seen from Figure.4.11 that the maximum voltage accumulated across the capacitor is 7.84 V and the capacitor is discharged completely in 300 ms. Using the formula,

$$E_{cap} = \frac{1}{2} C V_{cap}^2 \tag{4.8}$$

The amount of electrical energy that is harvested after the piezoelectric pushbutton is depressed is 67.61 μJ. As for the linear regulator, the output DC voltage is regulated at 3.3 V and it remains constant for around 50 ms before it starts to drop to zero in respect with the capacitor discharge rate. Hence the challenge is that within the 50 ms of regulated DC 3.3 V, the 12-bit address/data information has to be transmitted from the HT-12E encoder via the radio transmitter. As mentioned before, the harvested energy occurs only for a short pulse through actuation of the piezoelectric pulse generator, therefore in evaluating the performance of our energy harvesting circuit design, the voltage waveforms of the discharging capacitor together with the DC linear regulator and the 12-bit address/data information transmitted need to be examined closely.

The results obtained from the energy harvesting circuit design are illustrated in Figure.4.12. Channel 1 in the figure represents the discharging waveform of the storage capacitor. Channel 2 shows the 3.3 V DC signal output waveform from the linear regulator and Channel 3 represents the 12-bit address/data information transmitted by the HT-12E encoder via the radio transmitter. The energy consumption of the RF unit is calculated based on the operating and standby modes of the RF unit. The total latency time required for 1 digital word transmission is 20 ms where the time during which transmission is active is 10 ms and the time during which transmission is standby is 10 ms. During RF unit operating mode and standby mode, the currents drawn by the transmitter are 8 mA and 0.1 μA respectively. Therefore the peak powers required during transmission and standby are 2.64 mW and 0.33 μW respectively. The total maximum energy required for 1 digital word transmission is then 26.4 μJ. Knowing that the harvested electrical energy is 67.61 μJ and the energy required to transmit 1 digital word is 26.4 μJ, it

can be calculated that around 2.5 digital words can be transmitted with one push of the piezoelectric pushbutton igniter. This is verified in Figure.4.12. As shown in the figure, the regulated DC voltage from the linear regulator is sufficient enough to make at least two complete 12-bit information transmissions at 3.3 V DC. It can therfore be seen that the piezoelectric pushbutton energy harvesting circuit is able to harness enough energy for two complete transmissions at constant 3.3 V DC.

4.1.4 Summary

In this impact-based vibration energy harvesting research, special interest is placed on using a piezoelectric pushbutton igniter as the energy harvester because it is easy and simple to harvest mechanical force energy from human beings. An energy harvesting circuit design for the piezoelectric pushbutton generator is proposed and implemented efficiently for wireless radio frequency (RF) transmitter. This self-powered wireless transmitter is capable of transmitting a 12-bit digital word information using the mechanical force energy of 15 N harvested from depressing the pushbutton which is attached to the energy harvesting circuit. Experimental results show that when the piezoelectric pushbutton is depressed, 67.61 μJ of electrical energy is harvested and it is sufficient to transmit at least 2 complete 12-bit digital word information via the RF transmitter unit, which consumes 26.4 μJ of energy for 1 digital word transmission. As such, this research work has successfully demonstrated the feasibility of completely self-autonomous piezoelectric pushbutton wireless radio frequency (RF) transmitter which optimizes effectiveness in both size, weight and cost.

4.2 Impact-Based VEH using Prestressed Piezoelectric Diaphragm Material

Cabling has always been a hassle for applications like the design of a house's lighting system with the need to draw cables from lamps and bulbs to the switches mounted on the walls of the house. The need for in-wall cabling will often result in high costs for the homeowner. Undesirable re-cabling implications may also arise over time should the cable become faulty over time. Other than that, the conventional method to power onboard wireless communication and power electronic circuitries of the controllers are normally alkaline or rechargeable batteries. One major drawback with these commercially available battery-operated remote controllers is that batteries have limited energy supply. Every time the remote controllers operate, the energy level of the internal battery source depletes, until some time later where the controllers are no longer able to function. As such, regular maintenance of the controllers is required in order not to create any disruption to the user. To address this issue, an impact-based energy harvesting system using piezoelectric igniter has been carried out and discussed in Section 4.1. It is a simple and viable solution to harvest mechanical force energy from human beings to sustain the operation of the remote controller. Whenever someone depresses the pushbutton mechanism, a high impact force coming from the internal hammer strikes onto the piezoelectric material, which consists a stack of piezoelectric ceramic layers, and some electrical energy is generated. However, under this high stress cycling, it is mentioned by Kim *et al.* in [114] that the piezoelectric material stack of the pushbutton igniter may develop interfacial cracking or buckling, thus shortening its lifetime. On top of that, the piezoelectric igniter suffers from two more drawbacks namely: (1) high input force is required to release the hammer of the pushbutton mechanism and (2)

high output voltage and low output current of fews kV and μA are generated due to the piezoelectric stack structure. Because of that, the design and implementation of the power management circuit become complicated.

To overcome these drawbacks associated with the piezoelectric igniter system, another type of impact-based 31-mode piezoelectric generator, operating in mechanical non-resonant, has been explored to harvest impact or impulse forces from human pressing. There are several types of impact-based piezoelectric generators being described in the literature [104]-[106] and there are also some companies like LightningSwitch® [115] that apply this piezoelectricity technology on commercial products like wireless control switch. The self-powered wireless control switch with energy harvesting capability has two significant advantages, namely; (1) flexibility in positioning the power electronic devices at any part of the deployment area that is within the RF communication zone and (2) it eliminates the high manpower and material costs in laying wiring cables between the switches and the devices. A basic set of LightningSwitch®, consisting of one transmitter and one receiver, is shown in Figure.4.13. Inside the transmitter (see Figure.4.14), LightningSwitch® employs a uniquely-assembled cantilever design to mount and excite the commercially available piezoelectric transducer material for harvesting vibrational energy generated from human pressing.

Referring to Figure.4.14, whenever an user depresses onto the commercial available switch equipped with the energy harvesting feature, the harvested impact force is not directly applied to the energy harvesting material i.e. piezoelectric PZT material, instead it is transferred from the human depressing point through an in-built mechanical cantilevered structure to indirectly activate the material. The

Figure 4.13: A basic set of LightningSwitch® with one transmitter (left) & one receiver (right)

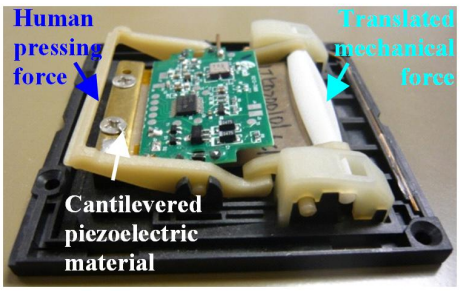

Figure 4.14: Internal design of LightningSwitch® transmitter

custom design mechanical structure translates the applied mechanical force onto the edge of the cantilevered piezoelectric transducer material. As the mechanical force is applied onto the piezoelectric material, it bends until which the mechanical structure releases the piezoelectric material, thus mechanical oscillating vibration is generated. The vibration energy is then converted into electrical energy using the cantilevered piezoelectric material. In the LightningSwitch® design, the whole energy conversion process involves many different stages from human depressing force to harvested electrical energy. During these conversion stages, certain portion of the harvested mechanical energy is lost due to energy efficiency drop at each of the individual stages. On top of that, the uniquely-assembled cantilever design used in LightningSwitch® products, which employs the extra complicated mechanical structure design, would also incurred more cost to develop and manufacture it.

Unlike the commercially available products and research prototypes, which employ complicated energy harvesting mechanism to excite its 31-mode piezoelectric generator, a relatively new concept of energy harvesting from depressing a prestressed piezoelectric diaphragm material has been proposed in this research to generate electrical power for a wireless radio frequency (RF) transmitter and its power management circuit to switch on/off electrical appliances such as lighting,

fans, etc. in a wireless manner. The main objective of this research is to fulfill a self-powered switch with less complicated as well as less costly energy harvesting technique. This is achieved by removing the excessive components of the energy harvesting mechanism.

4.2.1 Description of Prestressed Piezoelectric Diaphragm Material

The impact-based energy harvesting mechanism used in this research is simply a prestressed piezoelectric diaphragm material manufactured by FACE® International Corporation based upon the THUNDER® (THin layer UNimorph ferroelectric DrivER and sensor) technology originally developed by NASA in conjunction with the RAINBOW (Reduced and Internally Biased Oxide Wafer) design effort [116]. The prestressed piezoelectric diaphragm material, as shown in Figure.4.15, is electrically poled in the 31 coupling mode and it is initially curved, arc shaped and rectangular that elongates when a force is applied to the top of the arc. The elongation causes strain in the active material which produces a voltage. The device is simply supported and allows for movement only in the lateral direction.

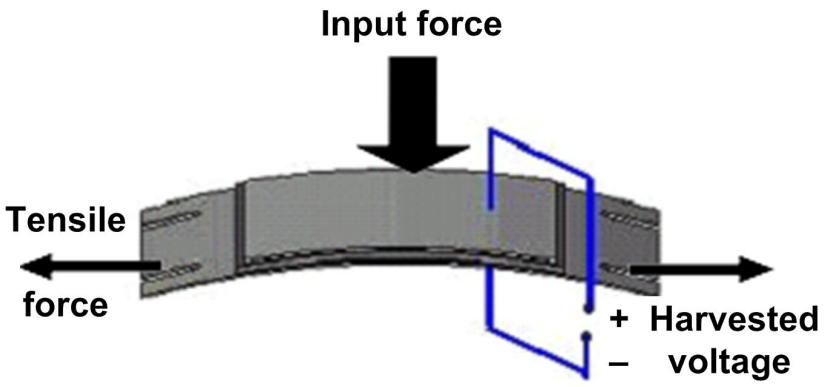

Figure 4.15: A diagram of the prestressed piezoelectric diaphragm material, TH7R

As an input force is applied at the centre of the warped structure doom shaped piezoelectric strip, a resultant tensile force is generated in the piezoelectric material along the 1-axis and voltage is harvested and poled along the 3-axis, as illustrated in Figure.4.15. Unlike the piezoelectric igniter that operates in the parallel compression mode or 33-mode of operation, this transverse configuration maximizes the piezoelectric transducer efficiency in converting mechanical energy to electrical energy in a low force environment. The innovative part of this research is the use of the nature characteristic and construction of the prestressed diaphragm material as an energy harvesting material (its unique characteristic is that when the material is depressed, it is deformed and it generates electrical energy) as well as a switch (its prestressed construction creates a bouncing reaction whenever the material is depressed at the centre).

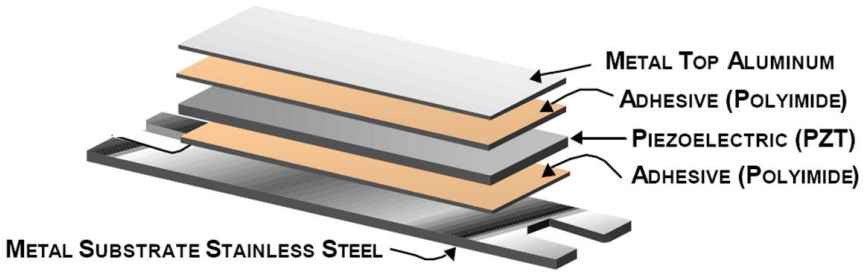

Figure 4.16: Construction of THUNDER® TH7R

Referring to Figure.4.16, the THUNDER® piezoelectric device consists of a piezoelectric ceramic layer, lead zirconate titanate (PZT), and a backing metal layer, held together with a polyimide adhesive as described by Bryant [117]. Several researchers have investigated this type of device and literature is widely available on its actuation and manufacturing details. However, very few researchers have examined its potential as an energy conversion mechanism [118]. As an energy harvesting device, few publications are available: Ramsay *et al.* in [54] demon-

strated the feasibility of utilizing the power generated in a bio-MEMS application; Mossi *et al.* in [119] compared different configurations of the device for actuation and energy harvesting; and Shenck *et al.* in [46] utilized this device for harvesting energy by mounting it on a shoe. Danak *et al.* in [120] also researched ways to optimize the design of an initially curved PZT unimorph power harvester. A mathematical model was created that predicts the power output of the device. From this model, relationships between generated charge and initial dome height, substrate thickness, PZT thickness, and substrate stiffness were established.

Table 4.1: Technical Specifications of TH7R

TH7R Dimensions & Physical Properties		
Weight	g	18
Dimensions	mm	95.3 x 73.4 x 0.53
PZT thickness	mm	0.25
Static Capacitance	nF	166
Maximum Voltage	V	300
Vertical displacement	mm	9.55

THUNDER® transducers are commercially available in a variety of sizes and force displacement characteristics, each with very different electromechanical characteristics. According to Danak *et al.* in [120], the power available from a flat piezoelectric transducer under 31-mode bending excitation is generally proportional to the volume of the material and the vertical displacement induced. Therefore, while constrained by the size, comfort and vertical displacement experienced by the human pressing, the volume of PZT piezoceramic is maximized when selecting the appropriate transducer. Hence, the TH7R piezoelectric device is chosen and its technical specifications are shown in Table.4.1.

4.2.2 Characteristic and Performance of THUNDER® PZT Unimorph

The unique prestressed characteristic and convex shape of the THUNDER® piezoelectric material is used as a natural 'press and release' mechanical switch. The natural 'press and release' process of the piezoelectric material illustrated in Figure.4.17 consists of displacing the transducer from its equilibrium position, reaching maximum displacement (stress), before allowing the transducer to return to its equilibrium position via the opposite direction. The change in direction of displacement, and hence direction of stress, causes a reverse in polarity and an AC voltage is generated at the output of the piezoelectric material. The impact-based energy harvesting process seen in Figure.4.17 can be described as follows: initially, at zero voltage state labelled as '1', the piezoelectric material is not depressed, so it can be seen from Figure.4.18 that no voltage is generated by the piezoelectric material. Upon depressing the material, which is illustrated by the positive voltage state labelled as '2' in Figure.4.17, the material is flattened and the electrical voltage developed across the material can be read from Figure.4.18 to be 110 V. Energy accumulated in the piezoelectric material is available for harvesting by the designed power management circuit and the connected wireless transmitter load. Similarly, upon releasing the material as illustrated by the negative voltage state labelled as '3' in Figure.4.17, the material bounces back to its original prestressed state and a rectified electrical voltage of 110 V is developed across the material and energy is stored in the material for harvesting.

The natural bouncing characteristic and power generation ability of the material has been utilized by this research to simplify the structure of the energy

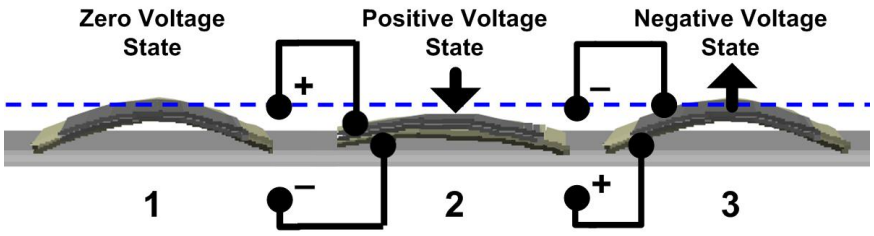

Figure 4.17: Illustration of a depressing cycle of the prestressed piezoelectric diaphragm material

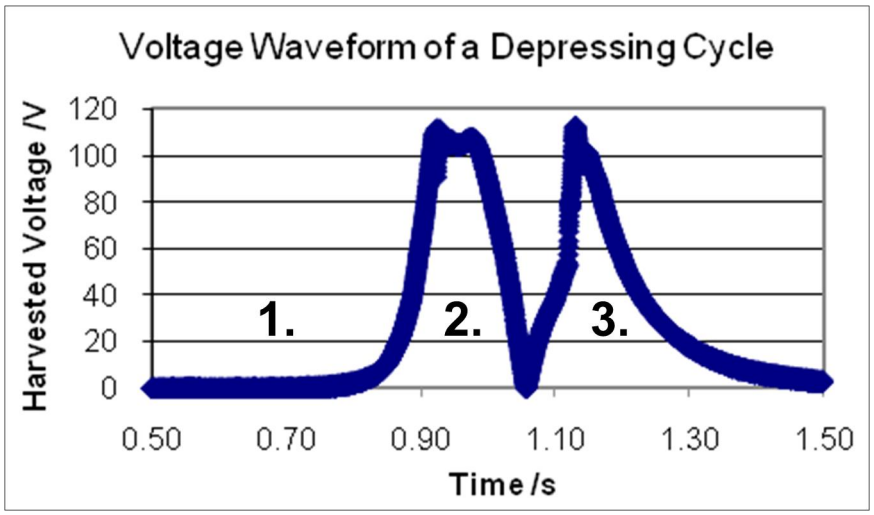

Figure 4.18: Voltage waveform of a depressing cycle of the prestressed piezoelectric diaphragm material

harvesting mechanism. By doing so, it is no longer necessary to have any additional mechanical structure, like the LightningSwitch® case shown in Figure.4.14, to translate the human pressing force into electrical energy. This is a great advantage of this research over the commercial products available in the market. Without the need of an extra energy translation mechanism, this proposed impact-based energy harvesting mechanism using a prestressed piezoelectric diaphragm material reduces the cost of manufacturing the switch to lower than that of the more complicated LightningSwitch® design. In summary, this research work, which uses a batteryless wireless control switch and pre-stressed piezoelectric diaphragm material, is less complicated to implement, is less susceptible to wear and tear due to less mechanical parts and enables more cost savings than similar product

available in market.

To determine the characteristic of the prestressed piezoelectric diaphragm material, different input forces i.e. hard (∼10 N), normal (∼5 N) and light (∼1 N) provided by human's thumb pressing are applied onto the piezoelectric material. For each applied input force, the output AC voltage, V_{ac}, of the piezoelectric material is rectified by a diode bridge into DC voltage, V_{dc}, for various loading resistances, R_{load}, to calculate the equivalent electrical energy being harvested. In this case, the voltage drop across the diode bridge is very low as compared to V_{ac}, hence it is reasonable to neglect the voltage loss in the diodes. Since the voltage generated by the piezoelectric material is time-variant as can be seen in Figure.4.18, the electrical energy harvested, $E_{harvested}$, has to be calculated based on the following equation,

$$E_{harvested} = \int \frac{|V(t)|^2}{R_{load}} dt \tag{4.9}$$

where $V(t)$ is the instantaneous voltage taken from the generated voltage waveform. In order to solve the integral, the oscilloscope readings are extracted into an ACSII file and is analyzed using MS Excel. Figure.4.19 demonstrates the method of estimating $E_{harvested}$ based on the integral of $V(t)$ by using 1^{st} order approximation.

Referring to Figure.4.19, since the oscilloscope reads in discrete measurements, the integral of $V(t)$ is estimated by approximating a straight line joining all the measured points, resulting in many trapeziums of equal width, and summing the areas of each trapezium. Hence, the integral of $V(t)$ can be calculated as

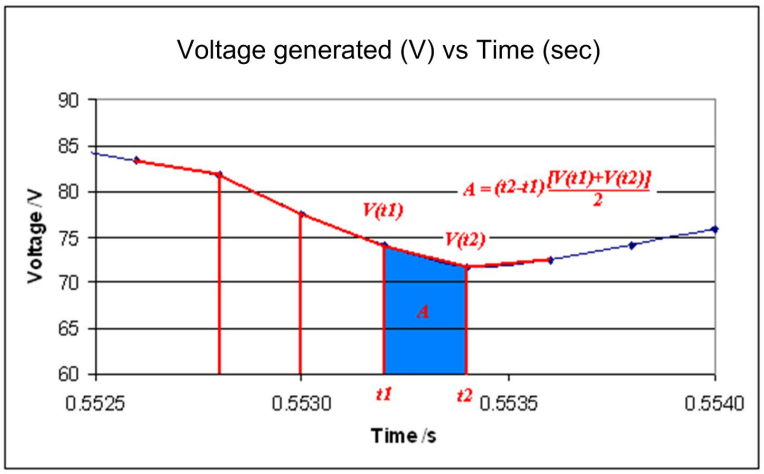

Figure 4.19: Estimating integral using 1st order approximation

follows,

$$\int |V(t)|\, dt = \Sigma \frac{1}{2} (t_{x+1} - t_x) [V(t_{x+1}) + V(t_x)] \tag{4.10}$$

The accuracy of the estimation depends on the sampling frequency. On the average, the sampling frequency of the oscilloscope is 5 kHz, hence each interval is 0.2 ms, which is sufficiently accurate for approximating the integral of $V(t)$, hence the electrical energy harvested, $E_{harvested}$. Based on eqns.4.9 and 4.10, the maximum harvested energy from the piezoelectric material with internal capacitance, C_{piezo}, of 164 nF is tabulated in Table.4.2 for various input forces provided by human's thumb pressing.

Table 4.2: Maximum energy available for harvesting under various input forces

Input force (N)	Peak Voltage (V)	Time span (sec)	Energy harvested (mJ)
Light / 1	73.3	1.112	0.88
Normal / 5	86.7	0.846	1.23
Heavy / 10	112.5	0.721	2.08

Apart from determining the optimal load condition, the optimal capacitance

that maximum energy can be transferred from the piezoelectric material and stored into the external storage capacitor has to be investigated as well. In this experimental test, the load connected to the output terminal of piezoelectric material is a capacitor with capacitance values ranging from 150 nF to 33 uF. The experiments are conducted to investigate the performance of the piezoelectric material in terms of its generated peak voltage and harvested energy for different capacitor values and their experimental results are illustrated in Figures4.20 and 4.21.

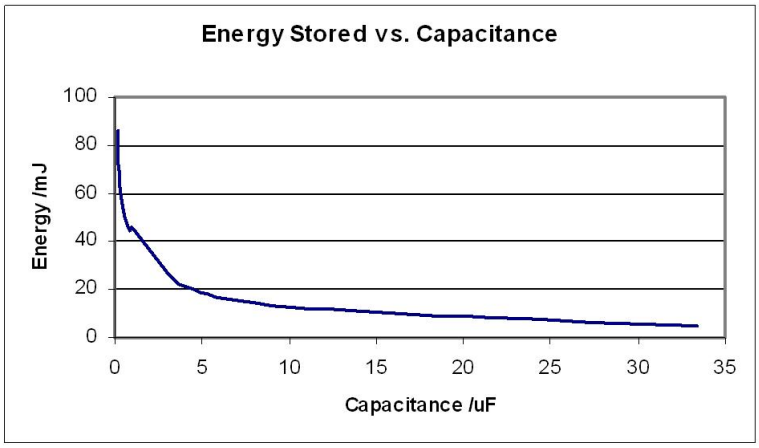

Figure 4.20: Peak output voltage generated at various capacitance values

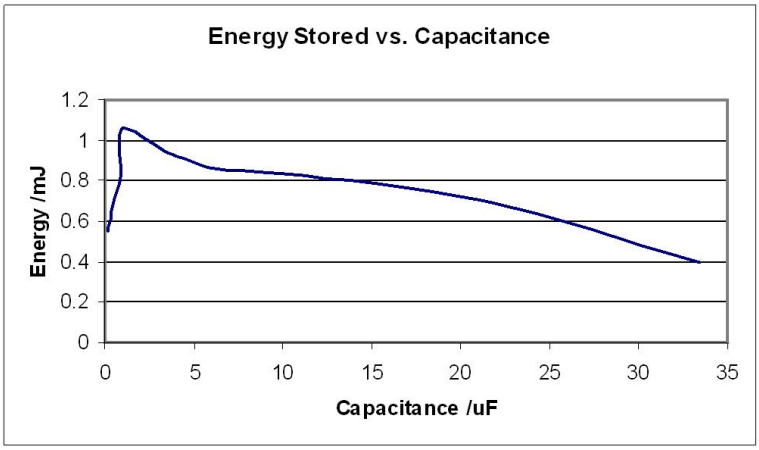

Figure 4.21: Harvested energy for various capacitance values

Referring to Figure.4.20, it can be observed that the peak voltage generated

across the capacitor falls with the capacitance value of the external capacitor. Based on the principle of conservation of charges, $Q = CV$, as the capacitance value increases, while the generated charges remain unchange, the voltage developed across the capacitor decreases. This is the voltage clamping effect of the capacitor. Similarly, with reference to Figure.4.21, it can be seen that the electrical energy stored in the capacitor decreases as the capacitance value increases. According to Shenck in [101], if there is impedance mismatch between the source capacitance of piezoelectric material and the load capacitance, energy loss is bound to occur in the energy transfer process. Hence, transferring energy from a fixed capacitor (source capacitor) to an increasingly large capacitor will result in greater mismatch and higher losses. Among the various capacitance values, 3.3 μF yields the highest stored energy of 1.1 mJ and so does its generated voltage of around 85 V. This high output voltage might cause great challenge to the design of power management circuit. As such, it is necessary to make a compromise between the harvested energy and the generated voltage to meet the energy requirement of the wireless load.

4.2.3 Power Management Circuit

In order to determine the technical specifications of the power management circuit, the power requirements of the RF transmitter has to be determined. The transmitter power requirement is more important as it is the load that the piezoelectric transducer supplies to. Since the input voltage and current varies according to the transmission range and data rate, there is a need to determine the relationship between the input voltage and transmission range, as well as the corresponding input current. An experiment is conducted to investigate on the relationship as shown in Table.4.3.

Table 4.3: Power consumption of RF transmitter load

V_{cc} (V)	I_{cc} (mA)	Min. transmission time (ms)	Range (m)	Power (mW)	Energy (mJ)
1.5	0.280	105	0.0	0.42	0.044
1.6	0.365	95	6.5	0.58	0.055
2.0	0.450	84	-	0.90	0.076
2.4	0.580	73	10.0	1.39	0.102
2.8	0.710	60	-	1.99	0.119
3.6	0.975	57	15.5	3.51	0.200
4.0	1.120	55	-	4.48	0.246
4.4	1.210	53	18.5	5.32	0.282
5.0	1.410	50	20.0	7.05	0.353
6.0	1.740	48	-	10.44	0.501
7.0	2.060	45	24.0	14.42	0.649

Since the wireless control switch is designed for indoor condition, the communication range of the transmitter is set to be around 20 metres, hence the power consumption of the load read from Table.4.3 is 5 V and 1.41 mA and the time duration to transmit three 13-bit signals is 50 msec. Apart from obtaining the power requirement of the RF transmitter load, the duration for a successful transmission is also required so as to determine the total energy required. Thus, the energy stored in the capacitor must be around 0.35 mJ to power the load at more than 5 V for at least 55 ms. From these specifications, with reference back to Figures.4.20 and 4.21, the 10 μF capacitor is the most suitable value as it has a peak voltage of 12 V and is able to store 0.83 mJ of energy when fully charged. The principle of operation of the proposed energy harvesting system is described as follows: whenever the switch is depressed, the mechanical force is applied onto the prestressed piezoelectric material and some of the mechanical energy is converted into electrical energy. The harvested electrical energy from one single pressing is stored in an energy storage device until a certain preset threshold level is reached before the stored energy is released through a power management circuit to power up the radio frequency (RF) transmitter. The RF receiver, which is connected to the electrical appliance, receives the transmitted signal and switches the appliance

ON/OFF by controlling its power supply. The schematic drawing of the proposed impact-based energy harvesting system and its power management circuit is shown in Figure.4.22.

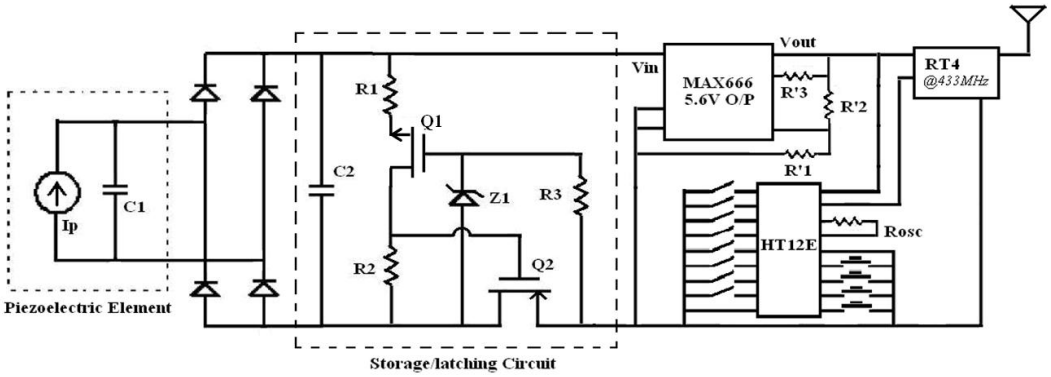

Figure 4.22: Schematic drawing of the proposed impact-based energy harvesting system

Referring to Figure.4.22, the operation of the circuit can be explained. Charges generated by the piezoelectric transducer are first transferred into the capacitor C2, while the regulator and transmitter (load) are isolated by the nMOSFET (nMOS) Q2, which cuts off the load ground from the source ground. The Zener diode Z1 disconnects the pMOSFET (pMOS) Q1 until the voltage across the capacitor C1 exceeds its reverse breakdown voltage plus the threshold voltage. Once Q1 is turned ON, the voltage across R2, adjustable by the potential divider formed by R1 and R2 exceeds the threshold voltage of Q2 and turns ON nMOS Q2. Thus, the source ground and load ground are connected and C2 starts discharging to the regulator and the RF transmitter. R3 acts as the latch to ensure that pMOS Q1, and in turn nMOS Q2, remain ON when the voltage across C2 drops below the Zener diode's breakdown voltage. This is because once the source and load ground are connected, current flows through R3, thus maintaining a voltage at the gate of pMOS Q1 to latch the regulator to the capacitor. The capacitor C2 stops

discharging once the voltage across it falls to an extent that the voltage across R2 is below the threshold voltage of Q2. The duration of the discharge must be at least as long as the time required to transmit 3 successive RF signals, so that the RF receiver can acknowledge the transmission and turn ON/OFF the electronic appliance it is attached to.

4.2.4 Experimental Results

To demonstrate the feasibility of this proposed impact-based energy harvesting system using a prestressed piezoelectric diaphragm material, the hardware prototype of the batteryless wireless control switch has been implemented [121] as shown in Figure.4.23.

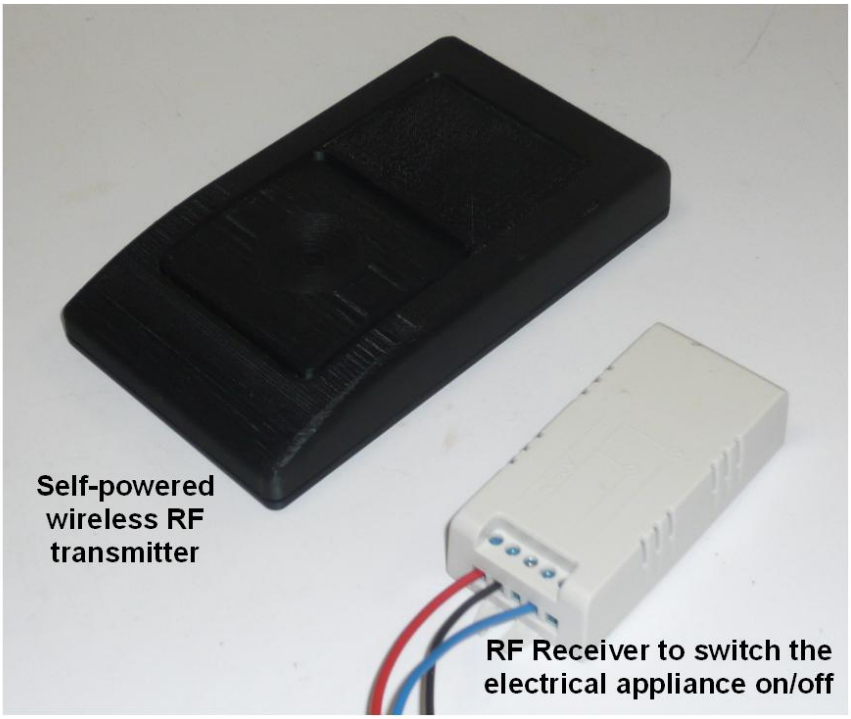

Figure 4.23: Prototype of proposed batteryless wireless control switch using prestressed piezoelectric diaphragm material

The component values of the schematic diagram of the proposed impact-based energy harvesting system shown in Figure.4.22 are determined with the following considerations. The first component to decide is the capacitor C2. As analyzed previously, 10 μF is chosen as it has a peak voltage of ∼12 V, it also has a suitable discharge time constant, and stores sufficient energy for wireless transmission (∼0.836 mJ). A complementary MOSFET (nMOS and pMOS) is chosen as it has a low threshold voltage (1.0 V) and is conveniently placed together as a single component. Therefore, a Zener diode with a reverse breakdown voltage of 11.0 V (12 V - 1 V) is selected. This ensures that the capacitor is charged to at least 12 V before it discharges to the regulator. However, a high breakdown voltage also implies that if the transducer is compressed too lightly and the maximum voltage of the capacitor fails to reach 12 V, no power will be supplied to the transmitter. R1, R2 and R3 should be as large as possible so that minimum current flows through them and resistive losses are minimized. As mentioned above, $R2/(R1+R2) > V_{GS}/V_{reg}$ and with V_{reg} at 5.0 V, R1 = 10 MΩ, R2 = 5 MΩ and R3 = 10 MΩ.

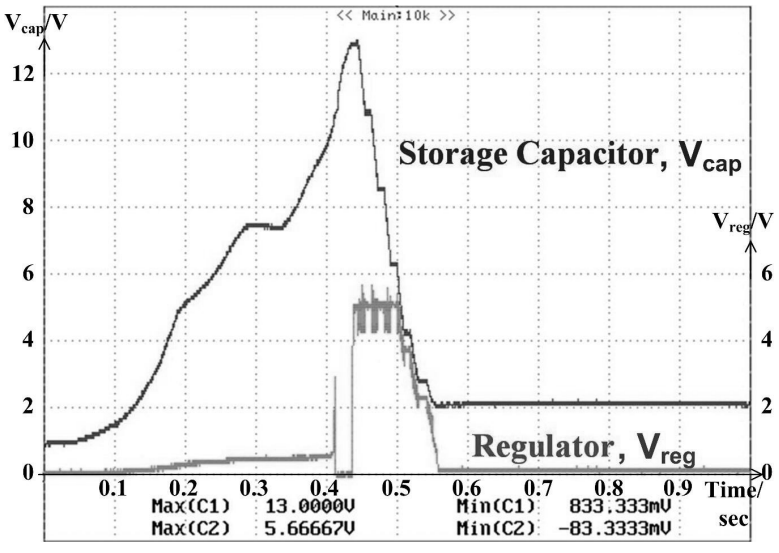

Figure 4.24: Voltage waveforms across storage capacitor (in yellow) and voltage regulator (in green)

Experimental results shown in Figure.4.24 illustrate the outcome of the designed power management circuit. The voltage waveforms in Figure.4.24 are measured across the storage capacitor (in yellow) and the voltage regulator (in green) of the power management circuit. During one depression cycle: (1) As the human's finger presses down onto the material; the harvested energy is stored in the capacitor and not release to the load as the source and load are disconnected. The capacitor's voltage rises to around 7 V. (2) As the human's finger releases the pressing; energy is harvested again and stored in the capacitor. The capacitor's voltage continues to rise to 13 V, which is more than the preset voltage level and energy is released to the load. Once the source and load are connected, energy is supplied to the load as it can be seen in Figure.4.24 where the output voltage of the load has been regulated by the voltage regulator.

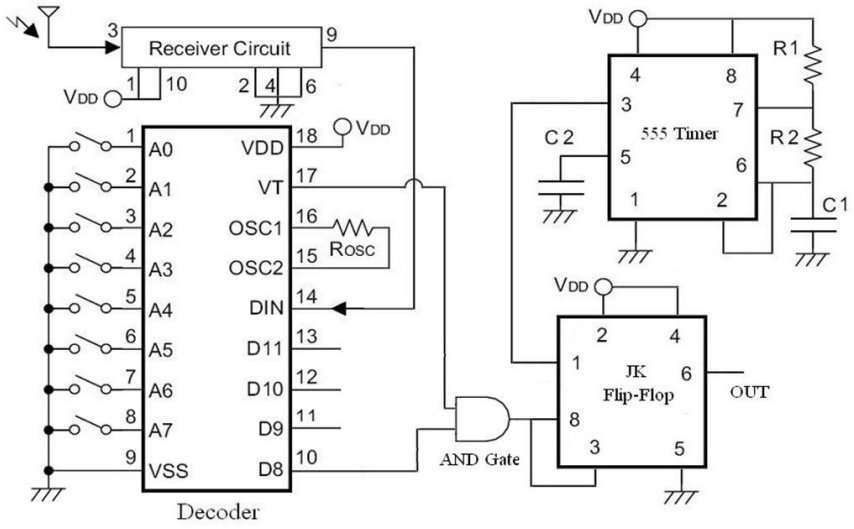

Figure 4.25: Schematic circuit diagram of the RF receiver circuit

The circuit design of the receiver unit is shown in Figure.4.25. The design basically comprises of a RF receiver circuit, a timer and a JK flip-flop. The JK flip-flop is used to implement the simplest toggle design by connecting its inputs

together. A 555 timer is used as a timing device. The decoder has a signal VT, which only turns high for a short duration when a signal from the transmitter is received. It is basically a square pulse with a width of ∼0.11 s. Thus, in order to ensure that the JK flip-flop is triggered during the rising edge of the clock when the signal VT sends in a pulse, the frequency of the timer is set to 9 Hz. For the clock cycle waveform and the square pulse signal VT observed in Figure.4.26, the duty cycle is set to 0.5 so that the rising edge is even the same for each cycle, and the timer components are related to the frequency, f = 1/0.11, by the equation: $(R1+2R2) = 1.44/(f*C1)$. The components chosen are: R1 = 1 KΩ, R2 = 80 KΩ, C1 = 1.0 μF, C2 = 10 nF. Rosc is fixed at 82 KΩ because it the RF transmitter is operating at 433 MHz. The output of the JK flip-flop can be connected to a relay to turn it the connected electrical appliances ON/OFF.

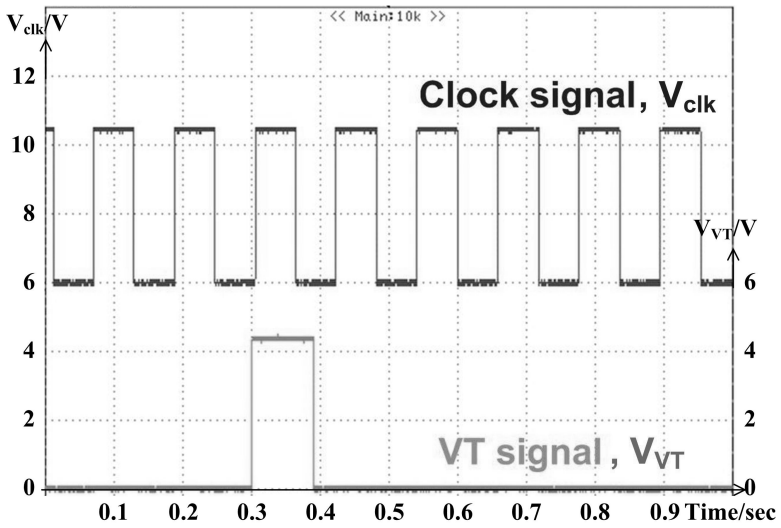

Figure 4.26: Voltage waveforms of VT and clock cycle generated by 555 timer

Referring to Figure.4.25, it can be seen that an AND gate is added to D8 of the decoder. This means that if the transmitter sends a 'high' on the corresponding data bit, it toggles this circuit. Thus, this circuit is considered to be 'tagged' with the 1st data bit and by the same logic, 3 more receivers each tagged to the other

3 respective data bits can be built. By doing so, a single transmitter will be able to control up to 4 different electronic devices. In addition, this design saves the cost of having to buy one switch for every appliance, especially when it comes to appliances that are usually grouped together, such as a set of 4 lights in a single room. This will also eliminates the hassle of having to find the individual switch for a particular appliance, as well as having to allocate space for 4 switches.

4.2.5 Summary

In this impact-based energy harvesting research, a batteryless wireless control switch using a prestressed piezoelectric diaphragm material has been proposed for applications in warehouses, commercial buildings, etc. to cut high wiring costs including material and reduce labour expenses in laying power and signal cables from control switches all the way to the electrical appliances can be reduced tremendously. On top of that, no maintenance cost and effort are required for the wireless control switches. In addition, the self-powered wireless control switch is highly suitable for those appliances located in remote locations that are too difficult or hazardous to access and also suitable for application where multiple electrical appliances have to be controlled simultaneously. Unlike the piezoelectric igniter system, the prestressed piezoelectric diaphragm material is more applicable for low force environment and its output voltage is relatively low. Since the electrical power throughput of the piezoelectric material is less than the power requirement, an energy storage and supply circuit has been implemented. By doing so, 0.83 mJ of energy is first stored in the capacitor until the preset voltage level of 12 V and the stored energy is supplied to the RF transmitter load through a voltage regulator of 64 % efficiency. From the experimental test results obtained, the harvested energy

output from the voltage regulator of 0.53 mJ is sufficient to power one successful wireless transmission for a distance of 20 m.

Chapter 5

Hybrid Energy Harvesting System

Small-scale energy harvesting (EH) is a fast growing research solution for powering wireless sensor node [122]-[125]. However, EH itself has an inherent problem, which is the intermittent nature of the ambient energy source. It is possible that the operational reliability of the sensor node get compromised for prolonged unavailability of the ambient energy source. To augment the reliability of the sensor node, hybrid energy harvesting (HEH) has been proposed in this chapter. For the HEH approach, a second ambient energy source available in the same environment as the first energy source is harvested to supplement the energy supply of the wireless sensor node. By doing so, more energy can be potentially harvested, such that the wireless sensor node are able to perform more power-intensive operations, such as increasing its transmission rate or increased support for external sensors and peripherals.

The concept of HEH has been recently discussed in the literature [35], [126]-[129] as a potential micro-power supply solution to minimize the size of the energy supply as well as to extend the operational lifetime of the wireless sensor node.

Researchers have considered a number of methods to combine different small-scale energy harvesting (EH) sources and these methods can be classified into four main categories.

- *Type 1: HEH using two different EH mechanisms on the same platform*

  Tadesse *et al.* [126] and Khaligh *et al.* [127] present a mechanical combinatory EH device structure of two different EH mechanisms on the same platform to harvest from the same vibration energy source. Due to the drastic difference in matching the internal impedances of the electromagnetic (Ω) and piezoelectric (MΩ) EH mechanisms with the external load resistance, it presents difficulty in combining the output power from the two different mechanisms and hence different power converters are thus required to process the harvested power separately.

- *Type 2: HEH using an electronic switch/multiplexer to switch between EH sources*

  Guilar *et al.* [128] and Lhermet *et al.* [129] proposed to combine EH using an electronic switch/multiplexer to switch between the two energy sources. Whenever both energy sources are present simultaneously, based on the priority given by the power management circuit, typically the higher power source, only one of the two energy sources would then be harvested. Hence it is not possible to harvest energy from both energy sources simultaneously.

- *Type 3: HEH using individual power converter for each EH source*

  According to Park *et al.* [35], each energy source has its own power management circuit, hence it allows energy to be harvested simultaneously from both energy sources. However, as the number of converters increases, this scheme becomes more complex and bulky with higher component counts and the

power loss in the individual converters control circuitry becomes especially significant for micro-power EH sources.

- *Type 4: HEH by directly connecting the energy sources in parallel/series configuration*

  Energy sources are directly connected together and they share a common power management circuit. Comparing with the energy sources selection method used in Type 2, this scheme allows energy to be harvested simultaneously from both energy sources. In addition, only one power electronic based converter with a simple and low power control circuitry is required instead of dedicating each individual energy source with a power converter described in Type 3. However, the challenge of this approach is that there could be impedance mismatch issue among the integrated energy sources.

Out of the above-mentioned four HEH methods, Types 1 and 2 are not adopted for the HEH research of this chapter. The reason is that Type 1 approach does not have the advantage of harvesting from another energy source. As for the Type 2 approach, even though there are two different energy sources available for harvesting, the HEH system does not have the capability to harvest from both the energy sources at one go. Hence, in this chapter, two types of small-scale HEH schemes namely: (1) hybrid of wind and solar energy harvesting scheme for outdoor application and (2) hybrid of indoor ambient light and thermal energy harvesting scheme for indoor application are investigated.

The first HEH system, illustrated in Section 5.2, is designed according to the Type 3 approach of combining the two energy sources together. In this Type 3 approach, each energy harvesting source is required to have its own unique power

management unit to condition the power flow from the energy source to its output load. However, this is not the case for the fourth HEH method which is utilized by the latter HEH system illustrated in Section 5.3. The proposed HEH system requires only one power management unit to condition the combined output power harvested from the solar and thermal energy sources. By avoiding the use of different power management units for multiple energy sources, the number of components used in the HEH system are lessen and the system's form factor, cost and power losses are thus reduced. Before proceeding into the details of the two HEH systems, the solar energy harvesting system common to both HEH systems is first investigated.

5.1 Solar Energy Harvesting System

There exist several mathematical models in the literature [130]-[132] to describe the operation of photovoltaic (PV) cells, from simple to more complex models that account for different reverse saturation currents. In this chapter, an electrical circuit with a single diode (single exponential) is considered as the equivalent photovoltaic model, which consists of n_s number of PV cells in series, as shown in Figure.5.1.

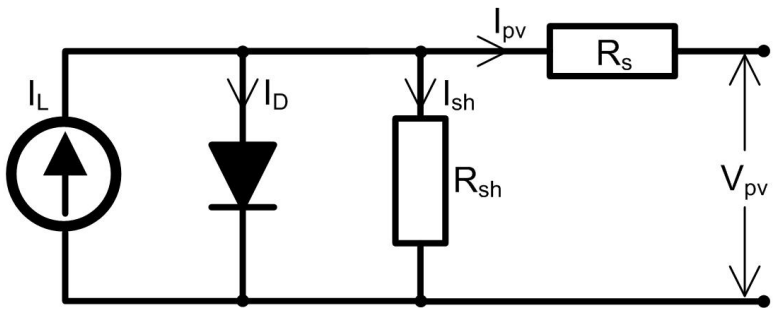

Figure 5.1: Equivalent electrical circuit for a photovoltaic module

Assuming that the shunt resistance, R_{sh}, as shown in Figure.5.1, is infinite, the current-voltage (I-V) characteristic of the photovoltaic (PV) module can be described with a single diode as the four-parameter model given by eqn.5.1 [130],

$$I_{pv} = I_L - I_o \left[exp\left(\frac{V_{pv} + I_{pv} R_s}{n_s V_t} \right) - 1 \right] \tag{5.1}$$

where I_L is the light-generated current (A) and I_o is the dark/reverse saturation current of the p-n diodes (1 x 10^{-9} A). R_s is the series resistance of the PV module and V_t is the junction terminal thermal voltage (V) depending on the cell absolute temperature, which is defined as

$$V_t = \frac{kT_c}{q} \tag{5.2}$$

where T_c is the cell absolute temperature (K), k is the Boltzmanns constant (1.3807 x 10^{-23} J K^{-1}), and q is the charge of the electron (1.6022 x 10^{-19} C). The ultimate goal is to determine whether the power harvested by the PV module is able to power the wireless sensor node, hence it is crucial to estimate the electrical power throughput of the PV module by leveraging on the relationship between the current and voltage of the PV module expressed by eqn.5.1. Referring to eqn.5.1, it can be deduced that the voltage drop across the series resistance, $V_{Rs} = I_{pv} R_s$, is comparably much lower than the output PV voltage, V_{pv}, due to the very low PV current, I_{pv}, of the order of μA flowing through the small series resistance, R_s, of few Ω, thus the $I_{pv} R_s$ term in eqn.5.1 can be neglected during the formulation of the output power of the solar panel, $P_{pv}(V_{pv})$, which is expressed as follows:

$$\begin{aligned} P_{pv}(V_{pv}) &= V_{pv} I_{pv} = V_{pv} I_L - V_{pv} I_o \left[exp\left(\frac{V_{pv}}{n_s V_t} \right) - 1 \right] \\ &\approx V_{pv} I_{sc} - V_{pv} I_o \left[exp\left(\frac{V_{pv}}{n_s kT_c/q} \right) \right] \end{aligned} \tag{5.3}$$

Note that the term $exp(V_{pv}/n_s V_t) \gg 1$ and the light-generating current, $I_L \approx I_{sc}$ [130]. The harvested PV power, $P_{pv}(V_{pv})$, as expressed in eqn.5.3, is formulated as a function of the PV voltage, V_{pv}, and it can be estimated based on the technical characteristics of the PV module and the environmental variables such as light irradiance and ambient temperature. Based on eqns.5.1 and the 5.3, the I-V and P-V curves of a solar panel at a particular solar irradiance and operating temperature are plotted in Figure.5.2.

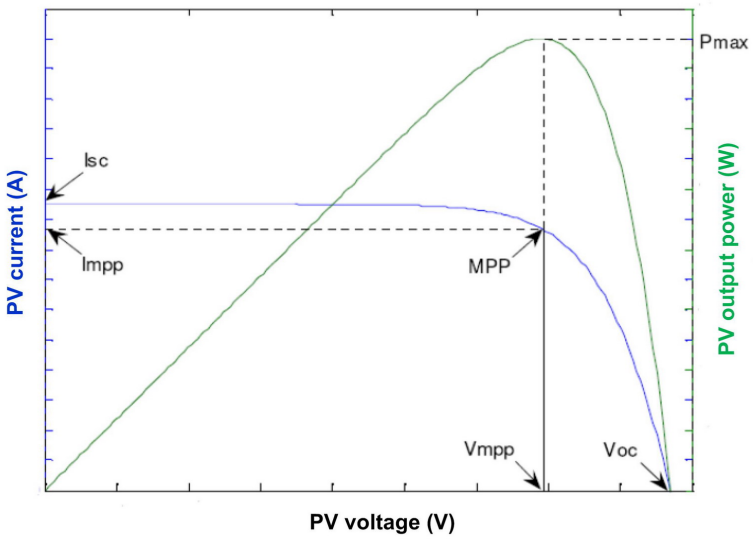

Figure 5.2: Maximum power points on I-V and P-V curves of a photovoltaic module

Referring to Figure.5.2, there exists a particular operating voltage and current of a photovoltaic (PV) module under a certain irradiance and temperature that yields the maximum power throughput, P_{max}. The maximum power point (MPP) of the photovoltaic module seen in Figure.5.2 corresponds to a specific operating voltage, V_{mppt}, and current, I_{mppt}. Various maximum power point tracking (MPPT) techniques have been discussed in the literature [133]-[134] to operate the PV module at its MPPs. These MPPT techniques include perturbation and observation (P&O), incremental conductance (IncCond), constant voltage (CV),

fractional open-circuit voltage (FOCV), etc.

Among the MPPT techniques, P&O method is most commonly used by the majority of researchers in large-scale PV systems [74] and [87]. It is an iterative method of obtaining MPP. It measures the PV characteristics and then perturbs the operating point of the PV module towards the maximum point when $dP_{pv}/dV_{pv} = 0$ is reached. IncCond is an alternative to the P&O method proposed by Hussein *et al.* in [135]. It is based on differentiating the PV power, P_{pv}, with respect to voltage, V_{pv}, and setting the result to zero. The maximum point is reached when the opposite of the instantaneous conductance, $G = I_{pv}/V_{pv}$, is equal to its incremental conductance, dI_{pv}/dV_{pv}. According to Esram *et al.* [133], the P&O and IncCond techniques are the most effective MPPT techniques, harvesting the most amount of energy in comparison. This is because both the MPPT techniques have the ability to track the true MPP of the PV module accurately under any solar irradiance level. However, the implementation of these MPPT techniques becomes complex and expensive. They require the use of energy-hungry devices like microcontroller and some sensory circuitries i.e. voltage and current to compute, process and track the desired output power in every processing iteration. In addition, at steady state, the operating point of the PV module tends to oscillate around the MPP, thus giving rise to the wasting of some amount of harvesting energy [74].

In contrast, the constant voltage (CV) technique is by far the simplest MPPT technique that can be implemented. The operating voltage of the PV module, V_{pv}, is kept near the PV's MPP by matching it to a pre-determined reference voltage. The reference voltage is chosen to be close to the MPPT voltage, V_{mppt}. However, according to Faranda *et al.* [134], the CV technique is mentioned to be

the least effective MPPT technique. This is because the MPPT voltage tends to shift with the varying solar irradiance and temperature. Hence there is a small voltage range where MPP occurs for the different operating conditions. Intuitively, CV technique will only yield approximate MPP. FOCV is an alternative to the CV method, which is also a simple and cheap solution. It is based on the voltage of PV module at the MPP, $V_{mppt} = kV_{oc}$, which is approximately linearly proportional, k, to its open-circuit voltage, V_{oc}. During the solar energy harvesting process, the normal operation of the PV system is interrupted to measure the open-circuit voltage, V_{oc}, of the PV module. This is done by disconnecting the PV module from the electrical load with an additional electronic switching circuitry operating at a certain frequency. Once the open-circuit voltage is obtained, it is multiplied with a predefined factor, k, to get the measured MPPT voltage, V_{mppt}. The drawback with FOCV method is that the interrupted system operation yields power losses when scanning the entire control range.

To overcome this drawback, a pilot PV cell is proposed by Brunelli *et al.* [136]. The pilot cell is supposed to share similar characteristics as the energy harvesting PV module so as to obtain the open-circuit voltage of the PV module through the pilot PV cell. It is thus not necessary to disconnect the PV module from the load in order to obtain the open-circuit voltage. However, the challenge with this approach is that it is difficult to source for a pilot cell that has the exact characteristic as the energy harvesting PV module. In short, each MPPT technique has its own pros and cons. Hence, for small-scale energy harvesting, it is crucial to choose an appropriate MPPT technique so as not to overload the energy harvesting system but at the same time to achieve the MPPT effect.

5.2 Composite Solar, Wind (S+W) Energy Sources

To understand the functionality and performance of the proposed hybrid energy harvesting (HEH) system in a better way, the circuit architecture of a wind-cum-solar-powered wireless sensor node is presented in Figure.5.3. The HEH wireless sensor node consists of the WEH and SEH sub-systems connected together in parallel configuration so that the harvested electrical power from either wind or solar energy source, P_{WEH} or P_{SEH} respectively, can be used to charged the energy storage device.

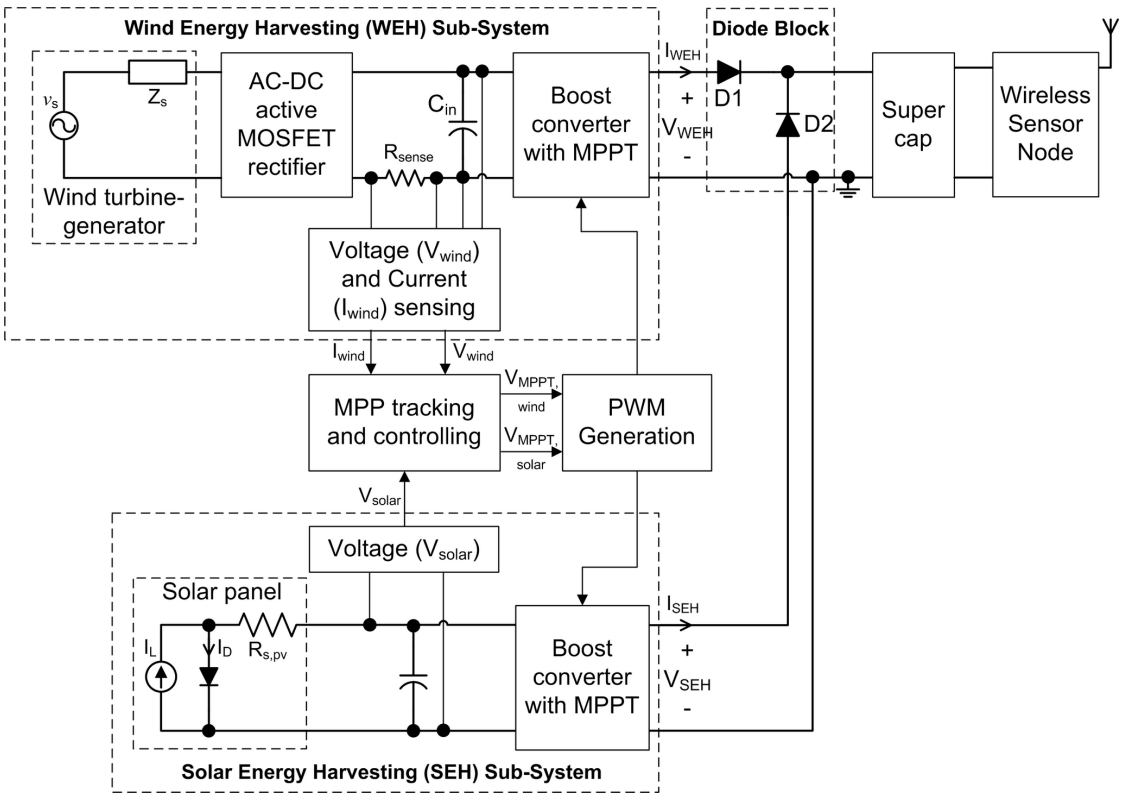

Figure 5.3: Functional block diagram of HEH wireless sensor node

A similar HEH research work was discussed by Park *et al.* [35], AmbiMax, that harvests simultaneously from two energy sources to sustain the operation of

the sensor nodes. Each energy source is allocated to charge its own supercapacitor and the energy stored in these supercapacitors is then transferred to the lithium-ion battery. Although simultaneous charging from two energy sources can be achieved, the drawback is that the physical size of AmbiMax becomes too large, bulky and heavy as compared to a miniaturized wireless sensor node.

In this chapter, the author proposes the use of one energy storage device for simultaneous charging from two energy sources and to develop a miniaturized HEH system for portability and concealment purposes in security applications [138]. Among the commonly available renewable energy sources, solar and wind are the most abundant energy sources in an outdoor environment and so they have been chosen to be utilized in the proposed HEH system. During the night, when the sun has set, wind energy that is mostly available throughout the whole day is present for harvesting. Therefore, it can be seen that the wind and solar energy sources complement one another. They form an ideal pair for a HEH system in powering wireless sensor nodes deployed in outdoor environment. However, the electrical characteristics of the wind and solar energy harvesters are different from one another. When these energy harvesters are combined together directly, it is bound to have the problem of internal impedance mismatch between them. This will result in a very poor power transfer efficiency between the energy harvesting sources and the electrical load.

To overcome this problem, a Type 3 HEH scheme is proposed where each energy source i.e. wind and solar has its own power management circuit for performing maximum power point tracking (MPPT). This ensures simultaneous charging of the energy storage device as well as powering of the wireless sensor node. The

rest of the chapter is organized as follows: Section 5.2.1 describes the electrical power generation from the WEH sub-system. Section 5.2.2 details the design of an efficient power management circuit to perform MPPT for the SEH sub-system. Section 5.2.3 illustrates how the WEH and SEH sub-systems are interfaced together to achieve the proposed HEH system. Following that, the experimental results of the optimized HEH wireless sensor node prototype are depicted in Section 5.2.4, with the summary reported in Section 5.2.5.

5.2.1 Wind Energy Harvesting Sub-System

The proposed hybrid energy harvesting (HEH) wireless sensor node is designed to be deployed in a sample remote sensing area where its environment has four seasons throughout the year viz. spring, autumn, summer and winter. The environmental condition of the deployment area for each season differs from the other season. Take for example, during the summer season, there are lots of sunshine, but only some gentle breeze. Conversely, when it comes to winter time, the duration of sunlight becomes short whereas the wind gets stronger. According to the global solar power map and Canada's wind energy atlas illustrated in [139] and [140] respectively, it is observed that the average sun hour and average wind speed in the northern part of the world like Toronto (Canada) are 1.0 peak sun hour and 4 m/s. The term, peak sun hour, represents the average amount of sun available per day throughout the year. The total amount of solar radiation energy can be expressed in hours of full sunlight per m^2 (1000 W/m^2) or peak sun hours [139]. Over a time span of 12 hours per day, 1 sun hour is worked out to be an average solar irradiance level of around 80 W/m^2. With reference back to the wind energy harvesting (WEH) system designed and developed in Chapter 2, at an average wind speed of 4 m/s,

it can been read from Figure.2.4 that the electrical power harvested by the wind turbine-generator at its maximal point is around 18 mW.

Based on the power analysis of the WEH system described in Section 2.1.3.2, it can be seen that the WEH system with maximum power point tracking (MPPT) scheme is able to harvest 4 times more electrical power than its counterpart WEH system using standard power management circuit. Although the developed WEH system is validated to deliver more electrical power, a larger energy storage device is required to store the higher amount of harvested energy. The stored electrical energy is used to prolong the operational lifetime of the sensor node in times when wind is not available. In this chapter, other than relying on the energy storage device to sustain the sensor node's operations, another energy harvesting system to harvest solar energy in the same environment as the WEH system is explored and then developed for proof of concept. The role of the additional solar energy harvesting (SEH) system is to augment the reliability and performance of the wind-powered wireless sensor node.

5.2.2 Solar Energy Harvesting Sub-System

An overview of the proposed solar energy harvesting (SEH) sub-system is illustrated in Figure.5.3. In the SEH sub-system, a small solar panel with a physical dimension of 60 mm x 60 mm is utilized as an energy harvester to harvest solar energy from the sunlight. The characteristic of the solar panel is first determined experimentally, followed by the design of a suitable power management circuit to ensure maximum power flow from the solar panel to the energy storage device, hence the electrical load i.e. wireless sensor node.

5.2.2.1 Characterization of Solar Panel

The experimental setup for the SEH sub-system is constructed to simulate sunlight in the laboratory with a controlled environment. It is difficult to conduct experiments in an outdoor environment where the natural sunlight tends to fluctuate over time. There is no control over the light intensity of the sunshine. Hence, the light intensity and spectrum of the sunlight is emulated with a light source that closely resembles the frequency spectrum of the sunlight. The light source is a OSRAM 300W Ultra Vitalux light bulb that has the sun-like radiation properties and it is widely used in industrial applications [141] for lighting purposes. To vary the solar irradiance of the emulated light, a variable transformer is used to control the electrical input power to the light bulb. The P-R and P-V curves (See Figures.5.4 and 5.5 respectively) of the solar panel are obtained experimentally through the variation of the solar irradiance level and with different load resistances connected across the solar panel. Throughout the characterization process of the solar panel, the temperature of the solar panel was kept constant by having a constant stream of air blowing across the solar panel.

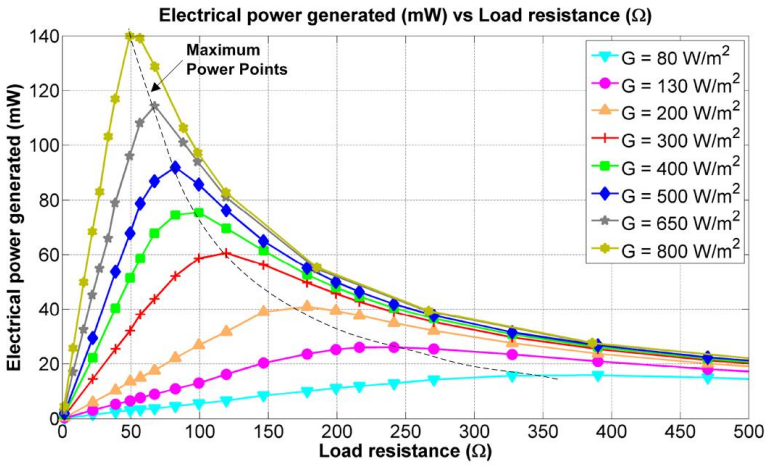

Figure 5.4: Power curves of solar panel over a range of load resistances

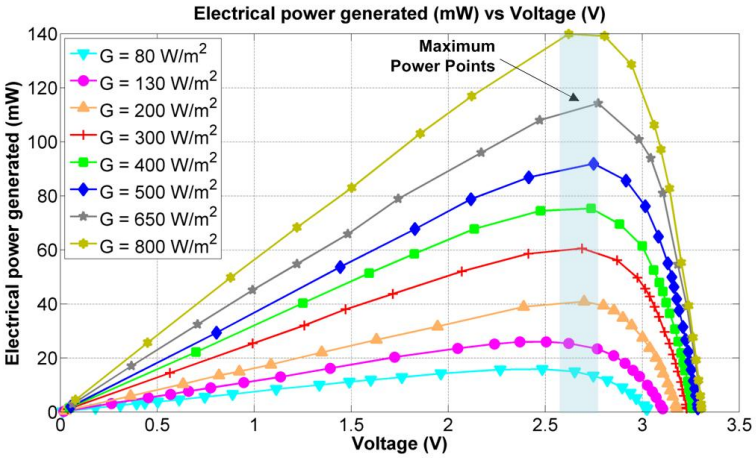

Figure 5.5: Power harvested by solar panel plot against generated voltage for a range of solar irradiance

The P-R curve seen in Figure.5.4 illustrates how the source impedance of the solar panel varies with the changing solar irradiance. As it can be seen, the source impedance of the solar panel decreases from 350 Ω to 50 Ω as the light irradiance level increases from 80 W/m^2 to 800 W/m^2. This is due to the higher output current generated by the solar panel at higher solar irradiance. Comparing between the P-R curves of wind turbine-generator and solar panel given Figure.2.4 and Figure.5.4 respectively, it is clearly seen that their characteristics are totally different. Unlike the wind turbine-generator's characteristic observed in Figure.2.4 where its internal impedance is almost the same for all incoming wind speeds, the internal impedance of the solar panel varies with the changing solar irradiance.

Conversely, it is observed from Figure.5.5 that the MPPT voltage, V_{mppt}, of the solar panel at which the harvested power is maximum is within a small voltage range of 2.55-2.75 V for different solar irradiance. The maximum electrical power that can be harvested from the solar panel across various solar irradiance levels of 80-800 W/m^2 is 16-141 mW. By keeping the operating voltage of the solar panel near to V_{mppt}, maximum electrical power is attainable from the solar

panel. Other than the complex and energy-hungry maximum power point tracking (MPPT) techniques [87] - [89] like perturbation and observation (P&O) method and incremental conductance (IncCond) method, there are several simple and low-power indirect MPPT techniques discussed in Section 5.1 i.e. fractional open-circuit voltage (FOCV), use of additional pilot solar cell and constant voltage (CV) that are suitable for small-scale SEH. However, there are some problems associated with the FOCV and pilot solar cell methods as discussed by Dondi *et al.* in [36]. To overcome the problems, the constant voltage (CV) method is used in the proposed SEH sub-system to achieve MPPT. With reference to Figure.5.5, the reference MPPT voltage, $V_{mppt,ref}$, of the solar panel is set as 2.58 V. At $V_{mppt,ref}$, all the harvested powers of the solar panel are close to its MPPs for a variety of solar irradiance from 80-800 W/m^2.

5.2.2.2 Boost Converter With Constant Voltage Based MPPT

To optimize the solar energy harvesting (SEH) sub-system, a DC-DC boost converter is designed to perform maximum power point tracking (MPPT) based on the chosen constant voltage (CV) scheme. The main functions of the boost converter in the power management circuit of the SEH sub-system (see Figure.5.6) are: (1) to step up the low DC voltage output of the solar panel, V_{solar}, to charge the energy storage device and (2) to perform near maximum power point tracking (MPPT) so that maximum power transfer takes place. Referring to Figure.5.6, there is a voltage sensing circuit, essentially a simple resistive voltage divider, to sense and divide the output voltage of the solar panel into two for the microcontroller to process. The power loss in this voltage divider circuit is very small, of few tens of μW and it is quite insignificant as compared to the harvested power of the order of

mW level. The feedback voltage signal, V_{fb}, obtained from the terminal of the solar panel is compared with the reference voltage signal, $V_{mppt,ref}$, in a microcontroller to perform the closed-loop MPPT control of the boost converter via the PWM generation circuit.

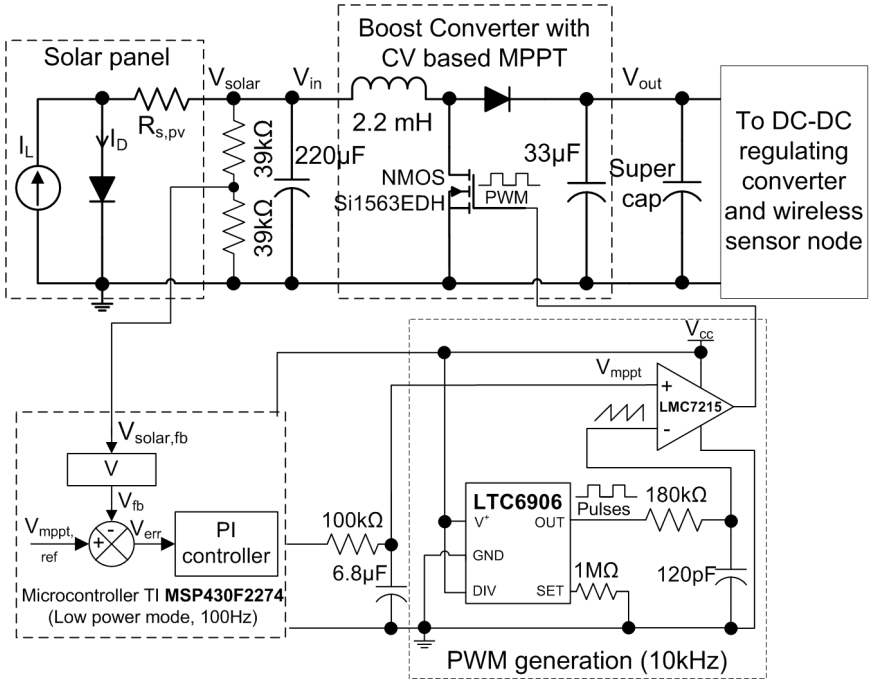

Figure 5.6: Schematic diagram of SEH sub-system

The PWM generation circuit, as seen in Figure.5.6, is used to convert the low frequency PWM control signal, ∼100 Hz, generated from the low-power microcontroller to a much higher switching frequency, 10 kHz, so that smaller filter components can be used in the boost converter to miniaturize the overall SEH sub-system. Depending on the voltage, hence the energy storage level of the supercapacitor, V_{cap} or V_{out}, the output voltage of the solar panel, V_{solar}, is manipulated to transfer maximum power to the supercapacitor by adjusting the duty cycle of the PWM gate signal of the boost converter such that V_{solar} is as close as possible to $V_{mppt,ref}$, the reference MPPT voltage of 2.58 V at which the harvested

power is near its maximum. As the energy level of the supercapacitor increases or decreases, the output voltage of the boost converter, V_{out}, varies with the supercapacitor's voltage. However, at the input voltage of the boost converter, V_{in}, it is fixed to the solar panel's reference MPPT voltage, $V_{mppt,ref}$, of 2.58 V, hence the optimal duty cycle of the boost converter, D_{opt}, that ensures near MPPT takes place for the solar panel is expressed as,

$$D = 1 - \frac{V_{out}}{V_{in}} \tag{5.4}$$

$$D_{opt} = 1 - \frac{V_{cap}}{V_{mppt,ref}} \tag{5.5}$$

To experimentally verify the concept of constant voltage approach to perform maximum power point tracking (MPPT) for small-scale SEH, a set of experiments were conducted. During the experiments, the MPP tracking capability of the designed boost converter circuitry is tested for different solar irradiance and the experimental results are shown in Figure.5.7.

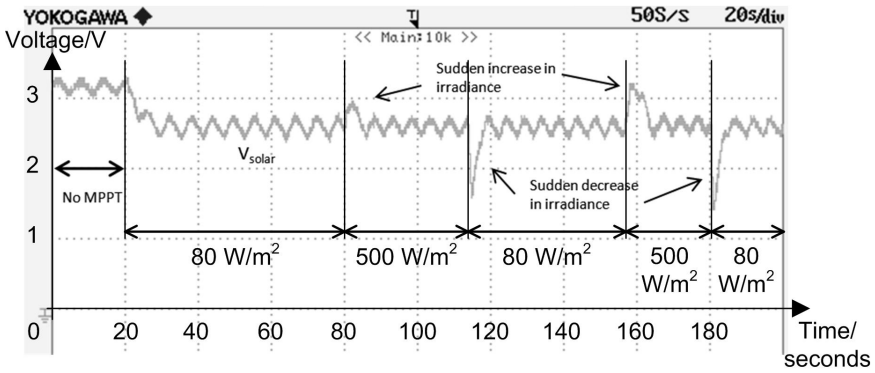

Figure 5.7: Performance of boost converter with CV based MPPT under varying solar irradiance

Initially, for the first 20 seconds, it is observed in Figure.5.7 that the boost converter is not controlled to operate the SEH sub-system at its maximum power

point. After which, the maximum power point (MPP) tracker utilizes the closed-loop PI controller to manipulate the duty cycle of the boost converter according to eqn.5.4, which in turn controls the input voltage of the boost converter towards the optimal reference voltage value of 2.58 V. Once the MPP of the power curve for wind speed of 80 W/m^2 is reached, the closed-loop MPP tracker controls the boost converter to maintain power harvested from the solar panel for all the other MPPs occurring at different solar irradiance. As can be seen in Figure. 5.7, there are several sudden variations of irradiance levels at different intervals. The closed-loop PI feedback control is able to correct the output voltage of the solar panel back to the MPPT voltage of 2.58 V. This shows that the changing operating conditions of the deployed environment is well taken care off by the proposed closed-loop constant voltage (CV) scheme of the designed boost converter.

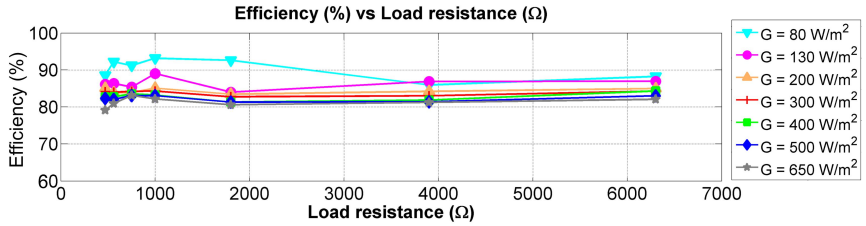

Figure 5.8: Efficiency of MPP tracking boost converter for various solar irradiance

The designed boost converter with CV based MPPT approach has been demonstrated to yield capability in extracting maximum power from the solar panel, but this comes at the expense of additional power losses in the converter. The efficiency of the boost converter, η_{conv}, is determined based on the function of its output load power, P_{load}, over its input DC power, P_{dc}. Taking the target deployment area with average solar irradiance of 80 W/m^2 as an example, the

efficiency of the converter is calculated to be as follows,

$$\begin{aligned} \eta_{conv} &= \frac{P_{out}}{P_{in}} * 100\% = \frac{V_{out}^2/R_{load}}{V_{in}I_{in}} * 100\% \\ &= \frac{3.98V^2/1200\Omega}{2.58V * 5.6mA} * 100\% = 91\% \end{aligned} \tag{5.6}$$

For all other illuminations and resistance loadings, the efficiencies of the boost converter are calculated using eqn.5.6 to be between 80-92 % and the computed results are shown in Figure.5.8. It is observed from Figure.5.8 that the efficiency of the boost converter generally drops as the irradiance level increases. This is due to increasing current output from the solar panel when light irradiance increases. The increased current contributes to ohmic losses, hence causing a lower efficiency level to be attained. Referring to Figure.5.8, it can be seen that even for low solar irradiance condition where the power harvested is small (around 14.4 mW), the boost converter is still able to achieve a reasonably good efficiency of 91 %. This exhibits the ability of the DC-DC boost converter to attain high efficiency in very low power rating condition.

5.2.2.3 Performance of SEH Sub-System

To evaluate the performance of the SEH Sub-System with maximum power point tracking (MPPT) and without MPPT, the electrical load is changed from a pure resistor to an energy storage device i.e. a supercapacitor. Unlike the resistor where its resistance is constant, the impedance of the supercapacitor is always changing in accordance with its energy storage level. During its charging process, the dynamic response of the supercapacitor is of importance to be considered in the design of the boost converter so as to ensure constant maximum power point tracking (MPPT) operation is achieved. Figures.5.9(a) and (b) show two separate experiments being

conducted on the SEH sub-system with MPPT and without MPPT respectively at a solar irradiance of 80 W/m^2.

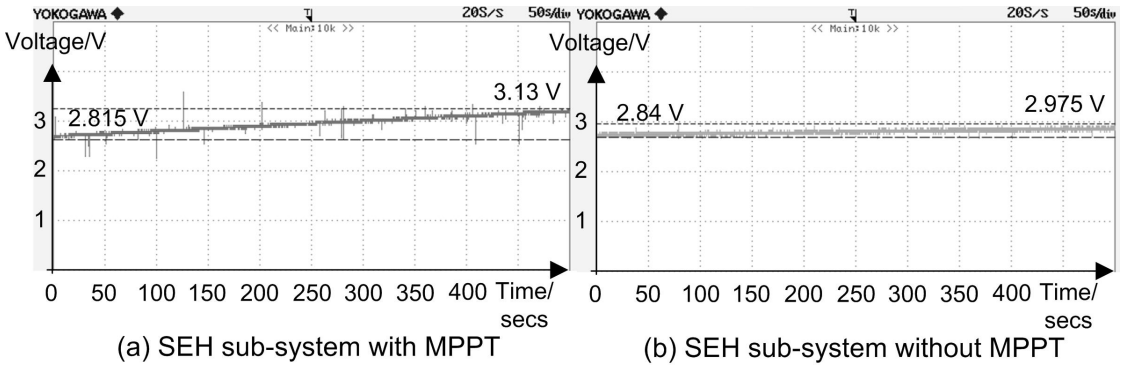

Figure 5.9: Performance of SEH sub-system with MPPT and without MPPT for charging a supercapacitor

Referring to Figure.5.9(a), it is observed that the SEH sub-system with MPPT charges the supercapacitor from a voltage level of 2.815 V to 3.13 V in 500 seconds, while in Figure.5.9(b), the supercapacitor is charged from 2.84 V to 2.975 V in 500 secs without any MPPT control. The total amount of energy stored in the supercapacitor is determined to be around 4.68 J, while its counterpart is only 1.96 J. It is obvious that SEH with MPPT control outperforms its counterpart without MPPT control. The amount of energy that is harvested by the SEH sub-system with MPPT is 2.39 times more than the amount of energy harvested without MPPT. This proves that MPPT is beneficial in maximizing the amount of energy that can be harvested from the solar panel.

5.2.3 Hybrid Solar and Wind Energy Harvesting System

In this hybrid energy harvesting (HEH) research, the outputs of the WEH and SEH sub-systems are connected together in parallel so that more power can be

delivered to the electrical load. The expected outcome of this hybrid topology is the summation of the harvested powers of the WEH and SEH sub-systems as shown in Figure.5.3. The two diodes as shown in Figure.5.3 connect the outputs of the WEH and SEH sub-systems together and they play a critical role in their successful combination. The role of the diode is to prevent any current flow from the output of either boost converter to the other sub-system as shown in Figure.5.10. As such, simultaneous charging from both energy sources is accomplished. In addition, with these blocking diodes, the proposed HEH topology is able to carry out MPPT operations in the WEH and SEH sub-systems. The WEH sub-system uses the resistor emulation (RE) technique while the SEH sub-system uses the constant voltage (CV) technique.

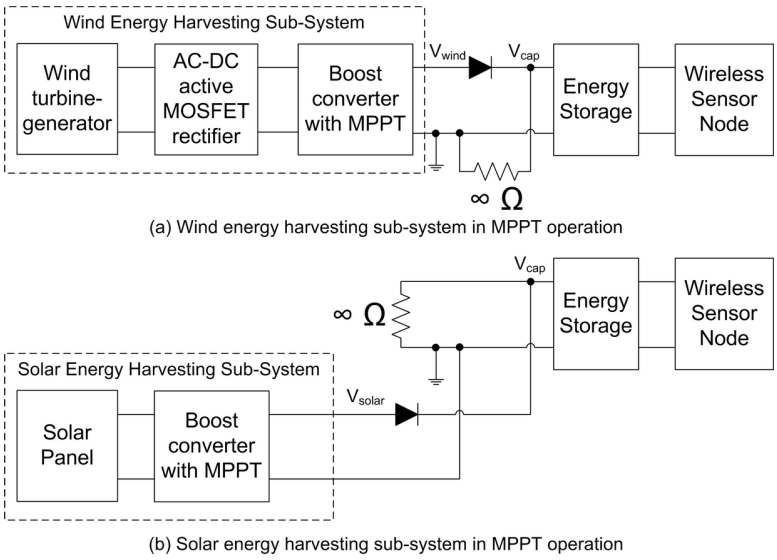

Figure 5.10: Efficiency plot of diode block under varying solar irradiance and resistance loadings

Referring to Figure.5.10(a), when the WEH sub-system is operating in MPPT mode, it is observed that the SEH sub-system appears as an infinite resistance to the WEH sub-system. The effective load experienced by the WEH sub-system is just simply the energy storage device. Similarly, for the SEH sub-system seen

in Figure.5.10(b), it sees the WEH sub-system as an infinite resistance, which is equivalent to an open-circuit condition. This is due to the diode at the output of the SEH sub-system that prevents current flow from the WEH sub-system as well as the energy storage. The constant voltage (CV) MPPT technique used in the SEH sub-system fixes the input voltage of its boost converter, while varying the output voltage of the boost converter according to the voltage, hence the energy storage level of the supercapacitor. The MPPT operation of either the WEH or SEH sub-system is independent of one another.

In this HEH system, the two diodes play an important role in insolating the two sub-systems so that maximum power is transferred from the energy source to the load. However, some amount of power loss would be incurred in the HEH system. The efficiency of the diode block is on average of about 93 % over a range of solar irradiance and resistance loading conditions. This positive outcome is attributed to the very low power loss in the schottky diode where the voltage drop across the schottky diode is low, in the range of 0.15-0.25 V. As such, it is viable to employ the diode block in the designed HEH system to ensure MPPT operations are performed by the WEH and SEH sub-systems. Other than the power loss in the boost converter and the diode block, another investigation is carried out to determine the power loss in the associated control, sensing and PWM generation electronic circuits. The supply voltage of the electronic circuits provided by a voltage regulator is 3 V. Based on the current requirement of each individual component in the sensing and processing circuits, a summary of the total power consumption of the electronic circuits is calculated and tabulated in

As can be seen in Table.5.1, the total power consumed by the associated

Table 5.1: Power consumption of associated control, sensing and PWM generation electronic circuits

Component	Subsystem	Qty	Current / µA	Power/ µW
Comparator	WEH	3	7*3 = 21	63
2 Op-Amps	WEH	1	90	270
Comparator	SEH	1	7	21
Voltage Divider	SEH	-	-	85
Oscillator	Both	1	12	36
Wireless Sensor Node/µC	Both	1	220	660

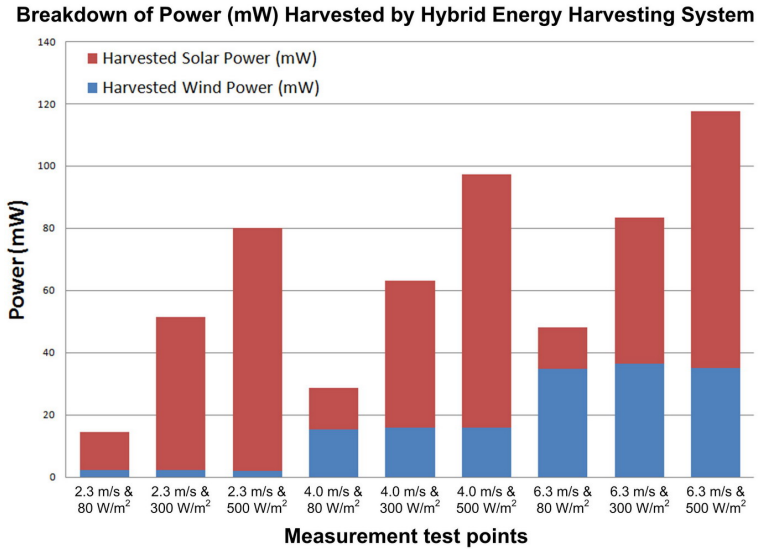

Figure 5.11: Power harvested by the hybrid wind and solar energy harvesting system

control, sensing and PWM generation electronic circuits of the WEH and SEH subsystems is calculated to be 1.135 mW. As compared to the near maximum power harvested by the optimized HEH system seen in Figure.5.11, which ranges from few tens to hundreds of mW, the power consumption of the designed electronic circuits is very low and insignificant. Taking the target deployment area with average wind speed of 4 m/s and average solar irradiance level of 80 W/m^2 as an example, it can be seen from Figure.5.11 that the total power harvested by the HEH system is 34 mW. The power loss of 1.135 mW is only a small fraction, around 5 %, of the

harvested power. Even for very low wind speed of 2.3 m/s and low solar irradiance of 80 W/m^2, the harvested power of 17 mW is still more than enough to sustain the operation of the wireless sensor node.

5.2.4 Experimental Results

The proposed concept of a self-powered hybrid energy harvesting (HEH) wireless sensor node using efficient power management circuit, as illustrated in Figure.5.12, has been implemented into hardware prototype to be tested in the laboratory environment. A photograph of the developed HEH wireless sensor node is depicted in Figure.5.13. Several tests are conducted during the experiments to validate the performance of the optimized HEH system using constant voltage (CV) based maximum power point tracking (MPPT) scheme in sustaining the operation of the wireless sensor node.

5.2.4.1 Performance of the HEH System

The experimental tests are conducted in accordance with the winter condition of the deployment ground illustrated in Section.5.2.1 where the average wind speed and average solar irradiance level are given as 4 m/s and 80 W/m^2 respectively. The HEH system is designed to sustain the wireless sensor node to transmit the sensed data i.e. temperature and wind speed in every second. A 1.5 F, 5.5 V supercapacitor is used to stored the harvested energy from the HEH system. Several experimental tests were conducted on the hardware prototype of the HEH wireless sensor. The experimental results as shown in Figure.5.14 are used to differentiate

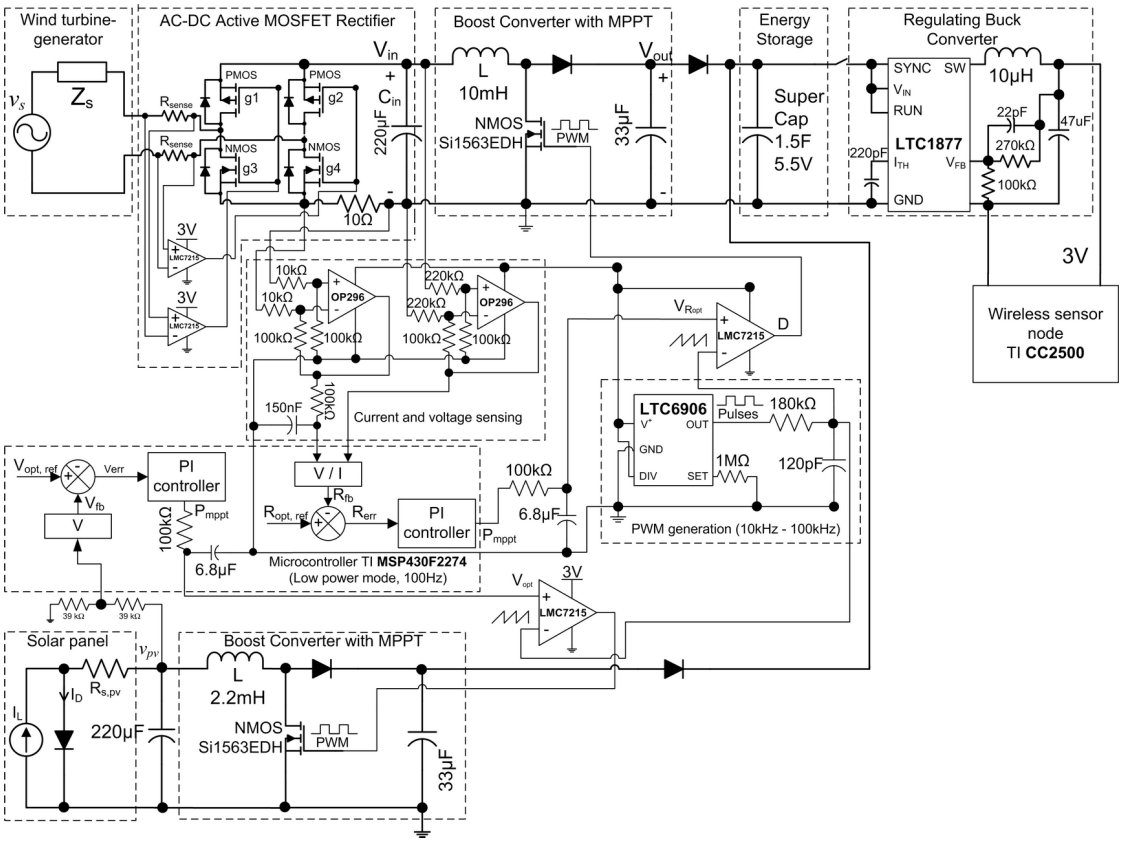

Figure 5.12: Schematic diagram of the wind-powered wireless sensor node augmented with SEH sub-system

the performance of the WEH and SEH sub-systems and their maximum power point tracking (MPPT) schemes in powering the electrical load consisting of a supercapacitor, sensing and control circuit and wireless sensor node.

In region A of Figure.5.14, the electrical load is at first powered with SEH sub-system with constant voltage based MPPT scheme. It can be seen from Figure.5.14 that the output voltage of solar panel, V_{solar}, is fixed at its MPPT reference voltage, $V_{mppt,ref}$, of 2.58 V. This tracking profile verifies that the SEH sub-system is operating at near its MPP. During this time duration of 90 seconds, the 1.5 F supercapacitor's voltage, V_{cap}, is charged from 3.1 V to 3.35 V and around 13 mW of electrical power is harvested by the SEH sub-system at an average solar

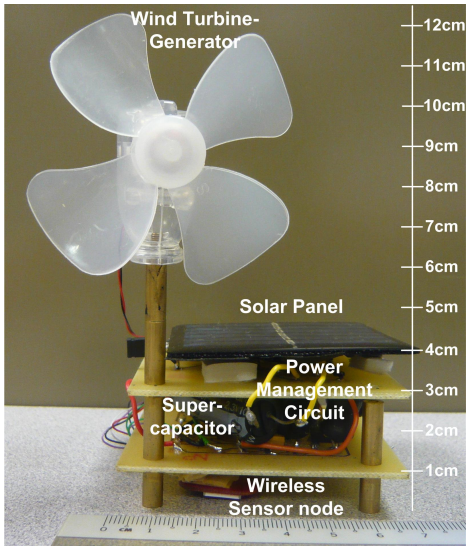

Figure 5.13: Hardware prototype of hybrid energy harvesting wireless sensor node

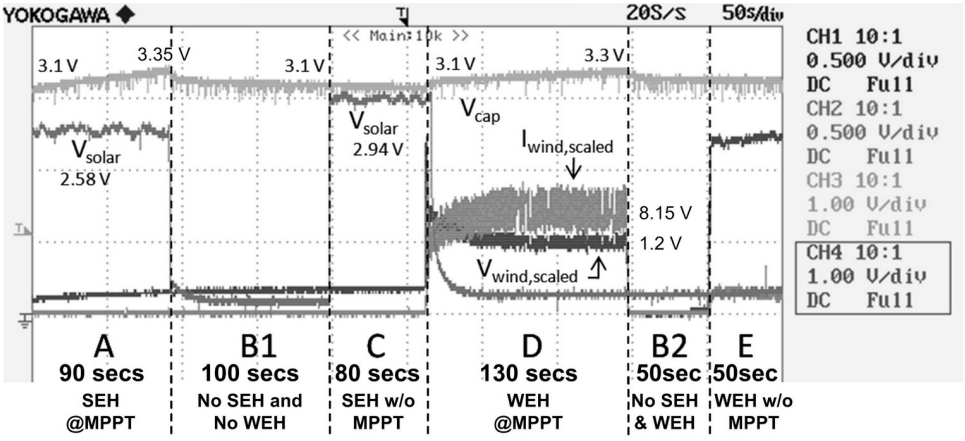

Figure 5.14: Operation of sensor node under various powering schemes

irradiance level of 80 W/m^2. However, in region B1 of Figure.5.14, when the SEH sub-system is disconnected from the load, the output voltage of the supercapacitor, V_{cap}, falls back to 3.1 V in 100 seconds. In region C, V_{cap} continues to decrease at a slower rate. This is because solar energy is again harvested but not at the MPP. The output voltage of the solar panel, V_{solar}, is seen in Figure.5.14 as 2.94 V, which is higher than the MPPT voltage reference of 2.58 V. Without MPPT control for the SEH sub-system, the harvested solar energy is not able to sustain the entire unit.

In region D of Figure.5.14, the WEH sub-system with resistor emulation based MPPT scheme is employed. It is observed from Figure.5.14 that the output voltage of the supercapacitor, V_{cap}, increases from 3.1 V to 3.35 V in 130 seconds. Referring to Figure.5.14, the DC voltage of the wind turbine-generator, $V_{wind,scaled}$ (scaled DC voltage of wind turbine-generator - multiply experimental value by 2.2 to get actual voltage, is 1.2 V while its current, $I_{wind,scaled}$ (scaled voltage equivalent of DC current of wind turbine-generator - multiply experimental value by 0.01 to get actual current in Amperes), is 8.15 mA. Hence, the calculated resistance of $R_{em} = \frac{1.2V}{8.15mA} = 147\Omega$ is equivalent to the emulated resistance of 150 Ω. This equivalence shows that the WEH sub-system is operating at near its MPP and it is able to harvest around 9.5 mW of electrical power at an average wind speed of 4 m/s. However, in region B2 of Figure.5.14, when the WEH sub-system is disconnected from the load, the output voltage of the supercapacitor, V_{cap}, falls back to 3.1 V in 50 seconds. In region E, it is observed that the supercapacitor's voltage continues to decrease even though wind energy is being harvested again but not at MPPT. The reason is that the voltage and current at the input of the boost converter of the WEH sub-system without MPPT is no longer controlled, resulting in a much lower amount of power harvested. As such, maximum power point tracking (MPPT) is important for optimal and effective energy harvesting performance of the WEH and SEH sub-systems.

Another set of experiments were conducted to evaluate the performance of the HEH system in comparison with the WEH and SEH sub-systems individually. The outcome of the performance comparison between single-source based energy harvesting system and multiple-source based energy harvesting system are illustrated in Figure.5.15.

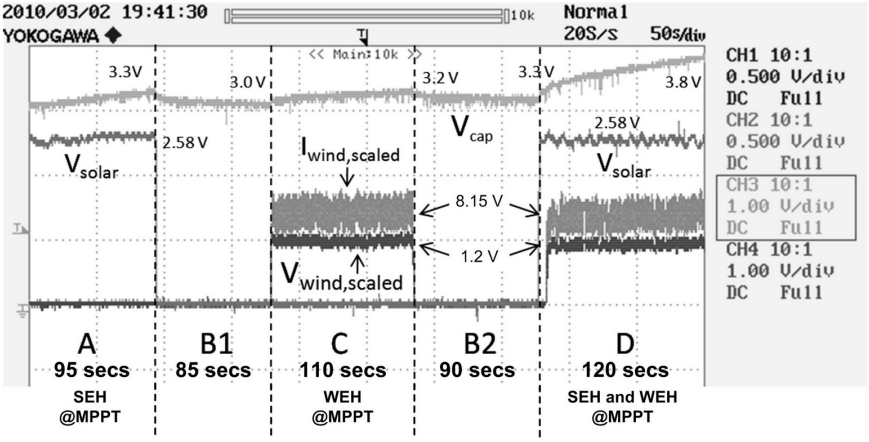

Figure 5.15: Comparison between single ambient energy source harvesting and hybrid energy harvesting

Referring to Figure.5.15, it can be observed from regions A and C that the single-source energy harvesting system i.e. SEH and WEH, operating in MPPT mode, are able to charge the 1.5 F supercapacitor as well as power their associated sensing and control circuit and wireless sensor node. The electrical power harvested by the SEH and WEH sub-systems are computed to be 13 mW and 9.5 mW respectively. In region D of Figure.5.15, it can be seen that the HEH system is harvesting simultaneously from both the solar and wind energy sources and so the supercapacitor's voltage increases at a much faster rate, from 3.3 V to 3.8 V in about 120 secs. Based on the net energy accumulated in the supercapcitor, the electrical power harvested by the HEH system, operating in MPPT mode, to charge the supercapacitor is calculated to be around 22.2 mW. This calculated output power of the HEH system is almost equivalent to the summation of the electrical power output from the SEH and WEH sub-systems, i.e. 12.65 mW and 9.85 mW respectively, of 22.5 mW. It is clearly demonstrated that hybrid energy harvesting has tangible benefits over single renewable ambient source energy harvesting. The supercapacitor charges much faster compared to single ambient source energy harvesting because of simultaneous charging from both solar and wind energy. As a

result, more energy is harvested in a shorter span of time, allowing duty cycling operations of the wireless sensor node to increase.

5.2.4.2 Power Conversion Efficiency of HEH System

The hybrid energy harvesting (HEH) system consists of two main energy harvesting sub-systems, namely the wind energy harvesting (WEH) and solar energy harvesting (SEH) sub-systems. In each sub-system, there are stages of efficiency loss and should be examined in greater detail to determine the amount of power lost per stage, and thus determine the performance of each stage. A line diagram to illustrate the input and output power available for each stage of both sub-system is provided in Figure. 5.16. It is intended to give a clearer picture on understanding how power is distributed at each power conversion stage.

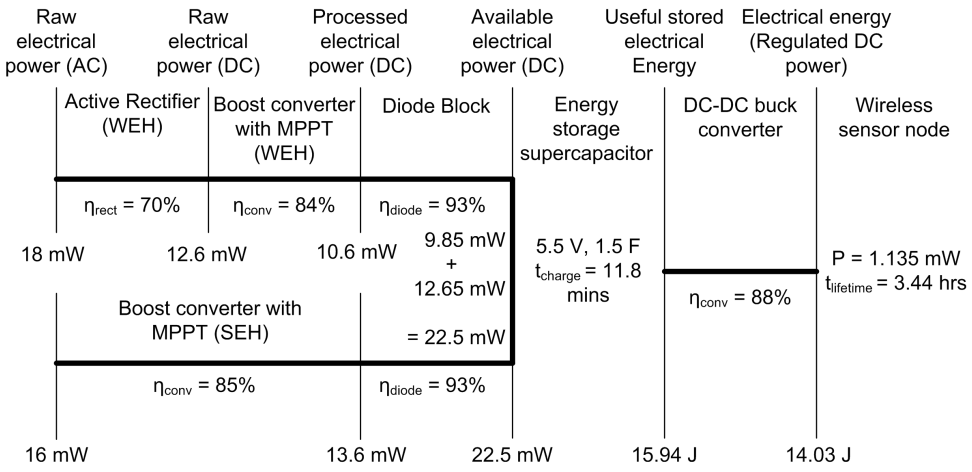

Figure 5.16: Line diagram of power distributed in the hybrid energy harvesting system

Referring to Figure.5.16, the line diagram of the WEH sub-system starts from the input with a wind speed of 4 m/s where 18 mW of raw electrical power (AC) is generated at the output of the wind turbine generator. Using the designed power

management circuit which includes an active rectifier and a boost converter with MPPT, the harvested AC power of 18 mW is converted into electrical DC power of 10.6 mW. In similar way, the SEH sub-system harvests around 13.6 mW of electrical DC power from an input of 16 mW of raw electrical power after the power loss in the boost converter. Comparing with the WEH sub-system, the SEH sub-system suffers comparatively lesser in efficiency loss as it has only one conversion stage. The effective power harvested from both sub-systems is input into the diode block with a high efficiency of 93 % and the combined output power is calculated to be 22.5 mW.

Since the supply voltage of the associated control, sensing and PWM generation electronic circuits is 3 V, the maximum amount of energy stored in the 1.5 F supercapacitor, starting from 3 V to 5.5 V is 15.94 J. To fully charge the supercapacitor, the required charging time, t_{charge}, is computed to be 11.8 mins when 22.5 mW of electrical power is supplied. A DC-DC buck converter with efficiency of 88 % is used to regulate the supply voltage at 3 V. This amount to 14.03 J of useful electrical energy stored in the supercapacitor. Referring to Figure.5.16, it is illustrated that the HEH system with its fully charged supercapacitor is able to sustain the operation of the wireless sensor node for 3.44 hrs. The line diagram seen in Figure.5.16 clearly illustrates that the amount of power harvested, 22.5 mW, by the hybrid energy harvesting system is nearly twice that of the individual WEH or SEH sub-system. Hence, the operational lifetime of the sensor node powered by the HEH system with MPPT scheme is twice of the sensor node powered solely by either the SEH or WEH sub-system, hence making the HEH system with MPPT scheme a viable solution for extending the lifetime of the WSN.

5.2.5 Summary

In this chapter, a hybrid of wind and solar energy harvesting (HEH) scheme is proposed for outdoor applications. The existing wind energy harvesting (WEH) sub-system is augmented with the developed solar energy harvesting (SEH) sub-system to extend the operational lifetime of the wireless sensor node. The proposed HEH topology uses diodes to enable maximum power point tracking (MPPT) operations to be carried out in the WEH and SEH sub-systems. The WEH sub-system uses the resistor emulation technique while the SEH sub-system uses the constant voltage technique. This ensures simultaneous optimal charging of the supercapacitor as well as powering of the wireless sensor node. Experimental tests were conducted in accordance with the winter condition of the deployed ground where the average wind speed and average solar irradiance level are given as 4 m/s and 80 W/m^2 respectively. The electrical power harvested by the SEH and WEH sub-systems of the HEH system are 13 mW and 9.5 mW respectively. The total electrical power harvested by the optimized HEH system is 22.5 mW, which is almost two times higher than the highest of the single-source based EH method.

5.3 Composite Solar, Thermal (S+T) Energy Sources

The concept of hybrid energy harvesting (HEH) from two readily available energy sources to augment the lifespan of a wireless sensor node powered by single source energy harvesting has been validated in Section 5.2. Many energy harvesting systems have already been developed and those reported in the literature are mostly for outdoor applications where solar energy is plentiful. Very few research works [143]-[144] have discussed the indoor energy harvesting from ambient light source, which has serious challenges to resolve. In this chapter, the concept of energy harvesting from two readily available indoor energy sources, i.e. ambient light energy from artificial lighting and thermal energy from machines heat, to sustain low-power electronic remote sensors for supervisory and alarm system has been proposed.

There are two main challenges associated with indoor energy harvesting: (1) ambient energy sources in the indoor environment are very weak, hence the harvested power is much lower than that of the outdoor condition and (2) availability of energy sources are dependent on the indoor environmental conditions. According to Randall *et al.* [30], it has been shown that the light intensity of artificial lighting conditions found in hospitals and office buildings is only a small fraction of the light intensity for outdoor sun of 100-1000 W/m^2. As such, the power density of an amorphous solar cell with efficiency of <10 % under indoor light intensity of <10 W/m^2 is significantly reduced to 100 μW/cm^2 [145]. This is even more challenging when indoor energy harvesting is available for a limited period of time. The ambient energy sources can be intermittent and inconsistent at times depending on the indoor environmental conditions. Take for example, indoor lighting is

only available during office hours and almost complete darkness for the rest of the day. Because these challenges related to the weak and uncertain energy sources, energy harvesting in indoor environment from a single energy source might not be adequate to sustain the operation or even to enhance the performance of the miniaturized wireless sensor nodes over the lifetime.

Hybrid energy harvesting (HEH) has been recently discussed in the literature [35], [126] - [129] as a potential micro-power supply solution to minimize the size of the energy supply as well as to extend the operational lifetime of the wireless sensor node. Researchers have considered a number of methods to combine different small-scale energy harvesting (EH) sources and these methods can be classified into four main categories as described in Section 5.2. For the first three HEH methods discussed in the literature, each energy harvesting source is required to have its own unique power management unit i.e. DC-DC converter and associated circuitry to condition the power flow from the energy source to its output load. As more energy sources are combined together, the number of power management unit for each individual energy source increases, hence more components are needed and larger volumetric size, higher power losses and costs are incurred. This is not the case for the fourth HEH method proposed in this chapter. The proposed HEH system requires only one power management unit to condition the combined output power harvested from the solar and thermal energy sources.

Emphasis of this chapter is placed on enhancing the performance of the wireless sensor node deployed in the challenging indoor context using hybrid energy harvesting (HEH) from solar and thermal energy sources. A near maximum power point tracking (MPPT) technique is explored for the HEH system to maximize

power transfer from the hybrid energy sources to the sensor node. The rest of the chapter is organized as follows: Section 5.3.1 provides an overview of the indoor energy sources. Section 5.3.2 illustrates the details of indoor solar energy harvesting (SEH) sub-system while Section 5.3.3 explains on the thermal energy harvesting (TEH) sub-system. Section 5.3.4 discusses how the SEH and TEH sub-systems are combined directly together in parallel configuration. Following that, the optimized HEH system using a single power management unit for indoor wireless sensor node prototype is illustrated in Section 5.3.5, which then ends with a summary and discussions in Section 5.3.6.

5.3.1 Overview of Indoor Energy Sources

The characteristics and performances of the renewable energy sources available in outdoor environmental conditions are very different from those found in indoor industrial, commercial and biomedical environments. Within the enclosed environment like offices, hospitals, factories, etc., the energy sources are generally generated by some artificial means. Table.5.2 shows a summary of the indoor energy sources and their characteristics.

Table 5.2: Characteristics of Indoor Energy Sources

Energy source	**Characteristics**	**Comments**
Solar	Intermittent	Illumination from artificial lighting during office hours
Wind	Continuous	Air circulation from air conditioner and electric fans
Thermal	Continuous/ Intermittent	Thermal gradient between body, machine heat and ambient
Vibration	Intermittent	Vibration from machine and human motion during walking, running, etc.

Referring to Table 5.2, it can be seen that the artificial energy sources found in indoor environment are generated from electrical appliances such as artificial lightings, air conditioners, machines, etc. and human movement. Each of these appliances and human bodies has its own primary purpose. Artificial lighting and air conditioner for example, are primarily used to generate light for visual function and air circulation for cooling purposes. During the normal operation of these electrical appliances and human movements, some stray energies are generated for energy harvesting. The availability of the artificial energy sources seen in Table 5.2 are largely dependent on the operational schedules of the electrical appliances and the lifestyles of the human beings. For some energy sources such as solar and vibration, they are only available at times, according to the intermittent operating profile of the artificial lighting, machine operation and human movement. Conversely, the wind and thermal energy sources exist in continuous form as the air conditioners and machineries of indoor industrial, commercial or biomedical environment are operated at a duty cycle close to 100 %.

Table 5.3: Performance of Energy Harvesters under Indoor Conditions (adapted from [27])

Energy Harvester	**Power Densities**	
	Indoor condition	***Outdoor condition***
Solar panel	100μW/cm^2 @10W/cm^2	10mW/cm^2 @STC
Wind turbine-generator	35μW/cm^2 @<1m/s	3.5mW/cm^2 @8.4m/s
Thermoelectric generator	100μW/cm^2 @5^{o}C gradient	3.5mW/cm^2 @30^{o}C gradient
Electromagnetic generator	4μW/cm^3 @human motion-Hz 800μW/cm^3 @machine-kHz	

Apart from the issue of availability of energy sources, another concern is the power harvesting throughput. The power densities of various energy harvesting

technologies per unit cm^2 or cm^3 are recorded in Table 5.3. Under the indoor condition, it can be observed that all the artificial energy sources become very weak. The power density of a solar panel, for example, with efficiency of <10 % under the indoor solar irradiance of 10 W/m^2 is only 100$\mu W/cm^2$ as compared to 10 mW/cm^2 under the outdoor standard testing condition (STC). Table 5.3 shows that the average power that can be harvested by all the artificial energy sources is 10-100 times lower than that of the outdoor ambient energy sources. As such, these weak and uncertain indoor energy sources pose significant challenges on energy harvesting from a single energy source for sustaining the operation of the wireless sensor nodes over the entire lifetime.

To enhance the performance of the wireless sensor node in indoor environment, hybrid energy harvesting (HEH) from solar and thermal energy sources is proposed in this chapter. Among the various artificial energy sources, solar and thermal energy sources share similar high power densities as can be seen in Table 5.3. In addition, the undesirable intermittent solar energy sources found in offices or factories lightings can be supplemented by the continuous thermal energy supply from waste heat generated by machineries. Whenever solar energy is not available, instead of solely relying on the energy stored in the on-board energy storage devices proposed by Nasiri *et al.* and Hande *et al.* in [143] and [144] respectively, an alternate approach is to harvest from the readily-available thermal energy source to continue powering the operation of the wireless sensor node before exhausting the energy stored in the energy storage device. Another key characteristic of the proposed HEH system is that the HEH system is able to harvest simultaneously from both energy sources whenever they are available instead of harvesting from individual energy source at one time [126] - [129], hence the performance of the

indoor wireless sensor node can be enhanced.

5.3.2 Indoor Solar Energy Harvesting Sub-System

The solar panel used in this chapter is specially selected for use under indoor conditions i.e. artificial lighting from fluorescent lamps and at room temperature (relatively less variation of temperature at indoor environment than outdoors [30]). The physical size of the chosen solar panel is 55 mm x 30 mm x 1 mm (2.1" x 1.18" x .04") and its cross-sectional area, A, can be calculated to be around 16.5 cm^2. At very low light illumination, for example $G = 380$ lux ($\approx 380/120 = 3.17$ W/m^2 [30]), the open circuit voltage, V_{oc}, and short circuit current, I_{sc}, are measured to be 4.14 V and 60 μA respectively. The output voltage and current obtained at maximum power point tracking (MPPT) points are $V_{mppt} = 3.5$ V and $I_{mppt} = 51.44$ μA respectively. For the given technical characteristics of the solar panel, the corresponding solar panel's efficiency can also be determined using the following equation given as,

$$\eta = \frac{P_{pv}}{G * A} * 100\% \tag{5.7}$$

Based on eqn.5.7, the efficiency of the solar panel can be calculated to be around 3.4 %, which is relatively lower than the outdoor solar panel [145]. Due to the low efficiency of the solar panel in the indoor condition, the power harvested is also low, hence it is necessary to optimize the indoor solar energy harvesting sub-system in order to maximize the power harvested from the solar panel. Further investigations were carried on the solar panel to investigate its performance at different lighting conditions. Figures. 5.17 and 5.18 show the indoor solar panel's P-V and P-R curves at different lux illuminations. Both the power curves of the

solar panel in relationship with the output voltage (P-V) and the load resistance (P-R) under a range of loads from short circuit to open circuit were generated at 5 different lighting conditions ranging from 380 to 1010 lux.

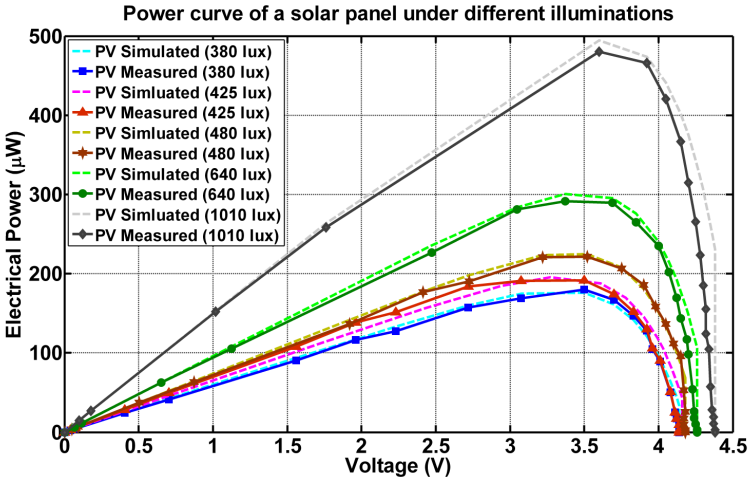

Figure 5.17: P-V curves of solar panel at different lux conditions

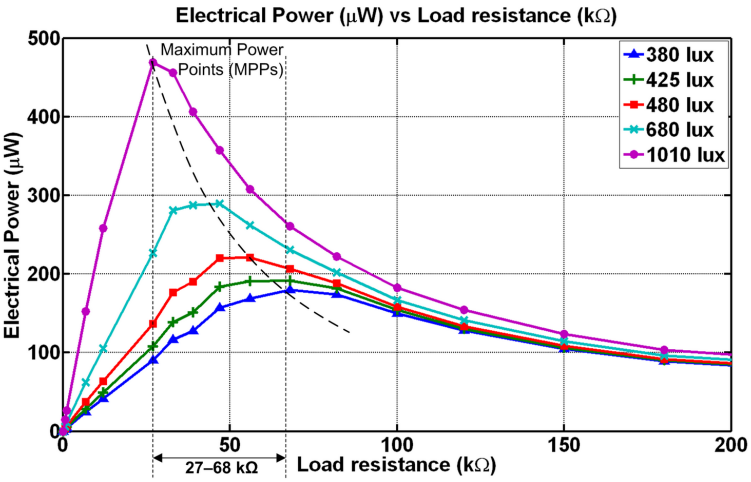

Figure 5.18: P-R curves of solar panel at different lux conditions

Taking into consideration the parameters extracted for the solar panel, the model of the solar panel expressed by eqn.5.3 has been simulated and the simulation results are recorded in Figure.5.17. The simulated P-V curves are verified with the measured P-V curves as seen in Figure.5.17 for varying solar irradiance con-

ditions, performed by a characterization setup based on a fluorescent light source. Figure.5.17 shows that all of the power curves peak near the solar panel output voltage of 3.6 V. Conversely, for the power curve (P-R) plotted in Figures.5.18, it can be observed that the maximum power points (MPPs) of the solar panel vary between 27-68 kΩ. As such, by setting the output voltage of the solar panel fixed at 3.6 V, maximum output power can be harvested from the solar panel under different solar irradiance. Within the indoor lighting conditions of 380-1010 lux, the maximum electrical power that the solar panel can harvest ranges from 180-480 μW respectively.

5.3.3 Thermal Energy Harvesting Sub-System

In the thermal energy harvesting (TEH) sub-system, a miniaturized thermoelectric generator (TEG) housed in the thermal energy harvester is used for converting thermal energy into electrical energy. The thermal energy, generated from the heat source at certain high temperature of T_H, is channelled through the enclosed thermoelectric generator (TEG) via a thin film of thermally and electrically conductive silver grease between them to the heatsink. The residual heat accumulated in the heatsink is then released to the surrounded ambient air at a lower temperature T_C. An equivalent thermal circuit model of the thermal energy harvester that illustrates its thermal and electrical characteristics is provided in Figure.5.19.

Referring to Figure.5.19, it can be observed that the temperature difference, ΔT_{TEG}, across the junctions of the thermoelectric generator (TEG) is lower than the temperature gradient, $\Delta T = T_H - T_C$, that is externally imposed across the thermal energy harvester. This is because of the thermal contacts and thermal

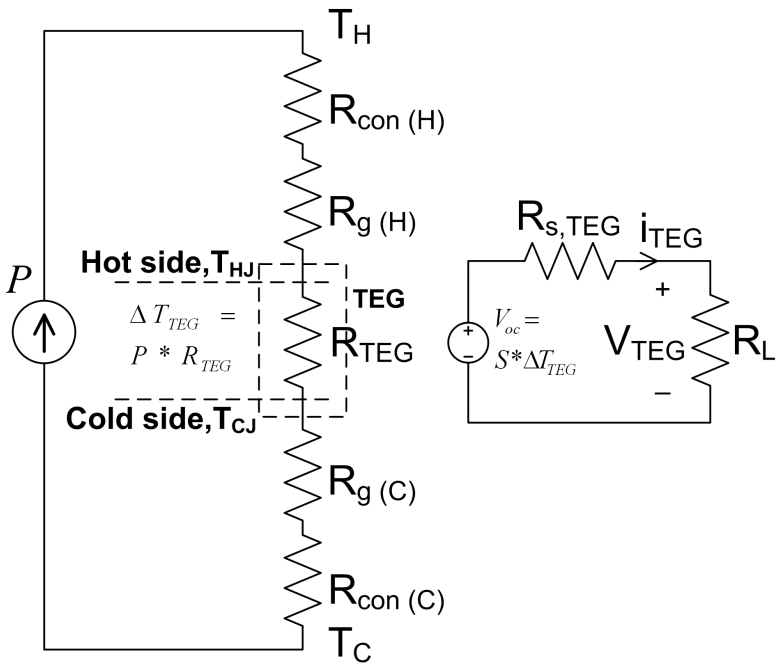

Figure 5.19: Equivalent electrical circuit of the thermal energy harvester

grease resistances residing in the cold and hot sides of the thermal energy harvester i.e. $R_{con(H)}$, $R_{con(C)}$ and $R_{g(H)}$, $R_{g(C)}$ respectively. To minimize this negative effect, the thermal resistance, R_{TEG}, of the TEG is made to be as high as possible and/or conversely, the rest of the thermal resistances of the thermal energy harvester are designed to be as small as possible. Taking these design considerations into account, the miniaturized thermal energy harvester, having the physical size of 20 mm x 20 mm x 20 mm, is designed in such a way that most of the heat is channelled through the TEG in order to maximize thermal energy harvesting.

Analysis and characterization works were conducted on the designed thermal energy harvester to evaluate the performance of the thermal energy harvesting sub-system in powering the wireless sensor node. According to Seebeck's effect, the open-circuit voltage, V_{oc}, of the TEG enclosed in the thermal energy harvester, which is composed of n thermocouples connected electrically in series and thermally

in parallel, is given as: -

$$V_{oc} = S * \Delta T = n * \alpha(T_H - T_C) \tag{5.8}$$

where α and S represent the Seebeck's coefficient of a thermocouple and a TEG respectively. When connecting a load resistance, R_L, electrically to the thermoelectric generator (TEG) via the thermal energy harvester as shown in Figure.5.19, an electrical current, I_{TEG}, flows in accordance to the applied temperature difference, ΔT, which is given as,

$$I_{TEG} = \frac{V_{oc} - V_{TEG}}{R_{s,TEG}} = \frac{n * \alpha(T_H - T_C) - V_{TEG}}{R_{s,TEG}} \tag{5.9}$$

where $R_{s,TEG}$ is the internal electrical resistance of the thermoelectric generator (TEG). Based on the current-voltage (I-V) characteristic of the TEG described in eqn.5.9, the output power, $P_{TEG}(V_{TEG})$, delivered by the TEG to the load, R_L, can be determined. By substituting I_{TEG} with eqn.5.9, the electrical power, $P_{TEG}(V_{TEG})$, harvested by the thermal energy harvester is derived as a function of its output voltage, V_{TEG}, which is expressed as: -

$$\begin{aligned} P_{TEG}(V_{TEG}) &= V_{TEG} * I_{TEG} \\ &= \frac{V_{TEG} * n * \alpha^*(T_H - T_C) - V_{TEG}^2}{R_{s,TEG}} \end{aligned} \tag{5.10}$$

Based on the technical specifications provided for the Thermo Life® thermoelectric generator (TEG) [91], the TEG used in this chapter is made up of 5200 thermocouples, each thermocouple has a Seebeck's coefficient, α, of 0.21 mV/K. For a given temperature difference, $\Delta T = T_H - T_C$, between 5-10 K, the model illustrated by eqn.5.10 is simulated for different TEG's output voltage, V_{TEG} and

the simulation results are presented in Figure.5.20. Experiments were carried out to characterize the TEG by applying a temperature difference between the thermal contact faces and both the electrical output voltage and current with different loads connected were measured. This experiment is repeated for various temperature differences in the range between 5 K and 10 K and the experimental results are shown in Figure.5.20.

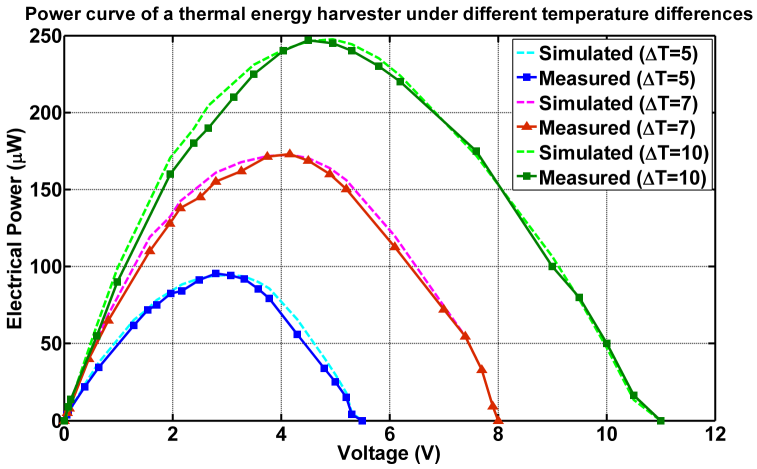

Figure 5.20: P-V curves of thermoelectric generator at different thermal gradients

Referring to the power curve (P-V) shown in Figure.5.20, it can be seen that the simulation results obtained using the model expressed in eqn.5.10 is comparable to the measurement results collected from the characterization of the thermal energy harvester under varying temperature differences. Figure.5.20 shows that the maximum obtainable power for each thermal gradient corresponds to an output voltage of the thermal energy harvester i.e. $P_{mppt,\Delta T=5K}$ = 96 μW @2.8 V, $P_{mppt,\Delta T=10K}$ = 247 μW @4.5 V, etc. This is unlike the indoor solar energy harvesting case whereby all their power curves (P-V) peak near a particular output voltage of the solar panel (see Figure.5.17).

However, this is not the case for another power curve (P-R) plotted for solar

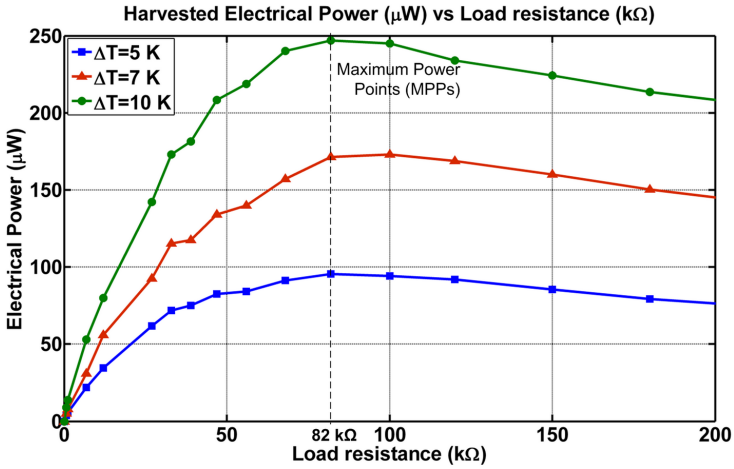

Figure 5.21: P-R curves of thermoelectric generator at different thermal gradients

and thermal energy harvesting as shown in Figures.5.18 and 5.21 respectively. It can be observed that the maximum power points (MPPs) of the solar panel vary between the load resistances of 27-68 kΩ whereas the MPPs of the thermal energy harvester is fixed at the internal impedance of the thermal energy harvester of 82 kΩ. Figure.5.21 shows that when the load resistance matches the source resistance of the thermal energy harvester, the harvested power is always maximum for different temperature differences. Because of that, it can be concluded from both power curves in Figures.5.18 and 5.21 that no common MPPT approach exists between the solar and thermal energy harvesting sub-systems.

5.3.4 Hybrid Energy Harvesting from Solar and Thermal Energy Sources

5.3.4.1 Characteristic of Solar Panel & Thermal Energy Harvester Connected in Parallel

For the hybrid energy harvesting (HEH) approach proposed in this chapter, the terminal output voltages of the solar panel and the thermal energy harvester, V_{pv}

and V_{TEG} respectively, are directly connected to the load, each via a schottky diode to block reverse-biased current flow. An overview of the equivalent electrical circuit of the hybrid energy harvester is shown in Figure.5.22.

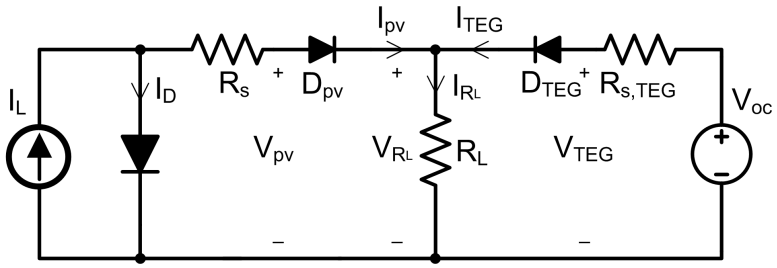

Figure 5.22: Equivalent electrical circuit of the proposed hybrid energy harvester

According to Figures.5.17 and 5.20, the output voltages of the two energy sources are not that low, typically of few volts, hence the series energy sources configuration is not used to step-up the voltage across the load, V_{R_L}. Instead, a parallel energy sources configuration, $V_{R_L} = V_{pv} = V_{TEG}$, is employed to produce more current flows i.e. $I_{R_L} = I_{pv} + I_{TEG}$. The power harvested from the solar panel, $P_{pv}(V_{pv})$, and the thermal energy harvester, $P_{TEG}(V_{TEG})$, expressed by eqns.5.3 and 5.10 respectively are summed together to power the load. The electrical power throughput of the hybrid energy harvester, $P_{HEH}(V_{R_L})$, as a function of its output voltage, V_{R_L}, is thus given by,

$$\begin{aligned} P_{HEH}(V_{R_L}) &= |P_{pv}(V_{R_L})| + |P_{TEG}(V_{R_L})| \\ &\approx |V_{R_L} * I_{sc,pv}| - \left| V_{R_L} * I_o \left[exp\left(\frac{V_{R_L}}{n_s k T_c / q} \right) \right] \right| \\ &\quad + \left| \frac{V_{R_L} * V_{oc,TEG} - V_{R_L}^2}{R_{s,TEG}} \right| \end{aligned} \tag{5.11}$$

Based on the technical specifications of the solar panel and the thermal energy harvester given in Sections 5.3.2 and 5.3.3 respectively, the harvested power

expression of the hybrid energy harvester, as expressed by eqn.5.11, is simulated over a range of output voltages, V_{R_L}, for different solar irradiance and temperature differences that correspond to the solar panel's short-circuit current, $I_{sc,pv}$, and the thermal energy harvester's open-circuit voltage, $V_{oc,TEG}$. A set of the simulation and experimental results extracted under the minimum (380 lux and ΔT = 5 K) and the maximum (1010 lux and ΔT = 10 K) power harvesting conditions are shown in Figure.5.23.

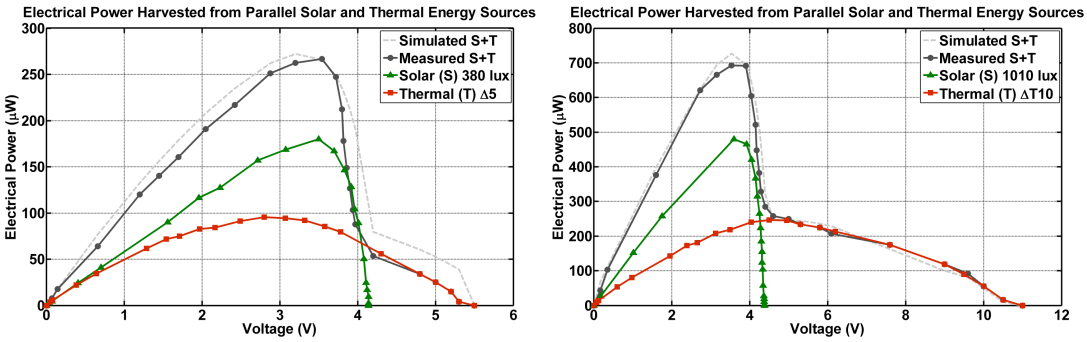

Figure 5.23: Compare experimental harvested power with simulated power under the least and most power harvesting conditions (a) 380 lux and ΔT=5^{o}C (top) and (b) 1010 lux and ΔT=10^{o}C (bottom) respectively.

Referring to Figure.5.23, it can be observed that the measured power curve (Measured S+T) of the hybrid energy harvester is the resultant of summing the individual power curves i.e. solar panel (Solar (S)) and thermal energy harvester (Thermal (T)) being superimposed into Figure.5.23 minus the negligible small power loss in the schottky diodes. At MPPT voltage, $V_{R_L,mppt}$, of 3.6 V, the output voltages of the solar panel and thermal energy harvester are slightly higher than $V_{R_L,mppt}$ such that the two isolation diodes are conducting in the forward bias condition, hence, with reference to Figure.5.23, it can be seen that the hybrid energy harvester can generate power at the minimum of 252 μW (P_{pv} = 167 μW, P_{TEG} = 85 μW) and at the maximum of 693 μW (P_{pv} = 466 μW, P_{TEG} = 227 μW)

respectively. In addition, Figure.5.23 shows that when $V_{R_L} \geq V_{pv}$, the solar panel operates in the open-circuit mode and therefore no solar power is harvested. This situation happens to the thermal energy harvester as well if $V_{R_L} \geq V_{TEG}$ (3.6 V).

Another observation seen in Figure.5.23 is that the simulated waveforms (Simulated S+T) based on the model expressed by eqn.5.11 and the measured waveforms (Measured S+T) obtained from experiments are quite similar. The positive outcome of this observation verifies the expression model derived in eqn.5.11, which can then be used to determine the electrical power throughput of the hybrid energy harvester, P_{HEH}, to sustain the operational lifetime of the wireless sensor node. More analysis and characterization works were conducted on the hybrid energy harvester to evaluate the performance of the hybrid energy harvesting (HEH) system in powering the wireless sensor node. Figures.5.24 and 5.25 show the power curves of the HEH system at fixed solar irradiance of 380 lux and 1010 lux respectively for varying thermal differences in the range of 5 - 10 K. Conversely, the HEH system is also subjected to fixed thermal differences of 5 K and 10 K, as shown in Figures.5.26 and 5.27 respectively, for various solar irradiance between 380 - 1010 lux.

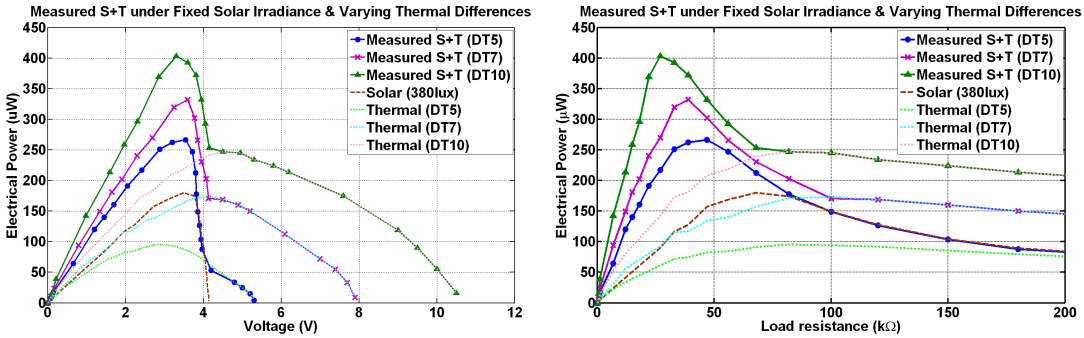

Figure 5.24: P-V and P-R curves of HEH system at fixed solar irradiance of 380 lux (3 W/m^2) and different thermal differences of 5-10 K.

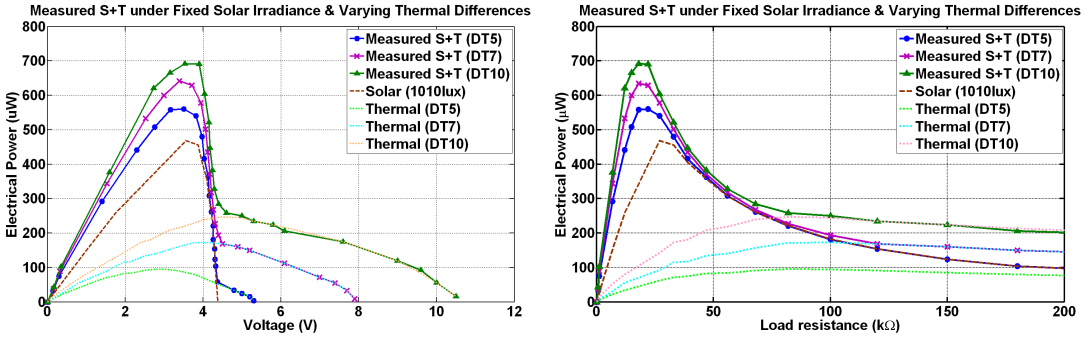

Figure 5.25: P-V and P-R curves of HEH system at fixed solar irradiance of 1010 lux (3 W/m^2) and different thermal differences of 5-10 K.

Referring to Figures.5.24 and 5.25, it can be seen from the P-R curves (Thermal ΔT5 - Thermal ΔT10) that the maximum power points (MPPs) of the standalone thermal energy harvester are fixed at its internal resistance of 82 kΩ under temperature differences in the range of 5-10 K. When the thermal energy harvester is paralleled with the solar panel under weak illumination of 380 lux and strong illumination of 1010 lux, it can be observed from the P-R curves (Measured S+T (ΔT5) - Measured S+T (ΔT10)) shown in Figures.5.24 and 5.25 that the MPPs are not longer fixed, but vary with the combined internal impedance of the solar panel and the thermal energy harvester in parallel. This is the resulting effect of the impedance mismatch between the two energy sources of the hybrid energy harvester. Although there is impedance mismatch issue in the proposed hybrid energy harvesting system, it is still possible to combine the two energy sources together without dedicating each individual energy source with a power converter to perform MPPT as proposed by Chulsung *et al.* in [35]. Referring to Figures.5.24 and 5.25, the P-V curves (Measured S+T (ΔT5) - Measured S+T (ΔT10)) show that all the MPPs of the hybrid energy harvester are fixed at around its output voltage of 3.6 V.

Likewise, for an illumination level of 380 lux and above as a common indoor

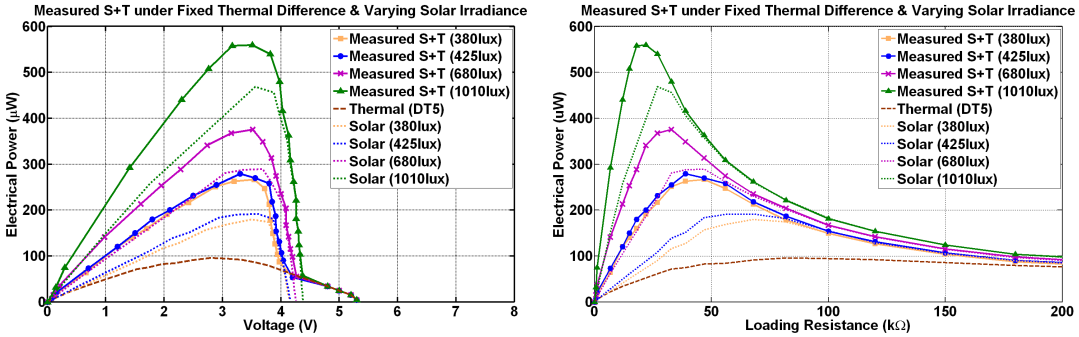

Figure 5.26: P-V and P-R curves of HEH system at fixed thermal differences of △T=5 K and varying solar irradiances of 380-1010 lux.

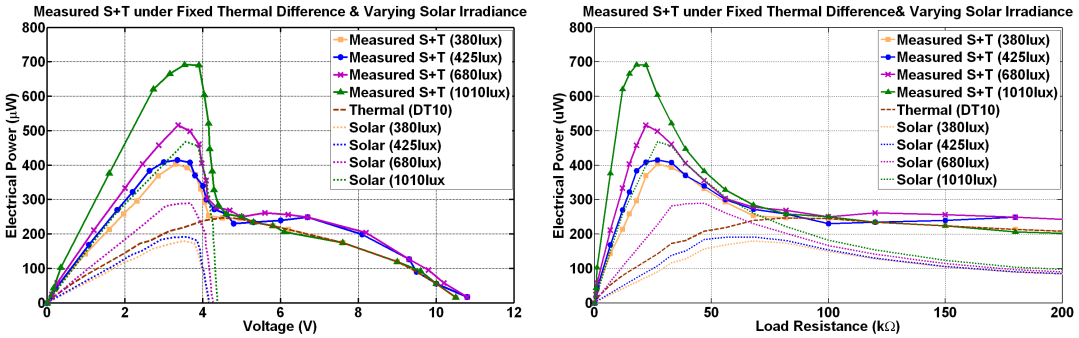

Figure 5.27: P-V and P-R curves of HEH system at fixed thermal differences of △T=10 K and varying solar irradiances of 380-1010 lux.

lighting condition, the hybrid energy harvester tested under fixed thermal difference of 5 K and 10 K, as shown in Figures.5.26 and 5.27, show that all of the P-V power curves (Measured S+T (380 lux) - Measured S+T (1010 lux) peak around 3.6 V. Reviewing through all the power curves shown in Figures.5.24 - 5.27, it can be observed that all the maximum power points (MPPs) of the P-V curves tend to cluster around a fixed voltage of 3.6 V, whereas the MPPs of the P-R curves are scattered out in the range of 20 - 50 kΩ. Hence, by deliberately setting the terminal voltage of the hybrid energy harvester to a value in the peak power range ($V_{R_L,mppt}$ = 3.6 V), it is possible to extract maximum output power from the hybrid energy harvester with a simple and ultra-low-power control circuit so as to place the panel at its MPPs, rather than using those energy hungry tracking techniques such as Perturb and Observe (P&O) and Incremental Conductance, which require high

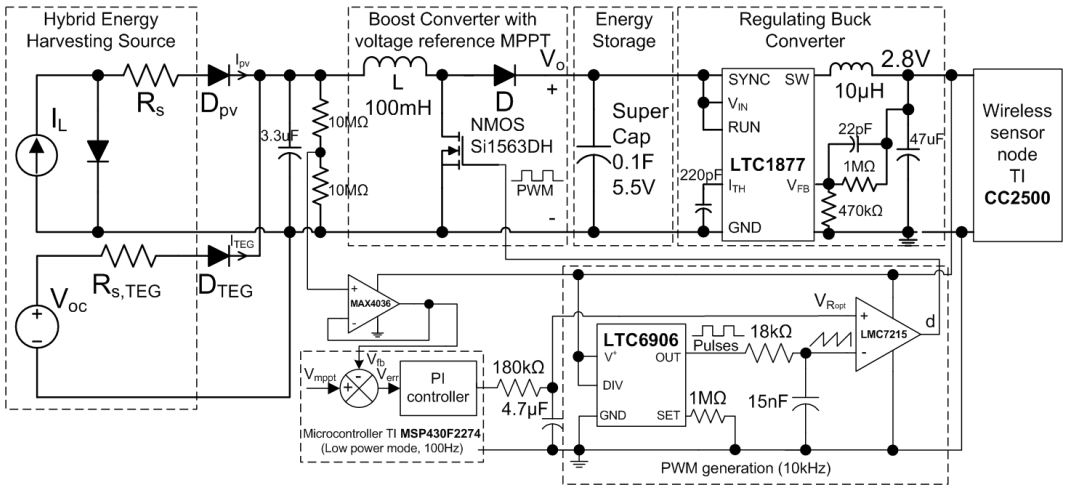

Figure 5.28: Functional block diagram of HEH system

computational power and cost.

5.3.4.2 Design and Implementation of Ultra-Low-Power Management Circuit

The schematic diagram of a self-autonomous indoor wireless sensor node powered by the proposed hybrid energy harvesting (HEH) system and its ultra-low-power power management circuit is illustrated in Figure.5.28. Referring to Figure.5.28, the designed power management circuitry with fixed voltage reference MPPT approach essentially consists of three main building blocks: (1) a boost converter with MPP tracker and its control and PWM generation circuit that manipulates the operating point of the hybrid energy harvesting scheme to keep harvesting power at near maximum power points (MPPs), (2) an energy storage element i.e. supercapacitor to buffer the energy transfer between the source and the load and (3) a regulating buck converter to provide constant voltage to the wireless sensor node and other electronic circuitries.

With reference to Figure.5.28, the operation of the boost converter based on the fixed voltage reference approach is given as follows: the MPPT voltage reference signal, V_{mppt}, of 3.6 V is compared with the feedback voltage signal, V_{fb}, from the output of the hybrid energy harvester. The resultant voltage error signal, V_{err}, is fed into a proportional-integral (PI) controller to generate a low frequency pulse width modulation (PWM) control signal, ∼100Hz, from a Texas Instruments microcontroller (TI MSP430F2274). In order to miniaturize the HEH system by using smaller passive components, the low frequency PWM control signal generated from the reduced clock speed microcontroller is transformed to a higher switching frequency of 10 kHz. This is achieved by designing an ultra-low-power PWM generation circuit made up of a micro-power resistor set oscillator (LTC6906) used for sawtooth generation and a micro-power, rail-to-rail CMOS comparator (LMC7215). The low frequency PWM signal, which represents the MPPT voltage reference, is compared with the sawtooth signal to generate the high frequency PWM gating signal to control the boost converter.

For indoor environment, the ambient energy sources such as solar and thermal gradient are not always available at all times and at a steady level, so there is a need to incorporate an energy storage device, i.e. supercapacitor, in the hybrid energy harvesting (HEH) system to store the excessive energy harvested from the solar panel and/or thermal energy harvester so as to buffer the indoor wireless sensor node for those times when energy sources are unavailable. Moreover, by drawing power simultaneously from both solar and thermal energy sources, the throughput power of the HEH system is increased which can enhance the performance of the indoor wireless sensor node. Supercapacitor is employed in this work because it has superior characteristics over batteries as described in [34]. These

characteristics include numerous full charge cycles (more than half a million charge cycles), long lifetime (10-20 years operational lifetime) and high power density (an order of magnitude higher continuous current than a battery) . Unlike the discrete capacitors which have very small capacitance values of pF - μF range, the supercapacitor has very large capacitance value of Farads range suitable for energy storage purpose.

Lastly, the switched-mode voltage regulator (LTC1877) obtained from Linear Technology is inserted after the supercapacitor to provide a constant operating voltage of 2.8 V_{DC} to the wireless sensor node and other electronic circuitries. The efficiency of the regulating buck converter is experimentally tested to be around 80-90 %, consuming an operating current of 12 μA. In this work, the operation of the wireless sensor node deployed in an application field comprises of: (1) sensing some external analog signals from sensory devices such as temperature, humidity, etc. and (2) communicating and relaying the sensed information to the gateway node in every 5 seconds time. Upon receiving the data at the base station, the collected data are then post-processed into usable information for any follow up action.

5.3.5 Experimental Results

The near optimal hybrid energy harvesting (HEH) wireless sensor node has been successfully implemented into hardware prototype for laboratory testing. Several experimental tests have been conducted to analyse the performance of the HEH system and its simple and ultra-low-power fixed reference voltage maximum power point tracking (MPPT) scheme in powering the connected load consisting of the su-

percapacitor, the sensing, control and PWM generation circuitries and the wireless sensor node.

5.3.5.1 Performance of Parallel HEH Configuration

As mentioned before, when the solar and thermal energy sources of different characteristics are combined together, it is bound to have the issue of impedance mismatch among the integrated energy sources. As such, the performance of the parallel hybrid energy harvester, which contains the combined characteristics of the solar panel as well as the thermal energy harvester, is investigated. With reference back to Figures.5.24 - 5.27, it is illustrated that the fixed reference voltage method is able to operate the hybrid energy harvester near its MPPs for different light intensities and temperature differences, but at the expense of some percentage of power loss in the harvested power. It is thus important to examine the significance of these power differences between the actual harvested power, $P_{HEH,actual}$, with respect to the MPPs, $P_{HEH,mppt}$, of the hybrid energy harvester as recorded in Figure.5.29.

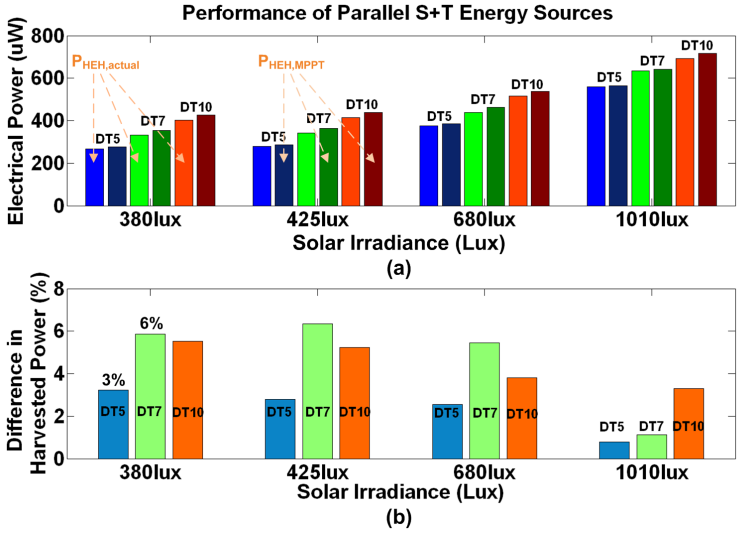

Figure 5.29: Performance of HEH system in parallel configuration

Considering an extreme operating condition, which is at low light illumination of 380 lux and small temperature difference of 5 K as seen in Figure.5.29(a), for example, the power harvested at the fixed reference MPPT voltage of 3.6 V, $P_{HEH,actual}$, and the maximum obtainable power, $P_{HEH,mppt}$, of the hybrid energy harvester, are 252 μW and 260 μW respectively. The power difference is only 8 μW, which is about 3 % of its harvested power as shown in Figure.5.29(b). The power loss of 8μW is due to the impedance mismatch issue between the solar panel and thermal energy harvester when they are connected directly without the use of separate power converters.

Similarly, the power differences between the actual harvested power, $P_{HEH,actual}$, with respect to the MPPs, $P_{HEH,mppt}$, for all the other operating conditions range between 8-35 μW (see Figure.5.29(a)), which are 3-6 % of the harvested power (see Figure.5.29(b)). Although the proposed hybrid energy harvesting (HEH) system i.e. hybrid energy harvester and its power management unit would incur power loss i.e. 8-35 μW in the overall harvested power, this power loss is so small and marginal as compared to those MPPT techniques that require high computational power and cost to fulfill their objective of precise and accurate MPP tracking. It is thus justifiable to utilize the simple and ultra-low-power fixed reference voltage method for the hybrid energy harvester.

5.3.5.2 Power Conversion Efficiency of HEH System

The power conversion efficiency of the hybrid energy harvesting (HEH) system is another important investigation being carried out. Other than the regulating buck converter, there are another two main contributors of power losses to the HEH

system, namely the boost converter itself, which acts as a maximum power point (MPP) tracker, and its associated sensing, control and PWM generation circuits. The efficiency of the boost converter, η_{conv}, can be expressed as a function of its output load power, P_{load}, over its input DC power, P_{dc}, under varying solar irradiance, temperature differences, ΔT, and loading, R_L, conditions. Take for example, at lux illumination, temperature difference and output load resistance of 380lux, 5K and 68kΩ respectively, the efficiency of the boost converter is given by,

$$\begin{aligned} \eta_{conv} &= \frac{P_{out}}{P_{in}} * 100\% = \frac{V_{out}^2/R_{load}}{V_{in}I_{in}} * 100\% \\ &= \frac{4.95V^2/68k\Omega}{3.6V * 109\mu A} * 100\% = 91.8\% \end{aligned} \tag{5.12}$$

and the calculated efficiency of 91.8 % is plotted in Figure.5.30. For all other solar irradiance, temperature differences and loading conditions, the efficiencies of the boost converter are calculated using eqn.5.12 and the computed results are plotted in Figure.5.30. It can observed from Figure.5.30 that the efficiency of the designed boost converter ranges between 80 % to 94 % over a range of load resistances of 50-330 kΩ. At heavy load condition say 50 kΩ, which signifies the discharge state of the supercapacitor, it can be seen in Figure.5.30 that the efficiency of the boost converter is high, around 94 %. This high-efficiency boost converter is very favourable and desirable to ensure optimal transfer of energy from the micro power sources of hundreds of microwatts or even lower to the energy storage.

As the loading gets lessen with the supercapacitor charges up, with reference to Figure.5.30, it can be seen that the efficiency of the converter decreases to around 82 % at a load resistance of 300 kΩ. This decreasing efficiency trend is due to the power loss in the boost converter. Even so, the efficiency at light load is lower, it is

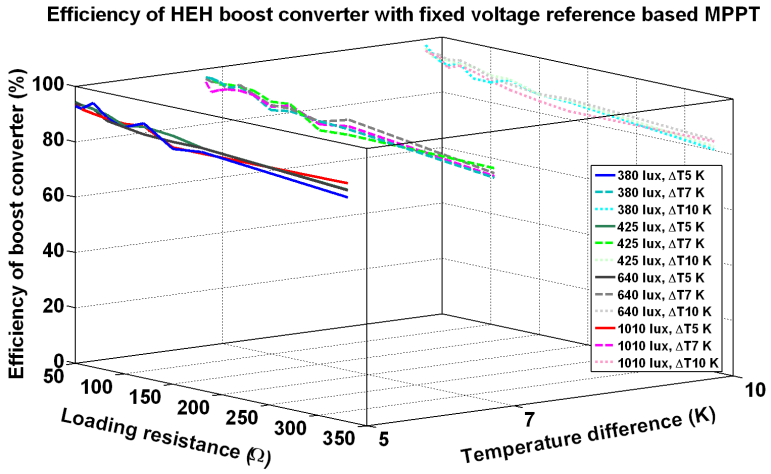

Figure 5.30: Efficiency of HEH boost converter

not as critical as the heavy load condition because the supercapacitor, by then, is already near full charge state and any surplus energy would not be stored. Another source of power loss in the HEH system is the power consumption of the associated sensing, P_{sense}, control, P_{ctrl}, and PWM generation, $P_{generate}$, electronic circuits. Based on the voltage and current requirements of each individual component in the hybrid energy harvesting (HEH) system shown in Figure.5.28, the total power consumption of the electronic circuits can be calculated as follows,

$$\begin{aligned} P_{consumed} &= P_{sense} + P_{ctrl} + P_{PWMgenerate} \\ &= 2.7V * (3\mu A + 15\mu A + 32\mu A) = 135\mu W \end{aligned} \tag{5.13}$$

Once all the power losses in the HEH system are identified, including the power difference factor due to impedance mismatch between two paralleled energy sources and the power losses in the voltage regulating and MPPT converters, the performance of the designed HEH system for enhanced performance in the indoor wireless sensor node are evaluated. In indoor applications like hospitals and factories, say the ambient condition is as follows: solar irradiance of 1010 lux and temperature difference of 10 K, referring back to Figures.5.17 and 5.20 with oper-

ating conditions of 1010 lux and 10 K, the maximum power obtained by summing the individual MPP of the thermal energy harvester, P_{TEG}, and solar panel, P_{pv}, is 727 μW and the actual harvested power, $P_{HEH,actual}$, measured from the two paralleled energy sources is 690 μW. The power difference between the calculated and measured powers, due to impedance mismatch between two paralleled energy sources, is 35 μW as shown in Figure.5.29. Taking into consideration both the power difference and the power losses in the voltage regulating and MPPT converters as shown in Figure.5.30, the net harvested power output to power the indoor wireless sensor node through the boost converter with efficiency of 90 % is 621 μW. This harvested power from the HEH system is more than what is harvested by each individual energy source i.e. ambient light of 432 μW or thermal energy source of 223 μW, hence the significance of the proposed HEH system is exhibited.

5.3.5.3 Performance of Designed HEH System for Indoor Wireless Sensor Node

In order to evaluate the designed hybrid energy harvesting (HEH) system for sustaining the operation of the wireless sensor node used in indoor environment, the maximum power point tracking (MPPT) performance of the boost converter based on fixed reference voltage scheme is investigated as shown in Figure.5.31. During the performance evaluation process, all the three main contributors of the power losses in the HEH system are also included in the power analysis. A fixed resistor of 68 kΩ is used, instead of a supercapacitor which requires a long time to charge and discharge, to be the load so that the dynamic and steady state responses of the MPP tracker can be examined for use in the power analysis. The load resistance represents the power consumed by the wireless sensor node for sensing and com-

municating operations as well the power losses incurred by the electronic circuitries associated to the voltage regulating and MPPT converters at a voltage level of 4.2 V.

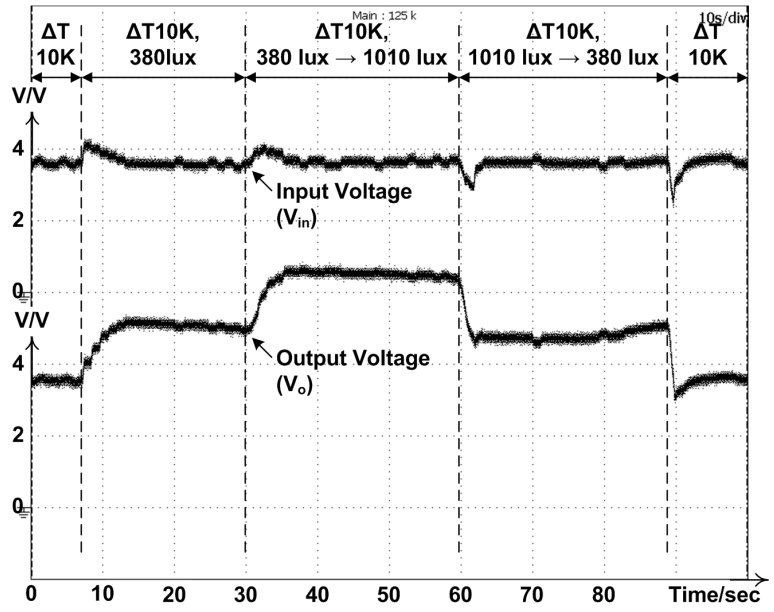

Figure 5.31: Performance of HEH System

Referring to Figure.5.31, it can be seen that from the initial start time, t, till the 7th seconds, there is only the presence of heat source applied to the HEH system. The power harvested by the thermal energy harvester at temperature difference, ΔT, of 10 K is about 190 μW @3.6 V, which is lesser than the power required by the load. In order to sustain the operation of the wireless sensor node, an additional energy source from the artificial lighting with illumination of 380 lux is inserted at $t = 7$ seconds. It can be seen from Figure.5.31 that the output voltage of the boost converter, V_o, connected to the load, rises from 3.6 V to 5 V in around 5 seconds and after which it settles down at 5 V. In the mist of that, the input voltage of the boost converter, V_{in}, surges and the HEH system shifts away from its maximum power point (MPP). Since a microcontroller-based MPP tracker with

closed-loop voltage feedback control is implemented in this chapter, the closed-loop MPP tracker manipulates the duty cycle of the boost converter to shift back V_{in} and maintain it always at the MPPT voltage (V_{mppt} = 3.6 V) of the HEH system. By doing so, the total power harvested by the HEH system is increased from 190 μW to 367 μW @5 V, which is more than the load power consumption.

To enhance the performance of the wireless sensor node, the solar panel is exposed to a stronger solar illumination of 1010 lux that can be found in indoor applications like hospitals and factories. Referring to Figure.5.31, for the time period of 30 - 60 seconds, there is even more electrical power harvested from the HEH system at solar irradiance of 1010 lux and ΔT of 10 K for powering the indoor wireless sensor node. Referring back to Figures.5.17 and 5.20 with operating conditions of 1010 lux and 10 K, the maximum power obtained by summing the individual MPP of the thermal energy harvester and solar panel is 727 μW and the actual harvested power measured from the two paralleled energy sources is 690 μW. The power difference between the calculated and measured powers, due to impedance mismatch between two paralleled energy sources, is 35 μW. Taking into consideration both the power difference and the power losses in the voltage regulating and MPPT converters, the net harvested power output to the load through the boost converter with efficiency of 90 % is 621 μW. This verifies the harvested power experimentally obtained from Figure.5.31 where the output voltage, V_o, of the boost converter connected to the load resistance of 68 kΩ, is around 6.5 V and its harvested power is calculated to be 621 μW.

5.3.6 Summary

A near optimal hybrid energy harvesting (HEH) system has been proposed for enhanced performance of indoor wireless sensor node. Theoretical studies on individual sub-system as well as hybrid solar and thermal energy harvesting system are conducted and simulated to understand the characteristic of the HEH system, which are then verified by experimental results. In this chapter, the proposed HEH system using one power management circuit has successfully implemented into hardware prototype for laboratory testing. Based on the power analysis, the efficiency of the power management unit with fixed reference voltage based maximum power point tracking (MPPT) scheme is around 90 % and its sensing, control and PWM generation circuitries consumes around 135 μW. Experimental results show that the HEH system can harvest an average electrical power of 621 μW from both energy sources at an average solar irradiance and thermal gradient of 1010 lux and 10 K respectively, which is almost 3.3 times higher than the conventional single thermal energy harvesting method so as to enhance the performance of the indoor wireless sensor node.

Chapter 6

Electrical Power Transfer with 'no wires'

In this chapter, the concept of electrical power transfer with 'no wires' has been introduced with a similar objective as energy harvesting, that is to enable remote charging of low-power electronic devices. Wireless power transfer (WPT) is the process by which a system delivers electrical energy from a power source to the load without any connecting wires. Almost 100 years ago before the advent of the electric grid, the genius inventor Nikola Tesla envisioned a future where huge towers would radiate energy directly into our homes for consumption [147]. But only over the past five years there has been a remarkable interest in researching commercially viable and safe methods of WPT mainly due to the surge in the use of low-power electronic devices like laptops, netbooks, smartphones, wireless sensor nodes, etc. that require regular charging and battery maintenance. It is obvious that WPT products can increase convenience and quality of life but what are not so obvious are the environmental and economic benefits that this technology could offer. There is great potential using WPT to directly power devices like clocks and remote controllers which would drastically reduce the 6 billion batteries

being disposed every year in the world today which is a source of contamination of groundwater and producer of toxic wastes when burnt in incinerators. In other cases where wiring is too expensive, hazardous or impossible WPT may be the only enabling technology.

Presently, several wireless power transfer (WPT) techniques are being pursued and they can be categorized in terms of their underlying power transfer mechanism to understand implications for range, adaptation and efficiency. Far-field WPT is one of the emerging techniques that uses propagating electromagnetic (EM) waves to transfer energy. This method has been successfully used to power radio-frequency identification (RFID) tags, those have no batteries and an operating range of ∼10 meters [148]-[149]. One of the drawbacks with far-field WPT approaches is the inherent tradeoff between directionality and transmission efficiency. There are many examples of radio frequency (RF) and microwave systems that use lasers or high gain antennas to transfer power over kilometer distances at efficiencies of over 90 % [150]-[151]. These systems suffer from the need for sophisticated tracking and alignment equipment to maintain an uninterruptible line of sight (point to point) connection in unstructured and dynamic environments. Alternatively, RF broadcast methods, which transmit power in an omni-directional pattern, allow for power transfer anywhere in the coverage area. In this case, mobility is maintained, but end to end efficiency is lost since power density decreases with a $1/r^2$ dependence, resulting in received power levels many orders of magnitude less than what is transmitted [152]. In order to provide power comparable to a typical wall-mounted dc power adaptor, the system would violate RF safety regulations [153] or has to use a large number of transmitters resulting in an impractical implementation. Therefore, far-field techniques are most suitable for very

low power applications unless they are used in less regulated environments such as military or space exploration.

According to Low *et al.* in [153], inductive coupling, which is non-radiative and near-field, has been one of the leading candidates in achieving wireless power transfer (WPT) at power levels ranging from several microwatts to several kilowatts. Its operating range is limited as power delivery and efficiency degrades rapidly with increasing distance between the transmitting and receiving unit. Inductive coupling, which does not rely on propagating EM waves, operate at distances less than a wavelength of the signal being transmitted [154]. Applications include rechargeable toothbrushes and the recently proliferating "power" surfaces [155]. These techniques can be very efficient, but are limited to transmission distances of about a centimeter. Alternatively, near-field RFID pushes the limit on distance by sacrificing efficiency. Near-field tags have a range of tens of centimeters, but only receive power in the microwatt range with 1-2 % transmission efficiency [148]. Previously demonstrated magnetically coupled resonators used for WPT [156]-[158] have shown the potential to deliver power with more efficiency than far-field approaches, and at longer ranges then traditional inductively coupled schemes. However, this prior work is limited to a fixed distance and orientation, with efficiency falling off rapidly when the receiver is moved away from its optimal operating point. This chapter explores both types of near-field wireless power transfer (WPT) techniques for remote charging of low-power electronic devices namely: (1) inductively coupled wireless power transfer from power lines (see Section 6.1) and (2) strongly coupled wireless power transfer with magnetic resonances (see Section 6.2).

6.1 Inductively Coupled Power Transfer from Power Lines

Inductive coupling has considerably increased in the last ten years because it permits the supply of power to electronic circuits remotely and also provides a means for exchange of data between two sensor nodes. Today in the industry, the most important part of inductive coupling applications is related to radio frequency identification (RFID) [159]. RFID is used for contactless smartcards or to sort and locate travelling objects, for e.g. postal parcels. In many buildings, door keys have been replaced by the use of electromagnetic badges. However, existing technologies that utilize near field wireless power transmission such as RFID tags generally operate only over limited distances with very low efficiency. Other than RFID application, power transmission and remote sensing by inductive coupling are also widely used in the field of sensors. The research work carried by Yang *et al.* [160] is to explore the concept of distributed sensing along power lines using sensornets. Power lines span long distances and sensing from remote substations, as is currently done, provides poor resolution. Hence distributed sensing along the length of the power line with intelligent sensors powered by inductive coupling would allow extraction of important local information from each sensor for a long period of time. Many possibilities of incorporating inductive coupling in medical applications as well are foreseen for examples permanent implants, supervising various parameters like the insulin rate for diabetic or the intraocular blood pressure and excitation of a retina with defective photoreceptors reported in [161].

Although, many research works on inductive coupling power transfer (ICPT) have been reported in the literature for instances Boys *et al.* in [162] and Kurs

et al. in [163], there is only a few research works on magnetic energy harvesting for wireless sensor nodes, like Yang *et al.* in [160]. They have proposed the use of inductive coupling from high power transmission and distribution lines to power the sensornets for power grid monitoring. In this chapter, the proposed magnetic energy harvesting idea is different from what Yang *et al.* have suggested. The main objective of this research work is to harvest the stray magnetic energy generated by electrical power cables deployed around the residential, commercial and industrial buildings. Through inductive coupling, the stray magnetic energy is harvested to power the wireless sensor nodes for condition-based maintenance of electrical energy system and equipment.

6.1.1 Magnetic Energy Harvester

The research work on magnetic energy harvesting via inductive coupling utilizes induction as the energy harvesting technology. It is based on the combination of the famous Ampere's law and the Faraday's law of induction. Ampere's law describes the magnetic flux density of the stray magnetic energy source available for induction by the surge coil. Faraday's law of induction states the induced electromotive force, V_{emf}, in a surge coil, which is directly proportional to the time rate of change of magnetic flux, ϕ, through the winding loop. The induced voltage, V_{emf}, generated at the output of the surge coil is processed by a power management unit and stored in an energy storage device i.e. capacitor. This stored energy is then used to power up the operation of a wireless sensor node.

In the experimental tests, the characterization process of the magnetic energy harvester is divided into two parts namely (1) the magnetic energy source i.e. mag-

netic field containing the magnetic energy governed by Ampere's law and (2) the magnetic energy harvester i.e. toroid-based surge coil wounded with many turns of wires, N, as per described by the Faraday's law of induction. The magnetic energy source is first characterized using the experimental setup shown in Figure.6.1. Since the magnetic flux density, B, along a current-carrying electrical power cable is a function of the current, I, flowing through the power cable and the radius distance, r_a, between the measurement point and the centre of the conductor, it is possible to determine the magnetic field lines that best described the magnetic energy generated by the current flowing in the power line.

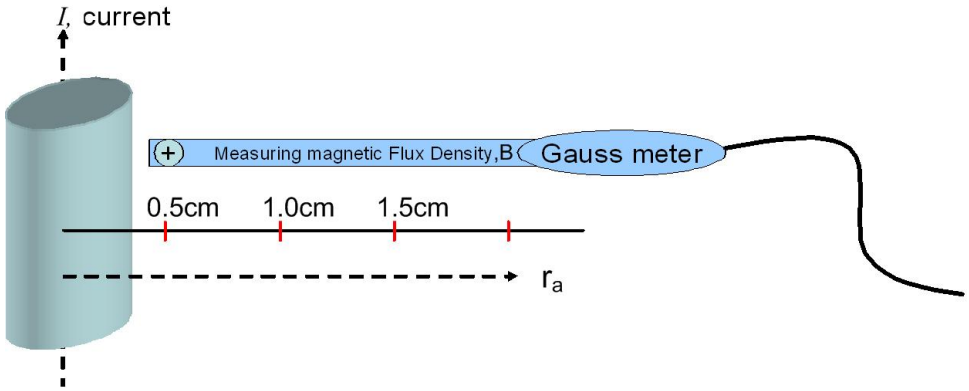

Figure 6.1: Characterization of magnetic energy source based on Ampere's law

The second part of the characterization process is to determine the voltage induced by the toroid-based magnetic energy harvester, constructed by physically winding N number of turns of copper wires on a circular ring shaped ferrite magnetic core as shown in Figure.6.2. When the current-carrying power cable is laid through the centre of the ferrite core as illustrated in Figure.6.3, magnetic field lines are generated. These magnetic field lines circulate around the ferrite core and its copper winding and an AC voltage is induced. The induced voltage is proportional to the rate of change in the number of flux lines enclosed by the loop per

unit time and the number of winding turns, N, in the loop. In other words, the induced voltage is related to the magnetic field, B, the loop area, A, the winding number of turns, N, and the frequency of the current, f.

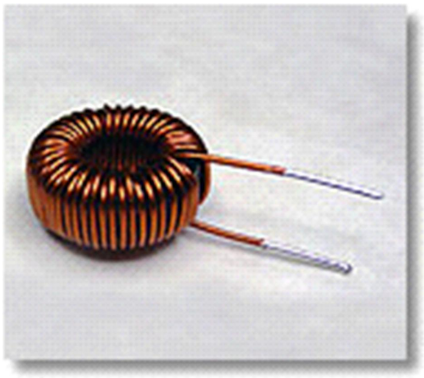

Figure 6.2: Top view of ferrite core windings

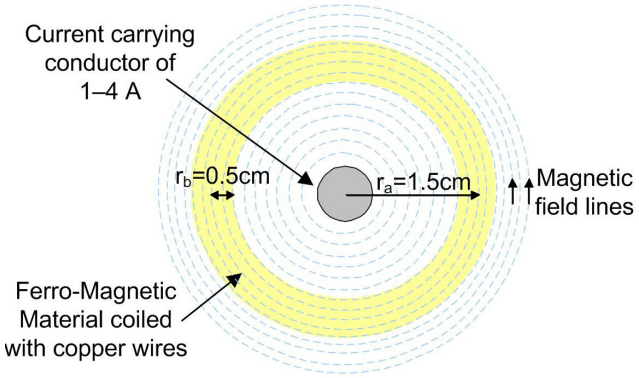

Figure 6.3: Top view of ferrite core with current carrying conductor

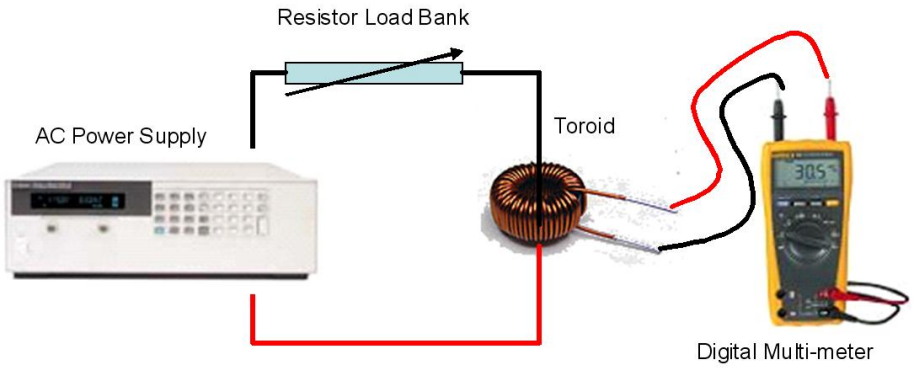

Figure 6.4: Characterization of magnetic energy harvester based on Faraday's law

The experimental setup to measure the induced voltage, V_{emf}, ($= \omega NBAsin(\omega t)$ where the negative sign is due to Lenz's law) from the toroid-based magnetic energy harvester via the current-carrying power cable is shown in Figure.6.4. The current flowing in the circuit is varies from 1-4 A by adjusting the voltage knob of the AC power supply. Due to the high current along the circuitry, the high wattage resistor load bank is utilized. A summary of the measured and calculated

induced emf voltage for difference current flowing in the primary side power line is tabulated in Table.6.1.

Table 6.1: Measured and calculated induced emf voltage for difference current flowing in the power line

Measured and Calculated Induced EMF Voltage $V_{emf} = \omega NBA\sin(\omega t)$							
I, Current flowing in power line	μ_r	ω $2\pi f$ f at 50Hz	N	B $\mu_0\mu_r I/2\pi r_a$ r_a at 1.5cm	Area (π r_b^2) r_b~0.5cm	Calculated V_{emf} (V_{rms})	Measured V_{emf} (V_{rms})
4A	1500	100π	500	0.08T	2.5x10^{-5} π	0.987	1.025
3A	1500	100π	500	0.06T	2.5x10^{-5} π	0.740	0.748
2A	1500	100π	500	0.04T	2.5x10^{-5} π	0.493	0.449
1A	1500	100π	500	0.02T	2.5x10^{-5} π	0.247	0.194

It can be observed from Table.6.1 that as the current flowing in the mainstream power line increases from 1 A to 4 A, the magnetic field, B, obtainable at 1.5 cm away from the centre of the conductor also increases from 0.02-0.08 T. For that reason, the induced voltage generated at the output of the toroid magnetic energy harvester has been increased. During the characterization process, the r_a distance of 1.5 cm is set as the reference point based on the practical considerations of the physical diameter of the power cables and the space taken by 500 turns of copper windings.

6.1.1.1 Performance of Magnetic Energy Harvester

To study how the magnetic energy harvester performs under various operating conditions, experiments were carried out on the designed magnetic energy harvester. Referring back to Table.6.1, the open-circuit voltage of the harvester, which consists of one toroid coil, is quite low, ranging from 0.2 V to 1 V. In order to achieve a higher output voltage, three sets of ferrite cores are connected in series. The

improved version of the magnetic energy harvester is connected to different loading resistances and the source current flowing in the power line is varied between 1 A to 4 A. This is to find out the performance of the harvester for various input and output operating conditions. The data collected are plotted into the current vs voltage (IV) curve and power curve as shown in Figures.6.5 and 6.6 respectively.

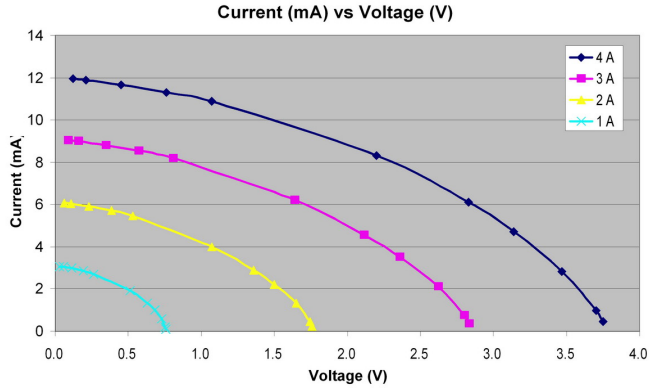

Figure 6.5: Voltage vs current curve for various input currents

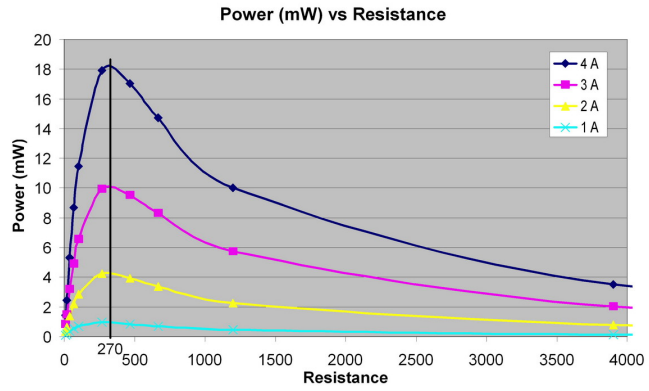

Figure 6.6: Electrical power harvested over a range of load resistances for different input currents

From the IV curve shown in Figure.6.5, it can be seen the obtainable open-circuit voltage for different currents flowing in the power line has increased by around 3 times, ranging from 0.7 V to 3.5 V. Although the output voltage of harvester has already been increased by series connecting three ferrite coils together,

the induced voltage at some operating points, especially when the magnetic field is weak due to low current flows in the AC power line, is considerable low. As such, the magnetic energy harvester may not be able to drive the electronic output load. This low output voltage generated from the magnetic energy harvester would pose challenge on the design of the power management circuit. Another analysis carried out is on the power curve shown in Figure.6.6 where maximum power is attainable at load resistance of 270 Ω. Referring to Figure.6.6, with the source current of 1-4 A flowing in the AC power line, the maximum electrical power available for harvesting ranges from 1-18 mW. The challenge here is that when the source current is low say 1 A, the radiated magnetic field becomes weak and so the maximum power available for harvesting drops tremendously to around 1 mW or so and may not be sufficient to power the RF transmitter load continuously. Hence, a power management circuit designed to address the low voltage and low power challenges of the magnetic energy harvester has been proposed.

6.1.2 Power Management Circuit

Based on the analysis and characterization performed on the designed magnetic energy harvester, the concept of harvesting stray magnetic energy via inductive coupled power transfer is found to be a viable solution for powering the low-power wireless sensor nodes. The block diagram in Figure.6.7 illustrates the energy harvesting scheme and its application for wireless sensor nodes. Since the voltage source is inherently AC from the power supply along the power line, thus the induced voltage, V_{emf}, would appear as an alternative voltage source to the connected load. However, the wireless sensor node (i.e. AM RF transmitter) requires a DC source to operate, therefore the induced voltage must be rectified to DC and regu-

lated prior to powering up the device. This is achieved by using a voltage doubler instead of a standard diode-based full-wave rectifier, which is capable of rectifying and amplifying the low AC voltage to a higher DC voltage.

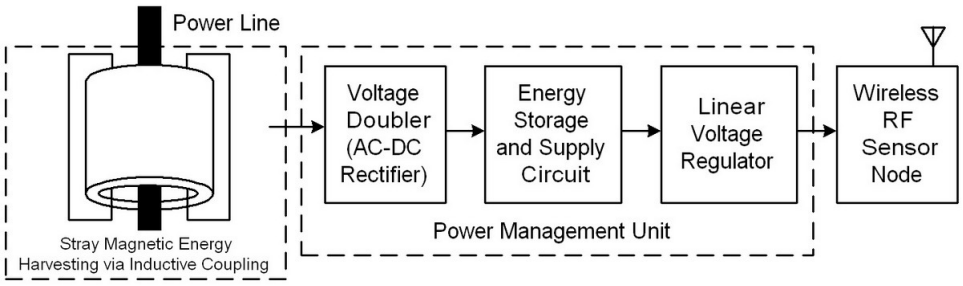

Figure 6.7: Block Diagram of Energy Harvesting and Wireless RF transmitter System

Referring to the power curve shown in Figure.6.6, the amount of power that is generated across the designed ferrite core wounded with copper wires is in few milli-watts range. With the limited power generation level, it is not feasible for the magnetic energy harvester to power the wireless radio frequency (RF) transmitter continuously. To overcome that, an effective energy storage and supply circuit discussed by Tan *et al.* in [166] is designed and inserted in-between the energy source and the wireless load. This is to ensure that the electrical energy is stored in the capacitor and the energy stored is sufficient to sustain the operation of several RF transmissions. When the energy level of the storage capacitor in the power management unit is sufficient for operations, the RF transmitter would then start to transmit digital encoded information to the RF receiver located at some distant away. The amount of energy consumed by the transmitter is dependent on the number of 12-bit digital encoded data to be transmitted.

The design specifications of the experiments to be carried out in the research

work have been defined according to the practical field condition. The specifications are stated as follows: (1) source frequency of 50 Hz, which is the operating frequency in Singapore context; (2) electrical current flowing in the mainstream power line is set to be 4 A and (3) number of turns in each winding is made to 500 turns. The advantage of the magnetic energy harvester is that it provides flexibility in the design parameters i.e. N, ω, B involved which can be designed accordingly to suit different operating conditions of the sensor node in certain specific applications. The experimental setup of the entire magnetic energy harvesting system which consists of the stray magnetic energy harvester, power management unit and wireless RF transmitter is shown in Figure.6.8.

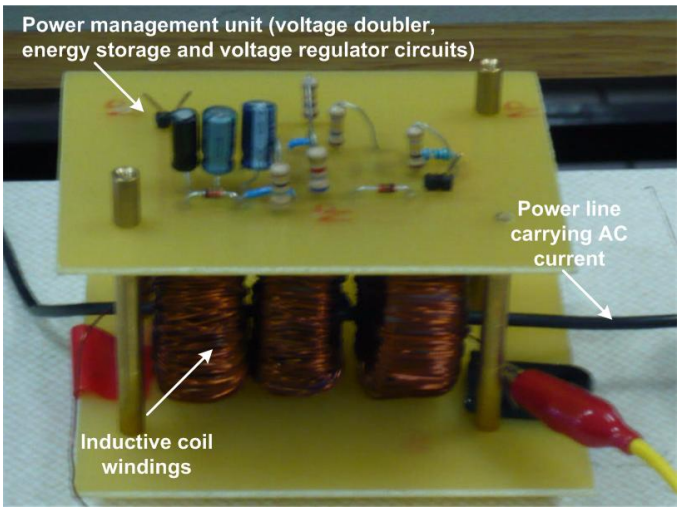

Figure 6.8: Photograph of the magnetic energy harvester system powering the wireless RF transmitter

Based on the electrical power requirements of the wireless RF transmitter and the electrical characteristic of the magnetic energy harvester i.e. N, ω and B, a magnetic energy harvesting prototype has been designed and successfully implemented. The schematic drawing of the prototype of the magnetic energy harvesting system is shown in Figure.6.9. The prototype is designed to be similar

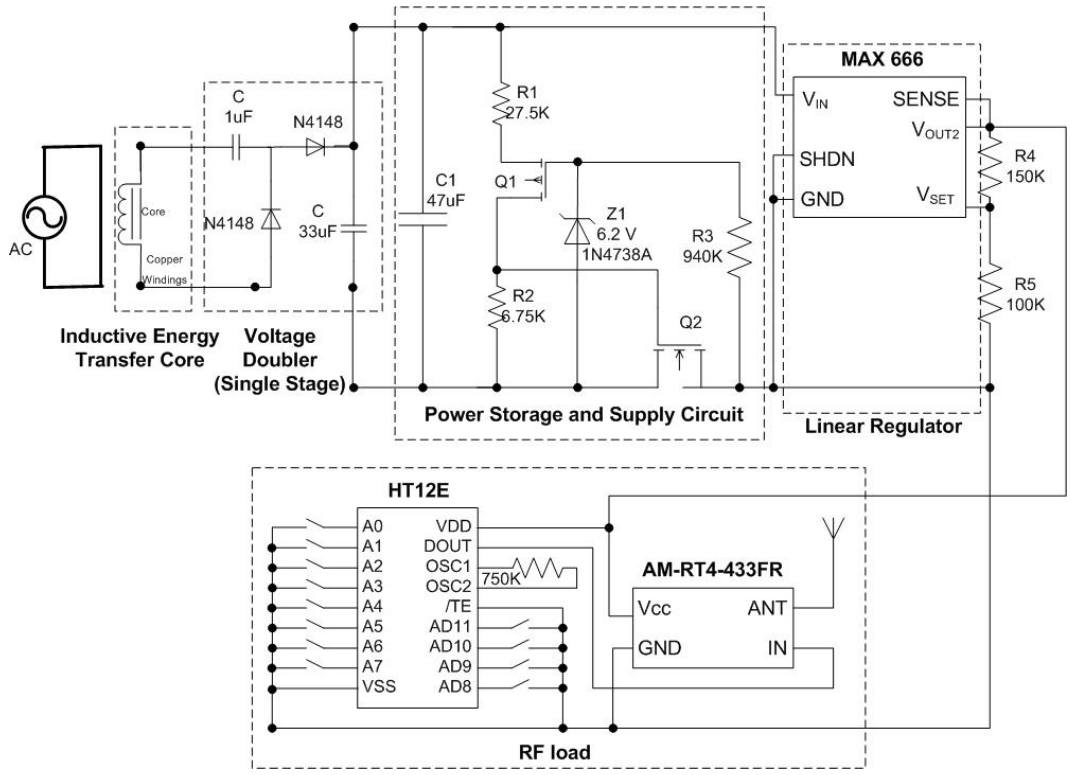

Figure 6.9: Schematic drawing of the magnetic energy harvesting system

to a transformer secondary winding which is capable of inducing AC voltage from the current carrying conductor single-turn primary winding to power up a wireless RF transmitter. The induced V_{emf} is first rectified to DC voltage by using a voltage doubler. Once the voltage from the secondary coil of the transformer is rectified, the electric current would flow to charge the electrolytic storage capacitor C1 of the power storage and supply circuit. The Q1 and Q2 MOSFETs residing in the power storage and supply system acts like a control switch that would initiate on or off signal to the storage capacitor to release the stored energy. Initially, both Q1 and Q2 are off so the ground lines of the linear regulator (MAX666) and the RF AM transmitter (RTFQ1- 433) are disconnected from C1. As C1 charges beyond the preset voltage of around 6.8 V (the preset voltage level is determined according to the induced voltage, V_{emf} in Figure.6.9 and the voltage level is preset by the zener diode Z1 as 6.2 V and the gate-source junction of Q1 as 0.6 V), the control switch

Q1 turns on. The moment when Q1 is on, there is a voltage drop across R2 that is higher than the threshold gate-source voltage ($V_{gs(th)}$) of Q2 in order to activate the control switch Q2. Once Q2 is activated, Q1 is latched. This connects the ground lines of MAX666 and AM-RTFQ1-433 with C1, allowing C1 to discharge through the circuitry. MAX666 acts like a low power series linear regulator, which produces a stable +3.3 V for the serial ID encoder (HT12E) and the RF AM transmitter (AM-RTFQ1-433) throughout the discharge of C1. When the voltage across C1 drops below around 4 V, the voltage drop across R3 causes Q1 to turn off and hence in turn deactivates Q2 from the latched stage. When this happens, the ground lines of MAX666 and AM-RTFQ1-433 are disconnected from C1 and the discharge of C1 is stopped. As the secondary coil of the transformer continues to induce V_{emf} to the voltage doubler and increases the voltage on C1, the cycle starts again.

6.1.3 Experimental Results

An experimental platform, which consists of a 220/230 V_{ac} power supply connected to a bank of load resistances of 60 Ω, has been setup as shown in Figure.6.23 to emulate the electrical current of 1 A to 4 A flowing in the power line [167]. Since the primary side power line is AC, the induced emf would be AC voltage. This experimental setup is used as a testing platform to evaluate the performance of the magnetic energy harvesting system.

Figure.6.11 shows the waveforms of the induced AC voltage, V_{emf}, output of the stray magnetic energy harvester and the output DC voltage of voltage doubler circuit. It can be observed that the induced voltage signal is a distorted sinusoidal wave rather than a smooth sinusoidal wave. The reason for this phenomenon may

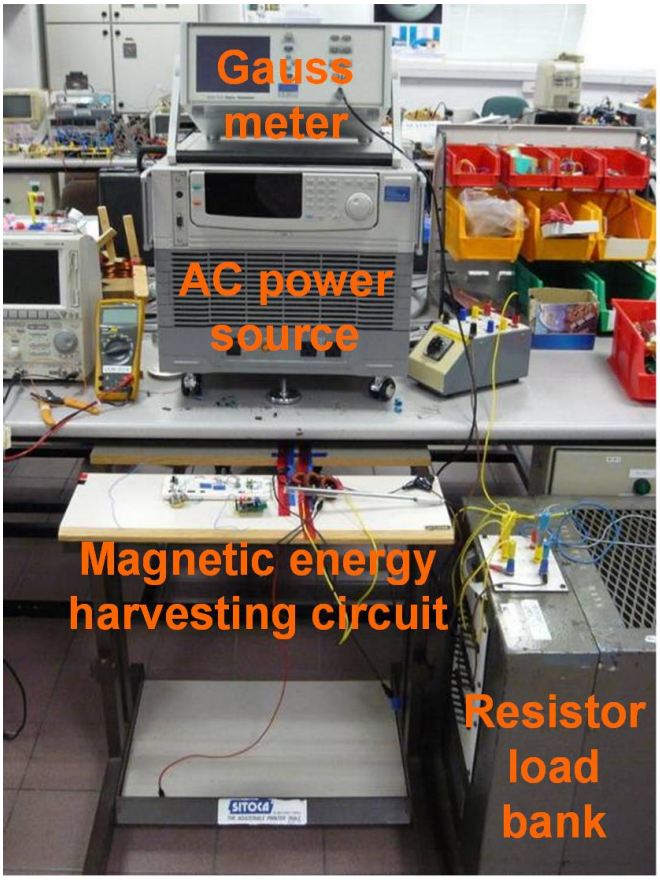

Figure 6.10: Experimental testing platform for the magnetic energy harvesting

be due to the magnetic hysteresis effect and the magnetic saturation of the toroid core.

Once the induced AC voltage, V_{emf}, of the stray magnetic energy harvester is inputted to the voltage doubler, the voltage doubler circuit outputs a DC and doubled voltage. By doing so, the design of the power management would be simpler. The voltage from the secondary coil of the transformer is rectified in the voltage doubler and then electric charge is accumulated on the electrolytic storage capacitor C1 of the power storage and supply circuit. The charging and discharging voltages of C1 are 4 V and 6.72 V respectively (as shown in Figure.6.12). The amount of electrical energy stored in the electrolytic capacitor C1 with capacitance

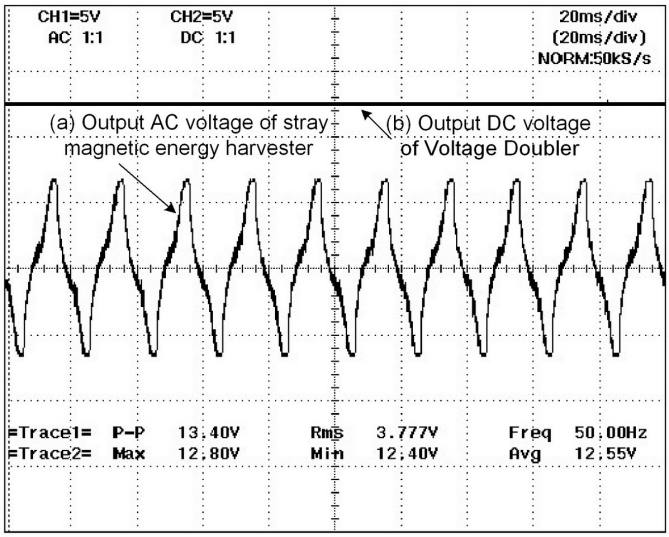

Figure 6.11: Waveforms of (a) Output AC voltage of stray magnetic energy harvester and (b) Output DC voltage of Voltage Doubler

value of 47 μF is calculated to be 685 μJ.

For each 12-bit digital data, the time taken for one transmission is 20 msec i.e. 10 msec of active time and 10 msec of idle time. During the active transmission time, the supply voltage and current of 3.3 V and 4 mA respectively are consumed by the RF transmitter load. As for the remaining time of 10 msec, the RF transmitter load is operating in idle mode which means that very minimal amount of energy would be consumed, so it is reasonable to exclude the power being consumed by the RF transmitter load during the idle time. By calculation, the average power and hence the energy consumed by the RF transmitter load for one digital encoded data transmission are 13.2 mW and 132 μJ respectively. Using the harvested stray magnetic energy in the power lines via inductive coupling, the experimental results shown in Figure.6.12 have verified that the RF transmitter is able to successfully transmit more than 10 digital encoded data over to the receiver remotely. This is verified by the number of digitally encoded data packets received at the RF receiver side.

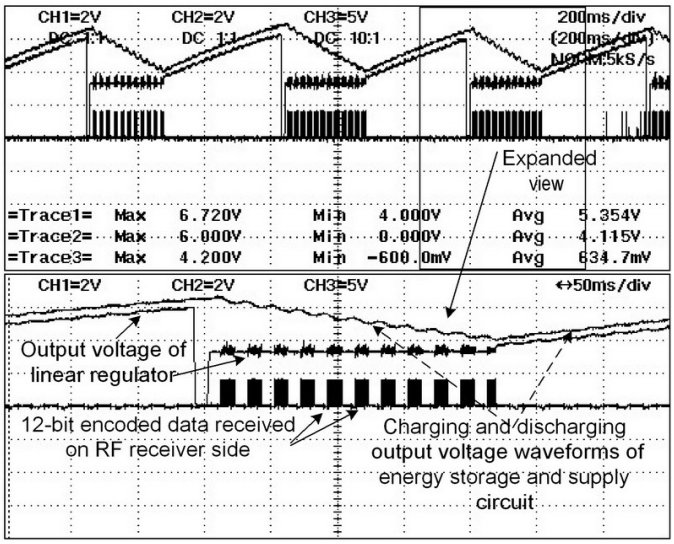

Figure 6.12: Waveforms collected at the RF receiver side to display number of 12-bits encoded data packets received using the harvested energy

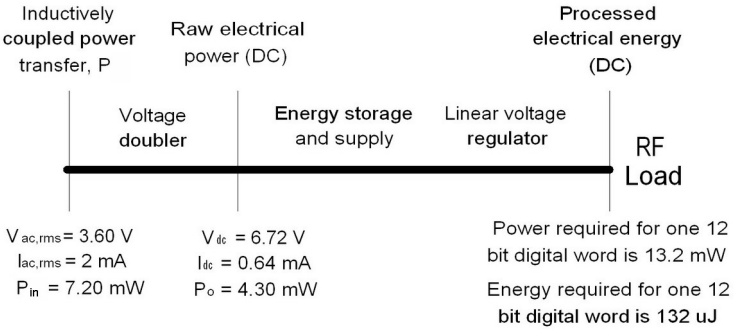

Figure 6.13: Line diagram of the power flow in the system

With the experimental platform, the power harvested and consumed by the source and the load respectively can be measured and they are illustrated in Figure.6.13. The line diagram shows the flow of power from the harvested power through inductive coupling to the power management circuit which consists of the voltage doubler circuit, energy storage and supply circuit and the regulator circuit and then to the RF transmitter load. It can be seen that the power generated by the source is not sufficient to power the load directly and continuously, therefore an energy storage element with supply control feature is placed in between the source

and the load. By doing so, the operation of the RF transmitter is no longer kept running instead it is more like intermittent type of operation. Although the amount of energy that the stray magnetic energy harvester can harness is relative small as compared to other energy harvesting sources i.e. solar and wind, nevertheless, the small amount of energy of 685 μJ is sufficient to power its RF transmitter load to transmit several digital encoded data in wireless transmission. The experimental results demonstrating the successful RF transmission using the harvested energy are shown in Section V. This imply that the magnetic energy harvester is able to meet its objective.

6.1.4 Summary

In this research work, the inductive coupling concept has been utilized for wireless power harvesting from power lines. Based on the Faraday's law of induction and Ampere's law, a toroid-based surge coil wounded with 500 turns of wires has been designed as a magnetic energy harvester. The magnetic energy radiated by a 50 Hz, 4 A, 230 V_{ac} current carrying power line/cable is harvested by the designed magnetic energy harvester via inductive coupling to power a wireless sensor node. The prototype of the inductive energy transfer system has been designed and developed to convert harvested AC voltage into DC voltage which then charge the storage capacitor until the preset energy storage level. After which, the stored energy is released to the linear regulator to provide a constant 3.3 V to the RF AM transmitter that requires 132 μJ of energy for communication. Finally, the self-powered wireless RF transmitter working prototype is capable of transmitting 10 packets of 12 digital bits information over a range of up to 70 meters in open field with line of sight.

6.2 Wireless Power Transfer via Strongly Coupled Magnetic Resonances

In recent years, mobile gadgets such as laptops, i-Pods, i-pads, mobile phones and digital cameras have become so common in the consumer world. These electronic devices and gadgets are typically powered by either the AC mains supply through power cords or solely alkaline/rechargeable batteries that need to be replaced and/or recharged regularly. People are getting so tired of the mess as illustrated in Figure.6.14 created by power cords and chargers of multiple electronic devices and the trouble of not able to locate these accessories when there is a need to recharge. In cases when people forget to replace the alkaline batteries in some electronic products, it damages the product due to leakage and chemical reactions which may lead to the disposal of the whole product. In other cases, lots of electrical wirings laid out from the mains power supply to the users is too expensive and hazardous. Apart from the technical issues, people are also concerned of the environmental and economical impacts arising from the disposal of batteries.

Figure 6.14: Tangled mess of power cords and chargers

Because of these concerns, there is an emergence of interest in the wireless power transfer (WPT) technology to deal with these challenges. WPT is neither a crazy idea nor a very new concept. If WPT can be realized in practical applications, the outcome of WPT technology could potentially revolutionize the way electrical energy is used for consumer electronic devices and portable gadgets and thereby reduce the dependence on plug-in power supply and disposable batteries to achieve the ultimate goals of *Wireless* and *Batteryless* electronic products. There are several wireless charger based products [168] i.e. Powermat, WildCharge, Fulton Innovation - eCoupled, Powercast, etc. already available in the market. These radiative and non-radiative WPT products are mostly for near field applications with short distance of few centimeters. Some application examples include the commonly used electric toothbrush chargers that transfer power to the brush handle through magnetic induction, wireless inductive charger for i-Phone [169], etc. In order to elongate the wireless energy transmission distance, WPT with magnetic resonance was first reported by Kurs *et al.* [163] in the literature and subsequently the concept has also been implemented and demonstrated by companies like Sony [170]. The prototype system developed by Sony is able to reach up to 60 % power efficiency with maximum power delivery at 60W for a range of 50 cm. However, as the distance between the coils increases by a little further, the efficiency and power throughput of the WPT system drops tremendously. Hence, there are still lots of room for improvement in the WPT technology used in products. What is lacking in these products is the combination and extension of WPT into a system to be incorporated in our daily-life.

In this chapter, the research focus is placed on the analysis, design and implementation of wireless power transfer (WPT) resonator coils with optimal efficiency

and form factor to charge the consumer electronic devices and portable gadgets in a connected manner. The research work has been divided into two parts namely: (1) to explore different ways to improve the efficiency of the WPT technique operating in a strongly coupled regime and (2) to network the designed high-efficiency WPT resonator coils together so as to achieve the ultimate goals of wireless and batteryless electronic products. Several design factors, which include coil size, coil structure and configuration and distance between coils, that could enhance the efficiency of the WPT system are explored and experimentally verified. The optimized resonant coils are then networked together to receive and relay electrical power from one resonant coil and to another nearby resonator coil. By doing so, the wireless power transmission distance between each gadget can be reduced and the form factor of the resonator coil can become smaller in size to fit into the mobile gadget. It is thus more viable to utilize WPT technology as a self-sustaining portable energy source for the mobile gadgets

6.2.1 Concept Principles of WPT with Magnetic Resonance

The concept of wireless power transfer (WPT) is very much similar to an air-core transformer where no ferromagnetic material is inserted between the primary and secondary sides of the transformer. The source power of alternating frequency is connected to the primary coil, setting up a constantly changing magnetic field which induces an electromotive force in the secondary coil according to Faraday's Law of Induction. This electromotive force then drives an induced current in the secondary coil. Efficiency of a transformer is maximized by having the secondary coil tightly wound around the primary in order to maximize the coupling between the coils. As the magnetic field strength, which is given by the Biot-Savart equation

as,

$$|dB| = \frac{\mu_o I dl}{4\pi r^2} \tag{6.1}$$

decreases with the square of the distance, r, separating the secondary coil from the primary coil, the magnetic coupling between the coils greatly reduces, hence the efficiency of the transformer or the WPT system. To strengthen the magnetic coupling, magnetic resonance for wireless power transfer has been discussed by Kurs *et al.* in [163] such that both the primary (transmitting) and secondary (receiving) coils are tuned to the same resonant frequency, making use of magnetic resonance to compensate for the weakened coupling due to the increase in separation distance. Magnetic resonance occurs when magnetic waves of certain frequencies are absorbed by an object, causing that object to resonate. The frequency absorbed by an object which causes that object to resonate is dependent on many variables, including molecular structure, shape, and size/length of the object. In an experiment conducted by Lucas *et al.* [171], the authors have a primary coil emitting evanescent, magnetic waves that a secondary coil absorbs. Evanescent waves are different from ordinary waves, because evanescent waves oscillate in time, but diminish over distance [171]. Assuming the coils are of the same size, shape, and mass, at a certain frequency (the resonant frequency) the primary coil will resonate and cause the secondary coil to resonate as well. An overview of the WPT system is shown in Figure.6.15.

According to Kurs *et al.* in [163], intuitively, two resonant objects of the same resonant frequency tend to exchange energy efficiently, while dissipating relatively little energy in extraneous off-resonant objects. In systems of coupled resonances, there is often a general "strongly coupled" regime of operation. If one can operate

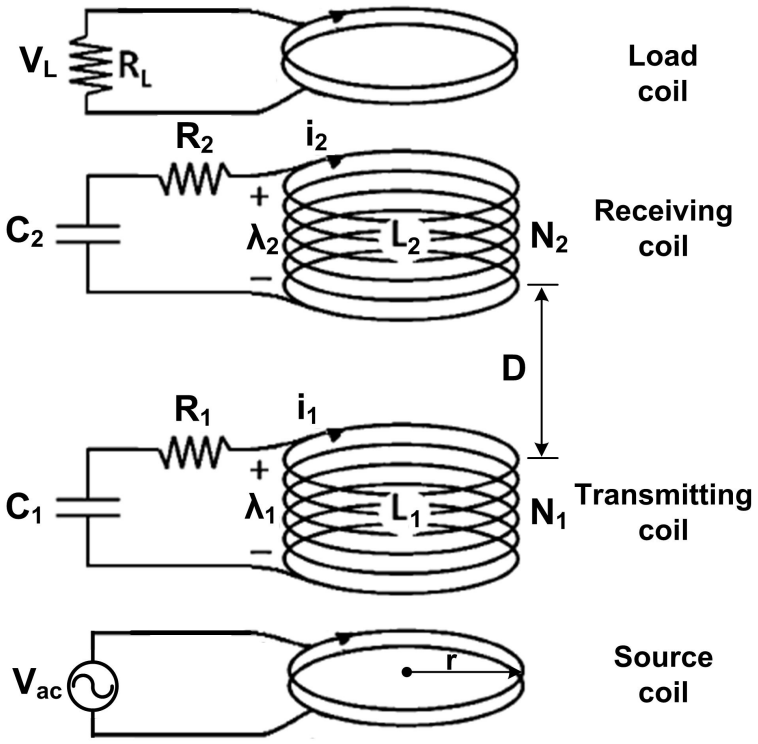

Figure 6.15: Overview of WPT system

in that regime in a given system, the energy transfer is expected to be very efficient. Mid-range power transfer implemented in this way can be nearly omnidirectional and efficient, irrespective of the geometry of the surrounding space, with low interference and losses into environmental objects. Based on this magnetic resonance concept, the transmitting and receiving coils of the WPT system are made of conducting loops with a capacitor attached to the ends. For this LC configuration, the resonant frequency of the circuit is determined by the equation

$$\omega = \frac{1}{\sqrt{LC}} \tag{6.2}$$

where ω is the resonant angular frequency, L is the inductance of the coil and C is the capacitance value of the external capacitor connected in parallel to the coil. At resonant frequency, ω, the RLC circuit acts like an oscillator/resonator that

transfers energy between the capacitor, C, and the inductor, L, where the collapsing magnetic field of the inductor generates an electric current in its windings which in turn charges the capacitor and then the discharging capacitor provides an electric current that energizes the magnetic field in the inductor. This energy conversion process repeats itself periodically. When the RLC circuit is set to operate at its resonant frequency, the complex part of the circuit's impedance, which is expressed as,

$$Z = R + j\left(\omega L - \frac{1}{\omega C}\right) \tag{6.3}$$

becomes zero and so the impedance of the electrical circuit is at its minimum, $Z = R$. As such, it is desirable to design the RLC circuit to operate at its resonant frequency, as expressed by eqn.6.2, by selecting the appropriate L and C based on the construction of the coils and the capacitors.

In this wireless power transfer (WPT) research work, the objective is to explore different ways to improve the efficiency of the WPT technique operating in the strongly coupled regime. The efficiency , η, of the WPT system with magnetic resonance in accordance to the coupled-mode theory, is a function of the coupling-to-loss ratio, κ/Γ, where κ is the coupling coefficient of the coils and Γ is the intrinsic loss rate, and it is expressed in [163] as,

$$\eta = \frac{\frac{\Gamma_W}{\Gamma_D}\frac{\kappa^2}{\Gamma_S\Gamma_D}}{\left[\left(1+\frac{\Gamma_W}{\Gamma_D}\right)\frac{\kappa^2}{\Gamma_S\Gamma_D}\right] + \left[\left(1+\frac{\Gamma_W}{\Gamma_D}\right)^2\right]} \tag{6.4}$$

where the source and device are identified by subscript S and D and an external load (subscript W) acts as a circuit resistance to the connected device. Referring to [163], Kurs *et al.* state that the efficiency of WPT system is maximized

when $\Gamma_W/\Gamma_D = [1+(\kappa^2/\Gamma_S\Gamma_D)]^{1/2}$. In addition, for two identical coils, $\Gamma_S = \Gamma_D = \Gamma$, the efficiency of the wireless power transfer (WPT) system can thus be expressed as,

$$\eta = \frac{\frac{\kappa^2}{\Gamma^2}\sqrt{1+\frac{\kappa^2}{\Gamma^2}}}{\left[\left(1+\sqrt{1+\frac{\kappa^2}{\Gamma^2}}\right)\frac{\kappa^2}{\Gamma^2}\right]+\left[\left(1+\sqrt{1+\frac{\kappa^2}{\Gamma^2}}\right)^2\right]} \tag{6.5}$$

For the WPT system to be efficient, the magnetic fields of the coils must be strongly coupled such that the coupling coefficient of the coils, κ, is high and the intrinsic loss rate, Γ, is low. If that is the case, $\kappa/\Gamma \gg 1$ and the efficiency of the WPT system with magnetic resonance expressed in eqn.6.5 can be further deduced as follows:

$$\eta = \frac{\frac{\kappa}{\Gamma}}{\frac{\kappa}{\Gamma}+1} \approx 1 \tag{6.6}$$

Hence, to maximize the efficiency of the WPT system, one important factor to be considered is the coupling coefficient, κ, of the coils [163]is given by,

$$\kappa = \frac{\omega M}{2\sqrt{L_1 L_2}} \tag{6.7}$$

where L_1 and L_2 are the inductances of the primary and secondary coils respectively. M is the mutual inductance of the coils, derived from Biot-Savart's law using simple approximations [172], which is expressed as,

$$M = \frac{\mu_o \pi N^2 r^2 r_b^2}{2\left(r^2+D^2\right)^{1.5}} \tag{6.8}$$

where $\mu_o = 4\pi$ x 10^{-7} NA^{-2} is the permittivity of free space. r and r_b are the primary and secondary coil radius respectively. N is the number of turns in the coil and D is the distance between coils. Another consideration factor is the intrinsic

loss rate, Γ, of the WPT system, which is discussed in [163] with the following equations, representing the ohmic or absorption loss, R_{ohmic}, and radiation loss, $R_{radiative}$. The intrinsic loss rate is defined by the following equation,

$$\Gamma = \frac{R_{ohmic} + R_{radiative}}{2L} \tag{6.9}$$

For a coil with N turns, radius r, height h and made of an electrically conducting wire with conductivity of σ, the ohmic resistance, R_{ohmic}, is expressed as,

$$R_{ohmic} = \frac{l}{4\pi a}\sqrt{\frac{\mu_o \omega}{2\sigma}} = \frac{rN}{2a}\sqrt{\frac{\mu_o \omega}{2\sigma}} \tag{6.10}$$

where the total length, l, of the wire with radius of a can be estimated as $2\pi r * N$. Other than ohmic loss, there is also power loss in the radiation resistance, which is given by,

$$R_{radiative} = \sqrt{\frac{\mu_o}{\varepsilon_o}}\left[\frac{\pi N^2}{12}\left(\frac{\omega r}{c}\right)^4 + \frac{2}{3\pi^3}\left(\frac{\omega h}{c}\right)^2\right] \tag{6.11}$$

According to Kurs *et al.* [163], the first term in eqn.6.11 is a magnetic dipole radiation term (assuming $r \ll 2\pi c/\omega$, where c is the speed of light) and the second term is due to the electric dipole of the coil. The second term is much smaller than the first term for this wireless power transfer (WPT) system parameters and so the second term of eqn.6.11 is ignored for simplicity. Hence, by substituting for ω and c, the radiative resistance is simplified into,

$$R_{radiative} = \sqrt{\frac{\mu_o}{\varepsilon}}\left[\frac{4\pi^5 N^2}{3}\left(\frac{r}{\lambda}\right)^4\right] = 15600\pi^2 N^2\left(\frac{r}{\lambda}\right)^4 \tag{6.12}$$

As mentioned earlier, for a system to operate in the strongly coupled regime, the term κ^2/Γ^2 must be greater than 1 so as to achieve a efficient WPT system.

Referring back to eqns.6.7 and 6.9, the coupling-to-loss ratio, κ/Γ, can be expressed as follows:

$$\frac{\kappa}{\Gamma} = \frac{\omega M L}{(R_{ohmic} + R_{radiative})\sqrt{L_1 L_2}} \tag{6.13}$$

The basic configuration of the transmitting and receiving coils is assumed to be the same dimensions and the WPT system is in tuned resonance. By doing so, eqn.6.13 can be further elaborated, by substituting $L_1 = L_2$ and the radius of both coils to be equal, $r = r_b$, as follows,

$$\frac{\kappa}{\Gamma} = \frac{\mu_o \pi \omega r^3}{(r^2 + D^2)^{1.5}} \left[\frac{N}{\frac{1}{a}\sqrt{\frac{\mu_o \omega}{2\sigma}} + \frac{\pi N r^3 \omega^4}{6c^4}\sqrt{\frac{\mu_o}{\varepsilon_o}}} \right] \tag{6.14}$$

Referring to eqn.6.14, it can be observed that there are some prominent factors in the equation that have effects on the coupling-to-loss ratio, hence the efficiency of the wireless power transfer (WPT) system. These factors include the conductivity and radius of the wire, the coil size i.e. radius and number of turns, the distance between two coils and the operating frequency of the WPT system. As can be seen in eqn.6.14, the equation is highly interdependent on various design factors, hence there is a need to find an optimum configuration for the WPT system. By conducting simulations and experiments, the relationships between these design factors and the efficiency of the system are determined.

6.2.2 Simulation Results

In order to improve the efficiency of the WPT system, four different simulations were conducted to determine the relationships between the efficiency of the system and the design factors: (1) frequency, f, (2) coil radius, r, (3) number of winding

turns in a coil, N, and (4) distance, D, between two coils [173]. All the simulations are based on the efficiency and coupling-to-loss-ratio equations expressed in eqns.6.6 and 6.14 respectively.

6.2.2.1 Simulation of Efficiency vs Frequency

The basic configuration of the two cylindrical coils to be used in this simulation is defined as follows: the coil radius, r, of 7.5 cm is made of 5 winding turns, N, of copper wire (SWG12) with conductor radius, a, of 0.13208 cm and conductivity of $59.6*10^6$ S/m. The separation distance, D, between the two coils is 10 cm. The efficiency, η, of the wireless power transfer (WPT) system is simulated over a range of operating frequency from 1 Hz to 1000 GHz and the simulation results are plotted in Figure.6.16.

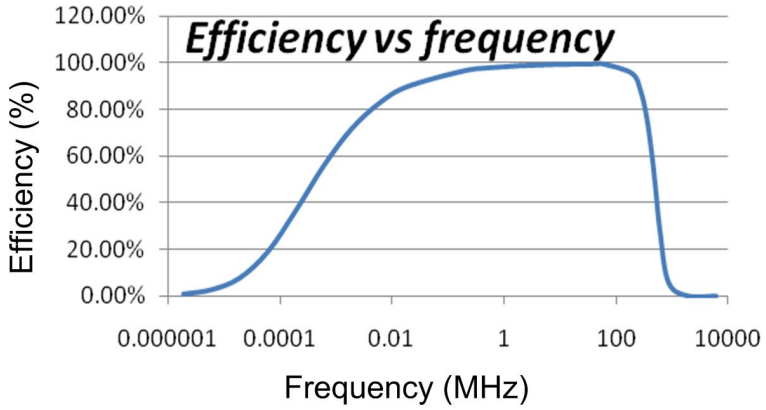

Figure 6.16: Efficiency of WPT system for various operating frequency

It is observed from Figure.6.16 that there exists a band of frequencies between 1-1000 GHz whereby the efficiency of the WPT system is optimal. This band of optimum efficiency is the strongly coupled regime where $\kappa/\Gamma \gg 1$ and maximum power transfer takes place. As the operating frequency shifts away from

the strong coupled regime, the WPT system efficiency starts to decrease. At lower frequency region, the coupling between the coils becomes weak as illustrated in eqn.6.7. Similarly, at higher frequency region, the power losses in the ohmic and radiative resistances become prominent as illustrated in eqn.6.9. It is only when the coupling-to-loss ratio balances will the efficiency of the WPT system be high.

6.2.2.2 Simulation of Efficiency vs Coil Radius

Like the previous simulation, the same basic configuration of the two coils are used except that the radius of the coils is changed between 5 cm to 100 cm. The range of different radii is chosen in conjunction to the needs of various commercial applications like miniaturized biomedical devices to electric vehicles. For each coil radius, the efficiency curve is swept across a range of frequency of 1-1000 MHz as shown in Figure.6.17

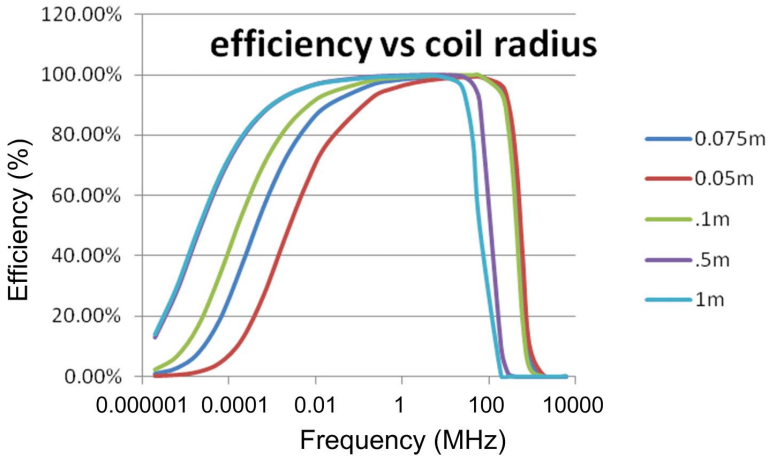

Figure 6.17: Efficiency of WPT system for various coil radius

Referring to Figure.6.17, as the radius of the coil increases, it is observed that the optimum efficiency band shifts towards the left of the figure and it gets widen.

From this observation, it is notable that for any frequency between 1-50 MHz, the efficiency of the WPT system still remains at its optimal for different coil radius between 5 cm to 100 cm. Take for example, at operating frequency of 100 kHz, it is observed from Figure.6.17 that the efficiencies of the WPT system with coil radius of 5 cm and 100 cm are 60 % and 95 % respectively. There is a significant difference in the system efficiency of around 35 % when the coil radius changes. As such, it is required to operate the WPT system with coil radius of 5-100 cm to be within 1-50 MHz so that maximum power throughput is achieved.

6.2.2.3 Simulation of Efficiency vs Number of Turns

In this case, the number of turns in each coil are varied for 3, 5 and 7 turns to determine the behaviour of the WPT system efficiency over a range of frequency. According to eqn.6.8, it can be seen that the mutual inductance, M, of the coils is a function of the square of N turns. As N increases, it is expected that M increases and so do the coupling coefficient, κ, where the relationship is illustrated in eqn.6.7. The simulated results are shown in Figure.6.18.

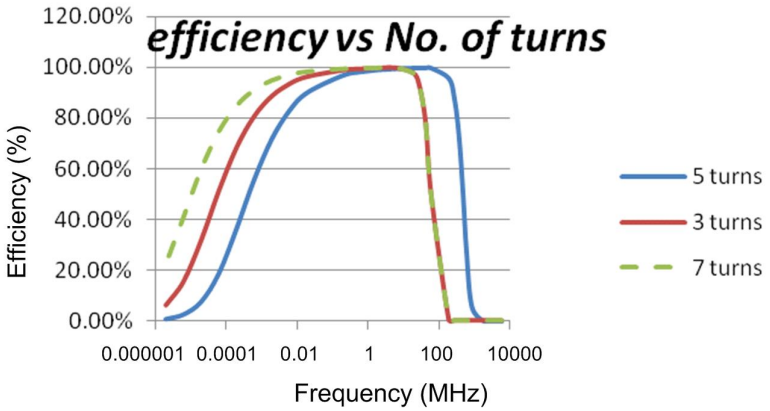

Figure 6.18: Efficiency of WPT system for different numbers of winding turns

Like the previous case, it is observed in Figure.6.18 that when the number of turns is changed from 3 turns to 7 turns, the optimum efficiency band starts to shift again towards the lower frequency region. This is because of the change in the ohmic and radiative resistances, as expressed in eqns.6.10 and 6.11 respectively, as well as the coupling coefficient, κ, which ends up changing the efficiency of the WPT system.

6.2.2.4 Simulation of Efficiency vs Distance

The mutual inductance of the coils, as expressed in eqn.6.8, is inversely proportional to the cubic of the separation distance, D, between the coils. As the distance between the two coils increases, the mutual coupling between the coils decreases as illustrated by eqn.6.7. The distance factor has no effect on the other performance indicators of the WPT system. In this simulation, the distance between the two coils is varied from 5 cm to 100 cm and the efficiency of the system over a range of frequency of 1-1000 GHz are plotted in Figure.6.19.

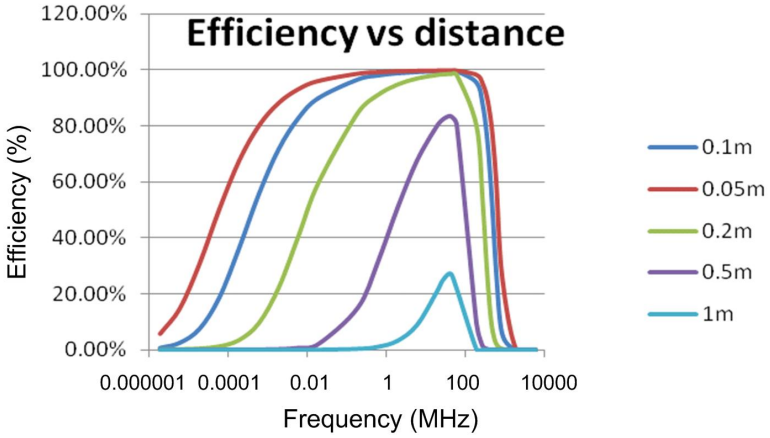

Figure 6.19: Efficiency of WPT system for different separation distances

With reference to Figure.6.19, it is observed that for shorter distance i.e. 5 cm

and 10 cm, the optimum efficiency band remains more or less the same due to the strong coupling between the coils. As the separation distance starts to increase, the efficiency of the WPT system decreases. At a distance of 50 cm, the peak attainable efficiency of the system has dropped to around 80 %. This reduction in the efficiency of the WPT system continue on and it drops to around 30 % when the separation distance between the coils is lengthen to 100 cm, which is twice of its counterpart of 50 cm. After conducting the simulations, the relationship between the WPT efficiency and the design factors is known and it is thus possible to leverage the understanding onto the experimental design of an optimal wireless power transfer system.

6.2.3 Characteristic of WPT System

Experiments were conducted to observe the performance of the WPT system with respect to the three more prominent design parameters namely: (1) frequency, (2) distance and (3) load. The rest of the design parameters are also investigated, however their effects are found to be not as significant as the chosen three parameters.

6.2.3.1 Experimental Efficiency vs Frequency

Referring back to the simulation shown in Section.6.2.2.1, the simulation results show that the efficiency of the WPT system is maximum for an optimal operating frequency. This optimum efficiency is the strongly coupled regime where $\kappa/\Gamma \gg 1$ and maximum power transfer takes place. As the operating frequency shifts away from the strong coupled regime, the WPT system efficiency starts to decrease.

The same deduction is also achieved in experiment and its experimental results are plotted in Figure.6.20.

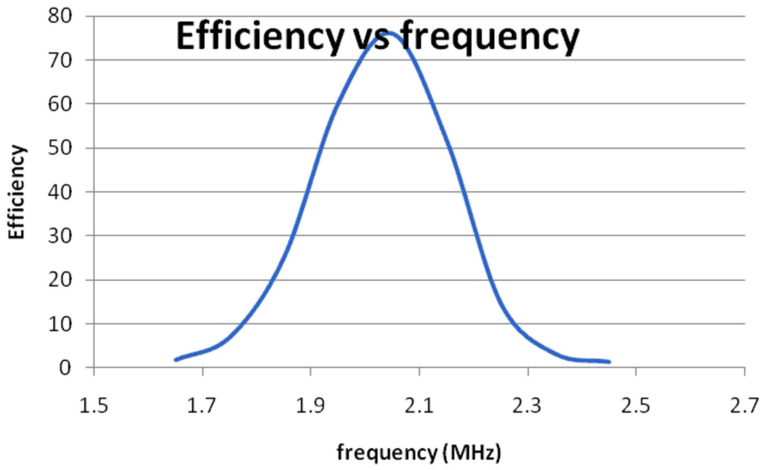

Figure 6.20: Experimental efficiency of WPT for various operating frequencies

Figure.6.20 verifies that the resonant frequency of the WPT system of 2.05MHz is well within the simulated frequency band of 1-40 MHz. At resonance, the maximum obtainable efficiency of the WPT system is around 75 %. Shifting away from the resonant frequency of 2.05 MHz by around ±10 %, it can be observed from Figure.6.20 that the WPT efficiency drops tremendously to less 15 %. It is necessary to design the WPT coils to operate at resonance using eqn.6.2 to achieve efficient wireless power transmission.

6.2.3.2 Experimental Efficiency vs Distance

In this experiment, the operating frequency of the power source is set at the resonance of the WPT system of 2.05MHZ and the separation distance between the transmitting and receiving coils is tested over a transmission range of 40 cm. The experimental results are collected and plotted in Figure.6.21.

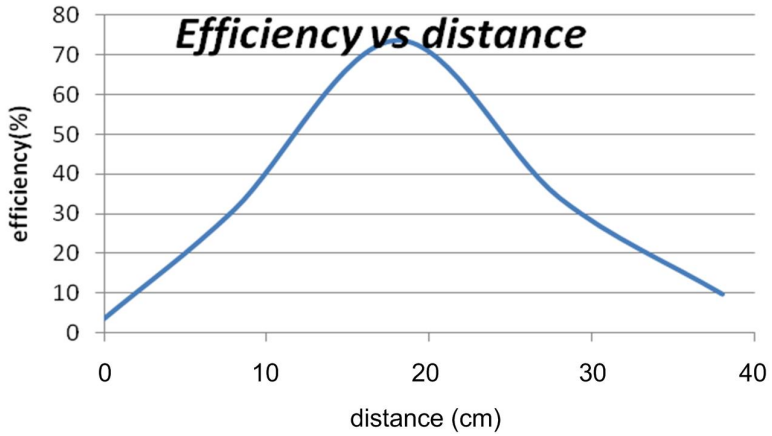

Figure 6.21: Experimental efficiency of WPT over a range of separation distances

Referring to Figure.6.21, it is observed that the efficiency of the WPT system is maximum at a separation distance of 20 cm. Beyond the distance of 20 cm where the coils are separated even further, the mutual coupling between the transmitting and receiving coils becomes weaker and weaker, so lesser and lesser electrical power is transferred wirelessly over to the load. Conversely, when the two coils get closer to each other, the mutual coupling between the coils becomes stronger but at the same time, the counter-electromotive force (emf) effect arises. The counter-emf is the voltage, or electromotive force, that pushes against the current which induces it. It is caused by a changing electromagnetic field which is represented by Lenz's law of electromagnetism. The voltage's polarity is at every moment the reverse of the input voltage. When a rapidly changing magnetic field induces an emf in a coil, a current caused by this emf flows. This current flow would in turn generate a magnetic field in the coil that opposes the original magnetic field that created it and this would ultimately reduce the induced emf in the coil. As such, it can be seen in Figure.6.21 that as the distance between the two coils decreases, the efficiency of the WPT system also decreases due to the counter-emf effect.

6.2.3.3 Experimental Efficiency vs Load

Once the resonant frequency and separation distance of the wireless power transfer (WPT) system are fixed at 2.05 MHz and 20 cm respectively, a load resistance ranging from 10 Ω to 10 kΩ is connected to the load coil to determine the characteristic of the WPT system. Figure.6.22 show the efficiency plot of the WPT system under different loading conditions.

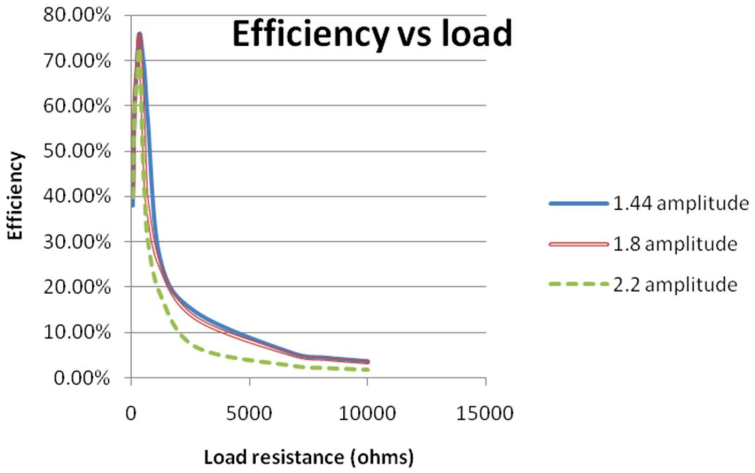

Figure 6.22: Experimental efficiency of WPT under different loading conditions

Referring to Figure.6.22, it is observed that maximum WPT efficiency of 75 % is attainable at matching load resistance of 220 Ω. However, for other loading conditions, shifting away from the internal resistance of the load coil of the WPT system, either very light or heavy electrical loads, the efficiency of the system drops significantly.

6.2.4 Experimental Results

The experimental setup of the WPT system, as shown in Figure.6.23, consists of a high-power high-frequency AC source, a set of source, transmitting, receiving and load coils, electrical testing loads and an oscilloscope. To achieve both high-power and high-frequency electrical supply from the AC source is very challenging, but it has been successfully implemented using a low-power high-frequency signal generator, capable of generating AC signal up to 500 MHz, and a high-power amplifier. The high-frequency AC signal generated by the signal generator is channelled to the power amplifier for amplification.

6.2.4.1 WPT System Powering Electrical Load(s)

The designed wireless power transfer (WPT) system is experimentally tested with an electrical appliance as the system load instead of a resistor to demonstrate and determine the wireless power capability of the system. To add a physical perspective to the WPT research work, a 12 V light bulb is used. Figure.6.24 shows a 12 V light bulb lit at a distance of 20 cm between the transmitting and receiving coils.

Based on the experimental results, the WPT system shown in Figure.6.24 is able to transmit an electrical output power of 1 W over a distance of 20 cm to the light bulb with an efficiency of around 51 %. During the experiment, whenever the coils separation distance is beyond the limit of 20 cm, the brightness of the light bulb diminishes quickly. This phenomenon is due to the low efficiency of the WPT system with weak coupling between the coils. The same experiment was conducted

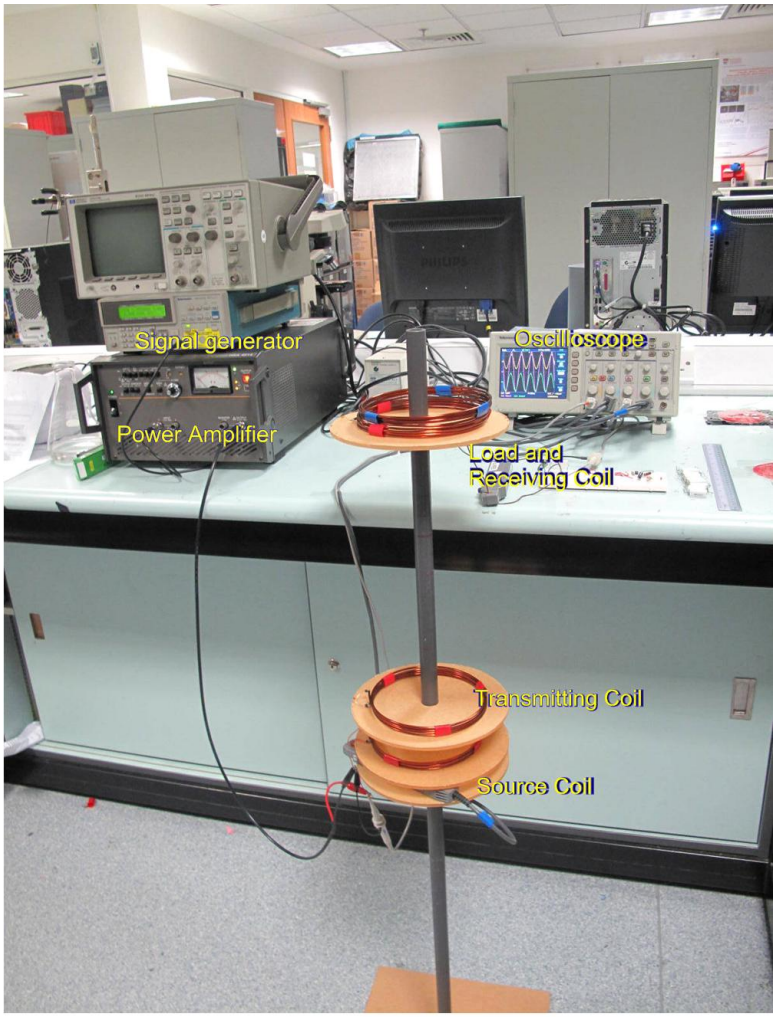

Figure 6.23: Experimental setup of WPT system

for different light bulbs of 2.4 V, 3.6 V and 7.2 V as well and their experimental results which include input power, P_{in}, at the source coil, output power, P_{out} at the load coil and efficiency, η_{WPT}, of the WPT system are recorded in Table.6.2.

Referring to Table.6.2, it can be observed that the output power and efficiency of the WPT system for different loading conditions i.e. 2.4-12 V light bulbs range between 0.6-1 W and 35-50 % respectively. One interesting observation to note from Table.6.2 is that for the 2.4 V light bulb, as the distance between the coils reduces from 20 cm to 15 cm, the WPT efficiency increases by more than a third

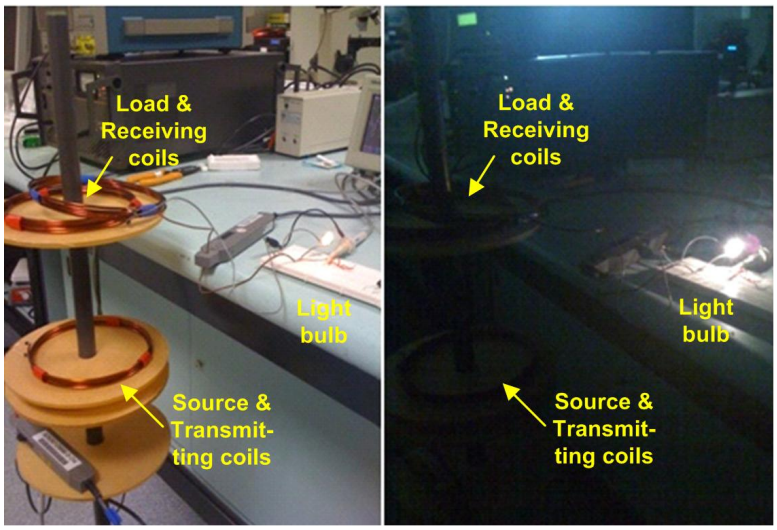

Figure 6.24: Demonstration of wireless power transmission of watt level

Table 6.2: Efficiency of WPT system powering different light bulbs

Bulb rating (V)	**Distance (cm)**	V_{in} **(V)**	I_{in} **(A)**	V_{out} **(V)**	I_{out} **(A)**	P_{in} **(W)**	P_{out} **(W)**	η_{WPT} **(%)**
2.4	15	5.9	0.12	1.05	0.32	0.708	0.336	47.5
2.4	20	6.5	0.28	1.64	0.39	1.820	0.640	35.2
3.6	20	7.2	0.29	2.05	0.39	2.088	0.800	38.3
7.2	20	8.1	0.26	2.40	0.35	2.106	0.840	39.9
12	20	8.5	0.25	3.17	0.34	2.125	1.078	50.7

to around 47.5 %. This positive observation is inline with the discussion concluded from the simulation carried in Section.6.2.2.4. Once the one-to-one WPT system is investigated, the following experiment shown in Figure.6.25 was designed to demonstrate the concept of powering multiple devices i.e. LED load 1 and light bulb load 2 of different geometries operating at the same resonant frequency.

With reference to Figure.6.25, it can be seen that a single source and transmitting coil is able to power up two separate load and receiving coils 1 & 2 of different dimensions tuned to the same frequency by adjusting their capacitances

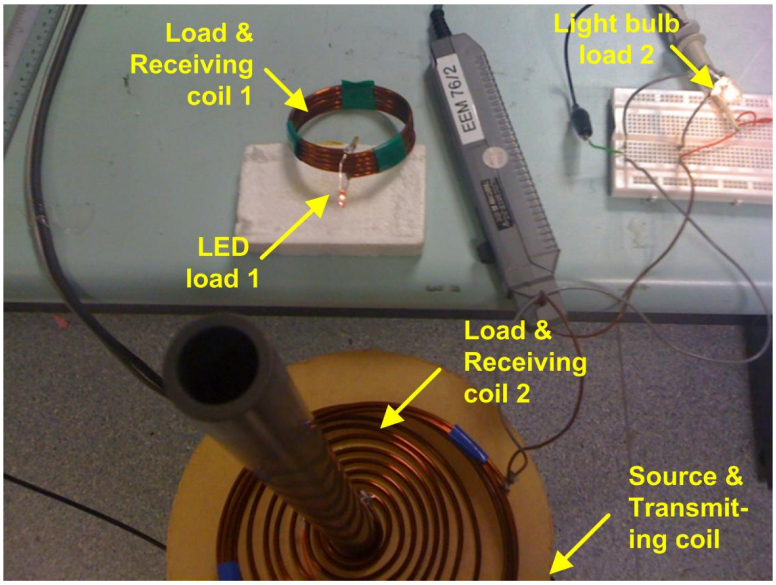

Figure 6.25: Powering multiple loads and effect of extraneous objects

based on the fundamental equation given by eqn.6.2. Both the LED and light bulb loads are lit up with the same WPT source and this exhibits the capability of the WPT system to transfer power to multiple electrical devices in a wireless manner. Another interesting observation to note from Figure.6.25 is that the smaller coil, i.e. load and receiving coil 1, placed on the table is out of the source coil's line of sight, magnetic waves are still able to power the load without interacting with the extraneous objects such as the wood and steel of the table between the transmitting and receiving coils. This is one of the unique advantages of using resonant magnetic waves as it does not interact with nonmagnetic materials such as plastic and wood. Even if there is magnetic material between the transmitting and receiving coils as can be seen in Figure.6.25 where load and receiving coil 1 is placed on the table made of wood and steel, energy is still able to be transferred wirelessly to the LED load 1. This is because of the fundamental nature of resonance dictates that resonant objects interact very weakly with other non-resonant extraneous objects such that very little electrical energy is loss.

6.2.4.2 Network of WPT Resonator Coils

Another objective of this wireless power transfer (WPT) research is to network the designed high-efficiency WPT resonator coils together so as to achieve the ultimate goals of wireless and batteryless electronic products. The designed resonator coils are networked together, as illustrated in Figure.6.26, such that each resonator coil in the network receives and relays electrical power from and to its neighboring resonator coil in accordance to the WPT routes illustrated by blue dotted lines in Figure.6.26.

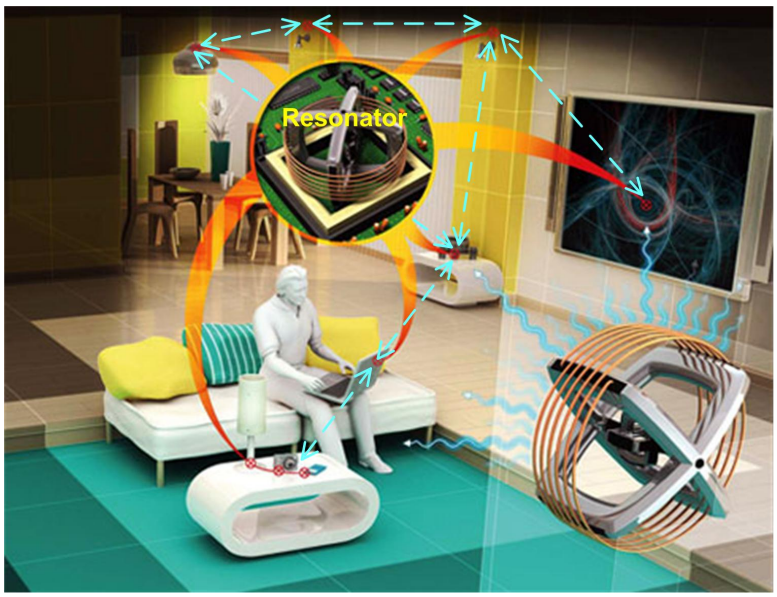

Figure 6.26: Illustration of resonators in network form to receive and relay electrical power

Referring to Figure.6.26, the mobile gadgets such as camera, iPhone, laptop, etc., are equipped with resonator coils and whenever these mobile gadgets enter into the room or rather the WPT network, they would be charged. In the mist of charging, the resonator coil also play the role of relaying the received electrical power to its nearby mobile gadget. By doing so, it is possible to reduce the wireless

power transmission distance between each gadget, hence the form factor of the resonator coil can be smaller in size to fit into the mobile gadget. It is thus more viable to utilize WPT technology as a self-sustaining portable energy source for the mobile gadgets. Figure.6.27 shows the powering of a LED at a separation distance of 60 cm away from the source and transmitting coil by using a network of resonator coils i.e. resonators #1 and #2.

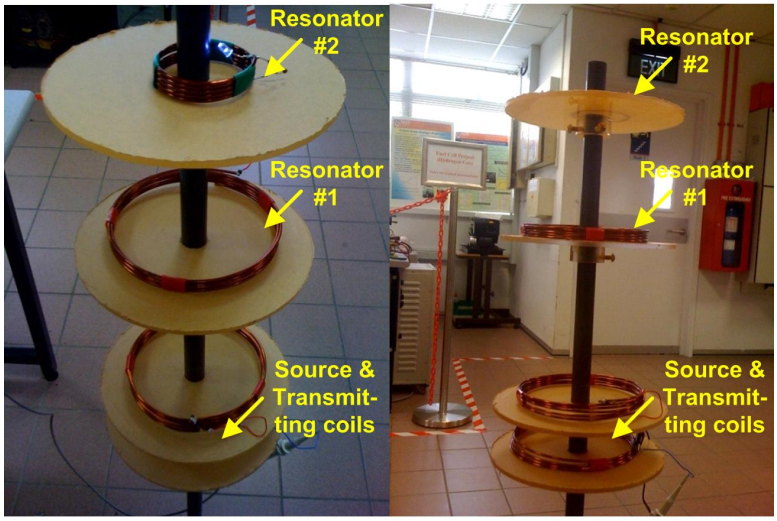

Figure 6.27: A resonant coil receives and relays electrical power to another nearby resonator coil

As compared to the experiment conducted in Section.6.2.4.1 where one pair of transmitting and receiving coils are used, it is observed that if an additional resonating coil, i.e. resonator #1, is placed between the transmitting and receiving coils, the transmission range of the wireless power transfer (WPT) system increases from 20 cm to 60 cm. Referring to Figure.6.27, it can be observed that the intermediate resonator coil #1 acts as a source for the next resonator coil #2 as well as a relay energy source for the subsequent resonator coils. Although more resonator coils are used to extend the wireless power transmission distance, the optimal design of the WPT system should take note of the additional ohmic loss

in each hop. Hence, the experiment has successfully demonstrated that a network of resonator coils can be used to transfer electrical power efficiently over a larger wireless transmission range to meet the target application.

6.2.5 Summary

The concept of using self resonant coils operating in the strongly coupled regime was experimentally demonstrated. It is obvious that this process far superior to simple inductive coupling. The equations and theory behind the concept were analyzed and further derivations and simulations helped in designing the appropriate system. Various design factors such as, resonant frequency, load and distance were changed and experimented. The results obtained were consistent with the derived equations and simulations. Experimental results shown that an electrical output power of 1 W is successfully delivered to the load which is a light bulb at efficiency of 51 % at a 20 cm coil separation distance with coils of 7.5cm radius.

Chapter 7

Conclusions and Future Works

This chapter concludes the thesis. It briefly restates the motivation of the thesis work, the identified problem areas and the various findings in each problem area. Finally, it shows the the direction of future research in this regard.

7.1 Conclusions

This thesis covers work done on design and development of various optimized energy harvesting systems for sustaining self-autonomous wireless sensor nodes. Conventionally, these tiny, smart and inexpensive sensor nodes, connected together into a wireless sensor network (WSN), are powered by alkaline or rechargeable batteries. They are scattered in the targeted deployment field to facilitate monitoring and controlling of physical environments from remote locations that are too difficult or dangerous-to-reach. However, as the coverage area of the WSN becomes larger, dense with many sensor nodes, problems arise in powering each of these battery-operated sensor nodes. The onboard batteries of the sensor nodes have

limited energy capacity and so after operating the sensor nodes for some times, the batteries depletes and the sensor nodes go into idle state. Hence, limitation of energy sources for sensor nodes becomes critical, even worst when one considers the prohibitive cost of providing power through wired cables to them or replacing batteries. Furthermore, when the sensor nodes must be extremely small, as tiny as several cubic centimeter, to be conveniently placed and used, such small volumetric devices are very limited in the amount of energy that the batteries can store and there would be severe limits imposed on the nodes' lifetime powered by the miniaturized battery that is meant to last the entire life of the node.

Energy harvesting emerges as a highly potential solution to make a paradigm shift from battery-operated conventional wireless sensor network towards truly self-autonomous and sustainable energy harvesting wireless sensor network (EH-WSN). The main focus of this research is to design and implement energy harvesting systems to resolve the energy supply problems faced by the wireless sensor nodes. In an energy harvesting (EH) system, there are generally four main parts namely; energy harvester (source), power management circuit, energy storage device and wireless sensor node (load). Power output per unit mass or volume i.e. power/energy density is a key performance unit for the energy harvester. Based on the characteristic and capability of each of the ambient energy source, the energy harvesting system is designed to suit the target application and its ambient conditions and event/task requirements. For the EH-WSN, various types of ambient renewable energy harvesting (EH) systems, based on wind energy harvesting, thermal energy harvesting, vibration energy harvesting, solar energy harvesting, hybrid energy harvesting and magnetic energy harvesting, are designed and then implemented into hardware prototypes for proof of concept. To optimize these EH systems, the harvested power

is conditioned to an appropriate form for either charging the system batteries or powering the connected load directly. Proper load impedance matching between the EH source and the electrical load is carried out to maximize the usage of the harvested energy. Several different types of power-electronic based management circuits such as active AC-DC converter, DC-DC converter with maximum power point tracking, energy storage and latching circuit, etc. have been introduced and implemented.

In all, the main objectives as laid out in Chapter.1 of this thesis have been achieved. The findings of this work have been published in book, international technical conferences, journals and research report, local newspaper and USA provisional patent for benefit of the future researchers and users of energy harvesting systems for wireless sensor nodes/network. A list of the publications from this thesis work is provided.

7.2 Future Research Works

In this energy harvesting research work, starting from scrap to what have been achieved so far, a wide coverage of breath studies and together with depth investigations on critical issues have been carried out. However, there are still rooms for more research, improvements and further optimization. Some possible future research works include: -

For the direct wind energy harvesting (WEH) research, the efficiency of the electric generator is relatively low because the generator is not optimized to operate at its rated speed. To overcome that, several ways have been suggested to improve

the efficiency of the electric generator like introduce a gearbox between the WTG hub and the generator and modify the two-pole generator to multi-pole generator. Other than the electric generator, the wind turbine itself is another possible area for future research. With adequate design of the blades of the wind turbine to suit the wind profile at the point of deployment, the aerodynamic efficiency can be improved. As for the indirect WEH research, the analysis for the wind power to electrical power conversion process through piezoelectric cantilever beam effect can be enhanced using computer-aided engineering software such as Ansys. By doing so, with prior knowledge of the incoming wind speed, the power throughput of the vibration-based piezoelectric wind energy harvester can be estimated. In addition, the mechanical resonant of the harvester's structure can be optimized to suit the need of a target application.

In the vibration energy harvesting (VEH) system, the energy extracted by the impact-based piezoelectric energy harvester is sufficient to power the radio frequency (RF) transmitter load. However, only a small fraction of the harvested energy has been extracted by the vibration energy harvester for use. As such, for the future research work, the energy extraction process can be optimized using dedicated power management techniques like synchronized electric charge extraction (SECE), parallel or series synchronized switch harvesting on inductor (SSHI), etc. In addition, further investigations are necessary for commercially viable, cheaper piezoelectric material with similar high-performance. This step is necessary for the commercialization of this impact-based VEH research work.

Hybrid energy harvesting (HEH) from two renewable energy sources has been proven with hardware prototype to yield more electrical power than a single en-

ergy harvesting (EH) source. The augmenting process of two energy sources are done by either using individual power converter for each EH source or directly connecting the energy sources in parallel. Other than the parallel configuration, for future research, the renewable energy sources can be stacked in series to produce higher voltage, but at the same time yield more electrical power. In addition, it is also worthwhile to explore energy harvesting from more than two energy sources available in the ambient environment. With more electrical energy harvested from different energy sources, the reliability of the wireless sensor nodes can be improved.

Lastly, in this thesis, the concept of magnetic energy harvesting via inductive coupling has been presented and demonstrated. An adequate power management circuit is developed to bridge between the magnetic energy harvester and the electrical load. However, there is no proper matching between the impedances of the source and the load. As such, in the future research work, an intelligent control of the power electronic converter to match the source and load impedances can be developed. With this proper impedance matching scheme in place, the harvested power from the magnetic energy harvesting would be maximum. This surplus in harvested energy would be useful for the operation of the electrical load. For the research work on wireless power transfer (WPT) via strongly-coupled magnetic resonances, it is clear that evanescent resonant coupling is able to transmit watt level of electrical power from the transmitting end to the receiving end over a distance of one to two metres. In order to further increase the power levels beyond few watts, there are two factors to be considered namely: (1) the power rating of the matching capacitors has to be increased. Capacitors using suitable material like tantalum that can withstand high current and also operate at MHz range frequency can be used to replace ceramic capacitors and (2) the use of high-frequency high-power

amplifier to generate an AC electrical power of MHz range and watt level of power.

Publications

Journal Papers

1. **Y.K. Tan**, Q.Y. Liu and S.K. Panda, "Hybride Wind and Solar Energy Harvesting Scheme for Wireless Sensor Node", *IEEE Transactions on Power Electronics*, submitted, 2010.

2. **Y.K. Tan** and S.K. Panda, "Energy Harvesting from Hybrid Indoor Solar and Thermal Energy Sources for Enhanced Performance of Wireless Sensor Nodes", *IEEE Transactions on Industrial Electronics*, submitted, 2010.

3. **Y.K. Tan** and S.K. Panda, "Resistor Emulation based Maximum Power Point Tracker for Optimal Thermal Energy Harvesting in Powering Wireless Sensor Nodes", *IEEE Transactions on Industrial Electronics*, submitted, 2010.

4. **Y.K. Tan** and S.K. Panda, "Self-Autonomous Wireless Sensor Nodes with Wind Energy Harvesting for Remote Sensing of Wind-Driven Wildfire Spread", *IEEE Transactions on Instrumentation and Measurement*, conditionally accepted, 2010.

5. **Y.K. Tan** and S.K. Panda, "Optimized Wind Energy Harvesting System Using Resistance Emulator and Active Rectifier for Wireless Sensor Nodes",

IEEE Transactions on Power Electronics, in-press, 2010.

Conference Papers

1. L.H. Tang, Y.W. Yang, **Y.K. Tan** and S.K. Panda, "Applicability of Synchronized Charge Extraction Technique for Piezoelectric Energy Harvesting", *The 10th International Workshop on Micro and Nanotechnology for Power Generation and Energy Conversion Applications (PowerMEMS'10)*, submitted, 2010, Leuven, Belgium.

2. D.C. Hoang, **Y.K. Tan** and S.K. Panda, "Thermal Energy Harvesting from Human Warmth for Wireless Body Area Network in Medical Healthcare System", *The Eighth International Conference on Power Electronics and Drive Systems (PEDS'09)*, pp.1277-1282, January 2009, Taipei, Taiwan.

3. **Y.K. Tan**, J.Y. Lee and S.K. Panda, "Maximize Piezoelectric Energy Harvesting using Synchronous Electric Charge Extraction Technique for Powering Autonomous Wireless Transmitter", *IEEE International Conference on Sustainable Energy Technologies (ICSET'08)*, pp.1254-1259, November 2008, Singapore.

4. **Y.K. Tan**, S.C. Xie and S.K. Panda, "Stray Magnetic Energy Harvesting in Power Lines through Inductive Coupling for Wireless Sensor Nodes", *The Proceedings for the 2008 nanoPower Forum (nPF'08)*, Darnell Group, June 2008, Irvine, Costa Mesa, California.

5. **Y.K. Tan** and S.K. Panda, "A Novel Piezoelectric Based Wind Energy Harvester for Low-power Autonomous Wind Speed Sensor", *33th Annual*

IEEE Conference of Industrial Electronics Society (IECON'07), pp.2175-2180, November 2007, Taipei, Taiwan.

6. R.J. Ang, **Y.K. Tan** and S.K. Panda, "Energy Harvesting for Autonomous Wind Sensor in Remote Area", *33th Annual IEEE Conference of Industrial Electronics Society (IECON'07)*, pp.2104-2109, November 2007, Taipei, Taiwan.

7. **Y.K. Tan** and S.K. Panda, "A Novel Method of Harvesting Wind Energy through Piezoelectric Vibration for Low-power Autonomous Sensors". *The Proceedings for the 2007 nanoPower Forum (nPF'07)*, Darnell Group, June 2007, San Hose, California.

8. **Y.K. Tan**, K.Y. Hoe and S.K. Panda, "Energy Harvesting using Piezoelectric Igniter for Self Powered Radio Frequency (RF) Wireless Sensors", *IEEE International Conference on Industrial Technology (ICIT'06)*, pp.1711-1716, December 2006, Mumbai, India.

Patent

1. **Y.K. Tan** and S.K. Panda, "Batteryless Wireless Control Switch Using Prestressed Piezoelectric Diaphragm Material", *US Provisional Patent*, Serial No. 61/302,996, registered on 10th February 2010.

Book Chapter

1. **Y.K. Tan** and S.K. Panda (2010). "Review of Energy Harvesting Technologies for Sustainable Wireless Sensor Network", *Wireless Sensor Networks*,

Tan Yen Kheng (Ed.), ISBN 978-953-7619-X-X, INTECH, accepted.

Newspaper Article

1. **Y.K. Tan** and S.K. Panda, "Remote powered by a single touch", *My Paper*, A Singapore Press Holdings Publication, 2009.

Research Report

1. **Y.K. Tan** and S.K. Panda, "Harvesting Wind Energy Through Piezoelectric Technology", *Advances in Energy Harvesting Technologies (Technical Insights)*, Frost & Sullivan, 2007.

Bibliography

[1] A. Kansal, J. Hsu, S. Zahedi and M.B. Srivastava, "Power Management in Energy Harvesting Sensor Networks", *ACM Transactions on Embedded Computing Systems*, pp.35, 2006.

[2] D.J. Cook and S.K. Das, "Wireless Sensor Networks", *Smart Environments: Technologies, Protocols and Applications*, John Wiley, New York, 2004.

[3] Technology Review, "10 Emerging Technologies That Will Change the World", *February 2003 Issue of Technology Review*, >http://www.technologyreview.com/Infotech/13060/?a=f< accessed on 07-06-2010.

[4] I.F. Akyildiz, W.L. Su, S. Yogesh and C. Erdal, "A Survey on Sensor Networks", *IEEE Communications Magazine*, vol.40, no.8, pp.102114, 2002.

[5] K. Sohrabi, J. Gao, V. Ailawadhi and G. Pottie, "Protocols for self-organization of a wireless sensor network", *IEEE Personal Communications*, vol.7, no.5, pp.1627, 2000.

[6] Tsung-Hsien Lin, W.J. Kaiser, G.J. Pottie, "Integrated low-power communication system design for wireless sensor networks" *IEEE Communications Magazine*, vol.42, issue.12, pp.142-150, 2004.

[7] A. Sinha and A. Chandrakasan, "Dynamic Power Management in Wireless Sensor Networks", *IEEE Design Test Comp.*, 2001.

[8] G.V. Merrett, B.M. Al-Hashimi, N.M. White, N.R. Harris, "Resource aware sensor nodes in wireless sensor networks", *Journal of Physics*, vol.15, no.1, pp.137-42, 2005.

[9] E. Lattanzi, E. Regini, A. Acquaviva, A. Bogliolo, "Energetic sustainability of routing algorithms for energy-harvesting wireless sensor networks", *Computer Communications*, vol.30, no.14-15, pp.2976-2986, 2007.

[10] C. Chong and S.P. Kumar, "Sensor Networks: Evolution, Opportunities, and Challenges", *Proceeding of the IEEE, Sensor Networks and Applications*, vol.91, no.8, pp.12471256, 2003.

[11] M. Kuorilehto, M. Hannikainen, T.D. Hamalainen, "A survey of application in wireless sensor networks", *EURASIP Journal on Wireless Communications and Networking*, vol.2005, no.5, pp.774-788, 2005.

[12] M. Tubaishat and S. Madria, "Sensor networks: an overview", *Potentials, IEEE*, vol.22, pp.2023, 2003.

[13] Edgar H. Callaway, "Wireless sensor networks: architectures and protocols", *Auerbach Publications*, Boca Raton, 2003.

[14] D. Culler, D. Estrin, and M. Srivastava, "Overview of sensor networks", *IEEE Computer*, vol.37, no.8, pp.4149, 2004.

[15] N. Kurata, S. Saruwatari, H. Morikawa, "Ubiquitous Structural Monitoring using Wireless Sensor Networks", *International Symposium on Intelligent Signal Processing and Communications*, pp.99-102, 2006.

[16] J. L. Hill and D. E. Culler, "Mica: A wireless platform for deeply embedded networks", *IEEE Micro*, vol.22, pp.1224, 2002.

[17] J. M. Rabaey, M. J. Ammer, J. L. da Silva, Jr., D. Patel, and S. Roundy, "Pico-Radio supports ad hoc ultra-low power wireless networking", *IEEE Computer*, vol.33, pp.4248, 2000.

[18] Massachusetts Institute of Technology (MIT), "μAmps projects", *Microsystems Technology Laboratories*, >http://www-mtl.mit.edu/researchgroups/icsystems/uamps/< accessed on 07-06-2010.

[19] TinyOS, "The TinyOS Project", *TinyOS Community Forum*, >http://www.tinyos.net< accessed on 07-06-2010.

[20] R. Verdone, D. Dardari, G. Mazzini and A. Conti, "Wireless sensor and actuator networks: Technologies, Analysis and Design", *Academic Pres*, Chapter.5: Network Lifetime, pp.115-116, 2008.

[21] Crossbow Technology Inc., "MPR-MIB Users Manual", *Crossbow Resources*, Revision A, 2007.

[22] J.W.Tester, "Energy Transfer and Conversion Methods", *Sustainable Energy Lecture Notes*, Topic on Energy Storage Modes, MIT, 2005.

[23] S.F.J. Flipsen, et al., "Alternative Power Sources for Portables and Wearables Part 1 - Power Generation and Part 2 - Energy Storage", *Technical report*, Personal Energy Systems programme, Delft University of Technology, 2004.

[24] G.E. Blomgren, "Perspectives on portable lithium ion batteries liquid and polymer electrolyte types", *Seventeenth Annual Battery Conference on Applications and Advances*, pp.141-144, 2002.

[25] V. Raghunathan, S. Ganeriwal, M. Srivastava, "Emerging techniques for long lived wireless sensor networks", *IEEE Communications Magazine*, vol.44, issue.4, pp.108-114, 2006.

[26] D. Niyato, E. Hossain, M.M. Rashid, V.K. Bhargava, "Wireless sensor networks with energy harvesting technologies: a game-theoretic approach to optimal energy management", *IEEE Wireless Communications*, vol.14, issue.4, pp.90-96, 2007.

[27] J.A. Paradiso, T. Starner, "Energy scavenging for mobile and wireless electronics", *IEEE Pervasive Computing*, vol.4, issue 1, pp.18-27, 2005.

[28] Cian Mathna, Terence O'Donnell, Rafael V. Martinez-Catala, James Rohan and O'Flynn Brendan, "Energy scavenging for long-term deployable wireless sensor networks", *Talanta*, vol.75, no.3, pp.613-623, 2008.

[29] J. P. Thomas, M. A. Qidwai, and J. C. Kellogg, "Energy scavenging for small-scale unmanned systems", *Journal of Power Sources*, vol.159, pp.1494-1509, 2006.

[30] J. F. Randall and J. Jacot, "Is AM1.5 applicable in practice? Modelling eight photovoltaic materials with respect to light intensity and two spectra", *Renewable Energy*, vol.28, issue.12, pp.1851-1864, 2003.

[31] M.A. Green, K. Emery, Y. Hisikawa, W. Warta, "SHORT COMMUNICATION Solar cell efficiency tables (version 30)", *Progress in Photovoltaics: Research and Applications*, vol.15, issue.5, pp.425-430, 2007.

[32] V. Raghunathan, A. Kansal, J. Hsu, J. Friedman and M. Srivastava, "Design considerations for solar energy harvesting wireless embedded systems",

Fourth International Symposium on Information Processing in Sensor Networks (IPSN), pp.457-462, 2005.

[33] X.F. Jiang, J. Polastre and D.E. Culler, "Perpetual environmentally powered sensor networks", *Fourth International Symposium on Information Processing in Sensor Networks (IPSN)*, pp.463-468, 2005.

[34] F.I. Simjee, P.H. Chou, "Efficient charging of supercapacitors for extended lifetime of wireless sensor nodes", *IEEE Transactions on Power Electronics*, vol.23, issue.3, pp.1526-1536, 2008.

[35] C. Park, P.H. Chou, "AmbiMax: Autonomous Energy Harvesting Platform for Multi-Supply Wireless Sensor Nodes", *3rd Annual IEEE Communications Society on Sensor and Ad Hoc Communications and Networks (SECON)*, vol.1, pp.168-177, 2006.

[36] D. Dondi, A. Bertacchini, D. Brunelli, L. Larcher & L. Benini, "Modeling and Optimization of a Solar Energy Harvester System for Self-Powered Wireless Sensor Networks", *IEEE Transaction on Industrial Electronics*, vol.55, issue.7, pp.2759-2766, 2008.

[37] Nicholas S. Hudak and Glenn G. Amatucci, "Small-scale energy harvesting through thermoelectric, vibration, and radio frequency power conversion", *Journal of Applied Physics*, vol.103, no.10, pp.101301(1-24), 2008.

[38] Francesco Cottone, "Nonlinear Piezoelectric Generators for Vibration Energy Harvesting", *Ph.D Thesis*, University of Perugia, Italy, 2008.

[39] T. Kanesaka, "Development of a Thermal Energy Watch", *Proc. 64th Conference on Chronometry (Socit Suisse de Chronomtrie)*, Le Sentier, Switzerland, pp.19-22, 1999.

[40] V. Leonov, T. Torfs, P. Fiorini, C. Van Hoof, "Thermoelectric Converters of Human Warmth for Self-Powered Wireless Sensor Nodes", *IEEE Sensors Journal*, vol.7, issue.5, pp.650-657, 2007.

[41] J.W. Stevens, "Heat transfer and thermoelectric design considerations for a ground-source thermo generator", *Proceedings of 18th International Conference on Thermoelectrics*, 1999.

[42] E.E. Lawrence and G.J. Snyder, "A study of heat sink performance in air and soil for use in a thermoelectric energy harvesting device", *Proceedings of 21st International Conference on Thermoelectrics (ICT 02)*, 2002.

[43] H.A. Sodano, G.E. Simmers, R. Dereux, D.J. Inman, "Recharging batteries using energy harvested from thermal gradients", *Journal of Intelligent Material Systems and Structures*, vol.18, no.1, pp.3-10, 2007.

[44] Clemens Moser, "Power Management in Energy Harvesting Embedded Systems", *Ph.D Thesis*, Swiss Federal Institute of Technology, Zurich, 2009.

[45] S. Roundy, P.K. Wright, J.M. Rabaey, "Energy Scavenging for Wireless Sensor Networks with Special Focus on Vibrations", *Kluwer Academic Press*, Boston, MA, 2004.

[46] N. Shenck and J. Paradiso, "Energy scavenging with shoe-mounted piezoelectrics", *IEEE Micro*, vol.21, issue.3, pp.30-42, 2001.

[47] Shadrach Joseph Roundy, "Energy Scavenging for Wireless Sensor Nodes with a Focus on Vibration to Electricity Conversion", *Ph.D Thesis*, University of California, Berkeley, 2003.

[48] J. Edmison, M. Jones, Z. Nakad, T. Martin, "Using piezoelectric materials for wearable electronic textiles", *Proceedings of Sixth International Symposium on Wearable Computers (ISWC)*, 2002.

[49] P. Glynne-Jones, M.J. Tudor, S.P. Beeby, N.M. White, "An electromagnetic, vibration-powered generator for intelligent sensor systems", *Sensors and Actuators*, vol.110, no.1-3, pp.344-349, 2004.

[50] S. Meninger, A.P. Amirtharajan and R.Chandrakasan, "Vibration-to-Electric Energy Conversion", *IEEE Transaction on VLSI System*, vol.9, pp.64-71, 2001.

[51] P.D. Mitcheson, T.C. Green, E.M. Yeatman, A.S. Holmes, "Architectures for Vibration-Driven Micropower Generators", *Journal of Microelectromechanical Systems*, vol.13, no.3, pp.429440, 2004.

[52] J.A. Paradiso and Mark Feldmeier, "A compact, wireless, self-powered push-button controller", *MIT Media Laboratory*, 2002.

[53] E. Braunwald, "Heart Disease: A Textbook of Cardiovascular Medicine", *W. B. Saunders Company*, Philadelphia, 1980.

[54] M. Ramsay and W. Clark, "Piezoelectric energy harvesting for bio-MEMs applications", *Proceedings of the SPIE - The International Society for Optical Engineering*, vol.4332, pp.429-439, 2001.

[55] Zhe Chen; J.M. Guerrero, F. Blaabjerg, "A Review of the State of the Art of Power Electronics for Wind Turbines", *IEEE Transactions on Power Electronics*, vol.24, issue.8, pp.1859-1875, 2009.

[56] Siegfried Heier (Author) and Rachel Waddington (Translator), "Grid integration of wind energy conversion systems", *John Wiley & Sons Ltd*, second edition, Chichester, West Sussex, England, 2006.

[57] Renewable Resource Data Center (RReDC). *National Renewable Energy Laboratory*, >http://www.nrel.gov/rredc/< accessed on 14-06-2010.

[58] C.T. Chen, R.A. Islam, S. Priya, "Electric energy generator", *IEEE Transactions on Ultrasonics, Ferroelectrics and Frequency Control*, vol.53, issue.3, pp.656-661, 2006.

[59] A.S. Holmes, G. Hong, K.R. Pullen, K.R. Buffard, "Axial-flow microturbine with electromagnetic generator: design, CFD simulation, and prototype demonstration", *17th IEEE International Conference on Micro Electro Mechanical Systems*, pp.568-571, 2004.

[60] Michael A. Weimer, Thurein S. Paing, and Regan A. Zane, "Remote area wind energy harvesting for low-power autonomous sensors", *37th IEEE Power Electronics Specialists Conference*, pp.2911-2915, 2006.

[61] S.Priya, C.T. Chen, Darren Fye, Jeff Zahnd, "Piezoelectric Windmill: A Novel Solution to Remote Sensing", *Japanese Journal of Applied Physics*, vol.44, no.3, pp.L104L107, 2005.

[62] R. Myers, M. Vickers, Kim Hyeoungwoo, S. Priya, "Small scale windmil", *Applied Physics Letters*, vol.90, no.5, p.54106-1-3, 2007.

[63] D. Maurath, C. Peters, T. Hehn, M. Ortmanns, and Y. Manoli, "Highly efficient integrated rectifier and voltage boosting circuits for energy harvesting applications", *Adv. Radio Science*, 6, pp.219225, 2008.

[64] Y.H. Lam, W.H. Ki, C.Y. Tsui, "Integrated Low-Loss CMOS Active Rectifier for Wirelessly Powered Devices", *IEEE Transactions on Circuits and Systems II: Express Briefs*, vol.53, issue.12, pp.1378-1382, 2006.

[65] M.D. Seeman, S.R. Sanders, J.M. Rabaey, "An ultra-low-power power management IC for energy-scavenged wireless sensor nodes", *IEEE Power Electronics Specialists Conference (PESC 2008)*, pp.925-931, 2008.

[66] E. Koutroulis and K. Kalaitzakis, "Design of a maximum power tracking system for wind-energy-conversion applications", *IEEE Transactions on Industrial Electronics*, vol.53, issue.2, pp.486-494, 2006.

[67] Z. Chen, E. Spooner, "Grid Interface Options for Variable-Speed, Permanent-Magnet Generators", *IEE Proc. -Electr. Power Applications*, vol.145, no.4, pp.273-283, 1998.

[68] Quincy Wang, Liuchen Chang, "An intelligent maximum power extraction algorithm for inverter-based variable speed wind turbine systems", *IEEE Transactions on Power Electronics*, vol.19, issue.5, pp.1242-1249, 2004.

[69] K. Khouzam & L. Khouzam, "Optimum matching of direct-coupled electromechanical loads to a photovoltaic generator", *IEEE Transaction on Energy Conversion*, vol.8, issue.3, pp.343-349, 1993.

[70] T. Paing, J. Shin, R. Zane & Z. Popovic, "Resistor Emulation Approach to Low-Power RF Energy Harvesting", *IEEE Transaction on Power Electronics*, vol.23, issue.3, pp.1494-1501, 2008.

[71] R.W. Erickson & D. Maksimovic, "Fundamentals of Power Electronics", *2nd ed. New York: Springer*, pp.637663, 2001.

[72] John Twidell and Anthony Weir, "Renewable energy resources", *New York: Taylor & Francis*, London, 2nd edition, 2006.

[73] The Bor Forest Island Fire Experiment Fire Research Campaign Asia-North (FIRESCAN), *IV. Bor Forest Island Fire Behavior and Atmospheric Emissions*, Available from: >http://www.fire.uni-freiburg.de/other_rep/research/rus/rus_re_1bor.htm<, accessed on 01-07-2010.

[74] V. Salas, E. Olias, A. Barrado, A. Lazaro, "Review of the maximum power point tracking algorithms for stand-alone photovoltaic systems", *Solar Energy Materials and Solar Cells*, vol.90, no.11, pp.1555-1578, 2006.

[75] M. Mitchell, "Animated Demonstration of Bernoulli's Principle", *Online article*, >http://home.earthlink.net/ mmc1919/ venturi.html< accessed on 01-07-2010.

[76] Stephen J. I'Anson, "Radius of Curvature", *Online article*, University of Manchester, >http://pygarg.ps.umist.ac.uk/ianson/ paper_physics/Radius_of_Curvature.html< accessed on 01-07-2010.

[77] Niell G. Elvin, Alex A. Elvin, "A general equivalent circuit model for piezoelectric generators", *Journal of Intelligent Material Systems and Structures*, vol.20, no.1, pp.3-9, 2009.

[78] J.G. Smits, S.I. Dalke, T.K. Cooney, "The constituent equations of piezoelectric bimorphs", *Sensors and Actuators)*, vol.A28, no.1, pp.41-61, 1991.

[79] J.L. Gonzalez, A. Rubio, F. Moll, "Human Powered Piezoelectric Batteries to Supply Power of Wearables Electronic Devices", *Int. J. Soc. Mater. Eng. Resour.*, vol.10 no.1. pp.34-40, 2002.

[80] Qing-Ming Wang, Xiao-hong Du, Baomin Xu, and L. Eric Cross, "Theoretical analysis of the sensor effect of cantilever piezoelectric benders", *Journal of Applied Physics*, vol.85, no.3, pp.1702 - 1712, 1999.

[81] J. Kymissis, C. Kendall, J. Paradiso, N. Gershenfeld, "Parasitic Power Harvesting in Shoes", *Second International Symposium on Wearable Computers*, pp.132-139, 1998.

[82] V.C. Gungor and G.P. Hancke, "Industrial Wireless Sensor Networks: Challenges, Design Principles, and Technical Approaches", *IEEE Transactions on Industrial Electronics*, vol.56, issue.10, pp.4258-4265, 2009.

[83] C. Alippi, G. Anastasi, M. Di Francesco and M. Roveri, "Energy management in wireless sensor networks with energy-hungry sensors", *IEEE Transactions on Instrumentation & Measurement Magazine*, vol.12, issue.2, pp.16-23, 2009.

[84] D. M. Rowe, "Thermoelectrics Handbook: Macro to Nano", *CRC, Boca Raton, FL/Taylor & Francis*, Boca Raton, 2006.

[85] J. Carmo, L. Goncalves and H. Correia, "Thermoelectric micro converter for energy harvesting systems", *IEEE Transaction on Industrial Electronics*, 2009.

[86] Wulf Glatz, Simon Muntwyler and Christofer Hierold, "Optimization and fabrication of thick flexible polymer based micro thermoelectric generator", *Sensors and Actuators A: Physical*, vol.132, pp.337-345, 2006.

[87] N. Femia, G. Petrone, G. Spagnuolo and M. Vitelli, "Optimization of perturb and observe maximum power point tracking method", *IEEE Transactions on Power Electronics*, vol.20, no.4, pp.963-973, 2005.

[88] Fangrui Liu, Shanxu Duan, Fei Liu, Bangyin Liu, Yong Kang, "A Variable Step Size INC MPPT Method for PV Systems", *IEEE Transactions on Industrial Electronics*, vol.55, issue.7, pp.2622-2628, 2008.

[89] T. Esram, J.W. Kimball, P.T. Krein, P.L. Chapman, P. Midya, "Dynamic Maximum Power Point Tracking of Photovoltaic Arrays Using Ripple Correlation Control", *IEEE Transactions on Power Electronics*, vol.21, issue.5, pp.1282-1291, 2006.

[90] Rae-Young Kim, Jih-Sheng Lai, B. York, A. Koran, "Analysis and Design of Maximum Power Point Tracking Scheme for Thermoelectric Battery Energy Storage System", *IEEE Transactions on Industrial Electronics*, vol.56, issue.9, pp.3709-3716, 2009.

[91] I. Stark, "Invited Talk: Thermal Energy Harvesting with Thermo Life", *International Workshop on Wearable and Implantable Body Sensor Networks (BSN 2006)*, pp.19-22, 2006.

[92] V. Leonov, "Thermal shunts in thermoelectric energy scavengers", *Journal of Electronic Materials*, vol.38, no.7, pp.1483-1490, 2009.

[93] S. Dalola, M. Ferrari, V. Ferrari, M. Guizzetti and D. Marioli, A. Taroni, "Characterization of Thermoelectric Modules for Powering Autonomous Sensors", *IEEE Transactions on Instrumentation and Measurement*, vol.58, issue.1, pp.99-107, 2009.

[94] T.S. Paing and R. Zane, "Resistor Emulation Approach to Low-Power Energy Harvesting", *37th IEEE Power Electronics Specialists Conference (PESC*, pp.1-7, 2006.

[95] Jian Sun, D.M. Mitchell, M.F. Greuel, P.T. Krein, R.M. Bass, "Averaged modeling of PWM converters operating in discontinuous conduction mode", *IEEE Transaction on Power Electronics*, vol.16, issue.4, pp.482-492, 2001.

[96] V. Vorperian, "Simplified analysis of PWM converters using model of PWM switch, Part II: Discontinuous conduction mode", *IEEE Transactions on Aerospace and Electronic Systems*, vol.26, pp.497-505, 1990.

[97] P.D. Mitcheson, P. Miao, B.H. Stark, E.M. Yeatman, A.S. Holmes and T.C. Green, "MEMS electrostatic micropower generator for low frequency operation", *Sensors and Actuators A: Physical*, vol.115, no.2-3, pp.523-529, 2004.

[98] Steven R. Anton, Henry A. Sodano, "A review of power harvesting using piezoelectric materials (2003-2006)", *Smart Materials and Structures*, vol.16, no.3, pp.R1-R21, 2007.

[99] S. Roundy, E.S. Leland, J. Baker, E. Carleton, E. Reilly, E. Lai, B. Otis, J.M. Rabaey, P.K. Wright, V. Sundararajan, "Improving power output for vibration-based energy scavengers", *IEEE Pervasive Computing*, vol.4, issue.1, pp.28-36, 2005.

[100] Wikipedia, the free encyclopedia, "Piezoelectricity", >http://en.wikipedia.org/wiki/Piezoelectricity< accessed on 07-05-2010.

[101] Nathan S. Shenck, "A Demonstration of Useful Electric Energy Generation from Piezoceramics in a Shoe", *Master Thesis*, Massachusetts Institute of Technology (MIT), 1999.

[102] M. Renaud, P. Fiorini, R. Van Schaijk, C. Van Hoof, "Harvesting energy from the motion of human limbs: The design and analysis of an impact-

based piezoelectric generator", *Smart Materials and Structures*, vol.18, no.3, 035001(16pp), 2009.

[103] S.P. Beeby, M.J. Tudor and N.M. White, "Energy harvesting vibration sources for microsystems applications", *Measurement Science & Technology*, vol.17, no.12, pp.R175-95, 2006.

[104] M. Umeda, K. Nakamura and S. Ueha, "Analysis of the transformation of mechanical impact energy to electric energy using piezoelectric vibrator", *Japanese Journal of Applied Physics*, vol.35, no.5B, pp.3267-3273, 1996.

[105] C. Keawboonchuay and T.G. Engel, "Maximum power generation in a piezoelectric pulse generator", *IEEE Transactions on Plasma Science*, vol.31 (2), no.1, pp.123-128, 2003.

[106] M. Renaud, P. Fiorini and C. Van Hoof, "Optimization of a piezoelectric unimorph for shock and impact energy harvesting", *Smart Materials and Structures*, vol.16, no.4, pp.1125-1135, 2007.

[107] J.F. Antaki, G.E. Bertocci, E.C. Green, A. Nadeem, T. Rintoul, R.L. Kormos and B.P. Griffith, "A gait powered autologous battery charging system for artificial organs", *American Society of Artificial Internal Organs Conference*, pp.M588-M595, 1995.

[108] J. Paradiso and M. Feldmeier, "A Compact, Wireless, Self-Powered Pushbutton Controller", *Ubicomp 2001: Ubiquitous Computing, LNCS 2201, Springer-Verlag*, pp.299-304, 2001.

[109] Frank Schmidt, Matthias Heiden, "Wireless Sensors Enabled by Smart Energy - Concepts and Solutions", *EnOcean GmbH*, Germany.

[110] Amin Rida, Li Yang and Manos Tentzeris, "Chapter 5: State-of-the-Art Technology for RFID/Sensors", *RFID-Enabled Sensor Design and Applications*, Artech House, 2010.

[111] Piezo Systems, Inc., "Introduction to piezo transducers", >http://www.piezo.com/tech2intropiezotrans.html< accessed on 17-05-2010.

[112] S.B. Dewan, G.R. Slemon and A. Straughen, "Power Semiconductor Drives", *John Wiely & Sons. Inc.*, Chapters 2 and 5, 1984.

[113] K.Y. Hoe, "An Investigation of Self Powered RF Wireless Sensors", *Bachelor Thesis*, National University of Singapore, 2006.

[114] Hyeoung Woo Kim, A. Batra, S. Priya, K. Uchino, D. Markley, R.E. Newnham, H.F. Hofmann, "Energy harvesting using a piezoelectric cymbal transducer in dynamic environment", *Japanese Journal of Applied Physics, Part 1 (Regular Papers, Short Notes & Review Papers)*, vol.43, no.9A, pp.6178-83, 2004.

[115] Bradbury R. Face, "Self-powered, electronic keyed, multifunction switching system", *Face International Corporation*, Patent: US7161276, 2007.

[116] Dausch, D. and Wise, S., "Compositional effects on electromechanical degradation of RAINBOW actuators", *NASA*, Hampton, Virginia, 1998.

[117] R.G. Bryant, "LaRC^{TM}-SI: a soluble aromatic polyimide", *High Performance Polymers*, vol.8, pp.607615, 1996.

[118] K. Mossi, C. Green, Z. Ounaies, E. Hughes, "Harvesting energy using a thin unimorph prestressed bender: Geometrical effects", *Journal of Intelligent Material Systems and Structures*, vol.16, no.3, pp.249-261, 2005.

[119] K. Mossi, Z. Ounaies and S. Oakley, "Optimizing Energy Harvesting of a Composite Unimorph Pre-stressed Bender", *16th Technical Conference of the American Society for Composites*, 2001.

[120] A.D. Danak, H.S. Yoon and G.N. Washington, "Optimization of electrical output in response to mechanical input in piezoceramic laminated shells", *ASME International Congress and Exposition,*, pp.309-315, 2003.

[121] J.T. Cher, "Design of a Piezoelectric Energy Harvesting Wireless Electronic Switch", *Bachelor Thesis*, National University of Singapore, 2008.

[122] M.K. Stojcev, M.R. Kosanovic and L.R. Golubovic, "Power management and energy harvesting techniques for wireless sensor nodes", *9th International Conference on Telecommunications in Modern Satellite, Cable, and Broadcasting Services*, pp.65-72, 2009.

[123] S. Taylor, N. Miller, W. Sifuentes, E. Moro, G. Park, C. Farrar, E. Flynn, D. Mascarenas and M. Todd, "Energy harvesting and wireless energy transmission for embedded sensor nodes", *Proceedings of the SPIE - The International Society for Optical Engineering*, vol.7288, pp.728810 (12 pp.), 2009.

[124] R. Torah, P. Glynne-Jones, M. Tudor, T. O'Donnell, S. Roy and S. Beeby, "Self-powered autonomous wireless sensor node using vibration energy harvesting", *Measurement Science and Technology*, vol.19, no.12, 2008.

[125] Y.T. He, Y.Q. Li, L.H. Liu and L. Wang, "Solar micro-power system for self-powered wireless sensor nodes", *Proceedings of the SPIE-The International Society for Optical Engineering*, vol.7133, pp.71333Z (8 pp.), 2008.

[126] Y. Tadesse, Shujun Zhang, S. Priya, "Multimodal Energy Harvesting System: Piezoelectric and Electromagnetic", *Journal of Intelligent Material Systems and Structures*, vol.20, no.5, pp.625-632, 2009.

[127] A. Khaligh, P. Zeng, C. Zheng, "Kinetic Energy Harvesting Using Piezoelectric and Electromagnetic Technologies - State of the Art", *IEEE Transaction on Industrial Electronics*, vol.57, no.3, pp.850-860, 2010.

[128] N.J. Guilar, T.J. Kleeburg, A. Chen, D.R. Yankelevich, R. Amirtharajah, "Integrated Solar Energy Harvesting and Storage", *IEEE Transactions on Very Large Scale Integration (VLSI) Systems*, vol.17, issue.5, pp.627-637, 2009.

[129] H. Lhermet, C. Condemine, M. Plissonnier, R. Salot, P. Audebert, M. Rosset, "Efficient Power Management Circuit: From Thermal Energy Harvesting to Above-IC Microbattery Energy Storage", *IEEE Journal of Solid-State Circuits*, vol.43, issue.1, pp.246-255, 2008.

[130] Ali Naci Celik and Nasir Acikgoz, "Modelling and experimental verification of the operating current of mono-crystalline photovoltaic modules using four- and five-parameter models", *Applied Energy*, vol.84, issue.1, pp.1-15, 2007.

[131] M.G. Villalva, J.R. Gazoli, E.R. Filho, "Comprehensive Approach to Modeling and Simulation of Photovoltaic Arrays", *IEEE Transaction on Power Electronics*, vol.24, no.5, pp.1198-1208, 2009.

[132] D. Sera, R. Teodorescu, P. Rodriguez, "PV panel model based on datasheet values", *IEEE International Symposium on Industrial Electronics (ISIE)*, pp.2392-2396, 2007.

[133] T. Esram and P.L. Chapman, "Comparison of photovoltaic array maximum power point tracking techniques", *IEEE Transactions on Energy Conversion*, vol.22, no.2, pp.439-449, 2007.

[134] R. Faranda and S. Leva, "Energy comparison of MPPT techniques for PV Systems", *WSEAS Transactions on Power Systems*, vol.3, issue.3, pp.446-455, 2008.

[135] K.H. Hussein, I. Muta, T. Hoshino and M. Osakada, "Maximum photovoltaic power tracking: an algorithm for rapidly changing atmospheric conditions", *IEE Proceedings - Generation, Transmission and Distribution*, vol.142, issue.1, pp.59-64, 1995.

[136] D. Brunelli, L. Benini, C. Moser and L. Thiele, "An Efficient Solar Energy Harvester for Wireless Sensor Nodes", *Design, Automation and Test in Europe*, pp.104-109, 2008.

[137] Y.Q. Li, H.Y. Yu, B. Su and Y.H. Shang, "Hybrid micropower source for wireless sensor network", *IEEE Sensors Journal*, vol.8, no.6, pp.678-81, 2008.

[138] D. Dudek, C. Haas, A. Kuntz, M. Zitterbart, D. Krger, P. Rothenpieler, D. Pfisterer and S. Fischer, "A wireless sensor network for border surveillance", *Proceedings of the 7th ACM Conference on Embedded Networked Sensor Systems*, pp.303-304, 2009.

[139] Solar4Power, "Global Solar Power Map #2: North America from Canada to Texas", >http://www.solar4power.com/map2-global-solar-power.html< accessed on 15-06-2010.

[140] Canadian Wind Energy Atlas, >http://www.windatlas.ca/en/index.php< accessed on 15-06-2010.

[141] Osram, "Special Lamps: Osram Lamp Technology", >www.friarsmarketing.com/Resources/SPECIAL%20LAMPS.pdf< accessed on 15-06-2010.

[142] Q.Y. Liu, "Hybrid Energy Harvesting from Wind and Solar Energy Sources to Power Wireless Sensor Nodes", *Bachelor Thesis*, National University of Singapore, 2010.

[143] A. Nasiri, S.A. Zabalawi, G. Mandic, "Indoor Power Harvesting Using Photovoltaic Cells for Low-Power Applications", *IEEE Transaction on Industrial Electronics*, vol.56, issue.11, pp.4502-4509, 2009.

[144] Abhiman Hande, Todd Polk, William Walker, Dinesh Bhatia, "Indoor solar energy harvesting for sensor network router nodes", *Microprocessors and Microsystems*, vol.31, no.6, pp.420-432, 2007.

[145] Julian F. Randall, "Designing indoor solar products: photovoltaic technologies for AES", *John Wiley & Sons, Ltd*, Hoboken, N.J., USA, 2005.

[146] A. Wickenheiser, E. Garcia, "Combined power harvesting from AC and DC sources", *Proceedings of the SPIE*, vol.7288, pp.728816-1-9, 2009.

[147] A.S. Marincic, "Nikola Tesla and the Wireless Transmission of Energy", *IEEE Transactions on Power Apparatus and Systems*, vol.PAS-101, issue.10, pp.4064-4068, 1982.

[148] S. Ahson and M. Ilyas, "RFID handbook: applications, technology, security, and privacy", *Boca Raton: CRC Press*, 2008.

[149] A. Sample, D. Yeager, P. Powledge, A. Mamishev, and J. Smith, "Design of an rfid-based battery-free programmable sensing platform", *IEEE Transactions on Instrumentation and Measurement*, vol.57, no.11, pp.26082615, 2008.

[150] W. Brown, "The history of power transmission by radio waves", *IEEE Transactions on Microwave Theory and Techniques*, vol.32, no.9, pp.12301242, 1984.

[151] J. McSpadden and J. Mankins, "Space solar power programs and microwave wireless power transmission technology", *IEEE Microwave Magazine*, vol.3, no.4, pp.4657, 2002.

[152] A. Sample and J. Smith, "Experimental results with two wireless power transfer systems", *IEEE Radio and Wireless Symposium*, pp.1618, 2009.

[153] Z.N. Low, R.A. Chinga, R. Tseng, J.S. Lin, "Design and Test of a High-Power High-Efficiency Loosely Coupled Planar Wireless Power Transfer System", *IEEE Transactions on Industrial Electronics*, vol.56, issue.5, pp.1801-1812, 2009.

[154] P. Sample, T. Meyer, R. Smith, "Analysis, Experimental Results, and Range Adaptation of Magnetically Coupled Resonators for Wireless Power Transfer", *IEEE Transactions on Industrial Electronics*, pp.1-11, 2010.

[155] PowerMat Inc., >http://www.powermat.com< accessed on 20-05-2010.

[156] C. Zhu, K. Liu, C. Yu, R. Ma and H. Cheng, "Simulation and experimental analysis on wireless energy transfer based on magnetic resonances", *IEEE Vehicle Power and Propulsion Conference*, pp.1-4, 2008.

[157] Z. N. Low, R. Chinga, R. Tseng and J. Lin, "Design and test of a high-power high-efficiency loosely coupled planar wireless power transfer system", *IEEE Transactions on Industrial Electronics*, vol.56, no.5, pp.1801-1812, 2009.

[158] J. Casanova, Z. N. Low and J. Lin, "A loosely coupled planar wireless power system for multiple receivers", *IEEE Transactions on Industrial Electronics*, vol.56, no.8, pp.3060-3068, 2009.

[159] B. Jiang, J.R. Smith, M. Philipose, S. Roy, K. Sundara-Rajan, A.V. Mamishev, "Energy scavenging for inductively coupled passive RFID systems", *IEEE Transactions on Instrumentation and Measurement*, vol.56, issue.1, pp.118-125, 2007.

[160] Y. Yang, D. Divan, R.G. Harley, T.G. Habetler, "Power line sensornet - a new concept for power grid monitoring", *IEEE Power Engineering Society General Meeting*, pp.1-8, 2006.

[161] G.X. Wang, W.T. Liu, M. Sivaprakasam, G.A. Kendir, "Design and analysis of an adaptive transcutaneous power telemetry for biomedical implants", *IEEE Transactions on Circuits and Systems I: Regular Papers*, vol.52, issue.10, pp.2109-2117, 2005.

[162] J.T. Boys, G.A.J. Elliott, G.A. Covic, "An Appropriate Magnetic Coupling Co-Efficient for the Design and Comparison of ICPT Pickups", *IEEE Transactions on Power Electronics*, vol.22, issue.1, pp.333-335, 2007.

[163] A. Kurs, A. Karalis, R. Moffatt, J.D. Joannopoulos, P. Fisher, M. Soljacic, "Wireless power transfer via strongly coupled magnetic resonances", *Science Magazine*, vol.317, no.5834, pp.83-86, 2007.

[164] David Penly, "Induction", >http://facstaff.gpc.edu/ dpenly/1112/Induct.pdf< accessed on 19-05-2010.

[165] Shashi M. Kanbur, "Induction and inductance", >http://www.oswego.edu/∼kanbur/phy313/Fard.pdf< accessed on 19-05-2010.

[166] Y.K. Tan and S.K. Panda, "A novel method of harvesting wind energy through piezoelectric vibration for low-power autonomous sensors", *nanoPower Forum (nPF'07)*, 2007.

[167] S.C. Xie, "Inductive Energy Transfer System", *Bachelor Thesis*, National University of Singapore, 2008.

[168] "Wireless power supply", >http://www.wirelesspowersupply.net/< accessed on 26-05-2010.

[169] Darren Murphy, "Case-mate's hug wireless iPhone charging solution shipping now for $100", >http://www.engadget.com/2010/03/09/case-mates-hug-wireless-iphone-charging-solution-shipping-now-f/< accessed on 26-05-2010.

[170] "Sony develops effective wireless power transmission up to 60W", >http://www.mydigitallife.info/2009/10/03/sony-develops-effective-wireless-power-transmission-up-to-60w/comment-page-1/< accessed on 26-05-2010.

[171] Lucas Jorgensen and Adam Culberson, "Wireless power transmission using magnetic resonance",

>http://www.cornellcollege.edu/physics/courses/phy312/Student-Projects/Magnetic-Resonance/Magnetic-Resonance.html< accessed on 26-05-2010.

[172] Pranesh Somasundaram, "Analysis and Optimization of Strongly Coupled Magnetic Resonance for Wireless Power Transfer Applications", *Bachelor Thesis*, National University of Singapore, 2010.

[173] W.J. Chow, "Wireless Transmission of Power with Magnetic Resonance", *Bachelor Thesis*, National University of Singapore, 2008.

[174] A. Karalis, J. Joannopoulos and M. Soljacic, "Efficient wireless non-radiative mid-range energy transfer", *ScienceDirect-Annals of Physics*, vol.323, no.1, pp.34-48, 2008.

[175] B. Cannon, J. Hoburg, D. Stancil and S. Goldstein, "Magnetic resonant coupling as a potential means for wireless power transfer to multiple small receivers", *IEEE Transactions on Power Electronics*, vol.24, no.7, pp.1819-1825, 2009.